Abstract

The performance of piezoelectric cantilever beam energy harvesters subjected to base excitation is considered in this work. Based on the linear assumption, a theoretical model is developed to predict the mechanical and electrical responses of the harvester and in comparison to other theoretical models, more accurate mode shape functions are used for the structural part of the harvester. The model is validated against experimental measurements and parameter studies are carried out to investigate the maximum power output in different situations.

In some applications, like powering tyre pressure monitoring sensors (TPMS), energy harvesters are subjected to large amplitude shocks and high levels of acceleration, which can cause large bending stresses to develop in the beam, leading to mechanical failure. In this work, a bump stop is introduced in the energy harvester design to limit the amplitude of vibration and prevent large amplitude displacement. A theoretical model is developed to simulate the energy harvester impacting a stop, and the model is used to investigate how the electrical output of the harvester is affected by the stop. The work demonstrates how the model can be used as a design tool for analysing the compromise between the electrical output and structural integrity.

Nonlinear behaviour of the energy harvester is observed to have a significant effect on the resonance frequencies when the harvester is subjected to large amplitude

base accelerations. To correctly predict the behaviour of the harvester, piezoelectric material nonlinearity and geometric nonlinearity are incorporated in the theoretical model. It is found that the nonlinear softening effect is dominated by the material nonlinearity, while the geometric nonlinearity is less significant. The nonlinear energy harvester model is used in conjunction with the bump stop and results obtained using the linear and nonlinear models are compared to experimental measurements to investigate the importance of using a nonlinear model. The inclusion of nonlinear behaviour is shown to improve significantly the accuracy of predictions under some circumstances.

The energy harvester models developed in this work are used to simulate the electrical power generated in a TPMS application, where the harvester embedded in the tyre is subjected to large radial accelerations as the tyre rolls along the road. The simulated results are compared to reported experimental work and agreement is found between the results.

Acknowledgement

I would like to thank Atlantic Inertia Systems (now Goodrich) and EPRSC for their financial support for this PhD research project, and particularly to thank Atlantic Inertia Systems for their technical support throughout the project as well.

I have to sincerely thank my supervisors, Dr. Stewart McWilliam, Prof. Atanas Popov and Prof. Colin Fox. I am very grateful and also it is my pleasure to have an opportunity to work with them. Their expertise and experience are priceless to me and the project. Their words and comments are always inspirational and motivational.

Colleagues in the ITRC Building are always friendly and nice to me. Especially for those who share the same office with me, I really want to say thanks for their help and advices, and more importantly the joy that we had in the office.

Of course I have to thank those who love, support and encourage me. Finally, I want to say thank you to my parents and my brother. It is simple but it contains many things that cannot be described by words.

TABLE OF CONTENTS

Nomenclature

Latin symbols

A_b	Cross-section area of the beam
A_p	Cross-section area of the piezoelectric layer
A_s	Cross-section area of the substrate layer
A_r	Cross-section area of the stop
B_{max}	Amplitude of base acceleration
b	Displacement of the base
$\mathbf{C}$	Structural damping matrix
C_p	Piezoelectric capacitance
C_s	Capacitance of the storage capacitance
D	Electric displacement
d	Offset distance of the tip mass
d_{31}	Piezoelectric constant
d_t	Tyre deformation
E_p	Young's modulus of piezoelectric material
E_s	Young's modulus of substrate
E_v	Electric field
e	Piezoelectric coupling coefficient
F	Contact force
f	Excitation frequency

g	Acceleration due to the gravity, 9.81 ms^{-2}
I	Generated current
I_b	Second moment of area
J	Moment of inertia of tip mass
$\mathbf{K}$	Stiffness matrix
K_e	Kinetic energy
$\mathcal{L}$	Lagrangian
L_b	Length of beam
L_r	Length of stop
M	Mass of tip mass
$\mathbf{M}$	Mass matrix
n_b	Number of modes for beam
n_r	Number of mode for stop
P_e	Potential energy
q	Electric charge
R	Resistance
R_t	Radius of the car tyre
S	Strain
s	Arclength of the inextensible beam
S_p	Strain in the piezoelectric layer
S_s	Strain in the substrate layer
T	Stress
T_p	Thickness of the piezoelectric layer
T_s	Thickness of the substrate layer

t	Time
t_s	Time step
V	Volume
V_p	Volume of the piezoelectric layer
V_s	Volume of the substrate
v	Voltage across a resistor
v_{Cp}	Voltage across an energy harvester
v_{Cs}	Voltage across a storage capacitor
v_d	Voltage drop in a diode
v_s	Voltage due to base acceleration
v_{imp}	Voltage due to impact
W	Work done
W_p	Width of piezoelectric layer
w_i	i^{th} mode of the generalised coordinate
X_c	Contact point along the beam
X_r	Contact point on the stop
Y	Displacement of beam
Y_s	Displacement of the beam due to base acceleration
Y_{imp}	Displacement of the beam due to impact
Y_x	Longitudinal displacement of the beam
Y_y	Transverse displacement of the beam
Z	Displacement of stop
Z_s	Displacement of stop due to base acceleration
Z_{imp}	Displacement of stop due to impact

Greek symbols

Δ	Initial gap between the beam and stop
ε_P	Permittivity of piezoelectric material
γ_b	Damping ratio of the beam
γ_r	Damping ratio of the stop
κ	Radius of gyration
ρ_p	Density of the substrate
ρ_s	Density of the piezoelectric layer
σ	Mechanical stress
σ_p	Stress of the piezoelectric layer
σ_s	Stress of the substrate layer
Φ_b	Mode shape function of the beam
Φ_r	Mode shape function of the stop
Θ	Electromechanical coupling matrix
Ω_t	Angular speed of the car tyre
ω_b	Natural frequency of the beam
ω_r	Natural frequency of the stop

Abbreviations

AC	Alternating current
AlN	aluminium nitride
DC	Direct current
FRF	Frequency response function
MEMS	Micro-electro-mechanical systems
mph	Miles per hour
N.A.	Neutral axis
ODE	Ordinary differential equation
PDE	Partial differential equation
PDVF	Polyvinylidene fluoride
PZT	Lead zirconate titanate
TPMS	Tyre pressure sensor system
RF	Radio frequency
rms	Root mean square
SHM	Structural health monitoring
SSHI	Synchronised switching harvesting with inductor
ZnO	Zinc oxide

List of figures

List of tables

Chapter 1. Introduction

1.1 Background

Energy harvesting has received much attention over the last decade and investigates mechanisms for converting energy available from the surrounding (e.g. motion, light, heat, RF, etc) into usable electrical energy. Energy harvesting is widely targeted for powering MEMS (**M**icro-**E**lectro-**M**echanical **S**ystems) devices, which have the potential to be more power efficient and less energy consuming due to their reduced size. Wireless sensors have become more practical for potential applications. The conventional approach to supplying electrical energy to wireless sensors is to use batteries. Although MEMS sensors have low power requirements, the relatively short lifetime of batteries cannot fulfil the requirements for some wireless sensors. This is particularly the case in applications where replacing batteries is difficult, dangerous and not cost effective. Energy harvesting has been proposed as a solution to this problem, enabling wireless sensors to be self-powered.

The development of energy harvesting technologies has seen rapid growth over the last few years. This can be attributed to the following reasons:

- Monitoring and surveillance using wireless sensor nodes are in great demand for military and commercial applications.
- Commercial awareness of the market demand for self-powered devices pushes

the growth of energy harvesting.

- The slow growth in battery technology does not meet the requirements for advanced miniature electronics, sensors, wireless modules and MEMS.
- A significant amount of research has been performed and is in progress on energy harvesting.

1.2 Research motivation and project objectives

Vibration energy exists almost everywhere and this type of energy can be converted into electrical energy through piezoelectric, electromagnetic and electrostatic transducers. Vibration-based energy harvesting using piezoelectric materials has received significant attention recently and has good potential for power generation. In the past few years, piezoelectric energy harvesting has been linked to safety applications in the automotive industry. This application is expected to have great impact on the energy harvesting market.

Nowadays, cars are equipped with a variety of sensors providing comprehensive real-time information to improve driver safety. Most of these sensors are MEMS devices. The advantages of MEMS sensors are that they are small and consume less power compared to macro-scale devices. Sensors are often placed at different locations, where wired connections are not possible and the use of wireless sensor nodes is necessary. A major issue with existing wireless sensors is that the electric power is normally supplied by batteries, and battery replacement can be difficult and not cost effective. For these reasons, energy harvesting has been targeted as a solution for the power supply to wireless sensors, by converting wasted or unused

energy available from ambient sources into usable electrical energy.

Tyre Pressure Monitoring Systems (**TPMS**) have become an important sensor system in vehicles. Over the last five years, development has grown rapidly as they become a mandatory feature for new vehicles [1]. The market for TPMS was predicted to grow by 50% in 2010 [2]. According to a marketing report in 2007 [3], the market for TPMS was expected to reach 300 million US dollars in 2012, based on the assumption that European legislation makes TPMS mandatory equipment on all new models of passenger vehicle. The European Parliament approved the legislation in 2009 and is scheduled to be introduced in November 2012 [4]. The US government has already approved a similar legislation, while the Far East countries intend to make TPMS mandatory on new vehicles [1].

The importance of appropriate tyre pressure is well recognised. TPMS was first introduced in the mid 1980s as a luxury feature in top range passenger vehicles, but they have not been widely adopted until recent years. The grip and braking performances of vehicles are affected by under- or over-inflated tyres. Tyres with the incorrect pressure also reduce the tyre lifetime and increase the rolling resistance, which is a significant contribution to fuel consumption that can be directly related to the CO_2 emissions [5]. TPMS will have a great impact in meeting the requirements for CO_2 emission reduction set by the European Union Emission Trading Scheme (EU ETS) [6]. For these reasons, it is essential that the tyre pressure is monitored.

Current TPMS consist of a MEMS pressure sensor and a wireless transmission

module to transmit data embedded inside tyres. They are normally required to serve between 7 to 10 years by car manufacturers. Using batteries is not an ideal method for supplying energy to these wireless sensors, because batteries fail to meet the lifetime requirement and they are also difficult to access inside the tyre to be replaced.

There is an abundance of vibration energy available in car tyres that can be converted into electrical energy using energy harvester methods. A recent patent proposed using piezoelectric materials to harvest energy for this application. The proposed energy harvesters consisted of a piezoelectric cantilever beam with a tip mass attached to the free end of the beam [7]. Literature for the design of piezoelectric energy harvesters is reviewed in Chapter 2.

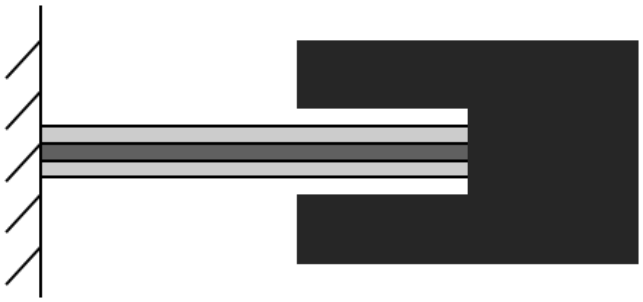

Figure 1.1 The proposed piezoelectric energy harvester used in the TPMS application [7]

In this application, the energy harvester is attached to the inner wall of the tyre, and it experiences high levels of acceleration due to tyre deformation and wheel rotation. The tyre deforms at the contact patch (where the harvester is located) once every wheel rotation, whenever the patch makes contact with the road. A rapid change in the shape of the deformed tyre causes high radial accelerations. In addition, the energy harvester is subjected to a centripetal acceleration, and the

magnitude of this acceleration depends on the square of the vehicle speed. High accelerations are beneficial for the generation of electrical energy by the harvester, but also make the energy harvester vulnerable to mechanical failures due to the high bending stresses developed. In order to prevent and reduce the possibility of mechanical failures, the displacement of the energy harvester needs to be limited to reduce the bending stress. In this work, this is achieved by using a bump stop in which the cantilever energy harvester makes contact with the stop if the displacement is too large.

The main objectives of this PhD project are to develop and validate a model for a piezoelectric energy harvester and investigate its ability to generate electrical power. The work performed to achieve these objectives includes:

- Developing a theoretical model for a cantilever piezoelectric energy harvester, based on the assumption that the system is linear, to predict the mechanical and electrical responses of the harvester.
- Extending the model to include the presence of a tip mass at the free end of the beam. Deriving the natural frequencies and mode shape functions for a cantilever beam with a tip mass whose centre of gravity does not coincide with the point of attachment.
- Carrying out experiments to test different samples of energy harvester and comparing experimental measurements to theoretical results to validate the theoretical model.
- Incorporating a bump stop in the energy harvester design to prevent large amplitudes of vibration and modelling the impact dynamics between the energy harvester and stop in order to investigate how the stop affects the

performance and bending stress in the harvester.

- Incorporating the effects of piezoelectric material nonlinearity and geometric nonlinearity in the mechanical vibration model for a cantilever beam energy harvester subjected to high levels of base acceleration.
- Developing and validating a nonlinear model for a piezoelectric energy harvester, which incorporates piezoelectric material nonlinearity and geometric nonlinearity of the cantilever beam to address frequency shifts due to high levels of base acceleration.
- Incorporating the nonlinear energy harvester in the impact model to investigate the improvement in the accuracy of predictions compared to the linear model.
- Simulating the energy harvester operating in the TPMS application to understand how the power is generated inside a car tyre.

1.3 Thesis overview

This section provides an overview of the contents for the chapters of the thesis. Chapter 2 provides introductory materials and a brief background of piezoelectric energy harvesting and reviews recent piezoelectric energy harvesting design concepts and applications. Chapter 3 presents a linear theoretical model for a piezoelectric energy harvester with a tip mass, and includes the natural frequency and mode shape calculations for the energy harvester structure. In Chapter 4, energy harvester samples are tested experimentally in order to validate the linear theoretical model developed in Chapter 3, and parameter studies are conducted in order to investigate the conditions when optimal power output is achieved. In

Chapter 5, the theoretical model developed in Chapter 3 is extended to include a bump stop, which is used to limit the amplitude of vibration of the cantilever beam. The model is used to investigate the influence of the electrical output and the potential reduction in bending stress for the harvester. Chapter 6 develops a theoretical model to investigate the influence of piezoelectric material and geometric nonlinearities on the performance of the harvester, and experimental measurements are compared to the theoretical results to validate the nonlinear model. In Chapter 7, the nonlinear energy harvester model developed in Chapter 6 is also used to incorporate the bump stop. In the presence of the stop, theoretical results from both linear and nonlinear models are compared to experimental measurements to investigate the importance of using the nonlinear model. Chapter 8 presents a case study to investigate how the electric power is generated inside a car tyre for the TPMS application. Simulation results are compared to published experimental measurements to make sure that the theoretical model offers realistic predictions. Chapter 9 summaries the conclusions for the work and makes suggestions for future work.

Chapter 2. Literature review

2.1 Introduction

The concept of energy harvesting has existed for many centuries in the form of windmills, watermills and solar power systems [8]. Over the year, these macro-scale energy harvesting technologies have been continually developed. Due to the energy shortages (i.e. fossil fuel) and the move towards sustainable energy sources, these technologies are becoming increasingly important and practical for converting ambient energy into usable electrical energy, also known as sustainable energy.

The energy harvesting concept has been extended from macro- to micro-scales to meet the needs of applications using wireless sensor networks. Wireless sensor nodes and networks are useful in medical, civil and military applications [9]. The breakthrough in MEMS technologies over the last two decades plays a significant role in reducing power consumption and increasing the power efficiency for electronics and electromechanical devices, such as pressure sensors, gyro sensors, accelerometers, scanning mirrors and ink jet heads [10]. However, using batteries to supply power to these sensors is not desired as battery replacement is a problem. Using energy harvesting is an attractive solution to powering wireless sensor nodes.

In recent years, interest in energy harvesting has increased rapidly, and harvesting vibration energy using piezoelectric materials has attracted a great deal of attention

[11]. In this chapter, selected literature on piezoelectric energy harvesting devices is reviewed with emphasis on modelling for the most typical design. This chapter also reviews some other designs and applications to date.

2.2 Piezoelectric energy harvesting

The piezoelectric effect was discovered in 1880 by the Curie Brothers, Pierre and Jacques. They observed the direct piezoelectric effect in experiments on crystals and noticed that certain materials become electrically polarised when a mechanical load is applied. Indeed, the piezoelectric effect also allows piezoelectric materials to deform when they are subjected to an electric field. Most piezoelectric materials are crystalline solids, and the piezoelectric effect is normally described by piezoelectric constitutive equations, in which the mechanical and electrical properties of the piezoelectric material are coupled together.

Piezoelectric materials are used widely in sensors, acoustic emission transducers, actuators, vibration controls and micro-positioning devices. In recent years, they have been used in vibration energy harvesting applications and much work has been published on modelling, experimental validation, energy harvesting circuitries, design and applications of piezoelectric energy harvesters.

There are two common modes available for piezoelectric energy harvesting to couple the mechanical strain and polarisation: the d_{31}-mode and the d_{33}-mode. Figure 2.1 illustrates that the direction of the applied force is perpendicular to the direction of the generated voltage for the d_{31}-mode, while the directions of the

applied force and potential voltage difference are the same in the 33-mode [12].

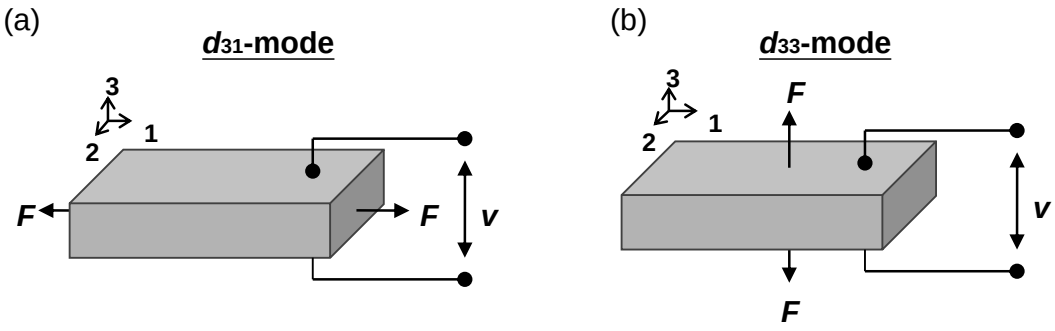

Figure 2.1 Operating mode for piezoelectric transducers: (a) d_{31}-mode; (b) d_{33}-mode

The choice of piezoelectric material can significantly influence the performance of an energy harvester. Lead zirconate titanate, also known as PZT, is a commonly used piezoelectric material. It was developed in the mid-1950s [13] and is widely used for energy harvesting nowadays. This material is very brittle and can crack under high frequency cyclic loads. Another common piezoelectric material is polyvinylidene fluoride, also known as PVDF. PDVF is more flexible than PZT but its ability to convert strain energy into electrical energy is not as good as PZT [11]. Sodano *et al.* [14] tested three piezoelectric actuators: MFC, Quick Pack IDE and Quick Pack as piezoelectric energy harvesters and compared the power outputs. It was found that Quick Pack outperformed the other two in terms of energy output. Also, the use of polyurea piezoelectric thin film in energy harvesters was proposed recently by Koyama and Nakamura [15]. In contrast to PZT, polyurea is lead-free as lead is a poisonous metal, and its fracture stress is higher.

2.2.1 **Designs and applications**

Different types of piezoelectric transducer can be used to harvest vibration energy,

including monomorph, bimorph, stack or membrane [12]. Each configuration has its own advantages and limitations, and in general it is not possible for one configuration of energy harvester to perform well in all applications. For this reason, energy harvesters are normally designed for a specific application and a particular frequency range of operation. The design of an energy harvester has significant influence on the performance of the power generation. Besides, the designs for power management and circuitries are equally important in an overview of an energy harvesting system because they can significantly affect the efficiency of energy conversion.

Different designs and applications for energy harvesters are reviewed in the following subsections. One of the most common designs is the cantilever beam configuration and this is reviewed in great detail. Also, one of the subsections reviews different circuits used to store the energy harvested.

2.2.1.1 Cantilever piezoelectric energy harvesters

The idea of using a piezoelectric material to harvest energy was first introduced in 1995 by Umeda *et al.* [16]. They proposed a mechanism for electrical power generation through mechanical impact on a piezoelectric transducer. (see Figure 2.2). A theoretical model was derived and the proposed mechanism was demonstrated and validated experimentally.

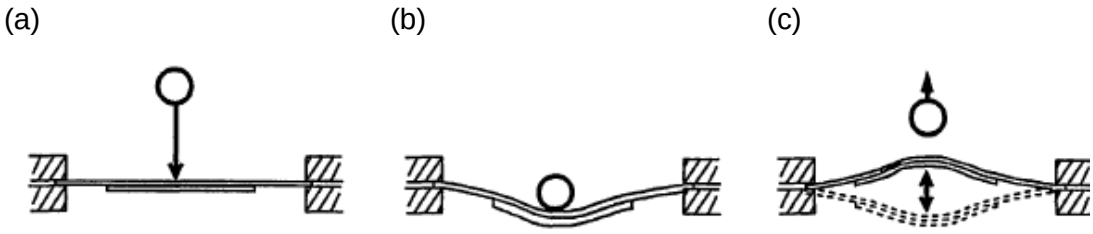

Figure 2.2 Illustration of the mechanism for the piezoelectric transducer proposed by Umeda [16]

More recently, several different designs have been proposed for piezoelectric energy harvesting [17]. The beam bending concept is the most popular due to the simplicity of the structure to be manufactured. Also, the most common design for piezoelectric energy harvesters uses the cantilever configuration to operate in the d_{31}-mode, see Figure 2.3. In general, the transverse vibration of these energy harvesters is designed to be excited by base motions. The transverse vibration causes the beam bending to have deformation in the axial direction along the beam and the electrical charge is generated through the thickness of the piezoelectric layer. Also, the higher modes are not normally used to harvest energy because the charge induced by the tensile and compressive strains cancel, reducing the electrical output [18].

Figure 2.3(a) and (b) show monomorph and bimorph configurations for cantilever piezoelectric energy harvesters, respectively. The monomorph consists of a layer of piezoelectric material attached to a substrate layer, while the bimorph has two layers of piezoelectric material attached to a substrate layer. For the bimorph configuration, the piezoelectric layers can be connected either in series or in parallel [19]. To maximise the power output of an energy harvester, the fundamental natural frequency of the harvester is tuned to match the excitation frequency by attaching a

tip mass to the free end of the cantilever. Although the tip mass is taken into account in modelling in some studies [20-22], the offset distance from the tip of beam and the inertia of the mass have not been considered previously.

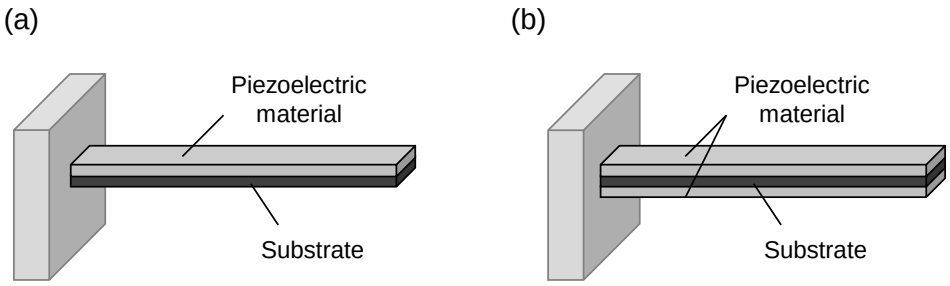

Figure 2.3 Cantilever piezoelectric energy harvester: (a) monomorph; and (b) bimorph configurations

2.2.1.1.1 Linear models

Analytical models for cantilever piezoelectric energy harvesters have been reported in [20-28]. Despite the different approaches used for the modelling, the authors all assumed the models to be linear (small vibration amplitude and linear piezoelectric constitutive equations).

There are two common energy harvesting circuits used in research studies. One is a simple resistive circuit where the energy harvester is connected directly to a load resistor in series as shown in Figure 2.4(a). Sodano *et al.* [23] developed a theoretical model for a bimorph energy harvester connected to a load resistor, and carried out a simple validation. Erturk *et al.* [29] conducted a similar study on bimorph energy harvesters but a tip mass was also incorporated in the model. More detailed experimental results were also included to validate the theoretical model. Another option is to use a charging circuit, where the electrical charge generated by

the energy harvester is stored in a capacitor. Theoretical models of a basic charging circuit for energy harvesting applications have been presented in the literature [30, 31]. In their studies, the energy harvester models are subjected to harmonic base excitation and generate alternating current (AC). AC cannot be used to directly charge a capacitor, and as shown in Figure 2.4, the AC is converted to DC using a full-wave diode bridge prior to charging the storage capacitor. Experimental work was also carried out to validate the theoretical model.

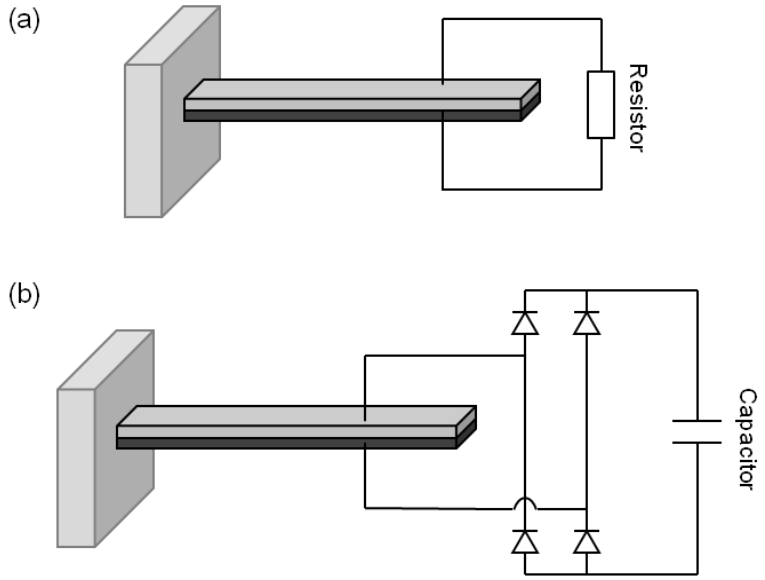

Figure 2.4 Energy harvester connected to: (a) resistive circuit; and (b) charging circuit

2.2.1.1.2 Nonlinear models

The aforementioned studies are based on the assumption that the electromechanical systems are linear. For example, the linear version of the piezoelectric constitution equations are used [32]. However, it is likely that the linear model will only be valid for low base accelerations because piezoelectric materials are well known to exhibit nonlinear behaviour under high amplitudes of mechanical or electrical excitation [33].

Some linear models for energy harvesters have been validated experimentally and have been shown to provide good agreement between theory and experiment [23, 27, 29]. In these studies, relatively low levels of excitation were used in the experimental validations. However, such models might not be valid for higher acceleration levels, like those present in TPMS (see Chapter 8). Since this is an important research area for piezoelectric materials and their applications, a number of studies have considered the influence of nonlinearity in piezoelectric materials [33-35].

Nonlinear effects can significantly affect the performance of energy harvesters. The main reason for this is that the resonance frequency is amplitude dependent and the performance of an energy harvester is critically dependent on the resonance frequency being excited. On this basis, the nonlinearities present in energy harvesters need to be considered, particularly if the energy harvester is subjected to large amplitude vibrations. Few studies have focused on nonlinearities in energy harvesting applications [36, 37] and most of these are for piezoelectric sensors and actuator systems [38-40]. Some of the theoretical models developed have been validated against experimental results [41, 42]. The typical nonlinear behaviour of an energy harvester is reflected in the dependence of the resonance frequency on excitation amplitude, and backbone curves can be used to describe the amplitude-frequency characteristics of nonlinear systems. Piezoelectric materials typically exhibit strong material nonlinearity which is determined by nonlinear material properties. Although linear material properties are widely available, there is limited literature for material properties beyond the linear range.

2.2.1.1.3 Beam shapes

The rectangular beam shape is adopted in the majority of studies for cantilever piezoelectric energy harvesters. However, Frank *et al.* [43] modelled and investigated an energy harvester with a triangular beam shape as shown in Figure 2.5. In their work, rectangular and triangular-shaped beam energy harvesters were made and the power outputs compared. It was found that the maximum displacement and maximum power out were increased using a triangular-shaped beam. A similar study examined the power output of energy harvesters with different shapes of piezoelectric layer, while the shape of the substrate layer is kept rectangular [44]. It was found that the trapezoidal shape can more than double the power output compared to rectangular-shaped beams [45]. The reason for this is that the strain distribution for a trapezoidal-shaped cantilever beam is more uniform throughout the structure. Similar findings were observed in [44].

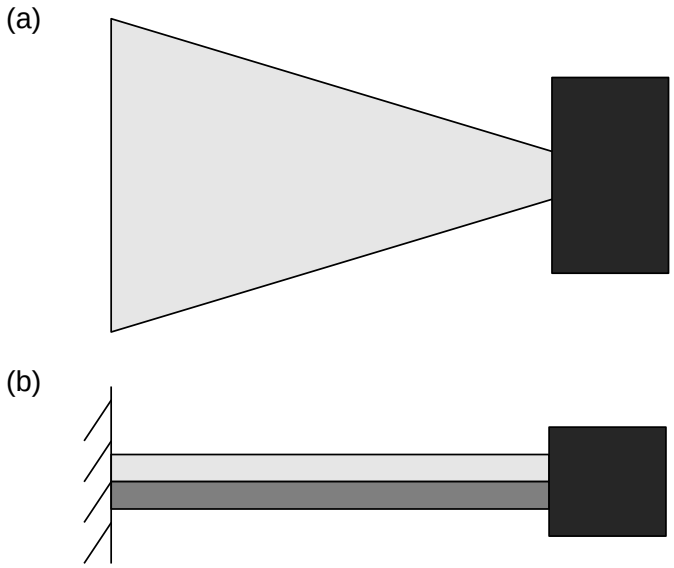

Figure 2.5 A triangular shaped beam is used for a piezoelectric energy harvester [43] (a) plan and (b) side views

2.2.1.1.4 Energy harvesting circuits

A theoretical model performed by Liao [46] showed that an additional capacitor in series with a piezoelectric energy harvester (see Figure 2.6) increases the bandwidth of the power spectrum. A parameter optimisation study for the energy harvester indicated that the optimal capacitance is independent of the optimal resistance.

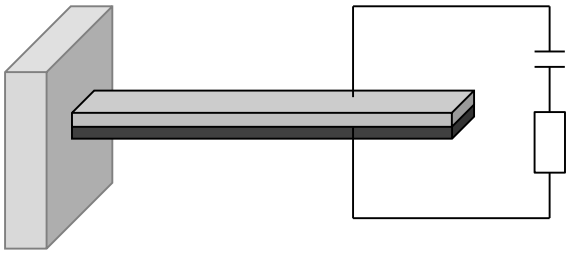

Figure 2.6 Energy harvester is connected to a capacitor and resistor in series

Some researchers pay more attention to interface circuits for piezoelectric energy harvesters to improve the power performance. Descriptions of the different circuits used in energy harvesting can be found in recent publications [47-51]. These circuits were developed to increase the efficiency of energy conversion and the power output from energy harvesters. For vibration-based energy harvesting, the electrical output is in AC form, so an AC-DC conversion is needed in a practical implementation. Since the harvested power fluctuates with time and can be small occasionally, the AC-DC conversion has to be efficient. Dallago *et al.* [52] proposed a doubler AC-DC converter for piezoelectric energy harvesting and an efficiency of 91% was achieved in the conversion. Lefeuvre *et al.* [53] described the characteristics and principles of three techniques used for energy harvesting interface circuits. Figure 2.7 shows the circuits investigated in their study and the performance was compared to the power output from a basic charging circuit, see

Figure 2.4(b). The work showed that the circuit shown in Figure 2.7(a) can increase the power by a factor of 4 compared to the basic charging circuit, while the other two circuits were able to increase the power for weakly coupled systems and required less piezoelectric material for a given power requirement.

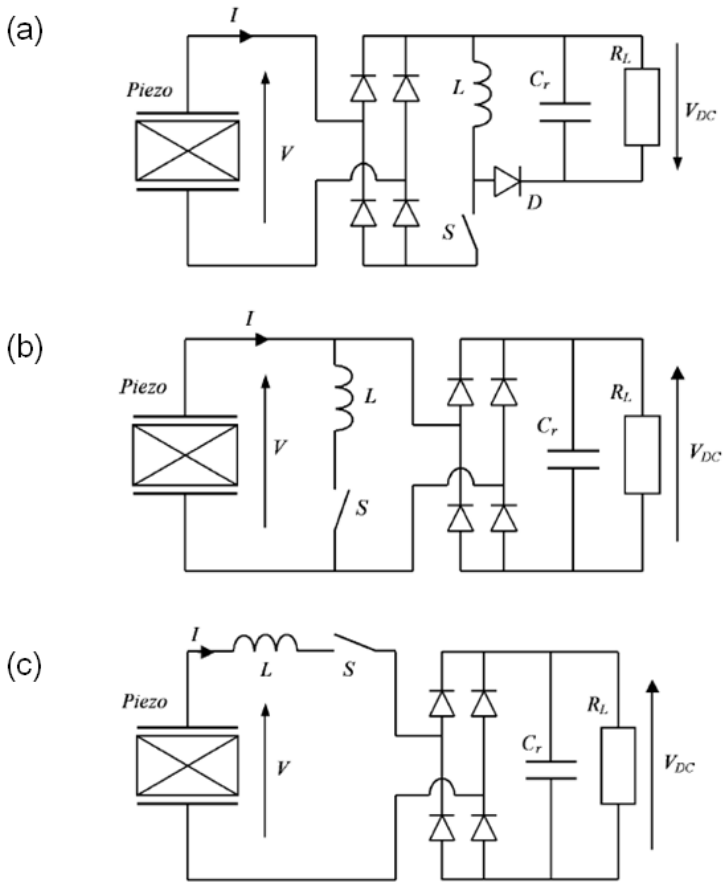

Figure 2.7 Three circuits investigated in [53]: (a) synchronous charge extraction interface circuit; (b) parallel-SSHI interface circuit; (c) Series-SSHI interface circuit

2.2.1.1.5 Power optimisation

Power optimisation for a piezoelectric energy harvester has been studied by Renno *et al.* [54]. The optimised energy harvester operates in the d_{33} mode and the additional inductor is connected to a resistor in parallel or in series. The effect of mechanical damping was studied and was found to have a significant effect on the

system optimisation. If the damping ratio is below a bifurcation damping ratio of the system, the power has two maxima and one minimum. Above the bifurcation damping ratio, only one maximum is obtained for the power.

For vibration-based piezoelectric energy harvesters, it is often possible to determine the optimum conditions (e.g. in terms of frequency) for the maximum power output of an energy harvester. However, ambient vibrations can vary and this can significantly affect the power output. Chao *et al.* [55] proposed a maximum power tracking scheme for piezoelectric energy harvesters, in which a hybrid scheme was used that switched between passive and active diodes to improve the efficiency or reduce the energy loss. The passive diode rectifier is used for start-up, while the active diode rectifier is used to reduce the voltage drop.

2.2.1.2 **MEMS-based piezoelectric energy harvesters**

For some applications, sensor systems are required to have a small size. Sensor size is not a major issue nowadays, as miniaturised devices can be realised using advanced MEMS technologies. Ironically, the size of batteries is often greater than the size of some sensor systems. Battery-less MEMS sensors have the potential to reduce the weight and size of sensor systems.

In many applications, vibration energy is converted by piezoelectric or electromagnetic energy harvesters. However, piezoelectric energy harvesting is more suitable for MEMS devices than electromagnetic energy harvesting because electromagnetic energy harvesters are more difficult to operate at optimal conditions [56]. Chao *et al.* [57] also discussed the challenges and important

considerations in the design of micro-scale energy harvesting systems. For example, the natural frequencies of MEMS devices are always high due to being miniaturised. Fabrication processes for different micro-scale piezoelectric energy harvesters have been reported by several researchers [58-63]. Jeon *et al.* [59] developed a MEMS piezoelectric energy harvester operating in the d_{33} mode, where the electric field direction is parallel to the strain direction. The energy harvester is designed to obtain a high open-circuit voltage to overcome the forward voltage drop in a diode bridge. Marzencki *et al.* [60] fabricated an energy harvesting system having a volume of 5 mm^3 that consisted of a 1 μm thin piezoelectric layer of aluminium nitride (AIN) and a Silicon-On-Insulator (SOI) substrate on which the AIN layer is deposited. The micro-generator was reported to be capable of powering a simple wireless sensor node. Shen *et al.* [63] fabricated a PZT-based cantilever energy harvester with a micro-machined silicon proof mass for low frequency applications. The volume of the harvester is about 0.769 mm^3. When the harvester is excited at an amplitude of 0.75g, the fundamental resonance is 183.8 Hz and the average power output is 0.32 μW at an optimal resistance of 16 kΩ. Muralt *et al.* [61] also fabricated a mirco-power generator with interdigitated electrodes in which the piezoelectric layer and silicon substrate are 2 μm and 5 μm thick, respectively. When the device was excited at 2g at 870 Hz, an output power of 1.4 μW was measured at optimal resistance.

2.2.1.3 **Arrays of piezoelectric energy harvesters**

As mentioned in Section 2.2.1.1, the cantilever design is one of the most typical types of piezoelectric energy harvester, but other designs have been considered and reviewed. A design for a mechanical band-pass filter has been studied by Shahruz

[64], see Figure 2.8. The energy harvester comprises an array of cantilever beams with tip masses. If the cantilever beams and tip masses are chosen correctly, the operational frequency bandwidth can be widened to guarantee the power output. Several studies have reported results for this type of piezoelectric energy harvester [65, 66]. Liu *et al.* [65] demonstrated the fabrication process and presented some experimental work for the piezoelectric generator shown in Figure 2.9. Also, an electrical connection for an array of cantilever beams was suggested to prevent cancellation due to the phase difference in the voltage. The frequency bandwidth covered the range from 226 Hz to 234 Hz and the power generator reported produced an electrical power of 3.98 μW and a DC voltage of 3.93 V with an acceleration of 0.5g. Compared to a single cantilever beam design, the advantage of the array design is that the power generation and the frequency bandwidth are enhanced. The disadvantages are the bulky size of the energy harvesting system and it is likely that only one cantilever beam is excited at resonance, while the other off-resonance cantilever beams produce much less power.

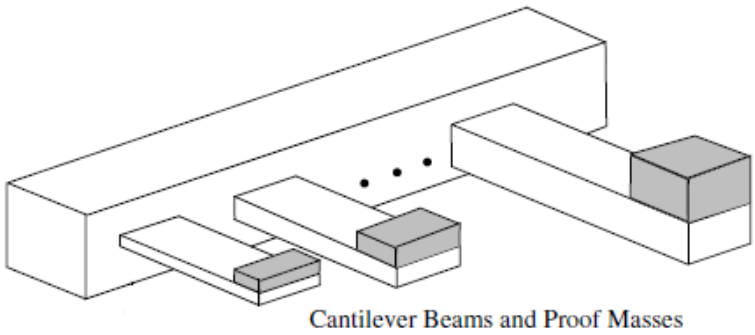

Figure 2.8 The design of a mechanical band-pass filter [64]

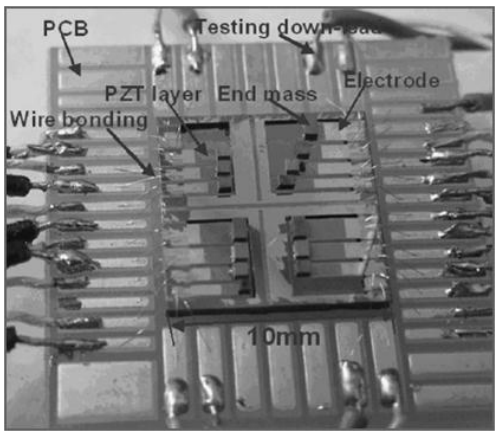

Figure 2.9 An array of piezoelectric generators reported in [65]

2.2.1.4 **Monitoring**

Many energy harvesting applications have been proposed for monitoring purposes. The low-power consumption of electronic devices improves the feasibility of adopting wireless sensors, and energy harvesting technologies resolve the battery lifetime problem by supplying power indefinitely through the collection of ambient energy. Structural Health Monitoring (SHM) is an important application domain for energy harvesting [67]. Wireless sensors used for SHM are usually embedded in the structure being monitored and this makes battery replacement difficult or impossible. In addition, a long-term monitoring is always required in SHM. This is why the emerging area of energy harvesting is essential for this kind of application.

Legislation requires TPMS to be mandatory in all new cars to improve driving safety [1]. Currently direct TPMS are MEMS-based and integrated sensor systems. These tyre-mounted TPMS are aimed to be functional with a lifetime of 10 years in the automotive industry. Existing energy storage methods, such as batteries, do not meet the power requirements and hence energy harvesting is targeted as an effective solution. Brusarosco *et al*. proposed a cantilever piezoelectric energy

harvester embedded in a tyre [7] to take advantage of the abundance of mechanical energy available in the tyre and the car body to generate electrical energy. The study demonstrated how the power output from the energy harvester is affected by car speed.

Another design was proposed for a TPMS application by Keck [68]. It is a simply supported beam design with a seismic mass attached to the middle of the beam, as shown in Figure 2.10. The piezoelectric material does not cover the full length of the beam and it is attached to the region of maximum stress located at the centre of the beam. A prototype has been tested with a diameter of 10.8 mm. The experimental results show that the energy harvester generates most power at a car speed of 80 km/h.

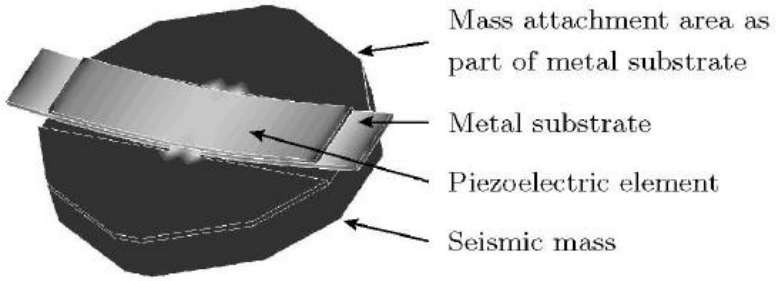

Figure 2.10 A proposed design of a piezoelectric energy harvester for TPMS [68]

2.2.1.5 **Wireless sensor networks**

Wireless sensor nodes have become available in the market recently, but these first generation products have not yet fully fulfilled expectations [56]. Wireless sensors can work individually or as a group. Wireless sensor networks are normally established using a number of sensors. The information obtained from these

sensors can be gathered for further signal processing or data exchange between the sensors. In some applications, sensor nodes have to be deployed for a long period of time and battery replacement is not possible, for instance in an animal-tracking application. For this reason, self-powered wireless transmission modules are becoming essential in many energy harvesting applications. The principle of operation and different circuitries for wireless transmission can be found easily in the literature [69, 70]. Cantatore and Ouwerkerk [70] investigated different energy harvesting methods for powering a wireless sensor that has a volume of 100 mm^3. Furthermore, an energy harvester is normally integrated with a wireless transmitter and a processor. Signal processing is a very important procedure in wireless sensor networks and several circuit techniques are discussed in [71].

2.2.1.6 **Nano-scale piezoelectric energy harvesting**

Currently most piezoelectric energy harvesters are either macro- or micro-scale, but the recent discovery of novel piezoelectric nano-materials provides a new area of research for harvesting energy using nanotechnology. ZnO is a piezoelectric and semiconducting material that is used extensively in nanostructures, such as nanowires, nanobelts, nanosprings, nanoflowers, etc [72]. Wang and Song *et al.* [73] have demonstrated that zinc oxide (ZnO) nanowires, see Figure 2.11, can be used to convert mechanical energy into electrical energy. A related work has been presented by Tong [74] to derive a theoretical model for predicting the electric response from the ZnO nanowires. These nano-wires were also proposed to be woven into cloth to capture energy from wind motion, acoustic vibration, friction and other mechanical energy, and convert it into electrical energy. The diameter of these nano-wires is typically about 30-100 nm. Research teams also claim that the generated energy

from the nano-wires would be able to power a personal mp3 player.

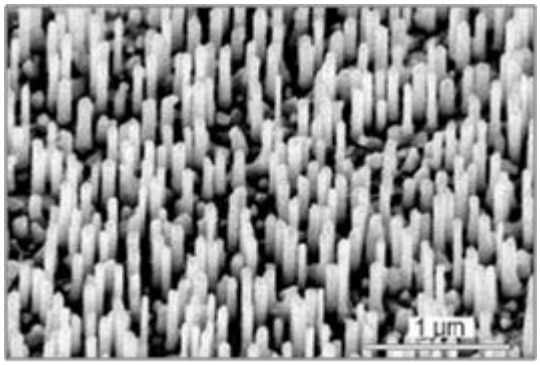

Figure 2.11 Microscopic image of ZnO nanowires captured by Wang [73]

Qin *et al.* [75] presented a nano-power generator where the ZnO nanowires grown radially around textile fibres are used to convert low-frequency vibration or friction energy into electric energy. They demonstrated the power generation ability of ZnO nanowires experimentally. The experimental setup is shown in Figure 2.12 where a ZnO-nanowire-covered fibre with a thin layer of gold coating is entangled with another fibre without the coating.

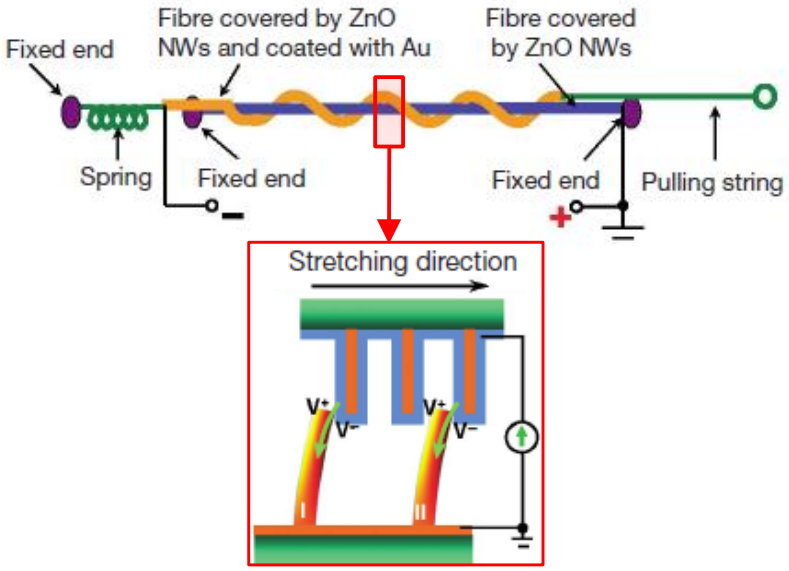

Figure 2.12 Schematics of the experimental setup: A fibre covered by ZnO nanowires and coating brushes another fibre covered by ZnO nanowires to generate power [75]

2.2.1.7 Vibration suppression using harvested energy

The power generated by a piezoelectric energy harvester converts mechanical energy into electrical energy, and leads to a reduction in the amplitude of vibration. This reduction is due to the presence of electrical damping that dissipates electrical energy through the electronics in the process of converting energy. Originally, piezoelectric transducers were used to work as shunt dampers to suppress unwanted vibrations in structures [76], and can be used for passive and active vibration control.

Active vibration control requires electrical power for operation. Wilhelm *et al.* [77] presented a novel method for suppressing vibration using both passive and active approaches. The concept of the proposed system is that the piezoelectric energy harvester generates electrical power, which is stored in a capacitor, and the vibration energy is reduced. Then, the stored electrical energy can be recycled for the operation of a fully active system to achieve vibration confinement.

2.3 Chapter conclusions

In this chapter, work related to piezoelectric energy harvesting has been reviewed. The majority of the references discussed were published within the last decade. The cantilever beam configuration operating in the d_{31}-mode is the most popular design in piezoelectric energy harvesting and has attracted much more attention than the other designs. In order to maximise the power output, researchers carried out system optimisations and examined different electrical interface circuits, especially

for charging a storage capacitor. To date, a few of this type of piezoelectric energy harvester have been fabricated at the micro-scale. Some designs and applications for piezoelectric energy harvesting have also been reported in this review.

The trends for the current developments of piezoelectric energy harvesting are to increase the power output, identify potential applications, increase design robustness and improve the MEMS fabrication process. To remove batteries as an energy source, power generation is understandably a key factor in energy harvesting and it is always essential that energy harvesters are able to supply sufficient power to electronic devices. However, not much research work has been performed related to the structural integrity of the energy harvester itself. Serious problems arise if the energy harvester undergoes mechanical failure. The advantage of batteries over energy harvesting is that mechanical failures do not happen easily to batteries. Mechanical failure is more likely to occur in energy harvesters with delicate moving parts, and particularly in MEMS where piezoelectric material can be brittle. In some applications, energy harvesters are subjected to undesired shocks and/or high levels of acceleration that have the potential to cause damage to the device. One of the aims for this project is to improve the structural integrity of a cantilever piezoelectric energy harvester. These questions will be addressed in the subsequent chapters.

Chapter 3. Theoretical model of a linear piezoelectric energy harvester

3.1 Introduction

Many energy harvesters adopt the cantilever configuration to generate electrical charge from piezoelectric materials. This is because of the simplicity of cantilever structures and the fact that they can be fabricated relatively easily. In this chapter, the theoretical model for a linear piezoelectric energy harvester will be presented. The energy harvesters considered here are in the cantilever configuration and are designed to operate in the 31-mode. The Euler-Bernoulli beam theory is employed in the modelling. The purpose of the theoretical model is to predict the mechanical response and electrical output of piezoelectric energy harvesters. Theoretical models for linear piezoelectric cantilever energy harvesters design are available in the research literature and some were discussed in Chapter 2, Section 2.2.1.1.

Normally, the natural frequency of an energy harvester has to be tuned to operate at resonance in order to maximise the electrical power output. In practice, this can be achieved by attaching a tip mass to the free end of the cantilever beam [26]. The influence of the tip mass on the natural frequencies and mode shapes of a cantilever beam are considered in [20, 43, 78]. These works consider the influence of mass and rotary inertia, but do not take account of the offset distance between

the beam end and the centre of mass of the tip mass. To [79] indicates that the offset distance can have a significant influence on the natural frequency and mode shape, and this is incorporated in the theoretical model presented in this chapter.

Two simple electrical circuits are considered in the modelling as described in Section 2.2.1.1. The first is a simple load resistance connected to dissipate the electrical energy generated by the energy harvester. The other circuit considered is a charging circuit that stores electrical energy in a storage capacitor. This circuit is very practical as some applications require a comparatively large amount of energy but for a short period of time so that the electrical energy can accumulate for an intermittent power supply.

In this chapter, a linear piezoelectric energy harvester model is derived. Both bimorph and monomorph configurations are considered. The approach used to model the system is based on energy methods (Sodano *et al.* [23]). The theoretical model is used to predict the mechanical and electrical responses of a piezoelectric energy harvester. Analytical steady-state solutions for the electromechanical system are obtained. Also, detailed numerical examples are presented in a later section of this chapter.

3.2 Theoretical model for linear piezoelectric energy harvesters

The theoretical model for an energy harvester is derived in this section, and is based on the bimorph configuration, which consists of two layers of piezoelectric material

and a layer of substrate as shown in Figure 3.1. The tip has a mass *M* and moment of inertia *J* about its centre of mass, attached to the free end of the beam at offset distance *d*. Attaching a tip mass to the energy harvester reduces the natural frequencies of the cantilever. The natural frequencies are not only affected by the mass of the tip mass, the offset distance and the geometry also affect the natural frequencies and the mode shapes [79], and need to be considered in the modelling.

The top and bottom surfaces of the piezoelectric layer are fully covered by electrode coatings. The piezoelectric material used operates in the d_{31}-mode in this design [80]. This means that the piezoelectric layer is polarised in the 3-direction so that the generated electrical charge will discharge from the electrodes in the 3-direction. The cantilever configuration allows the flexural vibration in the 3-direction to be coupled to the strain in the energy harvester developed along the 1-direction. The piezoelectric effect that couples the mechanical and electrical properties is described using the linear constitutive equations for piezoelectric materials [32]:

$$\begin{bmatrix} \sigma \\ D \end{bmatrix} = \begin{bmatrix} E_{\mathrm{p}} & -e^{\sigma} \\ e & \varepsilon_P{}^{\mathrm{S}} \end{bmatrix} \begin{bmatrix} S \\ E_{\mathrm{v}} \end{bmatrix} \tag{3.1}$$

In these equations, *D* is the electric displacement, while σ and *S* are the axial stress and strain of the piezoelectric material, respectively. The electric field in each piezoelectric layer E_v is assumed to be uniform throughout the entire layer and is defined as the voltage potential difference of each layer $v(t)/2$ divided by the thickness of the layer (T_p):

$$E_{\mathrm{v}} = \frac{v(t)}{2T_{\mathrm{p}}} \tag{3.2}$$

The Young's modulus for the piezoelectric material E_{p} is measured at constant

electric field, while the permittivity of the piezoelectric material ε_P^S is measured at constant stress. The piezoelectric coupling coefficient e is a product of the piezoelectric constant d_{31} and the Young's modulus:

$$e = d_{31} E_p \tag{3.3}$$

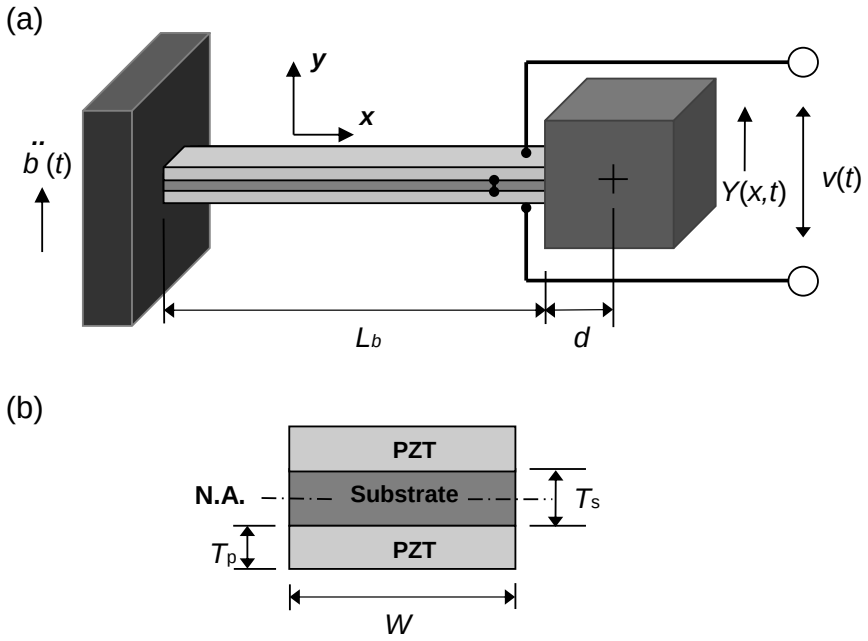

Figure 3.1 (a) The configuration of cantilever beam with PZT attached; (b) the cross section of the beam

The mechanical strain within the piezoelectric layers in the 1-direction is the product of the second derivative of displacement $Y(x,t)$ with respective to x, and the distance y from the neutral axis:

$$S(x,y,t) = -y\frac{\partial^2 Y(x,t)}{\partial x^2} \ , \tag{3.4}$$

Piezoelectric energy harvesters are electromechanical systems and Lagrange's equation or Hamilton's principle can be used to derive the equation of motion [23, 77]. Hamilton's principle is used to derive the equations of motion for the

electromechanical system:

$$\delta\int_{t_1}^{t_2}\left(\mathcal{L}+W\right)\mathrm{d}t=0\,, \tag{3.5}$$

$$\mathcal{L}=K_{\mathrm{e}}-P_{\mathrm{e}}\,, \tag{3.6}$$

where K_e is kinetic energy, P_e is the potential energy, and W is the external work done on the system by the base excitation.

The energy terms in the system have to be identified. The kinetic and potential energies are given by:

$$K_{\mathrm{e}}=\frac{1}{2}\int_{V_{\mathrm{s}}}\rho_{\mathrm{s}}\dot{Y}^2\,\mathrm{d}V+\int_{V_{\mathrm{p}}}\rho_{\mathrm{p}}\dot{Y}^2\,\mathrm{d}V+\frac{1}{2}M\left(\dot{Y}_{x=L_{\mathrm{b}}}+d\dot{Y}'_{x=L_{\mathrm{b}}}\right)^2+\frac{1}{2}J\dot{Y}'^{\,2}_{x=L_{\mathrm{b}}}\,, \tag{3.7}$$

$$P_{\mathrm{e}}=\frac{1}{2}\int_{V_{\mathrm{s}}}S\sigma\,\mathrm{d}V+\int_{V_{\mathrm{p}}}S\sigma\,\mathrm{d}V-\int_{V_{\mathrm{p}}}E_{\mathrm{v}}D\,\mathrm{d}V\,. \tag{3.8}$$

The integration boundaries V_{s} and V_{p} in equations (3.7) and (3.8) are the volumes of substrate and piezoelectric material, respectively. The mass densities of substrate and piezoelectric material are ρ_{s} and ρ_{p}, respectively. Also, (′) and (·) represent the differentiation with respect to x and t, respectively.

Equation (3.1) is substituted into equation (3.8) to yield:

$$P_e=\frac{1}{2}\int_{V_s}S^2E_s\,\mathrm{d}V+\int_{V_p}S^2E_p\,\mathrm{d}V-\int_{V_p}SeE_v\,\mathrm{d}V-\int_{V_p}E_vSe\,\mathrm{d}V-\int_{V_p}E_v{}^2\varepsilon^s\,\mathrm{d}V\,, \tag{3.9}$$

If base excitation $\ddot{b}(t)$ is applied to the bimorph, the external work δW is given by:

$$\delta W=\left[\int_{V_{\mathrm{s}}}\rho_{\mathrm{s}}\delta Y\,\mathrm{d}V+2\int_{V_{\mathrm{p}}}\rho_{\mathrm{p}}\delta Y\,\mathrm{d}V+M\int_0^{L_b}\delta Y\left(L_{\mathrm{b}}\right)+d\delta Y'\left(L_{\mathrm{b}}\right)\mathrm{d}x\right]\ddot{b}\left(t\right)-qv\,, \tag{3.10}$$

where q is electric charge generated by the piezoelectric material, and the negative sign in the term qv indicates that electrical energy is withdrawn from the system.

Substituting equations (3.7), (3.9) and (3.10) into equation (3.5) yields:

$$\delta\int_{t_1}^{t_2}\frac{1}{2}\Bigg[\int_0^{L_b}\rho_s\dot{Y}^2dV_s+2\int_0^{L_b}\rho_p\dot{Y}^2dV_p+M\left(\dot{Y}_{x=L}+d\dot{Y}'_{x=L}\right)^2+J\dot{Y}'^2_{x=L_b}$$
$$-E_s\int_{V_s}S^2dV_s-2E_p\int_{V_p}S^2dV_p+2\int_{V_p}Se^{\sigma}E_vdV_p+2\int_{V_p}E_veSdV_p+2\int_{V_p}E_v{}^2\varepsilon^sdV_p\Bigg]+ \qquad (3.11)$$
$$\left(\rho_s\ddot{b}\int_{V_s}\dot{Y}dV_s+2\rho_p\ddot{b}\int_{V_p}\dot{Y}dV_p-vq\right)\mathrm{d}t=0$$

In order to solve (3.11) to obtain the equation of motion for the system, the variables of the displacement of the beam, $Y(x,t)$, are separated and expressed by an infinite series of mode shape functions and generalised coordinates:

$$Y(x,t)=\sum_{i=1}^{\infty}Y_i(x,t)=\sum_{i=1}^{\infty}\phi_{\mathrm{bi}}(x)w_{\mathrm{i}}(t)=\boldsymbol{\phi}_{\mathrm{b}}(x)\mathbf{w}(t), \qquad (3.12)$$

where $\boldsymbol{\phi}_{\mathrm{b}}(x)$ are the mode shape functions for the beam with an offset tip mass and $\mathbf{w}(t)$ are the generalised coordinates. The mode shape functions can be obtained using Euler-Bernoulli beam theory with appropriate boundary conditions applied to the cantilever beam. The mode shape functions for the cantilever beam with offset tip mass are defined in Section 3.3.

Substituting (3.12) into (3.11) and solving the equation yields:

$$\left(\mathbf{M}_{\mathrm{T}}+\mathbf{M}_{\mathrm{J}}\right)\ddot{\mathbf{w}}+\mathbf{K}_{\mathrm{T}}\mathbf{w}-\boldsymbol{\Theta}^{\mathrm{T}}v=\mathbf{m}_{\mathrm{T}}\ddot{b}, \qquad (3.13)$$

$$\boldsymbol{\Theta}^{\mathrm{T}}\mathbf{w}+C_{\mathrm{p}}v=q, \qquad (3.14)$$

where

$$\mathbf{M}_{\mathrm{T}}=\rho_{\mathrm{s}}\int_{V_s}\boldsymbol{\phi}_{\mathrm{b}}{}^T\boldsymbol{\phi}_{\mathrm{b}}\,\mathrm{d}V+2\rho_{\mathrm{p}}\int_{V_p}\boldsymbol{\phi}_{\mathrm{b}}{}^T\boldsymbol{\phi}_{\mathrm{b}}\,\mathrm{d}V+M\boldsymbol{\phi}_{\mathrm{b}}{}^T(L_{\mathrm{b}})\boldsymbol{\phi}_{\mathrm{b}}(L_{\mathrm{b}})$$
$$+Md\left[\boldsymbol{\phi}_{\mathrm{b}}(L_{\mathrm{b}})\boldsymbol{\phi}_{\mathrm{b}}{}'(L_{\mathrm{b}})+\boldsymbol{\phi}_{\mathrm{b}}{}'(L_{\mathrm{b}})\boldsymbol{\phi}_{\mathrm{b}}(L_{\mathrm{b}})\right]+Md^2\boldsymbol{\phi}_{\mathrm{b}}{}'(L_{\mathrm{b}})^T\boldsymbol{\phi}_{\mathrm{b}}{}'(L_{\mathrm{b}}) \quad , \qquad (3.15)$$

$$\mathbf{M}_{\mathrm{J}} = \frac{1}{2} J \boldsymbol{\phi}_{\mathrm{b}}'(L_{\mathrm{b}})^{T} \boldsymbol{\phi}_{\mathrm{b}}'(L_{\mathrm{b}}) \quad , \tag{3.16}$$

$$\mathbf{K} = E_{\mathrm{s}} \int_{V_{\mathrm{s}}} y^2 \boldsymbol{\phi}_{\mathrm{b}}''^{\mathrm{T}} \boldsymbol{\phi}_{\mathrm{b}}'' \, \mathrm{d}V + 2E_{\mathrm{p}} \int_{V_{\mathrm{p}}} y^2 \boldsymbol{\phi}_{\mathrm{b}}''^{\mathrm{T}} \boldsymbol{\phi}_{\mathrm{b}}'' \, \mathrm{d}V \quad , \tag{3.17}$$

$$\mathbf{m}_{\mathbf{T}} = \rho_s \int_{V_s} \boldsymbol{\phi}_{\mathrm{b}} \, \mathrm{d}V + \rho_p \int_{V_p} \boldsymbol{\phi}_{\mathrm{b}} \, \mathrm{d}V \quad , \tag{3.18}$$

$$\boldsymbol{\Theta} = -2 \int_{V_{\mathrm{p}}} \frac{y \boldsymbol{\phi}_{\mathrm{b}}''^{\mathrm{T}} e}{T_{\mathrm{p}}} \mathrm{d}V \quad , \tag{3.19}$$

$$C_{\mathrm{p}} = \frac{L_{\mathrm{b}} W_{\mathrm{p}} \varepsilon_{\mathrm{P}}^{\,s}}{2T_{\mathrm{p}}} \quad . \tag{3.20}$$

In the equations of motion, $\mathbf{M}_{\mathrm{T}}+\mathbf{M}_{\mathrm{J}}$ and $\mathbf{K}$ are the square matrices for mass and stiffness of the system, respectively. The electromechanical coupling, $\boldsymbol{\Theta}$, is a measure of the conversion of mechanical energy into electrical energy for each generalised coordinate and is a column vector. C_p is the internal capacitance of the energy harvester.

Structural damping exists in practical systems and this is taken into account here by representing the damping matrix as $\alpha(\mathbf{M}_{\mathrm{T}}+\mathbf{M}_{\mathrm{J}}) + \beta\mathbf{K}$ and including terms in equation (3.13) as follows:

$$\left(\mathbf{M}_{T} + \mathbf{M}_{\mathrm{J}}\right)\ddot{\mathbf{w}} + \mathbf{C}\dot{\mathbf{w}} + \mathbf{K}\mathbf{w} - \boldsymbol{\Theta}^{\mathrm{T}} v = \mathbf{m}_{\mathrm{T}} \ddot{b} \tag{3.21}$$

In practice the empirical coefficients α and β are determined experimentally.

The approach to model a monomorph energy harvester is exactly the same as the model derivation above. However, the potential and kinetic energies used in the Lagrangian are different based on the configuration of the energy harvester. These terms are modified as:

$$K_{\mathrm{e}}=\frac{1}{2}\int_{V_{\mathrm{s}}}\rho_{\mathrm{s}}\dot{Y}^{2}\,\mathrm{d}V+\frac{1}{2}\int_{V_{\mathrm{p}}}\rho_{\mathrm{p}}\dot{Y}^{2}\,\mathrm{d}V+\frac{1}{2}M\left(\dot{Y}_{x=L_{\mathrm{b}}}+d\dot{Y}'_{x=L_{\mathrm{b}}}\right)^{2}+\frac{1}{2}J\dot{Y}'^{2}_{x=L_{\mathrm{b}}}, \tag{3.22}$$

$$P_{e}=\frac{1}{2}\int_{v_{s}}S\sigma\,\mathrm{d}V+\frac{1}{2}\int_{v_{p}}S\sigma\,\mathrm{d}V-\frac{1}{2}\int_{V_{p}}E_{v}D\,\mathrm{d}V \tag{3.23}$$

The equations of motion are once again obtained using Hamilton's principle. It can be shown that equations (3.21) and (3.14), originally derived for the bimorph also apply to the monomorph configuration. However, the mass, stiffness, electromechanical coupling and capacitance terms are redefined as follows:

$$\begin{aligned}\mathbf{M}_{\mathrm{T}}=&\rho_{\mathrm{s}}\int_{V_{\mathrm{s}}}\boldsymbol{\phi}_{\mathrm{b}}^{\mathrm{T}}\boldsymbol{\phi}_{\mathrm{b}}\,\mathrm{d}V+\rho_{\mathrm{p}}\int_{V_{\mathrm{p}}}\boldsymbol{\phi}_{\mathrm{b}}^{\mathrm{T}}\boldsymbol{\phi}_{\mathrm{b}}\,\mathrm{d}V+M\boldsymbol{\phi}_{\mathrm{b}}^{\mathrm{T}}(L_{\mathrm{b}})\boldsymbol{\phi}_{\mathrm{b}}(L_{\mathrm{b}})\\&+Md\left[\boldsymbol{\phi}_{\mathrm{b}}(L_{\mathrm{b}})\boldsymbol{\phi}_{\mathrm{b}}'(L_{\mathrm{b}})+\boldsymbol{\phi}_{\mathrm{b}}'(L_{\mathrm{b}})\boldsymbol{\phi}_{\mathrm{b}}(L_{\mathrm{b}})\right]+Md^{2}\boldsymbol{\phi}_{\mathrm{b}}'(L_{\mathrm{b}})^{T}\boldsymbol{\phi}_{\mathrm{b}}'(L_{\mathrm{b}}),\end{aligned} \tag{3.24}$$

$$\mathbf{K}_{\mathrm{T}}=E_{s}\int_{V_{s}}y^{2}\boldsymbol{\phi}_{\mathrm{b}}''^{\mathrm{T}}\boldsymbol{\phi}_{\mathrm{b}}''\,\mathrm{d}V+E_{p}\int_{V_{p}}y^{2}\boldsymbol{\phi}_{\mathrm{b}}''^{\mathrm{T}}\boldsymbol{\phi}_{\mathrm{b}}''\,\mathrm{d}V\quad, \tag{3.25}$$

$$\mathbf{m}_{\mathrm{T}}=\rho_{s}\int_{V_{s}}\boldsymbol{\phi}_{\mathrm{b}}dV+\rho_{p}\int_{V_{p}}\boldsymbol{\phi}_{\mathrm{b}}dV+M\left[\boldsymbol{\phi}_{\mathrm{b}}(L_{\mathrm{b}})+d\boldsymbol{\phi}_{\mathrm{b}}'(L_{\mathrm{b}})\right], \tag{3.26}$$

$$\boldsymbol{\Theta}=\int_{V_{\mathrm{p}}}\frac{y\boldsymbol{\phi}_{\mathrm{b}}''e^{\mathrm{T}}}{T_{\mathrm{p}}}\mathrm{d}V\quad, \tag{3.27}$$

$$C_{P}=\frac{L_{b}W_{p}\varepsilon_{P}^{S}}{T_{p}}\quad. \tag{3.28}$$

The main differences in the equations of motion between the bimorph and monomorph models are the additional mass and stiffness to the mechanical structure for the bimorph, and that the equivalent capacitance is halved and the electromechanical coupling terms are doubled due to the series connection between the piezoelectric layers in the bimorph.

3.2.1 Energy harvesting circuits

The electrical representation of the piezoelectric energy harvester and circuits are considered here. A potential difference develops between the electrodes on the top and bottom surfaces of the PZT layer as shown in Figure 3.2. The energy harvester can be regarded as an internal electrode capacitor in parallel with a current source [22, 32]. As mentioned at the beginning of the chapter, two different circuits will be connected to the energy harvester.

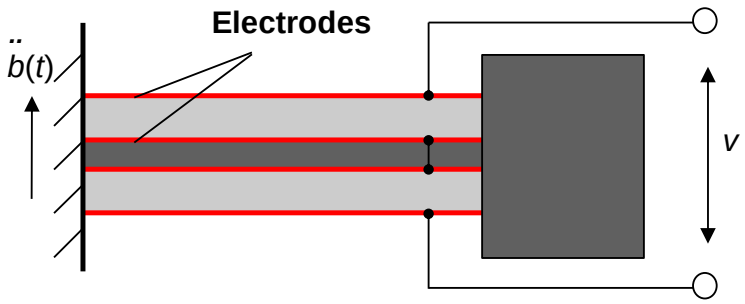

Figure 3.2 Piezoelectric layers are in series connection for the bimorph energy harvester

3.2.1.1 Resistance load in series

When a resistor is connected in series with the energy harvester (the equivalent energy harvester circuit is shown in Figure 3.3), A potential difference develops between the electrodes on the top and bottom surfaces of each piezoelectric layer, so each layer can be considered as an internal electrode capacitor C_p' with a current source I'. The C_p expressed in (3.20) is the overall equivalent capacitance C_p for the bimorph. Also, the overall current flowing out from the bimorph is:

$$I(t) = -\boldsymbol{\Theta}^{\mathrm{T}}\dot{\mathbf{w}}(t) \quad . \tag{3.29}$$

The electrical equation governing the energy harvester (3.14) is differentiated with respect to time to yield:

$$\boldsymbol{\Theta}^{\mathrm{T}}\dot{\boldsymbol{w}} + C_{\mathrm{p}}v = \dot{q} \quad . \tag{3.30}$$

In this case, the rate of change of charge, $\dot{q}$, is the current flowing through the resistor, which is equal to $-v/R$. Therefore, the governing equation for the circuit is:

$$C_p\dot{v} + \frac{1}{R}v = -\boldsymbol{\Theta}\dot{\mathbf{w}} = I(t) \quad . \tag{3.31}$$

Note that equation (3.31) obeys Kirchhoff's law of current. Also, it has to be associated with the mechanical equation of motion (3.21) to obtain solutions.

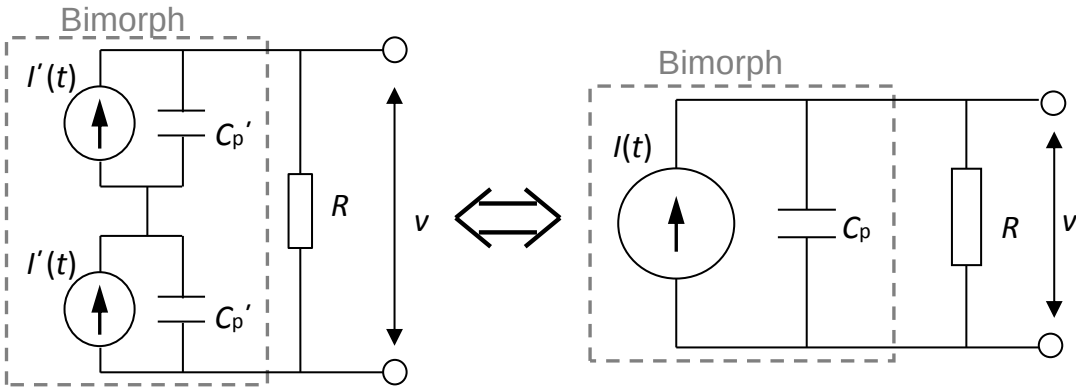

Figure 3.3 Equivalent circuit for a bimorph energy harvester with series connection for the piezoelectric layers

3.2.1.2 Full wave diode bridge charging circuit

To charge up a capacitor, a DC potential across it is required. Since the energy harvester generates AC, these have to be converted into DC and this can be achieved by using a full wave diode bridge to rectify the AC voltage [53]. In this thesis, the AC voltage will be rectified by the diode bridge before it charges a storage capacitor and the charging circuit is shown in Figure 3.4. The electrical representation of the energy harvester remains the same and the right side of the circuit will be replaced by a full wave diode bridge and a storage capacitor, C_s.

Having a different electrical connection will not affect the equation of motion for the mechanical side. However, the voltage in equation (3.21) becomes the voltage across the energy harvester, v_{Cp}, in Figure 3.4 instead of the voltage across the resistor.

The storage capacitor will only be charged when the diode bridge conducts. When the voltage across the energy harvester is higher than the voltage across the storage capacitor, the current can flow through the diode bridge and into the storage capacitor. It is worth mentioning that the voltage will drop by V_d across each diode that current passes through.

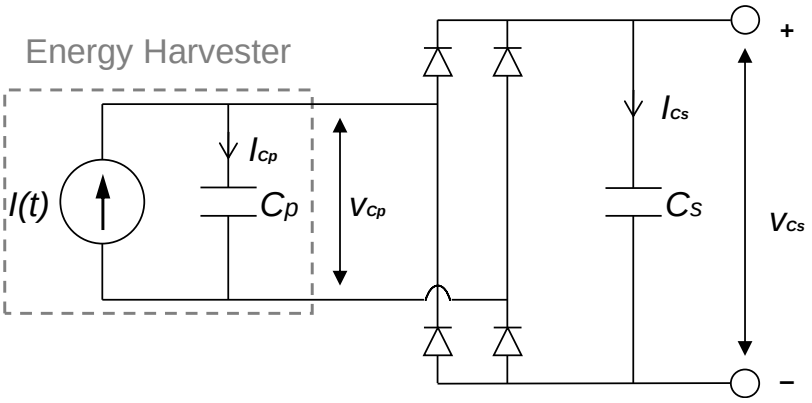

Figure 3.4 The energy harvester is connected to a diode bridge to charge storage capacitor

If the diode bridge does not conduct, i.e. $v_{Cp} < v_{Cs} + 2v_d$, the current flows through the internal capacitance, I_{Cp}, and is simply equal to I and no current flows beyond the diode bridge. Therefore, the voltage across the internal capacitance is given by:

$$v_{Cp} = \frac{1}{C_p}\int I\,\mathrm{d}t + v_0 \quad , \tag{3.32}$$

where v_0 is initial voltage which is assumed to be zero.

When the diode bridge starts to conduct, i.e. , $v_{Cp} \geq v_{Cs} + 2v_d$, the currents flowing through the internal capacitance, I_{Cp}, and the storage capacitor, I_{Cs}, are:

$$I_{Cs} = \frac{C_p}{C_p + C_s}|I| \quad , \tag{3.33}$$

$$I_{Cp} = \frac{C_s}{C_p + C_s} I \quad , \tag{3.34}$$

The corresponding voltages across the internal capacitor and storage capacitor become:

$$v_{Cp} = \frac{1}{C_p}\int I_{Cp}\,\mathrm{d}t \quad , \tag{3.35}$$

$$v_{Cs} = \frac{1}{C_s}\int I_{Cs}\,\mathrm{d}t \quad . \tag{3.36}$$

Note that the above expressions are obtained for initial conditions $v_{Cp}(0)=0$ and $v_{Cs}(t)= 0$.

If the energy harvester is connected to a charging circuit, then the dynamical and electrical responses can be obtained by solving the equations of motion (3.21), (3.32)–(3.36).

3.3 Mode shape functions for the energy harvester

In order to solve the coupled equations of motion (3.21) and (3.31) for the resistive circuit or (3.21), (3.32)–(3.36) for the charging circuit, the mode shape functions, $\boldsymbol{\phi}_{\mathbf{b}}(x,t)$, of the energy harvester have to be defined. As mentioned in Chapter 2, previous theoretical models only consider the mass of the tip mass and ignore its geometry. It is important that mode shapes considering these key factors have to be

used in the modelling to ensure the accuracy of the theoretical model.

The energy harvester can be treated as a composite beam. Figure 3.5 depicts the composite beam and has the equivalent Young's modulus, E_b, second moment of area, I_b, cross section, A_b, and density ρ_b. It is assumed that the beam is slender and the rotary inertia of the beam is negligible, allowing Euler-Bernoulli beam theory to be used. The tip mass has mass M, moment of inertia J about its centre of mass, and radius of gyration κ [79]. The centre of mass of the tip mass is offset from the free end of the beam by a distance d and lies on the neutral axis of the beam.

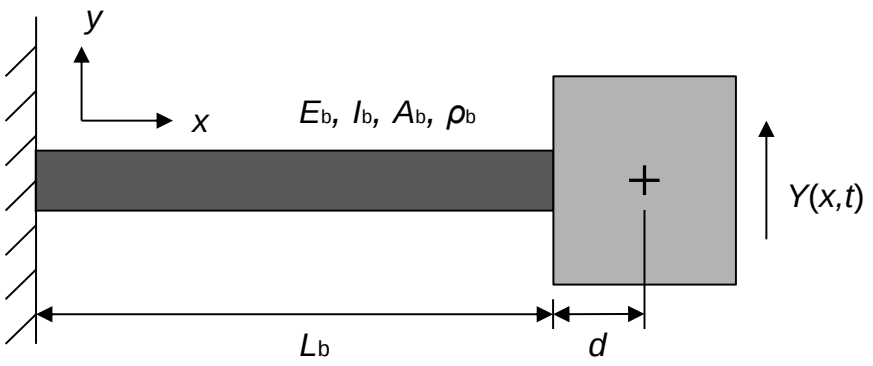

Figure 3.5 The configuration of a cantilever beam with an offset tip mass attached

The boundary conditions at the clamped end (i.e. $x = 0$) of the beam are:

$$Y(0,t) = 0 \tag{3.37}$$

$$\frac{\partial}{\partial x} Y(0,t) = 0 \tag{3.38}$$

The boundary conditions at the free beam end (i.e. $x = L_b$) are:

$$E_b I_b \frac{\partial^2}{\partial x^2} Y(L_b,t) = -(J + Md^2) \frac{\partial^3}{\partial x \partial t^2} Y(L_b,t) - Md \frac{\partial^2}{\partial t^2} Y(L_b,t)\,, \tag{3.39}$$

where the moment at the tip of the beam has been equated to the moment from

the tip mass, and:

$$E_b I_b \frac{\partial^3}{\partial x^3} y(L_b,t) = M \frac{\partial^2}{\partial t^2} Y(L_b,t) + Md \frac{\partial^3}{\partial x \partial t^2} Y(L_b,t) \quad , \tag{3.40}$$

where the shear force at the tip of the beam has been equated to the shear force from the tip mass.

To determine the mode shapes and natural frequencies, let beam displacement $Y(x,t)=w(t)\phi_b(x,t)$ and assume that the beam response is harmonic such that $w(t)=R\mathrm{e}^{i\omega_b t}$, where R is a constant and ω_b is the natural frequency associated with mode shape $\phi_b(x,t)$. In general the mode shape function can be expressed as:

$$\phi_b(x) = B_a\left[B_1\cos\left(\frac{u}{L_b}x\right) + B_2\sin\left(\frac{u}{L_b}x\right) + B_3\cosh\left(\frac{u}{L_b}x\right) + B_4\sinh\left(\frac{u}{L_b}x\right)\right], \tag{3.41}$$

$$u = \lambda L_b, \tag{3.42}$$

$$\lambda^4 = \frac{\rho_b A_b \omega_b^{\,2}}{E_b I_b}. \tag{3.43}$$

In the mode shape function, the non-trivial solutions for coefficients, B_1, B_2, B_3 and B_4 are determined by applying the boundary conditions (3.37)–(3.40) and the characteristic equation is also obtained, while B_a is an arbitrary constant and can be determined by satisfying the orthogonality condition:

$$\begin{aligned} B_1 = {} & 1 - \sin u \sinh u + \cos u \cosh u + (\cos u \cosh u - \sin u \sinh u - 1)\left(R_2^{\,2} - \alpha_0 u R_1\right) \\ & - 2(\cos u \cosh u + \sin u \sinh u)R_2 - 2R_1 \cos u \sinh u - 2\alpha_0 u \sin u \cosh u \quad , \end{aligned} \tag{3.44}$$

$$\begin{aligned} B_3 = {} & 1 + \sin u \sinh u + \cos u \cosh u + (\sin u \sinh u + \cos u \cosh u - 1)\left(R_2^{\,2} - \alpha_0 u R_1\right) \\ & + 2(\cos u \cosh u - \sin u \sinh u)R_2 - 2R_1 \sin u \cosh u + 2\alpha_0 u \cos u \sinh u \quad , \end{aligned} \tag{3.45}$$

$$B_2 = -B_4 = (\sin u \cosh u + \cos u \sinh u)\left(R_1 \alpha_0 u - R_2^{\,2} - 1\right) + 2R_1 \sin u \sinh u + 2R_2(\sin u \cosh u - \cos u \sinh u) - 2\alpha_0 u \cos u \cosh u \quad , \tag{3.46}$$

$$1 + \cos u \cosh u + (\cos u \cosh u - 1)R_2^{\,2} - 2R_2 \sin u \sinh u - [\sin u \cosh u + \cos u \sinh u + \alpha_0 u(\cos u \cosh u - 1)]R_1 + \alpha_0 u(\cos u \sinh u - \sin u \cosh u) = 0 \quad . \tag{3.47}$$

where

$$\alpha_0 = \frac{M}{\rho A L}, \quad \alpha_1 = \frac{d}{L}, \quad \alpha_2 = \frac{\kappa}{L}$$

$$R_1 = \alpha_0 u^3 \left(\alpha_1^{\,2} + \alpha_2^{\,2}\right), \quad R_2 = \alpha_0 \alpha_1 u^2 \quad .$$

In the above expressions, α_0, α_1 and α_2 are the ratio of the tip mass to the mass of the beam, the ratio of offset distance to the length of the beam, and the ratio of the radius of gyration to the length of the beam, respectively. Characteristic equation (3.47) is a transcendental equation and there appears to be no analytical solution available for the roots u. Also, it contains hyperbolic terms which make the equation difficult to solve numerically. The natural frequencies are obtained by substituting numerically calculated values of u into equation (3.42) and (3.43). The mode shape functions are obtained by substituting equations (3.44)–(3.46) into equation (3.41), and choosing the arbitrary constant B_a so that the mode shape is normalised. It can be shown that the mode shape functions satisfy the following orthonormality condition [81]:

$$\int_0^{L_b} \rho_b A_b \phi_{bm} \phi_{bn} dx + M\omega_m^{\,2} \phi_{bm}(L_b)\phi_{bn}(L_b) + 2Md\omega_m^{\,2} \phi_{bn}(L_b)\phi_{bm}'(L_b) + (J + Md)\omega_m^{\,2} \phi_{bn}'(L_b)\phi_{bm}'(L_b)\mathrm{d}x = \delta_{mn}, \tag{3.48}$$

where m and n are positive integers and δ_{mn} is the Kronecker delta function.

3.4 Analytical solutions and numerical simulations of the energy harvester model

The mode shape functions for a cantilever beam with an offset tip mass were defined in the previous section and they are used to evaluate the coefficients in the equations of motion with or without a tip mass. Since the mode shapes have been normalised to satisfy orthogonality condition (3.48), the equation of motion (3.21) can be simplified as:

$$\ddot{\mathbf{w}} + 2\boldsymbol{\gamma}_b\boldsymbol{\omega}_b\dot{\mathbf{w}} + \boldsymbol{\omega}_b^2\mathbf{w} - \boldsymbol{\Theta}^T v = \mathbf{m}_T\ddot{b}\,, \tag{3.49}$$

where $2\boldsymbol{\gamma}_b\boldsymbol{\omega}_b$ and $\boldsymbol{\omega}_b^2$ are diagonal matrices.

Equations of motion derived in this chapter can be solved either numerically or analytically. There are a few numerical methods available to solve ordinary differential equations (ODEs), such as the Runge-Kutta method, for the time domain solutions. However, it will be useful to obtain analytical solutions and steady state solutions of the energy harvester responses in the frequency domain to analyse the system later.

3.4.1 Analytical solutions to the equations of motion

The equation of motion (3.49) is a linear second order ODE. If only a single mode is considered from (3.49), i.e. a single modal equation of motion, then the analytical solutions can be written in the form of Duhamel's integral as follows [82]:

$$w_i(t) = \int_0^t \left[m_{Ti}\ddot{b}(\tau) - \Theta_i v(\tau) \right] e^{-\gamma_{bi}\omega_{bi}(t-\tau)} \sin\omega_{bdi}(t-\tau)\,d\tau \quad , \tag{3.50}$$

where γ_b is the damping ratio, ω_{bdi}, is the damped natural frequency and is equal to $\omega_{bi}(1\text{-}\gamma_b)^{0.5}$.

Hence, the displacement of the energy harvester is expressed by using equation (3.50) in (3.12):

$$Y(x,t)=\sum_{i=1}^{\infty}\int_0^t\left[m_{\mathrm{T},i}\ddot{b}(\tau)-\Theta_{\mathrm{i}}v(\tau)\right]g_{\mathrm{bi}}(x,t-\tau)\mathrm{d}\tau \quad , \tag{3.51}$$

where g_{bi} is known as the impulse response function and expressed as follows:

$$g_{bi}(x,t)=\mathrm{e}^{\gamma_{bi}\omega_{bi}t}\frac{\phi_{\mathrm{bi}}(x)}{\omega_{\mathrm{bdi}}}\sin\omega_{\mathrm{bdi}}t \quad . \tag{3.52}$$

The governing equation of the electrical circuit, (3.31), can also be expressed analytically. The first order linear ODE (3.31) is solved by using the integrating factor, $\mathrm{e}^{t/(C_pR)}$:

$$v(t)=-\mathrm{e}^{-\frac{t}{RC_p}}\int e^{\frac{t}{RC_p}}\boldsymbol{\Theta}^{\mathrm{T}}\dot{\mathbf{w}}\mathrm{d}t \quad . \tag{3.53}$$

Note that the initial voltage is assumed to be zero in the expression above.

3.4.2 **Steady state responses of the energy harvester**

This section considers the response of the energy harvester to a harmonic excitation, and assuming the harmonic excitation is in the following form:

$$\ddot{b}(t)=B_{\max}\mathrm{e}^{\mathrm{j}2\pi ft} \tag{3.54}$$

where B_{max} and f are the excitation amplitude and frequency (in Hz) respectively.

The energy harvester is assumed to respond harmonically so the generalised coordinate and the voltage of the harvester can be written as:

$$Y(x,t) = Y_{\max} e^{j2\pi ft} \tag{3.55}$$

$$v(t) = v_{\max} e^{j2\pi ft} \tag{3.56}$$

where Y_{max} and V_{max} are the amplitudes of the displacement at distance x along the beam and the voltage respectively.

The general solutions (3.55) and (3.56) are substituted into the coupled equations of motion (3.49) and (3.31), and then manipulating the resulting equations to obtain the state-steady displacement and voltage of the electromechanical system [25]:

$$Y_{\max}(L_b) = \frac{m_b B_{max} \left| \phi_{bi}(L_b) \int_0^{L_b} \phi_{bi} dx \right| \sqrt{1 + \left(fC_p R \right)^2}}{\sqrt{\left[{\omega_{bi}}^2 - f^2 \left(1 + 2C_p R \gamma_{bi} \omega_{bi} \right) \right]^2 + \left[2\gamma_{bi} \omega_{bi} f + C_p R f \left(\frac{{\Theta_i}^2}{C_p} + {\omega_{bi}}^2 - f^2 \right) \right]^2}} \tag{3.57}$$

$$v_{\max} = \frac{m_b f B_{max} C_p R \left| \frac{\Theta_i}{C_p} \int_0^{L_b} \phi_{bi} dx \right|}{\sqrt{\left[{\omega_{bi}}^2 - f^2 \left(1 + 2C_p R \gamma_{bi} \omega_{bi} \right) \right]^2 + \left[2\gamma_{bi} \omega_{bi} f + C_p R f \left(\frac{{\Theta_i}^2}{C_p} + {\omega_{bi}}^2 - f^2 \right) \right]^2}} \tag{3.58}$$

3.4.3 Numerical simulations for harmonic base excitation

3.4.3.1 Energy harvester in a resistive circuit

In the following numerical examples, harmonic base excitation is applied to a monomorph energy harvester, so equation (3.54) can be used for the base acceleration in equation (3.21). Table 3.1 lists the mechanical properties and dimensions of the substrate and the PZT used in the monomorph energy harvester. It is worth mentioning that the mechanical properties and dimensions are found from the energy harvester sample tested in the next chapter. Table 3.2 shows the

main parameters used in the following numerical example.

Monomorph - mechanical properties and dimensions

	Substrate (aluminium)	PZT
Length, L (mm)	35.94	35.94
Width, W(mm)	6	6
Thickness, T (mm)	0.65	0.5
Young Modulus, E (GPa)	69	66
Density, ρ (kg/m^3)	2700	7800
Piezoelectric constant, d_{31} (m/V)	–	180x10^{-12}
Relative Dielectric constant, k_3	–	1750

Table 3.1 Mechanical properties and dimensions of the monomorph energy harvester

f (Hz)	B_{max} (m/s^2)	γ_{b1}	R (Ω)
520	1	0.01	10000

Table 3.2 Parameters used in the monomorph model

In the example, the fundamental natural frequency of the monomorph is 524.6 Hz when no resistance load is connected. The monomorph is excited near the fundamental natural frequency at 520 Hz and a resistor of 10 kΩ is connected in series. Figure 3.6 shows the simulation results of the displacement at the tip of the monomorph and the voltage across the resistor. Only a single mode response is considered in the example as the monomorph is excited near the fundamental resonance. The frequency response functions for the tip displacement of the monomorph and the peak voltage across the resistor are shown in Figure 3.7 and are obtained by solving steady state solutions (3.57) and (3.58). Both the peak displacement and voltage are found to occur at 524.9 Hz. The natural frequency of

the system shifts by 0.3 Hz when a resistor of 10 kΩ is connected to the monomorph.

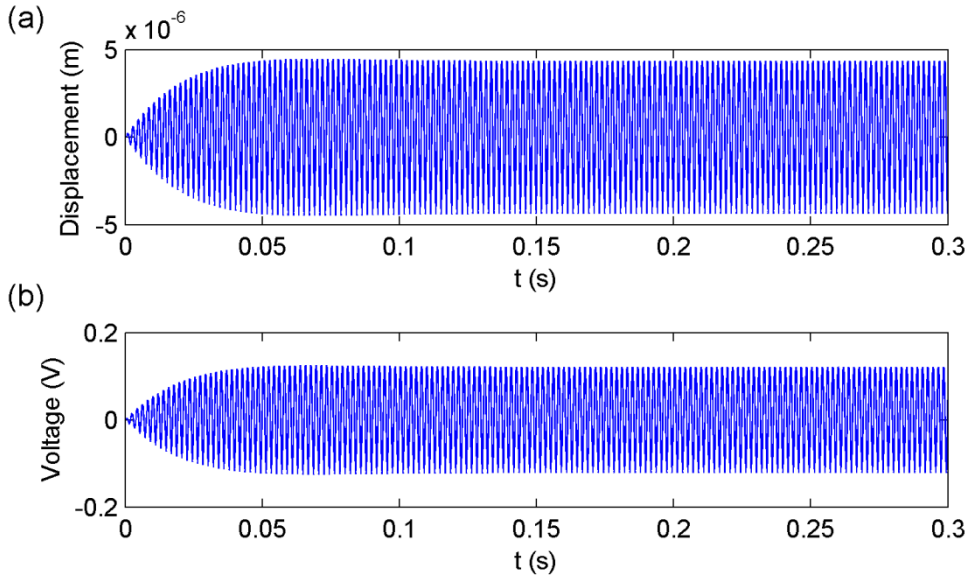

Figure 3.6 The time domain simulation of the monomorph energy harvester

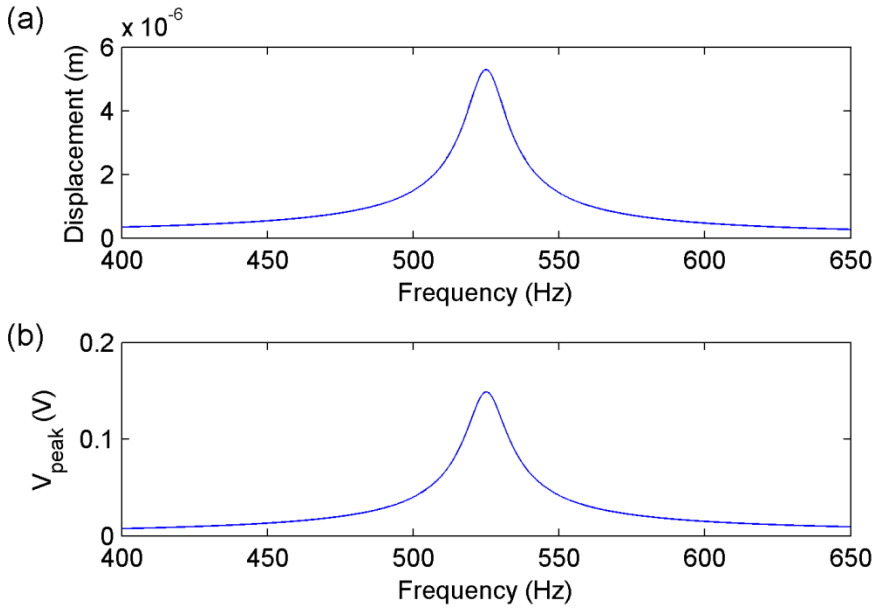

Figure 3.7 The frequency response functions of the monomorph energy harvester

Numerical results for a bimorph energy harvester are also considered and will be tested in the next chapter. In the experimental work (see Chapter 4), the PZT layers

used for the monomorph and bimorph are supplied by two different manufacturers and they have different physical properties. Also, the substrate of the bimorph is made from copper. Table 3.3 shows the mechanical properties and dimensions of the bimorph, while Table 3.4 shows the main parameters used in the simulation. In this example, the bimorph sample is excited at its fundamental structural natural frequency which is 365.2 Hz, so again only a single mode is considered in the simulation. Figure 3.8 shows the time domain simulation for the tip displacement and voltage. The frequency response functions of the bimorph are shown in Figure 3.9 and the resonance frequency of the system also slightly shifts as seen in the monomorph example. This phenomenon will be investigated and explained in the next chapter.

Bimorph - mechanical properties and dimensions

	Substrate (copper)	PZT
Length, L (mm)	29	29
Width, W (mm)	6.4	6.4
Thickness, T (mm)	0.14	0.26
Young Modulus, E (GPa)	100	66
Density, ρ (kg/m^3)	8700	7800
Piezoelectric constant, d_{31} (m/V)	–	190x10^{-12}
Relative Dielectric constant, k_3	–	1800

Table 3.3 Mechanical properties and dimensions of the bimorph energy harvester

f (Hz)	B_{max} (m/s^2)	γ_{b1}	R (Ω)
365	1	0.01	10000

Table 3.4 Parameters used for the bimorph model

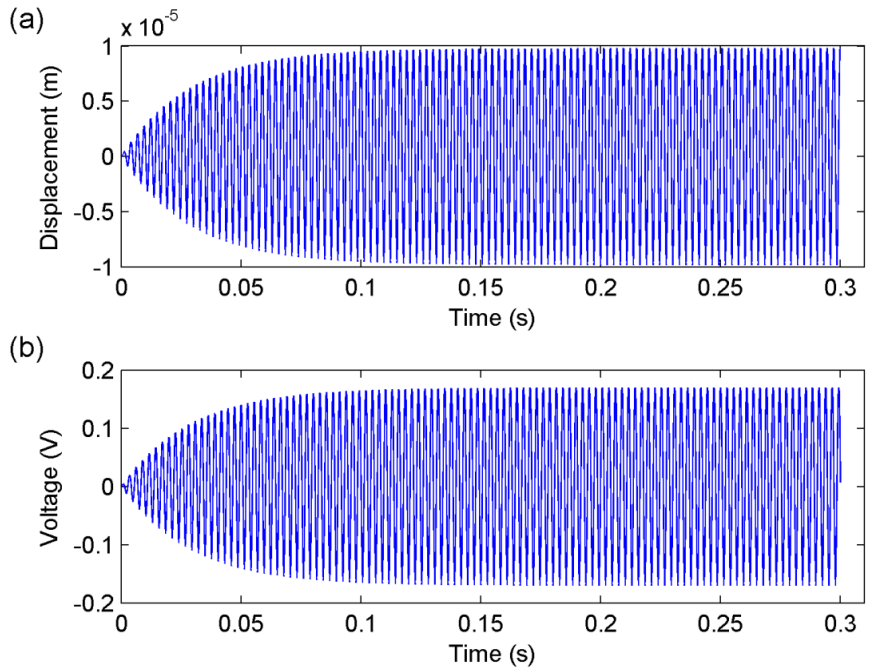

Figure 3.8 The time domain simulation of the bimorph energy harvester

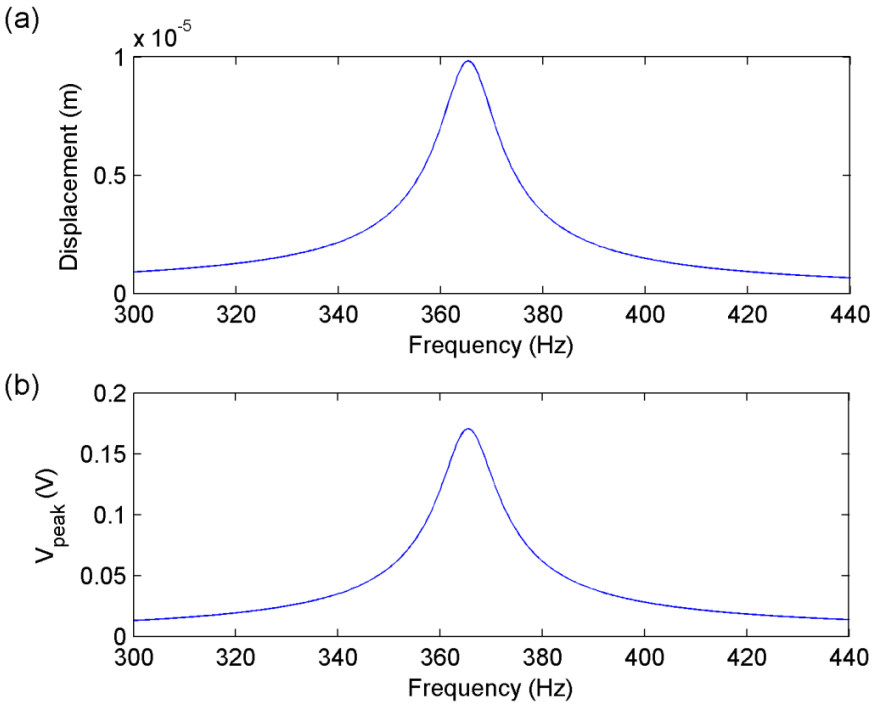

Figure 3.9 The frequency response functions of the bimorph energy harvester

The next example is used to quantify the importance of considering the physical parameters of a tip mass. A mass is attached to the free end of the bimorph used in the previous example. The tip mass is 2.4 g, an offset distance *d* of 3.2 mm and a

moment of inertia of 1.68×10^{-8} kgm^2. The length of the modified bimorph, L_b, is 20.4 mm. The other parameters used here are the same as those in the previous example. In this investigation, theoretical results are compared when different combinations of *M*, *d* and *J* are included in the theoretical model. Figure 3.10 compares the FRFs for the displacement and voltage near the fundamental resonance frequency of the modified bimorph. It is clearly seen that excluding *d* in the theoretical model makes a significant difference to the fundamental resonance frequency compared to results including *M*, *d* and *J*. It is also noticed that *J* is less influential to the resonance frequency. The investigation indicates that the inclusion of *M*, *d* and *J* in the theoretical model are essential in this example, otherwise inaccurate predictions would be obtained.

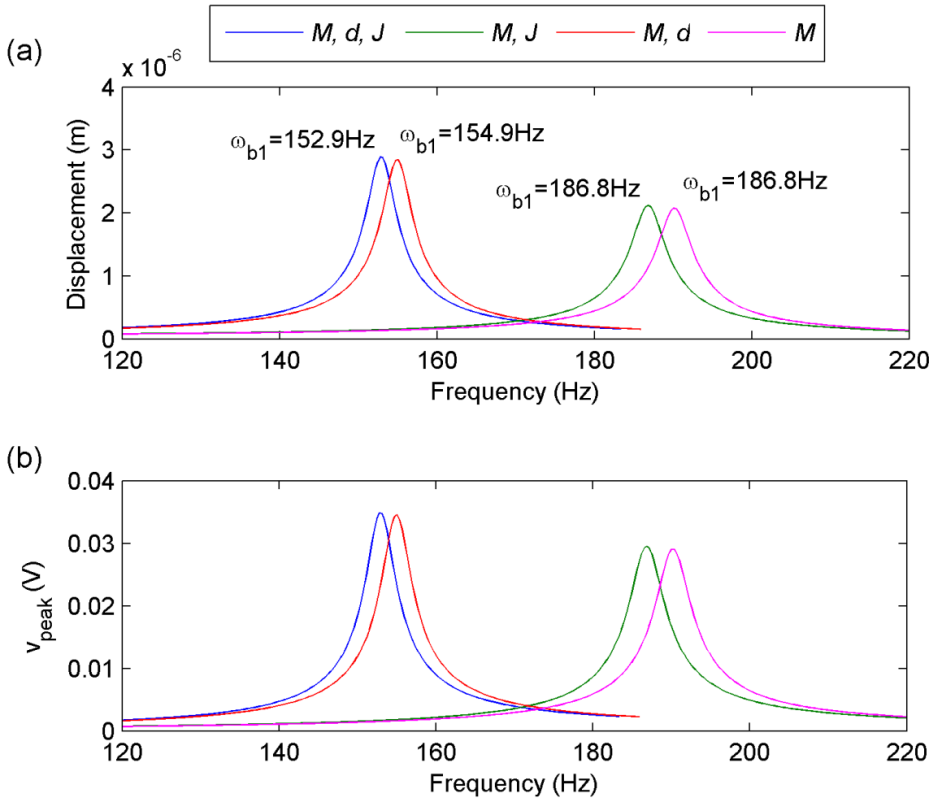

Figure 3.10 The frequency response functions are compared for different tip mass parameters considered in the theoretical model for the bimorph energy harvester

3.4.3.2 Energy harvester in a charging circuit

The final numerical simulation shown here considers an energy harvester being used to charge a storage capacitor of 1 μF. The energy harvester considered is the bimorph with the tip mass used in the previous example. The base acceleration excites the bimorph energy harvester at 365 Hz with an amplitude of 2 m/s^{-2}. The voltage drop on each diode is assumed to be 0.2 V in the simulation. The simulation parameters are listed in Table 3.5. Notice that the diode bridge does not conduct if the maximum voltage of the internal capacitance is lower than the total voltage drop in the diode bridge. The amplitude of the base acceleration chosen in this example is 10 times higher than the previous example to ensure the generated voltage is higher than the voltage drop so that the diode bridge conducts and the storage capacitor is charged.

Figure 3.11 shows the tip displacement, voltage across C_p and C_s and the currents through C_p and C_s. When the storage capacitor is charging, less current flows through the diode bridge as the voltage of the storage capacitor increases. Moreover, the duration of the phase where the capacitor is charged, Ψ, will also become smaller. Figure 3.12 depicts how the size of the charging phase changes at different periods of time in the charging process. It is obvious that the displacement reduces when the capacitor is fully charged. This is because the amplitude of the voltage across the internal capacitor increases, leading to more electrical damping being added to the energy harvester. The charging process takes about 0.25 second to fully charge the storage capacitor to 0.55 V in this example.

f (Hz)	B_{max} (m/s^2)	γ_{b1}	C_s (μF)	v_d (V)
350	2	0.01	1	0.2

Table 3.5 Parameters used for the monomorph model

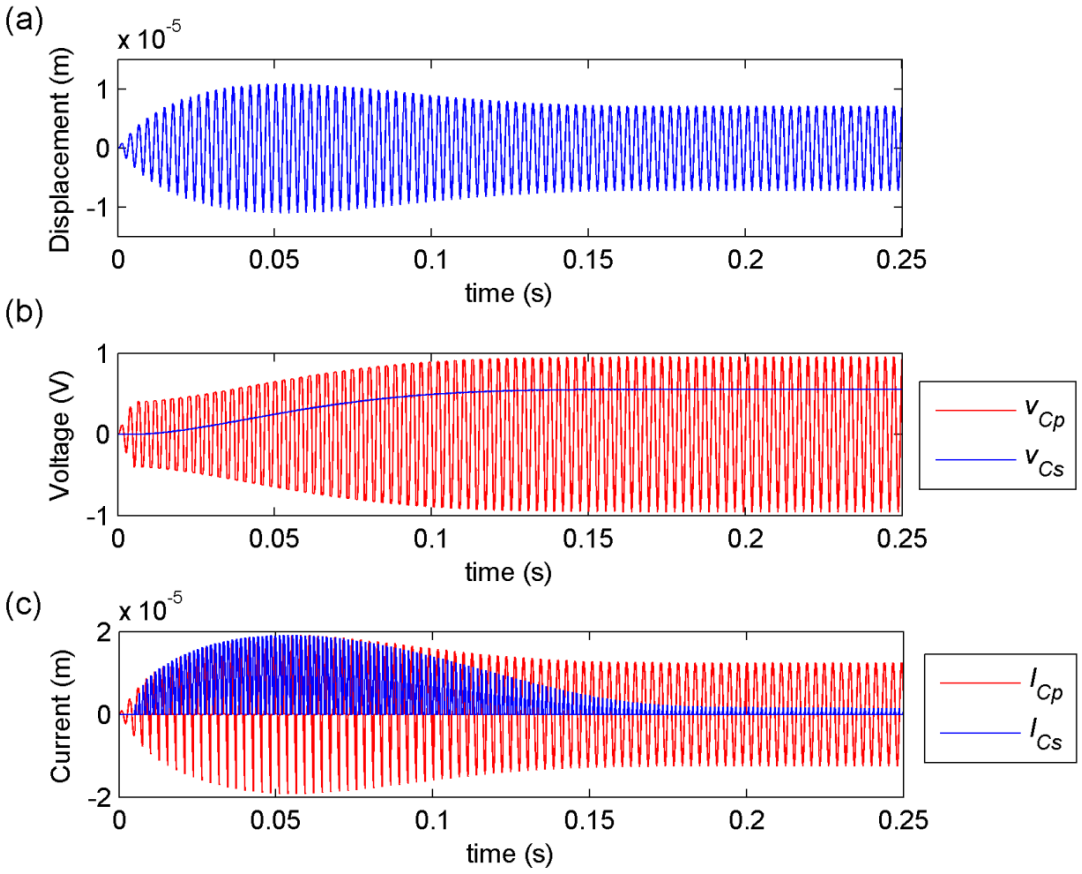

Figure 3.11 Time domain simulation of a bimorph energy harvester

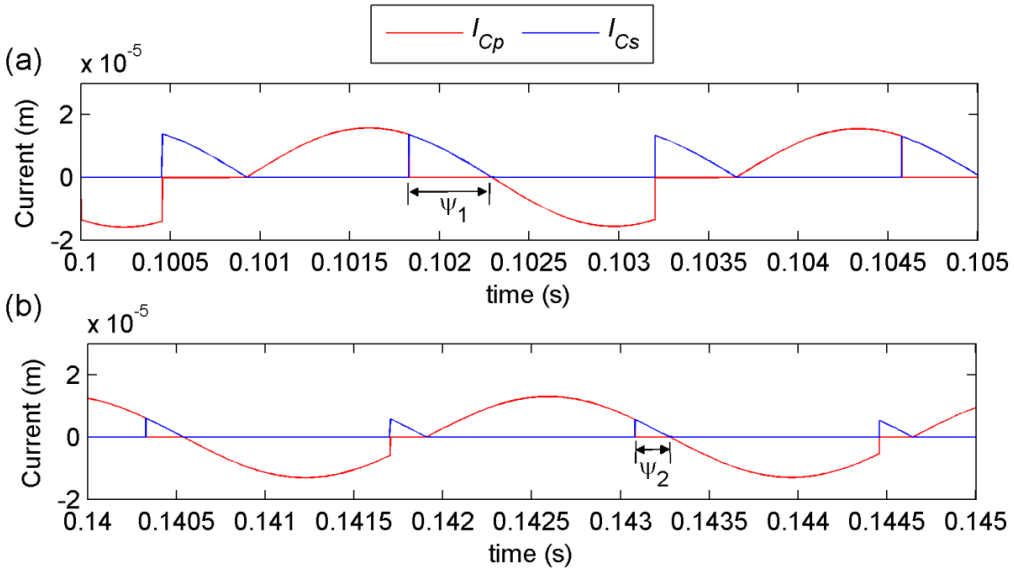

Figure 3.12 Illustration of the phase where the diode bridge conducts in different periods(a) 0.01<*t*<0.105 (b) 0.14<*t*<0.145

3.5 Chapter conclusions

In this chapter, a theoretical model for a piezoelectric energy harvester with different configurations has been presented. The model predicts the mechanical and electrical responses of the harvester. It also demonstrates how the electrical energy is generated when the energy harvester is connected to a load resistance and a capacitor in a charging circuit. The main contribution of this work is to use more accurate mode shapes compared to other studies that consider both the mass and geometry of the tip mass in the modelling. Also, the derived mode shape functions can be used for a cantilever beam with or without an offset tip mass.

The coupled equations of motion for the electromechanical systems were derived and the time domain analytical solutions expressed in the form of Duhamel's integral. The closed-form steady state solutions have also been obtained for the

energy harvester connected to a resistor under harmonic excitation. The steady-state solutions obtained are useful for investigating the behaviour of the electromechanical system and also to facilitate investigations into the energy harvesting performance and power optimisation, which will be presented in the next chapter. In addition, a numerical example was used to demonstrate both mechanical and electrical responses of the energy harvester in a charging circuit. The simulation predicted the time required to fully charge a storage capacitor, which is important to know in many energy harvesting applications. Also, an investigation was performed to justify the importance of considering both the offset distance and inertia of the tip mass in the theoretical model to avoid inaccurate predictions.

The model will be validated in the next chapter, where both bimorph and monomorph energy harvesters will be tested experimentally and the experimental measurements compared to the theoretical results.

Chapter 4. Experimental validations and parameter studies

4.1 Introduction

A theoretical model for piezoelectric energy harvesters was developed in Chapter 3. The theoretical model can be used to predict the mechanical and electrical responses of a piezoelectric energy harvester and is useful for investigating the performance of the electromechanical system. However, the theoretical model needs to be validated with experimental measurements to ensure the correctness of the model, and this is the main purpose of this chapter.

Monomorph and bimorph samples are considered in the experiments and connected with different load resistors. In the experimental validation, the frequency response functions for the displacement and voltage of different samples will be measured and compared to analytical predictions. In general, cantilever piezoelectric energy harvesters are designed to operate near the fundamental frequency of the mechanical structure and are rarely designed for high-mode operation because both positive and negative charge will be generated and cancelled out [83]. On this basis, the experimental validation focuses on the fundamental mode only.

Although the main objective of this chapter is to validate the theoretical model by comparing experimental measurements to analytical solutions, the other objectives are to gain improved understanding of the behaviour of an energy harvester and determine the conditions for optimum power output. This includes carrying out parameter studies to examine the effect of load resistance in the circuit, the thickness ratio of substrate to piezoelectric layer, and the tip mass geometry. Parameter studies are presented to determine the optimum conditions for maximum power output.

4.2 Experimental setup

In the experiment, the energy harvester samples are mounted as a cantilever beam on a steel clamping fixture, which is attached to a shaker (see Figure 4.1). The shaker provides base excitation to the samples and the excitation is harmonic. A resistor is connected in series to the clamping fixture, which conducts to the energy harvester in the d_{31}-mode, to establish the electrical circuit shown in Figure 4.2. In the experiment, the displacement of the beam and the voltage across the resistor are recorded to obtain frequency response functions for the displacement and voltage. The base excitation applied to the sample is measured by a shear accelerometer which is located on the clamping fixture. The accelerometer is supplied by PCB PIEZOTRONICS (model number is 352C22 [84]) and was calibrated by the manufacturer prior to taking measurements. The output signals of the accelerometer are amplified by an ICP® Sensor Signal Conditioner before the signals are read. Also, the sensitivity of the accelerometer provided by the manufacturer is 1.014 mV/m/s^2. The experimental setup is shown in Figure 4.3.

A PolyTec OFV-055 single point laser vibrometer unit [85] is used in the experiment to measure the dynamical response of the energy harvester. The laser vibrometer provides non-contact vibration measurements and no physical equipment is required so there is no interference, such as from the accelerometer mass, affecting the measurements. The laser beam shone by the vibrometer sensor head can point to any position on the energy harvester to measure the velocity normal to the surface. The output signals of the measured velocity are electrical voltage and this is fed to a Stanford Research Systems Model SR785 Signal Analyser [86]. The signal outputs from the vibrometer needs to be converted to displacement and velocity and the conversion rate is based on the sensitivity chosen in the measurement settings.

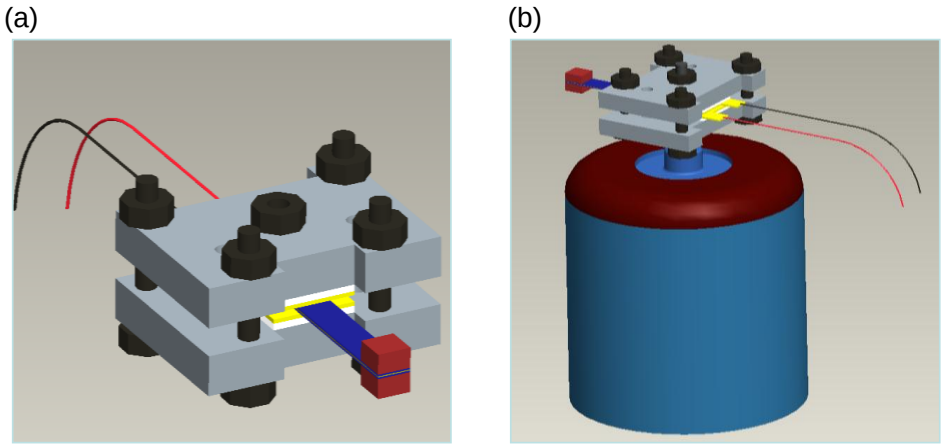

Figure 4.1 (a) An energy harvester is mounted on the clamping fixture; (b) The clamping fixture is attached to a shaker.

The voltage across the resistor is measured directly by the signal analyser as shown in Figure 4.2. The internal resistive load of the signal analyser is approximately 1 MΩ which is relatively small compared to the internal load of a voltmeter. Ideally, a

voltmeter should be used to measure the voltage to minimise the leakage from the equipment. However, using a signal analyser will facilitate the measurement for FRFs. Due to the limitation of the signal analyser, the signal analyser is only capable of accurately measuring the voltage across the resistance load up to 60 kΩ as found through experiments, otherwise there will be a large leakage from the signal analyser. Therefore, the range of resistance loads connected to the energy harvesters are in the range 0 to 60 kΩ in the experiments.

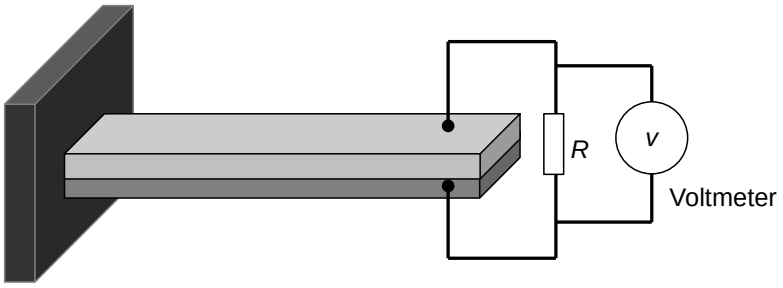

Figure 4.2 The voltage across the resistor is measured in the experiment

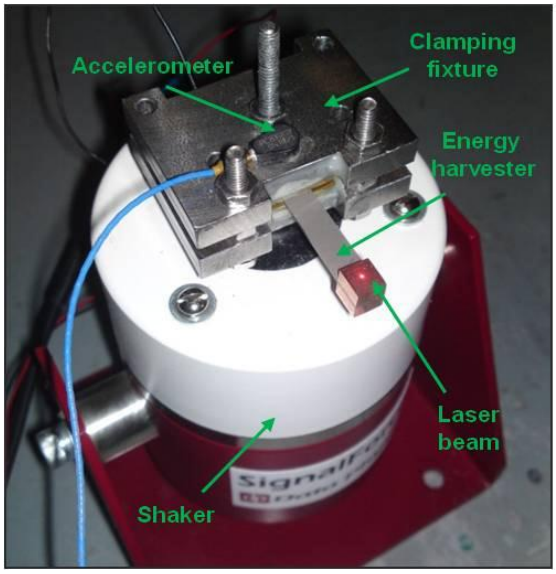

Figure 4.3 The experimental setup for testing

4.3 Experiments

Three energy harvester samples are tested. The first sample tested is a monomorph, which is prepared at the University of Nottingham. The second sample is a premade bimorph supplied by Piezo Systems. The third sample tested is a modified version of the premade bimorph, which has a tip mass attached at the free end.

4.3.1 Monomorph energy harvester

4.3.1.1 Sample preparation

The monomorph sample was prepared at the University of Nottingham. It consists of a layer of PZT and a layer of aluminium. The PZT used for the monomorph is PIC 255 supplied by PI Ceramic. PIC 255 is classified as soft PZT in the supplier's catalogues. Soft piezoceramics have relatively high domain mobility and a resulting ferroelectrically soft behaviour [87]. PIC 255 is supplied as a square sheet with a thickness of 0.5 mm. It is cut to have a beam size of 50 mm x 8 mm. Initially, the PZT sheet was cut using a waterjet but this offered a relatively rough and jagged cutting surface and occasionally damaged the electrode coating. Using a laser cutting machine burnt the cut edges of the PZT, which would potentially damage the piezoelectric polarisation due to the high temperature of the laser. The best solution found to cut the PZT sheet was to use a silicon carbide cutting wheel, which offered much improved cut edges and no high temperature to damage the PZT properties.

The PZT beam layer was attached to the aluminium substrate. The length and width of the substrate are fully covered by PZT but the thickness of the substrate was 0.65 mm. 3M Scotch-Weld^{TM} Epoxy Adhesive DP 460 is a 2-part 2:1 epoxy applied

between the PZT and substrate to form a strong adhesive bond. According to the manufacturer's data sheet, the curing time to handling strength is about 6 hours at room temperature. Also, the shear and peel strengths are 31 MPa and 107 N/cm respectively. Furthermore, DP460 is not electrically conductive so a small patch of conductive adhesive was applied at one end of the sample to allow electrical conduction. The ratio of the adhesive area of the conductive adhesive to DP 460 is about 1:10. A monomorph sample is shown in Figure 4.4.

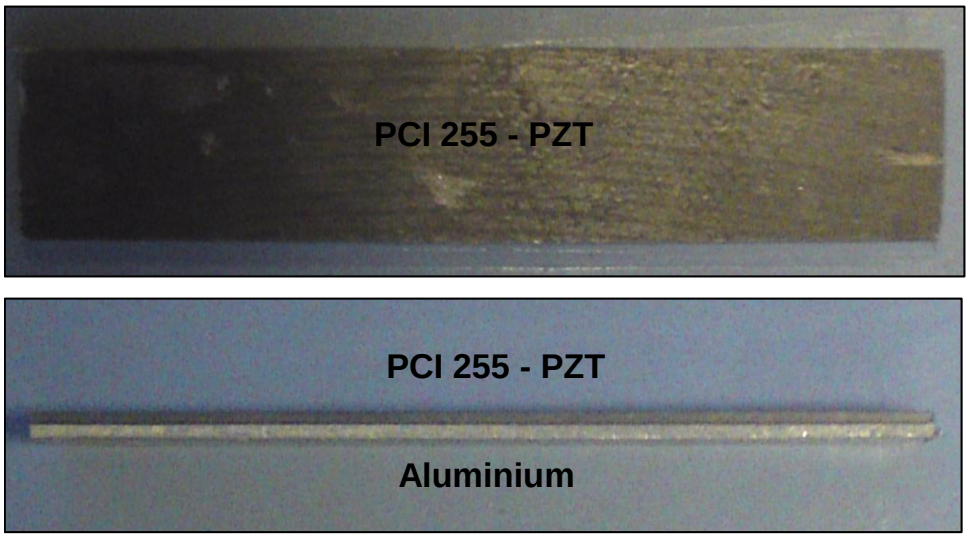

Figure 4.4 Monomorph sample prepared for experimental testing

4.3.1.2 Experimental measurements and validation

When the monomorph is mounted on the clamping fixture, it is in a cantilever configuration with length 35.94 mm. The dimensions and material properties are listed in Table 4.1. Before carrying out the experiment, it is necessary to determine the mechanical damping of the monomorph sample. This can be achieved by disconnecting all electrical loads (i.e. resistance = 0 Ω) from the monomorph since the resistance will change the damping of the electromechanical system by

dissipating electrical energy through the resistor. The damping ratio of the fundamental mode was found using the half power method and had a value 0.0032. In addition, the measured natural frequency of the monomorph is 524.7 Hz. A harmonic excitation of 0.1 m/s^2 is applied to the monomorph in the experiment. Figure 4.5 shows the measured tip displacement of the monomorph and the voltage across the resistor for different resistors. As mentioned earlier, the frequency response functions are measured near the fundamental resonance of the monomorph in the experiment. In the experimental results, the resonance frequency increases when the resistance is increased in the circuit. Also, the displacement decreases and voltage increases as the resistance increases. This will be investigated in Section 4.4.1.

Monomorph - physical properties and dimensions

	Aluminium substrate	PZT PCI 255
Length, *L* (mm)	35.94	35.94
Width, *W* (mm)	6	6
Thickness, *T* (mm)	0.65	0.5
Young Modulus, *E* (GPa)	69	66
Density, ρ (kg/m^3)	2700	7800
Piezoelectric constant, d_{31} (m/V)	–	$180x10^{-12}$
Relative Dielectric constant, k_3	–	1750

Table 4.1 Mechanical properties and dimensions of the monomorph energy harvester

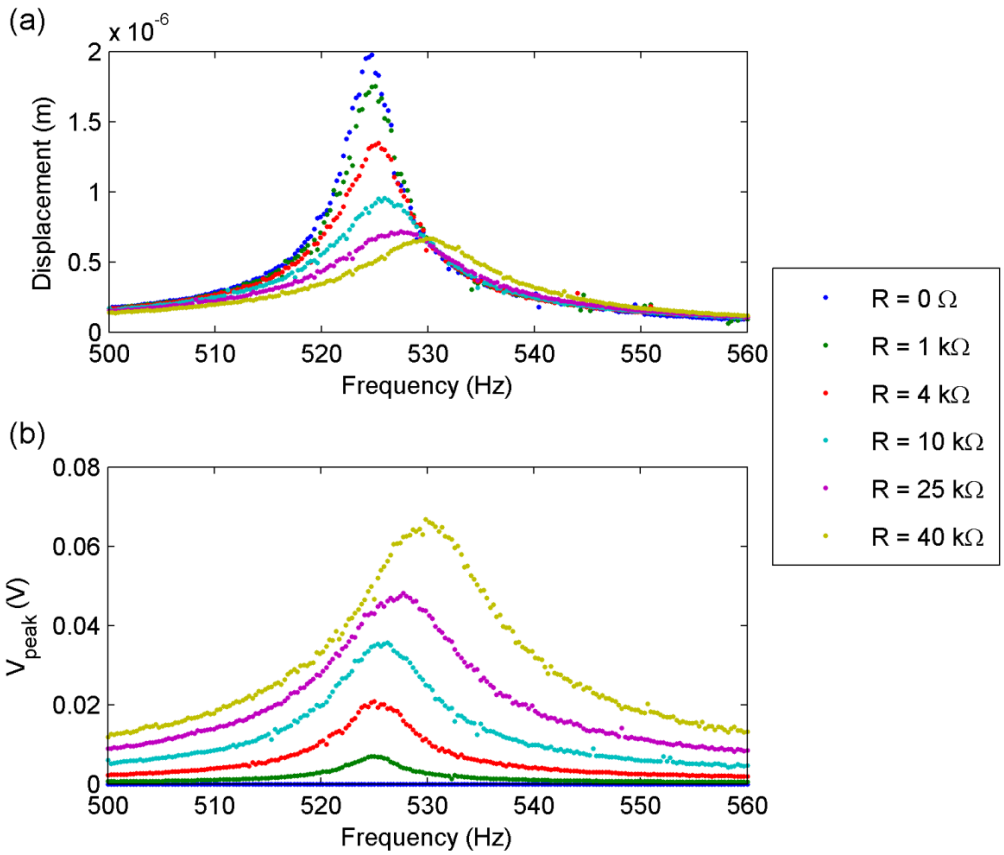

Figure 4.5 Measured frequency response functions for different resistors with a constant excitation amplitude: (a) tip displacement; (b) voltage

The measurements are compared to theoretical results to validate the model. Figure 4.6(a) and (b) compare the frequency response functions for the tip displacement and the voltage for load resistances R = 0 Ω, 1000 Ω and 4000 Ω. There is good agreement between the measurements and theoretical results as both the resonance frequencies and amplitudes match very well. Also, there is no obvious resonance frequency shift seen from R = 0 Ω to R = 4000 Ω as the resonance frequency is insensitive to this range of resistance. The sensitivity of the resonance frequency to load resistance will be discussed in a later section of this chapter.

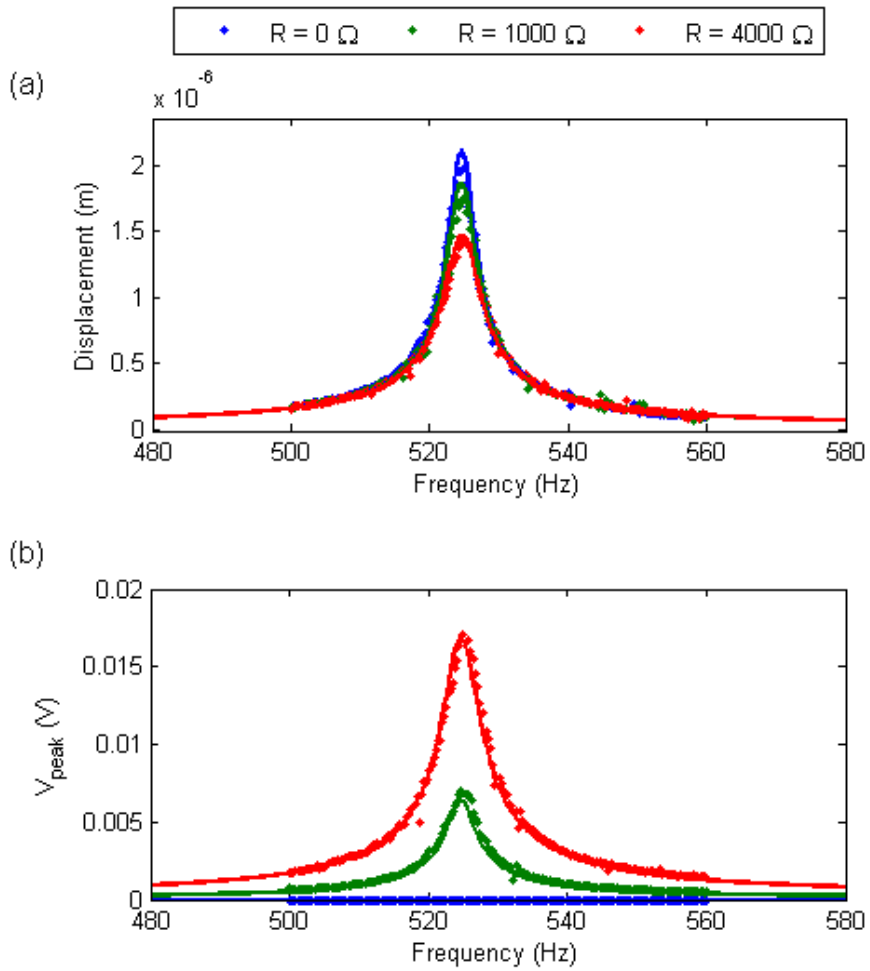

Figure 4.6 Frequency response functions for resistance of 0 Ω, 1000 Ω and 4000 Ω: (a) tip displacement; (b) voltage

The measurements for higher resistances (R = 10 kΩ, 25 kΩ and 40 kΩ) are compared to the analytical results in Figure 4.7(a) and (b). Good agreement is shown again for both the amplitudes and resonance frequencies between the theory and experiment. The electrical power output from the monomorph must be increased with these higher resistances, because it has been observed in the experiment that the displacement decreases by more a factor of two from 2.01 µm to 0.67 µm. This indicates the mechanical energy is reduced when more electrical energy is generated and dissipated through the resistor.

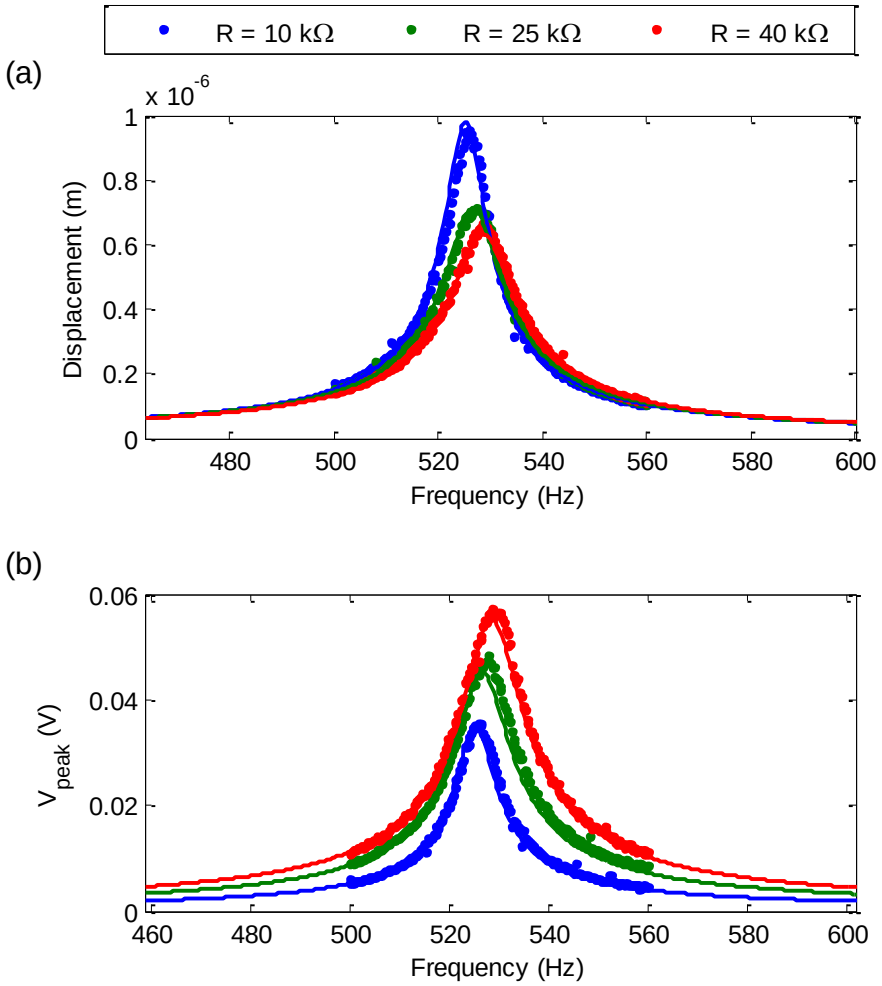

Figure 4.7 Frequency response functions for resistance of 10 kΩ, 25 kΩ and 40 kΩ: (a) tip displacement; (b) voltage

4.3.2 Bimorph energy harvester

4.3.2.1 Introduction to the premade sample

The other energy harvester sample tested was PSI-5A4E (Piezo Systems [88]), see Figure 4.8. It is in the bimorph configuration and a brass substrate layer is sandwiched between two identical layers of PZT. The bimorph is completely covered by PZT and has length 31.8 mm and width 6.4 mm. The thicknesses of the substrate and PZT layers are 0.14 mm and 0.26 mm respectively. The dimensions and properties of the bimorph are listed in Table 4.2. Also, the PZT layers are configured

to a series connection with the same polarity. It is worth mentioning that the PZT layers could be configured to parallel connection. However, this is not considered in this work.

The adhesive bond between the brass and PZT layers was analysed using an electron microscope. The adhesive is uniformly spread throughout the bimorph and its thickness is approximately 12 µm, as seen in the microscopic image in Figure 4.9. The effects of the adhesive are assumed to be negligible in the theoretical model.

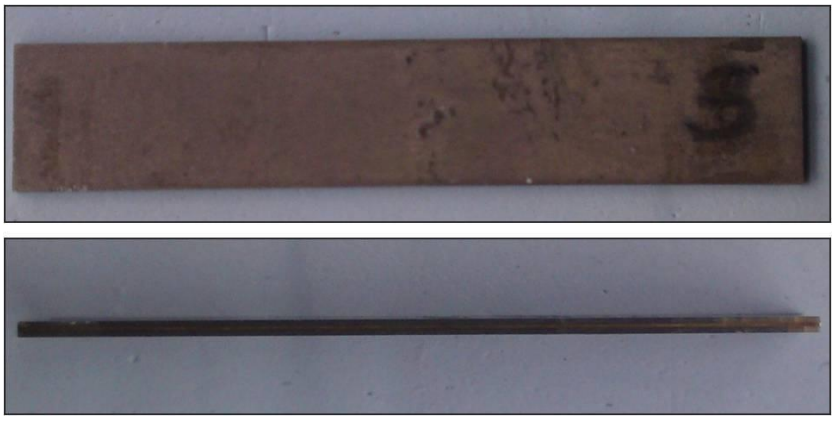

Figure 4.8 The bimorph sample tested in the experiment

Bimorph - mechanical properties and dimensions

	Substrate (copper)	PZT
Length, *L* (mm)	29.0	29.0
Width, *W* (mm)	6.4	6.4
Thickness, *T* (mm)	0.14	0.26
Young Modulus, *E* (GPa)	100	66
Density, ρ (kg/m^3)	8700	7800
Piezoelectric constant, d_{31} (m/V)	–	190×10^{-12}
Relative Dielectric constant, k_3	–	1800

Table 4.2 Mechanical properties and dimensions of the bimorph energy harvester

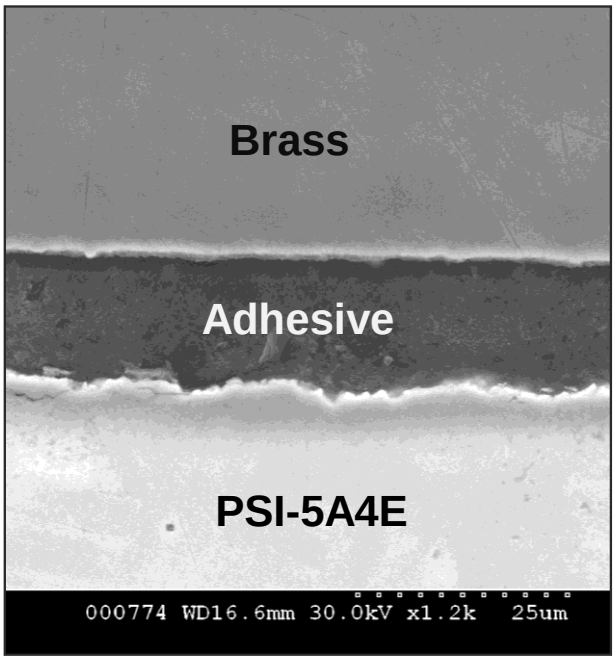

Figure 4.9 Microscopic image of the bimorph PSI-5A4E

4.3.2.2 Experimental measurements and validation

The experimental work conducted on the bimorph sample is identical to the experimental work performed on the monomorph sample described in Section 4.3.1. The bimorph is excited by a shaker with a base acceleration of 0.1 ms^{-2}. Figure 4.10 shows the tip displacement of the bimorph and the voltage across the resistor for six different resistors over the range 0 to 50 kΩ. Similar trends are observed to the previous testing. The resonance frequency increases by approximately 7 Hz from R = 0 Ω to R = 50 k Ω and the peak displacement also decreases from 1.98 µm to 0.45 µm.

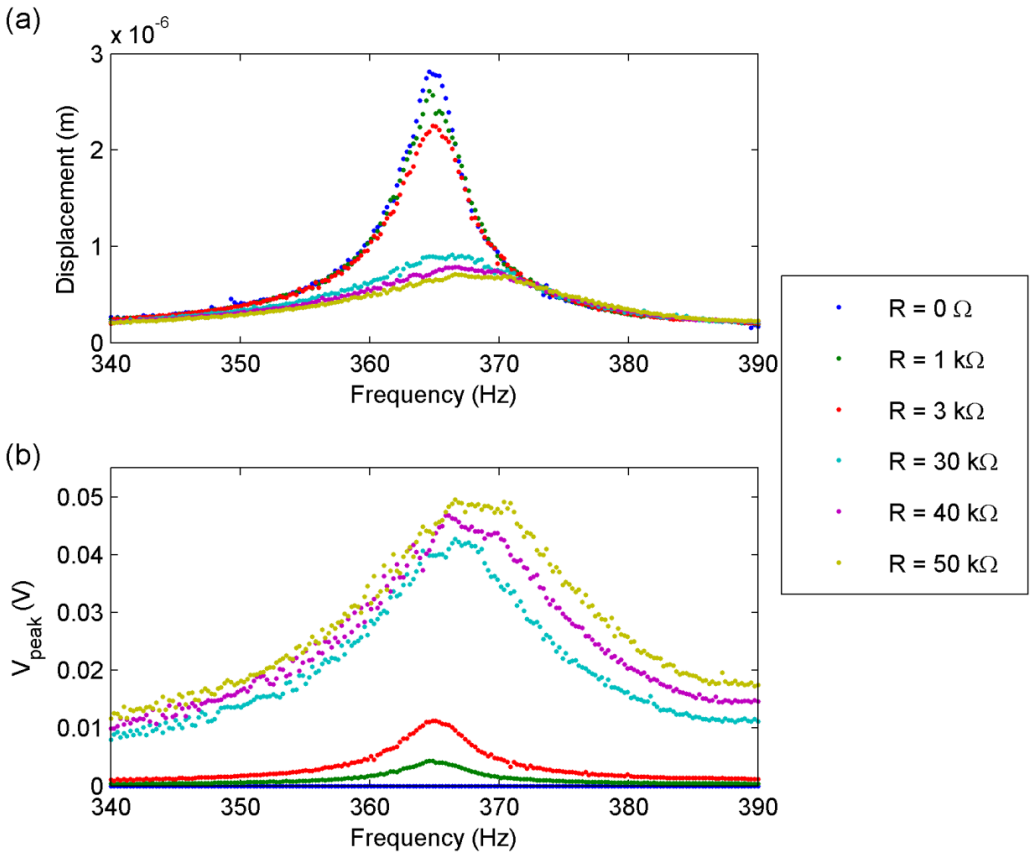

Figure 4.10 Measured frequency response functions for different resistors: (a) tip displacement; (b) voltage

The mechanical damping of the bimorph is found in a similar way to the monomorph sample by disconnecting the electrical load from the bimorph (i.e. R = 0 Ω). The damping ratio for the first mode is found to be 0.0051. The FRFs for R = 0, 1000 and 3000 Ω are compared to the measurements in Figure 4.11, while the analytical and measured FRFs for R = 30, 40 and 50 kΩ are compared in Figure 4.12. The comparisons show good agreement between the measurements and predictions as both the natural frequency and amplitude match very well.

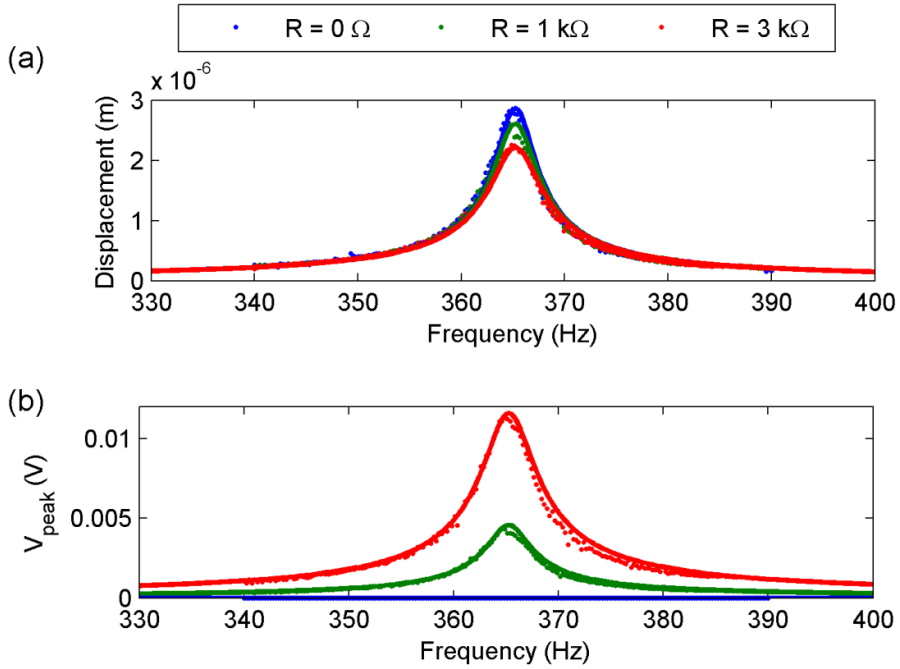

Figure 4.11 Frequency response functions for resistance of 0 Ω, 1000 Ω and 3000 Ω: (a) tip displacement; (b) voltage

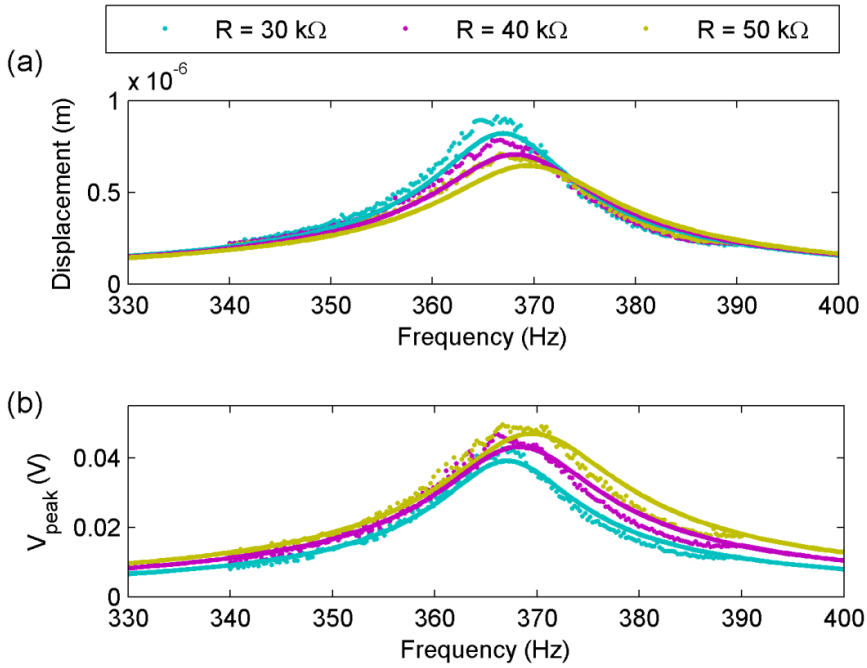

Figure 4.12 Frequency response functions for resistance of 30 kΩ, 40 kΩ and 50 kΩ: (a) tip displacement; (b) voltage

4.3.3 Bimorph energy harvester with an offset tip mass

4.3.3.1 Modified bimorph sample

The bimorph tested in Section 4.3.2 is modified by attaching a tip mass to the beam as shown in in Figure 4.13 and Figure 4.14. Two blocks of copper are attached to the top and bottom surfaces of the PZT layers using 3M adhesive DP 460. The size of each copper block is 6.4 mm x 6.4 mm x 3 mm and the offset distance of the tip mass is 3.2 mm. The density of copper is typically 8700 kg/m^3, so the mass added to the tip is 2.14 gram. The radius of gyration is calculated to be 2.7x10^{-3} m, while the moment of inertia of the tip mass about its centre is 1.68x10^{-8} kgm^2. These physical parameters for the tip mass are essential for obtaining the natural frequencies and mode shape functions as described in Section 3.3. Also, the length of the beam, L_b, is 20.4 mm.

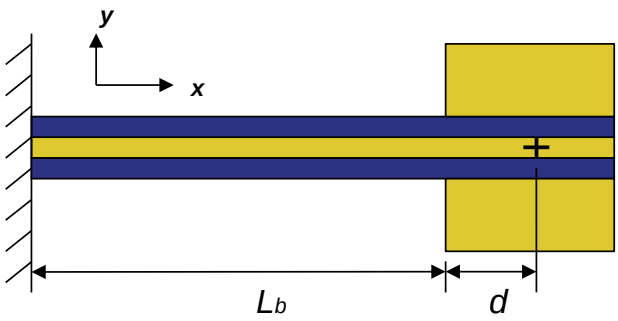

Figure 4.13 Two blocks of copper mass are attached to the bimorph sample

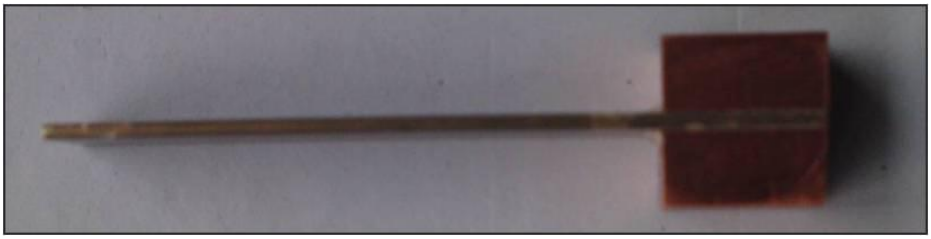

Figure 4.14 The modified bimorph sample tested in the experiment

4.3.3.2 **Experimental measurements and validation**

The modified bimorph is excited by the shaker at an acceleration amplitude of 0.1 m/s^2. Figure 4.15 shows the measured FRFs for the displacements at the centre of the tip mass and the voltages for different load resistors. The measured fundamental natural frequency of the modified bimorph is 153.15 Hz, while the predicted natural frequency is 152.92 Hz, i.e. a percentage error of 0.15%. The mechanical damping ratio is found to be 0.006 at R = 0 Ω and this value is used in the theoretical model.

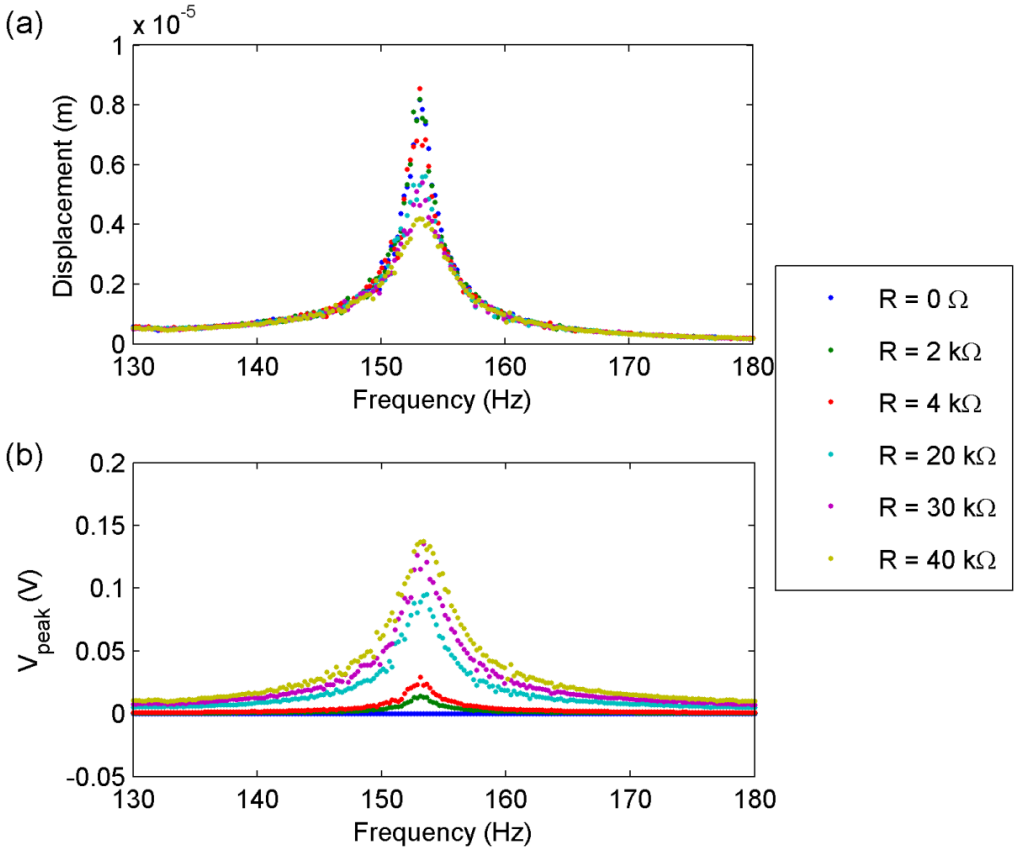

Figure 4.15 Measured frequency response functions for different resistors: (a) tip displacement; (b) voltage

Figure 4.16 compares the measured and analytical FRFs for the displacement and voltage when R = 0 Ω, 2 kΩ and 4 kΩ. Figure 4.17 compares the analytical and

experimental results for R = 20, 30 and 40 kΩ. In all cases, both the predicted resonance frequency and the amplitude match well with the measurements.

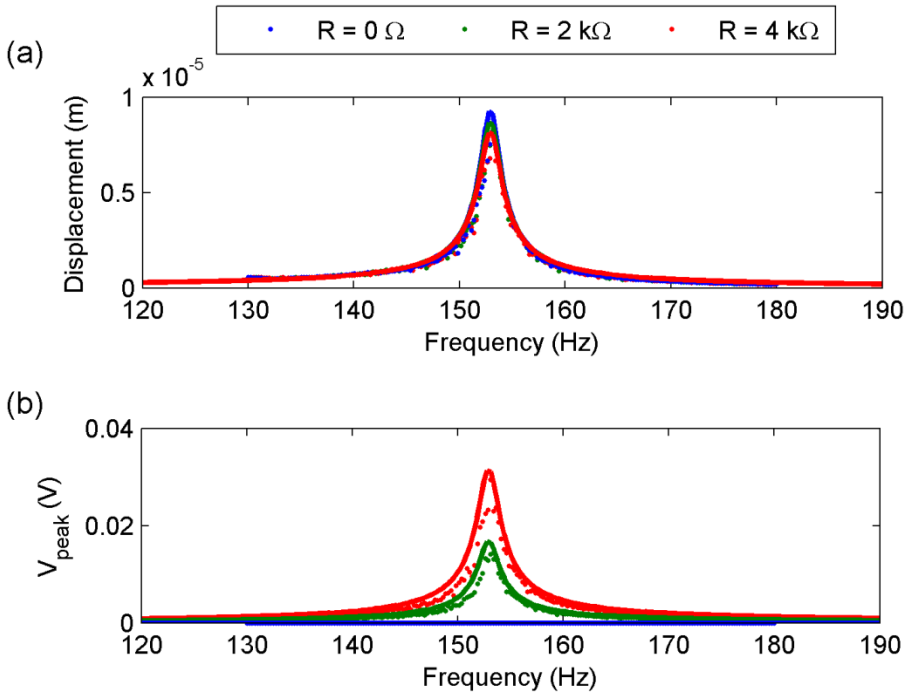

Figure 4.16 Frequency response functions for resistance of 0 Ω, 2000 Ω and 4000 Ω

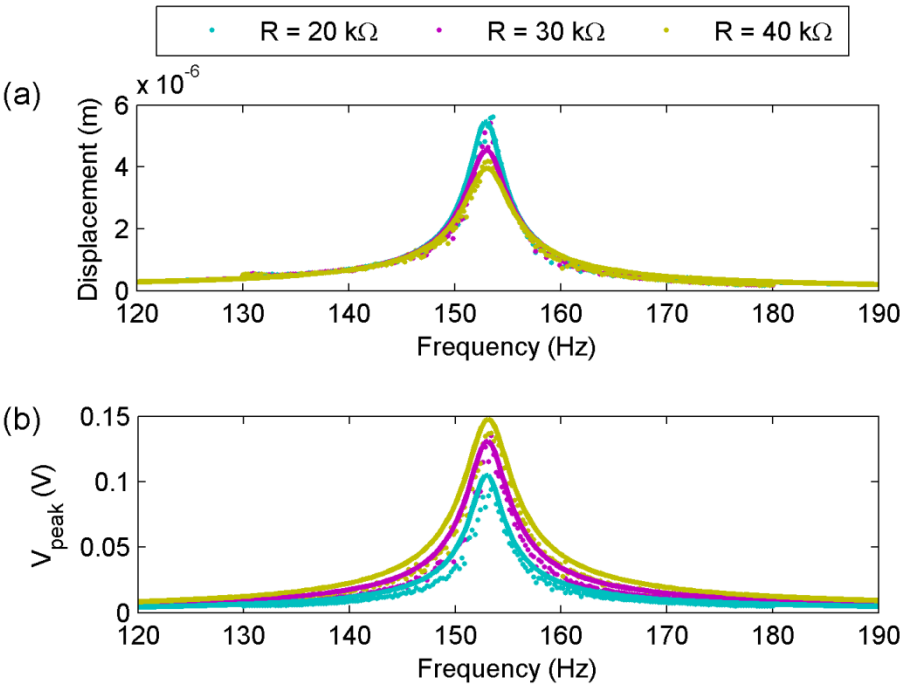

Figure 4.17 Frequency response functions for resistance of 20 kΩ, 30 kΩ and 40 kΩ

4.4 Parameter studies

The theoretical model for the piezoelectric energy harvester has been validated against the experimental results for different harvester samples in Section 4.3. The validation gives confidence in the theoretical results and confirms the model should be reliable for further investigations. In this section, the performance of the piezoelectric energy harvester is studied and the optimum working conditions are determined to optimise the electrical power output. The key parameters, including electrical loads, material properties and geometries are studied individually to analyse the effects on the performance of the energy harvester and the power output.

It has been observed in the experiments that the amplitude of the displacement of the energy harvester sample is reduced dramatically when the resistance increases from 1 kΩ to 10 kΩ and this is an indication of more electrical energy being removed from the system. However, the maximum power output should not be judged by the peak displacement amplitude because the power output is not necessarily inversely proportional to the displacement. In the experiment, the electrical power cannot be measured directly and it is not intuitive to determine at what resistance value the power is maximised. However, the electrical power, *P*, can be calculated simply as:

$$P = \frac{v^2}{R} \tag{4.1}$$

The electrical power of the monomorph tested in Section 4.3.1 is calculated using equation (4.1) for load resistances of 10 kΩ, 25 kΩ and 40 kΩ and the frequency response functions for the power are shown in Figure 4.18. In this example, the

maximum peak power occurs at R = 10 kΩ but the bandwidth of the frequency response function is narrower than the other two frequency response functions. The effects of resistance on power output are investigated in detail in the following section.

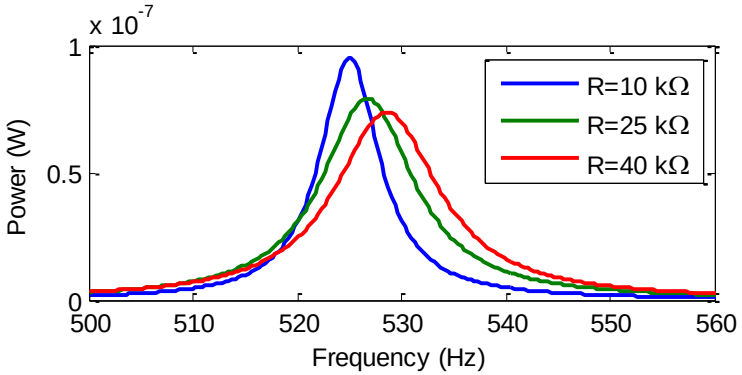

Figure 4.18 The power generated by the monomorph for different electrical loads

4.4.1 Effects of resistance and optimum resistance for maximum power

It has been seen that the resonance frequency of the energy harvester increases when a resistor is connected and the frequency shift varies with load resistance. The monomorph tested in Section 4.3.1 is analysed here to investigate the effects of resistance on the resonance frequency. This is achieved by plotting the resonance frequency against resistance, R, see Figure 4.19. The resonance frequency is comparatively insensitive to the resistance when the resistance is below 10 kΩ or above 1 MΩ. Nevertheless, the resonance frequency increases rapidly from 525 Hz to 533.5 Hz between 10 kΩ and 1 MΩ. If the resonance frequency is expressed as a function of resistance, the resonance frequency = 533.6 Hz is the asymptote of the function, which means the frequency does not go beyond 533.6 Hz. This frequency can be referred to as the open circuit resonance frequency. The other asymptote of

the function corresponds to a resonance frequency = 524.6 Hz and similarly the resonance frequency does not drop below this value. This can be referred to as the short circuit resonance frequency [25]. Therefore, the conditions for the open circuit and short circuit resonance frequencies occur as R → 0 and R → ∞, respectively.

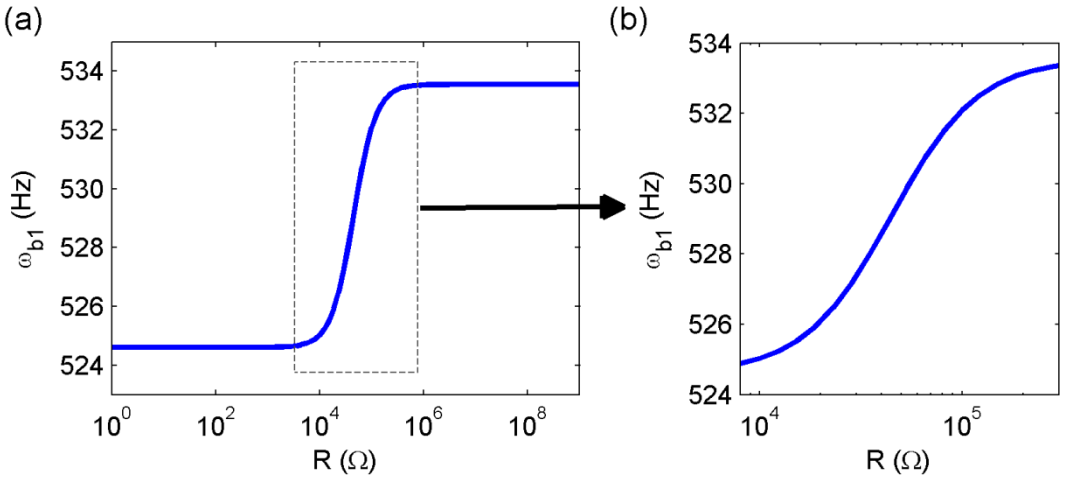

Figure 4.19 Fundamental resonance frequency varies with the resistance

Besides the variation in resonance frequency, the peak displacement, peak voltage and peak power output of the energy harvester also vary with the resistance. They are again expressed as functions of resistance *R* and plotted in Figure 4.20(a), (b) and (c) respectively. Note that the mechanical damping ratio used is fixed to 0.003 in this analysis. Figure 4.20(a) indicates the minimum displacement is in the dip of the curve at 45.5 kΩ but the corresponding power at 45.5 kΩ is not the maximum power. It lies between the two peaks of the power spectrum and is approximately a quarter less than the maximum power. Figure 4.20(c) shows the maximum power of 0.96 μW can be obtained with a resistance 7.8 kΩ or 240.9 kΩ. These double peaks represent the two maxima, while the turning point at R = 38.5 kΩ represents the local minimum point [54]. It is worth mentioning that the corresponding resonance

frequencies for the two peaks in Figure 4.20(c) lie close to the short circuit and open circuit resonance frequencies respectively, as shown in Figure 4.21. Furthermore, the open voltage obtained from Figure 4.20(b) is 0.314 V. The sensitivities of the displacement, voltage and power to the resistance are very similar to the resonance frequency mentioned above. The change in dynamical and electrical responses can hardly be seen for load resistances between 0 Ω and 1000 Ω. When the resistance is greater than 1000 Ω, the system begins to generate more noticeable power and also the amplitude displacement and voltage change rapidly until the resistance is greater than 2 MΩ.

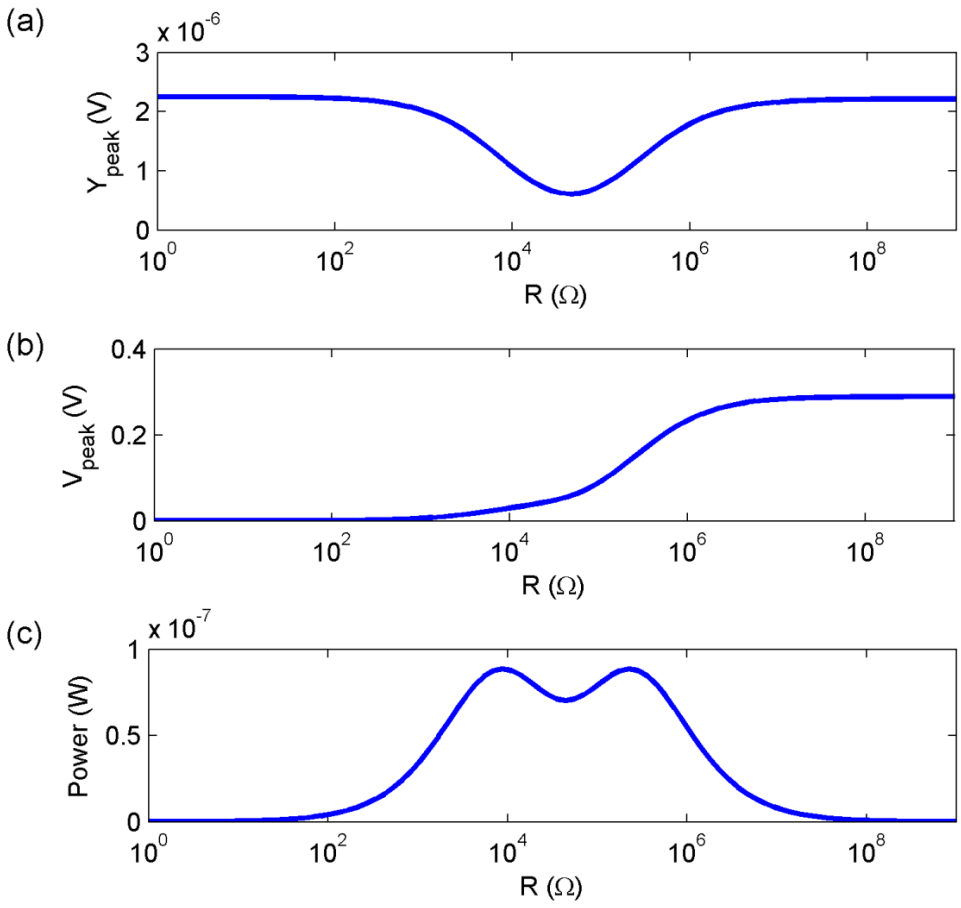

Figure 4.20 (a) Displacement; (b) Voltage; (c) Power vary with the load resistance

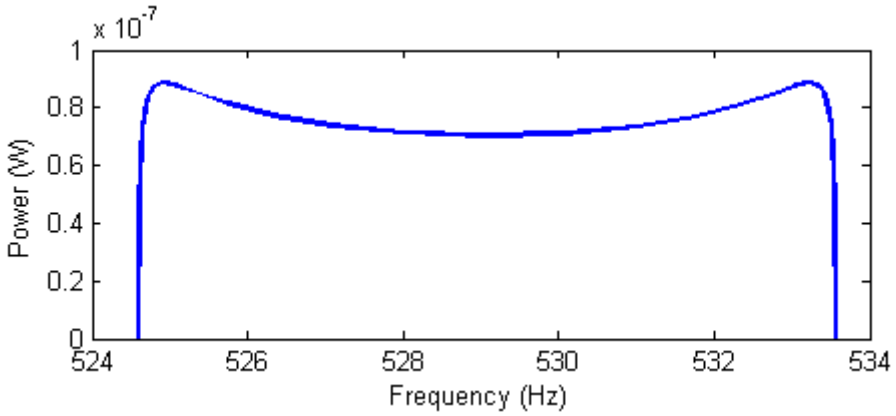

Figure 4.21 The peaks locate near the short circuit and open circuit resonance frequencies

The variations in peak displacement, voltage and power to changes in load resistance have been presented so far. However, it would be more meaningful to perform a comprehensive analysis of the energy harvester for a given bandwidth of excitation frequency and different resistances. This is because energy harvesters are rarely excited exactly at resonance in practice and the excitation frequency may be slightly offset from the resonance frequency.

The displacement, voltage and power are respectively mapped to the excitation frequency near resonance and load resistance. The surface plot in Figure 4.22(a) shows the tip displacement of the monomorph while the contours are shown in Figure 4.22(b). Figure 4.23(a) and (b) also show the surface plot and the contours for the voltage across the resistor. More importantly, the variation of power output to excitation and resistance of the monomorph are shown in Figure 4.24(a) and (b). The contours indicate the power level for different combinations of resonance frequency and resistance and also show the trend of the power shift.

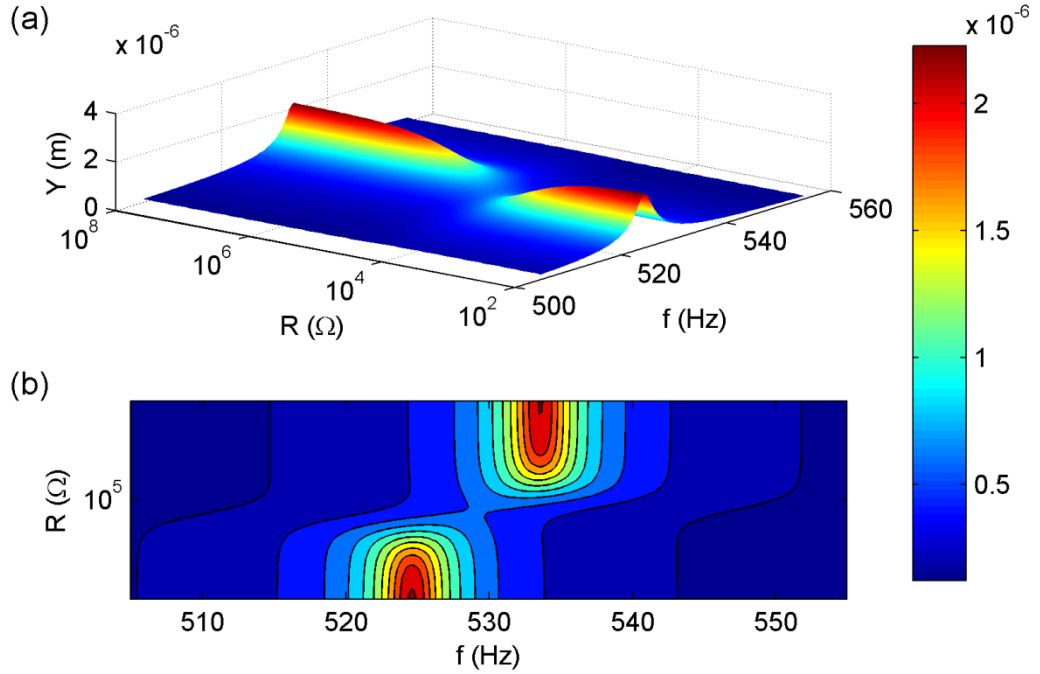

Figure 4.22 The tip displacement of the monomorph are plotted as: (a) a surface (b) contours

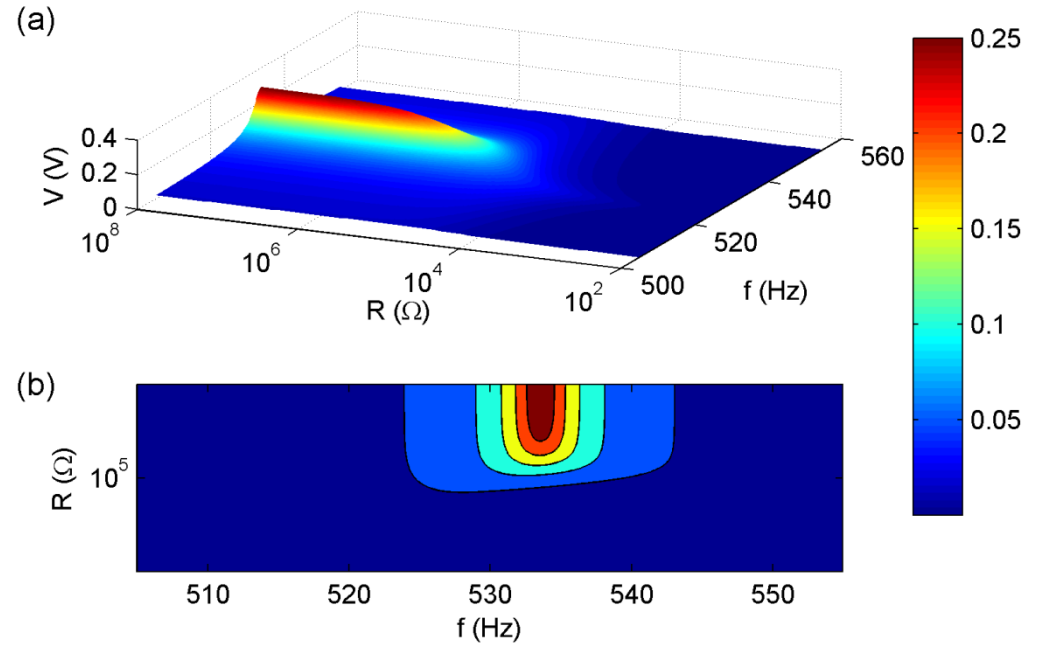

Figure 4.23 The voltage across the resistor are plotted as: (a) a surface (b) contours

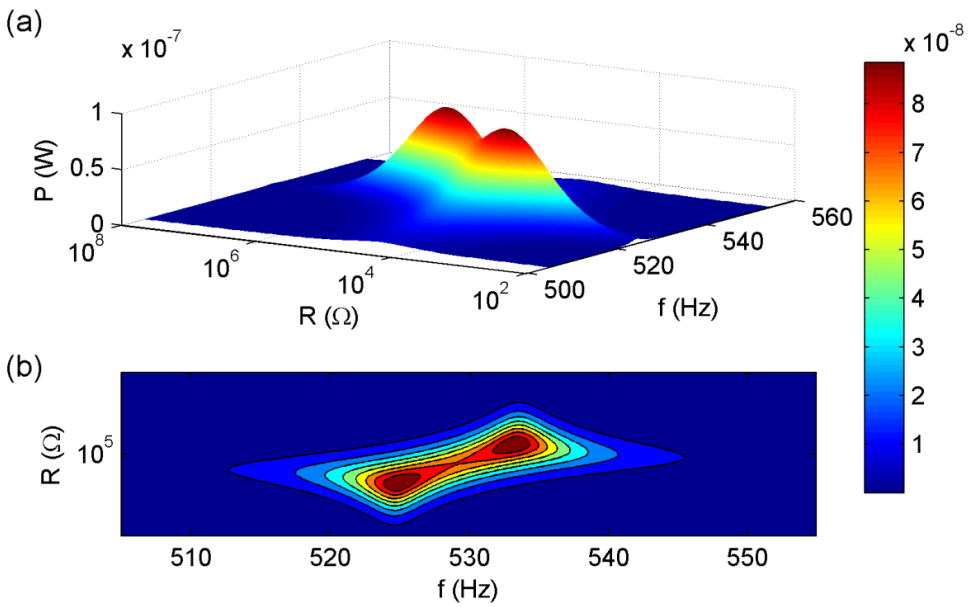

Figure 4.24 The power output of the monomorph are plotted as: (a) surface (b) contours

The performance of the monomorph has been analysed and the next sample to be investigated is the bimorph tested in Section 4.3.2. The effects of resistance on the performance of the bimorph will be anaylsed and the optimum power output conditions will be determined. In the analysis, the mechanical damping ratio is fixed to 0.0057 which is the same as was used for the monomorph.

Figure 4.25(a)–(d) show the resonance frequency, peak displacement, peak voltage and peak power as functions of the resistance. It can be seen from Figure 4.25(a) that the short circuit and open circuit resonance frequencies are 362.7 Hz and 376.8 Hz respectively. Both the displacement and voltage are comparatively more sensitive between 1 kΩ to 10 MΩ than for other resistance values as seen in Figure 4.25 (b) and (c). The maximum power output of the bimorph is 62 nW at an acceleration of 0.1 m/s^{-2} and can be obtained at a resistance of 10 kΩ or 533 kΩ. The contours for the displacement, voltage and power are mapped in Figure 4.25(a), (b) and (c) respectively to show the performance of the bimorph for different

combinations of excitation frequency and load resistance. In general, the trends seen in the contours for the bimorph are very similar to the contours for the monomorph.

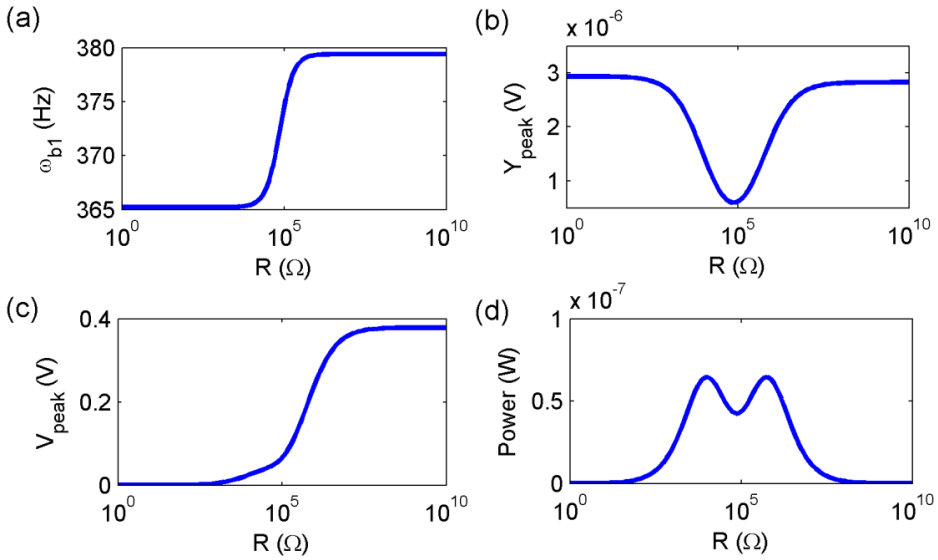

Figure 4.25 (a) Frequency (b) Displacement (c) Voltage (c) Power vary with the resistance for the bimorph sample

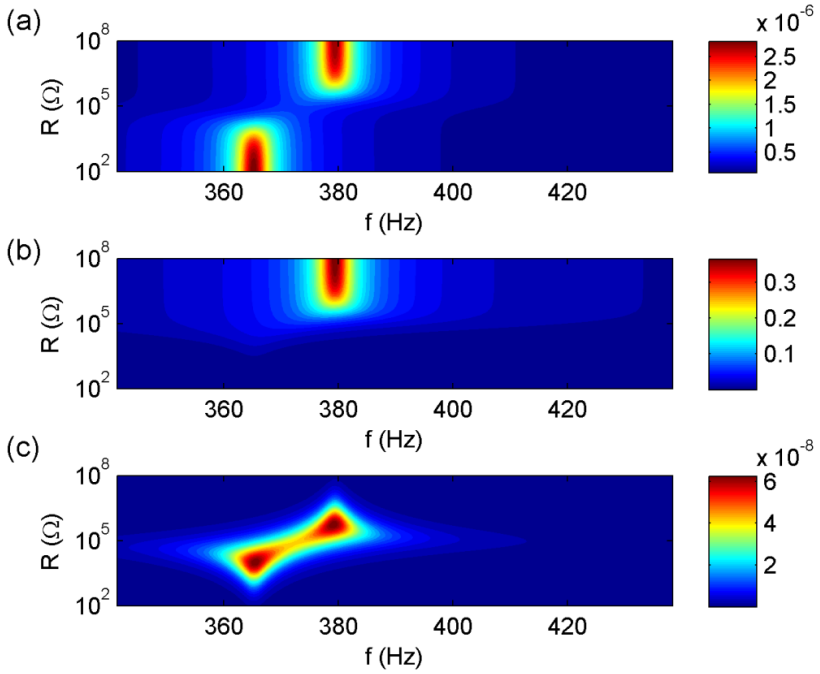

Figure 4.26 The variations in (a) displacement; (b) voltage; (c) power of bimorph are presented in contours

Finally, the modified bimorph, which has an offset tip mass attached, tested in Section 4.3.3 is investigated to obtain the optimum resistance for performance. The mechanical damping ratio is fixed to 0.0057 in the analysis. In this case, the optimum resistances for maximum power observed in Figure 4.27(d) are 27.05 kΩ and 2.15 MΩ. The contours for the displacement, voltage and power output are also provided in Figure 4.28(a) – (c) respectively.

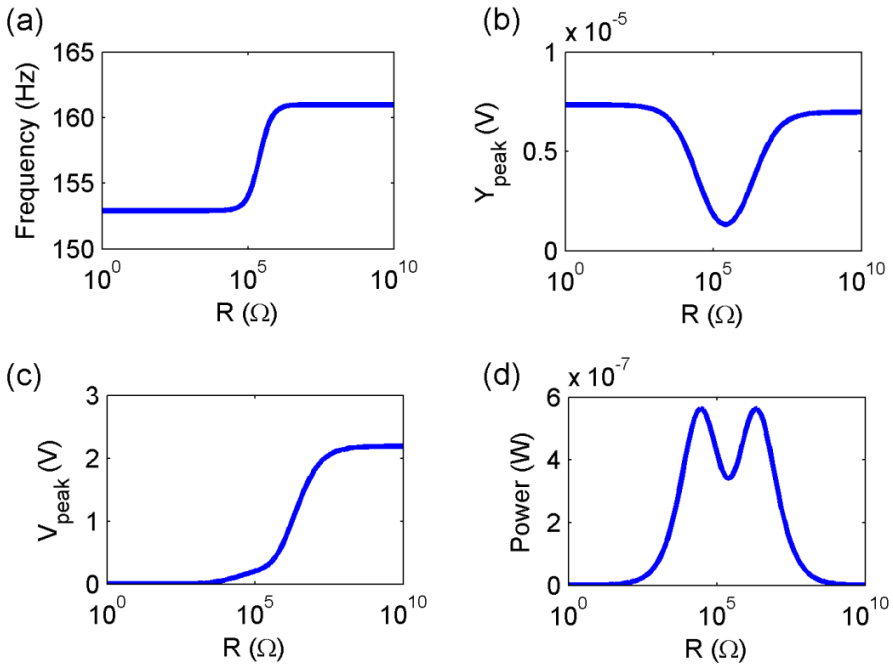

Figure 4.27 (a) Frequency (b) Displacement (c) Voltage (c) Power vary with the resistance for the modified bimorph sample

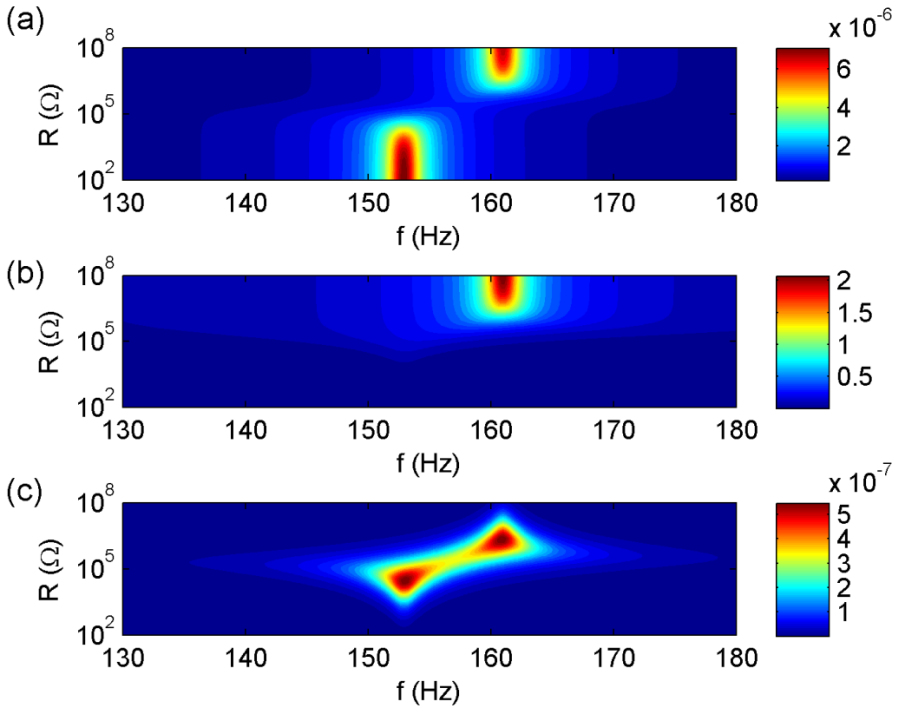

Figure 4.28 The variations in (a) displacement, (b) voltage and (c) power of the modified bimorph are presented in contours

4.4.2 Effects of the mechanical damping to power output

In the last section, the optimum resistance was determined for maximum power output. It is not surprising that the mechanical damping affects the amplitude of the mechanical vibration and the voltage across the resistor. However, it is not obvious that the mechanical damping will affect the optimum resistance for maximum power output although it does not affect the resonance frequency.

The monomorph sample is used to explain the effect of damping ratio on maximum power output. Figure 4.29(a) – (c) show the tip displacement, voltage across the resistor and power output against load resistance with different mechanical damping ratios. The amplitude of the displacement reduces as the damping ratio increases but the trends of displacement to resistance remain the same for different

mechanical damping. The trends of voltage also remain the same with different mechanical damping. However, the variation of power to the resistance changes with different levels of mechanical damping. The two peaks in the power functions can be seen clearly when the damping is low but the two-peak phenomenon disappears when the damping increases as shown in Figure 4.29(c).

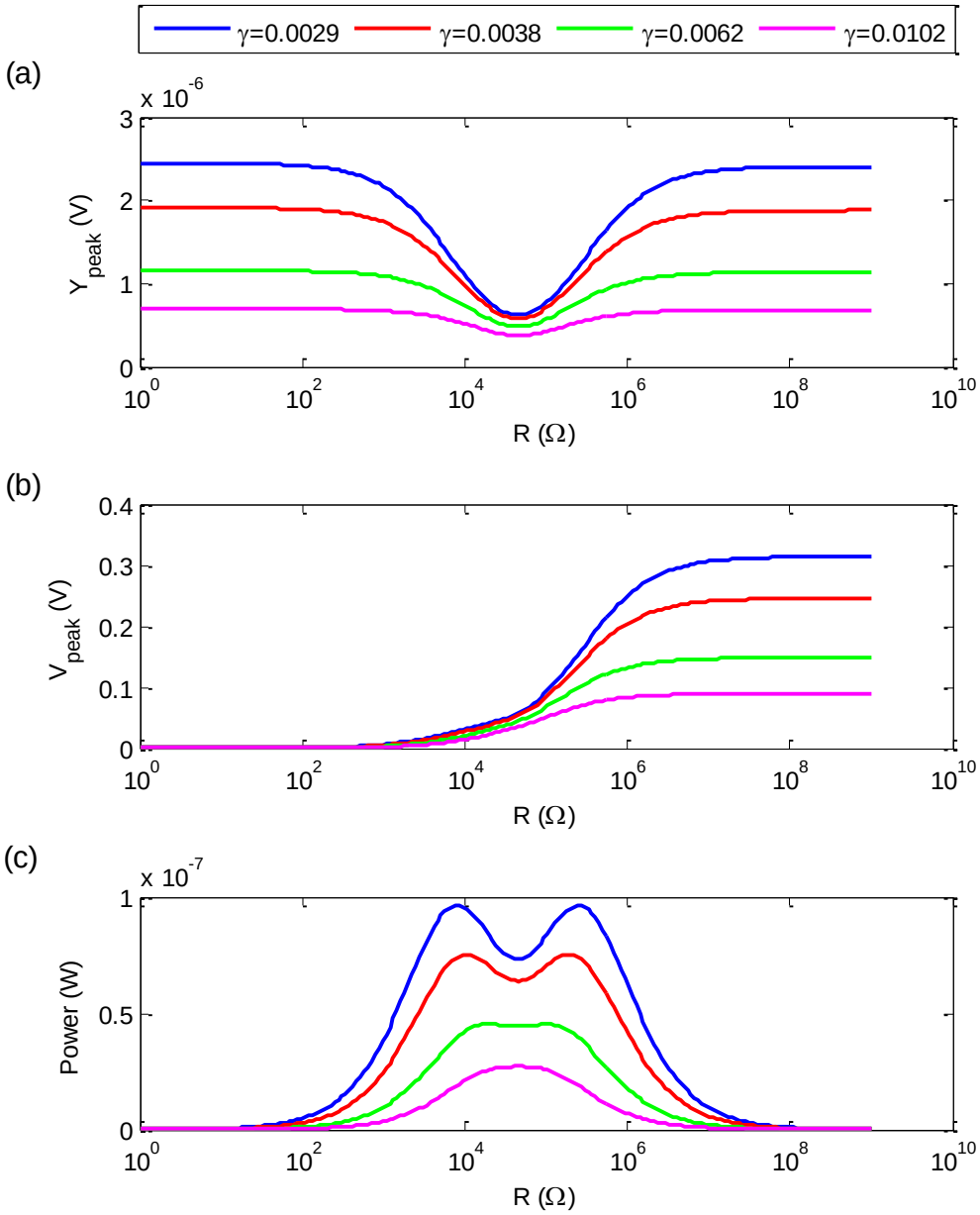

Figure 4.29 (a) Tip displacement; (b) Voltage across the resistor; (c) Power output with different damping ratio

The power contours are mapped by the resonance frequency and resistance for damping ratios of 0.0029 and 0.0102 respectively in Figure 4.30(a) and (b). It is clear to see that the two peaks in Figure 4.30(a) merge to a single peak in Figure 4.30(b).

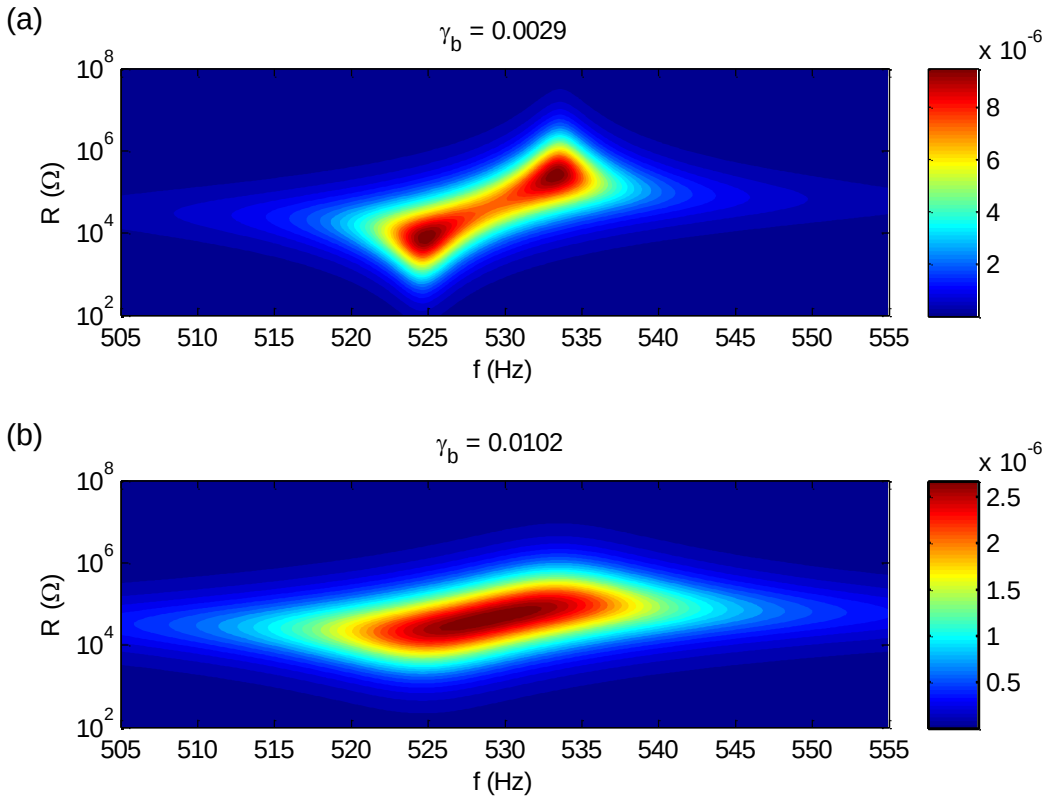

Figure 4.30 The contours of power output for damping ratio of (a) 0.0029; (b) 0.0102

4.4.3 Effects of the ratio of piezoelectric layer to substrate layer

In this section, the ratio of the thickness of the substrate layer, T_s, to the thickness of the piezoelectric layer, T_p, is varied to see how the power is affected. In this analysis, the overall thickness of the monomorph energy harvester is fixed to 1 mm while the ratio is varied. Aluminium and copper are used for the substrate layer in this analysis respectively. The other parameters used remain the same as the tested monomorph sample in Section 4.3.1. Also, the damping ratio is fixed to 0.0034.

Figure 4.31 shows that the fundamental natural frequency of the monomorph for the aluminium substrate increases as the ratio of T_s to T_p increases, while the change in natural frequency is very small for the copper substrate monomorph. This is due to the fact that the neutral axis position shifts, and the mass and stiffness of the substrate are different. Therefore, there is a larger variation in power on the thickness ratio for the aluminium substrate shown in Figure 4.32(a), while the maximum levels of the power are stable to the thickness ratio for the copper substrate in Figure 4.32(b). It can be deduced that the thickness ratio is less important if the stiffness of the PZT is similar to the stiffness of the substrate. If there is a large difference in stiffness between the PZT and substrate, the thickness ratio needs to be chosen carefully to ensure that the power output from the energy harvester is maximised.

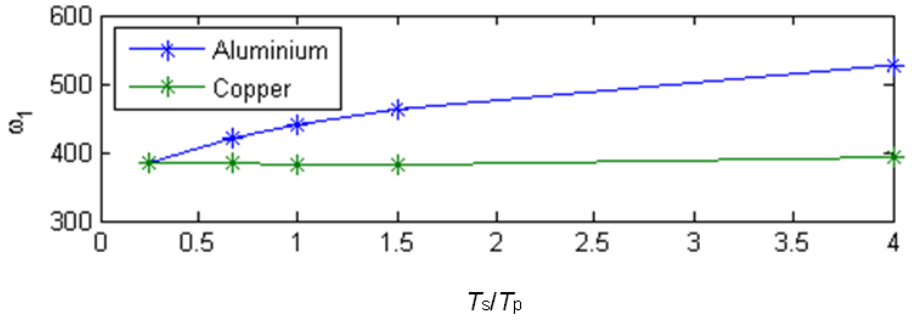

Figure 4.31 The variation in frequency with different thickness ratios for two substrate materials (a) Aluminium (b) Copper

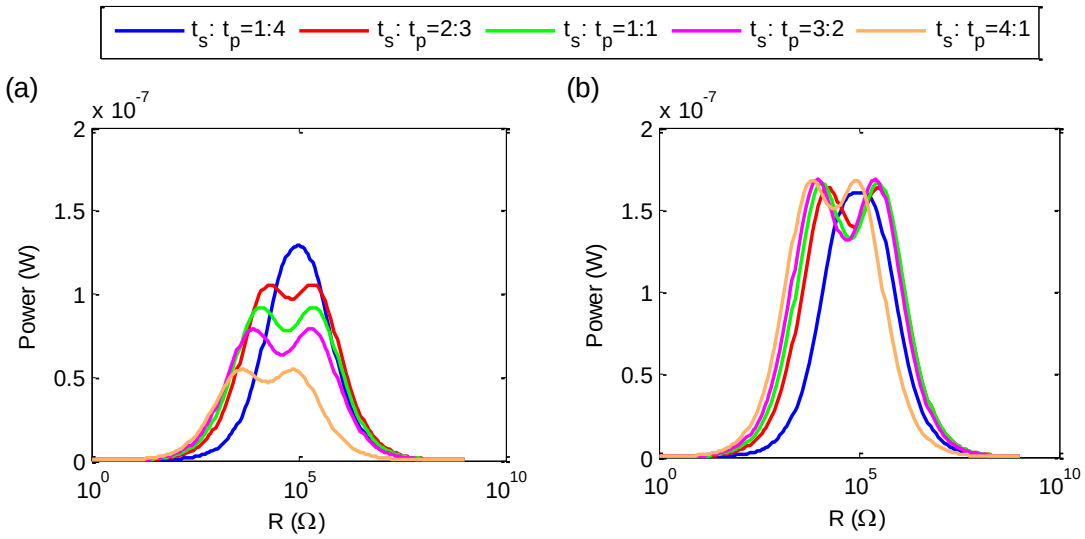

Figure 4.32 The power spectrum for different thickness ratios for two substrate materials: (a) Aluminium; (b) Copper

4.4.4 Effects of geometry and mass of tip mass

As mentioned earlier, a mass attached at the free end of the beam can tune the natural frequencies of the beam structure to match the excitation frequency, so as to achieve maximum power output. However, as yet the sensitivity of the natural frequency to mass, offset distance and geometry of the tip mass, has not been discussed.

If the energy harvester is a MEMS device, its natural frequencies will inevitably be comparatively high due to its size. For these devices, attaching a tip mass is useful as it reduces the natural frequencies. In what follows, the effect of the mass of the tip mass on the natural frequency is investigated. The mass of the tip mass can be altered without changing the dimensions by using different materials. This means that the offset distance and radius of gyration are unchanged. Table 4.3 lists the mass of the tip mass with different materials for the fixed dimensions of 6.4 mm x

6.4 mm x 6.4 mm. Figure 4.33 shows the change in the fundamental natural frequency of the structure with different materials used for the tip mass. The maximum power is plotted as a function of resistance in Figure 4.34. It can be seen that the power increases as the mass increases.

	Density (kg/m^3)	Mass (g)
Silicon	2330	0.61
Aluminium	2700	0.71
Steel	7850	2.06
Copper	8700	2.28
Silver	10500	2.75
Gold	19300	5.06

Table 4.3 Different materials are used for the tip mass

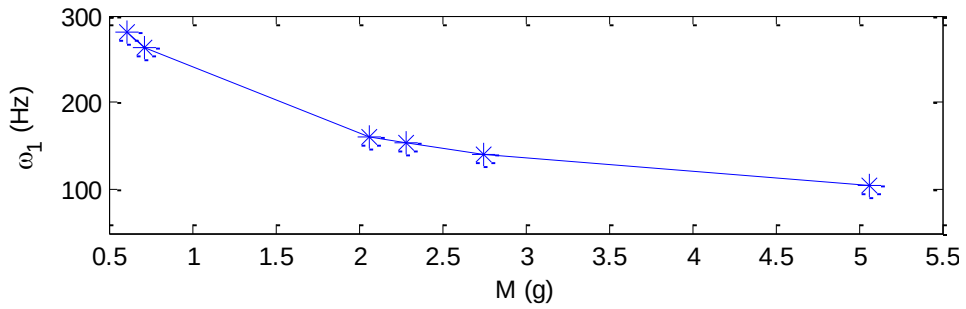

Figure 4.33 The fundamental natural frequency reduces as the heavy materials are used

Often MEMS devices are quite compact due to limited space and in practice there are few options for materials in MEMS fabrication. In the next case considered, the tip mass material is assumed to be fixed and the volume of the mass is limited, so that the natural frequencies of the device cannot be reduced by increasing the volume. Alternatively, the natural frequencies can be reduced by changing the offset distance and geometry of the tip mass.

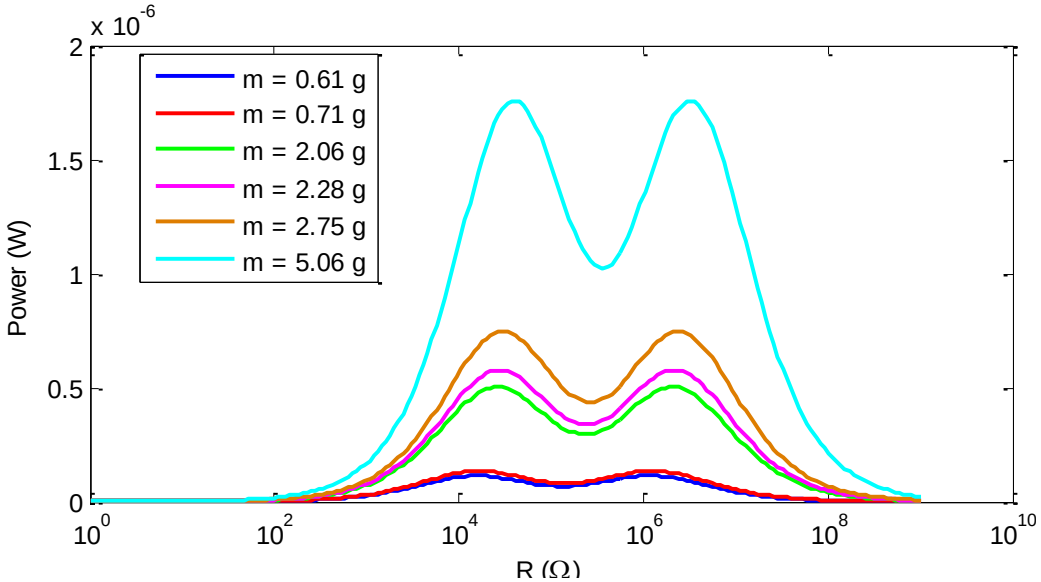

Figure 4.34 The maximum power as a function of resistance for different tip mass materials

The natural frequencies of a cantilever beam with an offset tip mass can be determined by solving characteristic equation (3.47). The effect of the offset is studied first. In the analysis, the shape of the tip mass is maintained as a rectangular block and its mass is kept constant (1 gram) by adjusting the height correspondingly and changing the offset distance as shown in Figure 4.35. Also note that the length of the mass is always twice the offset distance.

Figure 4.36(a) shows the change in radius of gyration, κ, for the offset distance, d. The height of the mass has to be increased to maintain the mass when d is small and hence incurs a large value of κ due to the specific criteria used. Therefore, the highest natural frequency does not occur for the smallest d in Figure 4.36. The natural frequency begins to decrease when d is longer than approximately 0.9 mm.

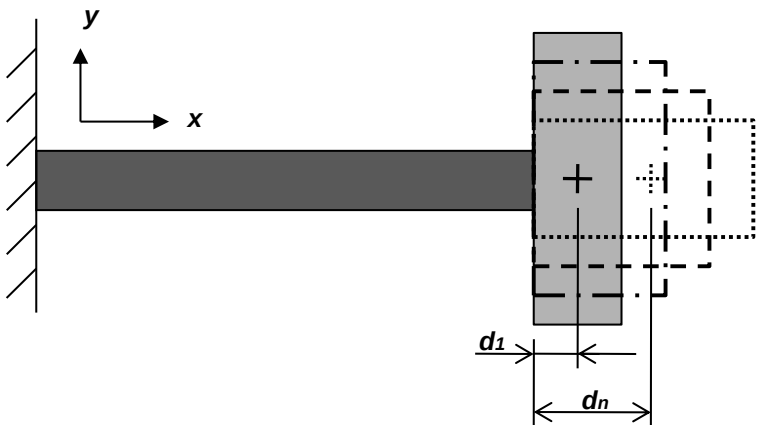

Figure 4.35 The offset distance and geometries change while the mass is kept constant

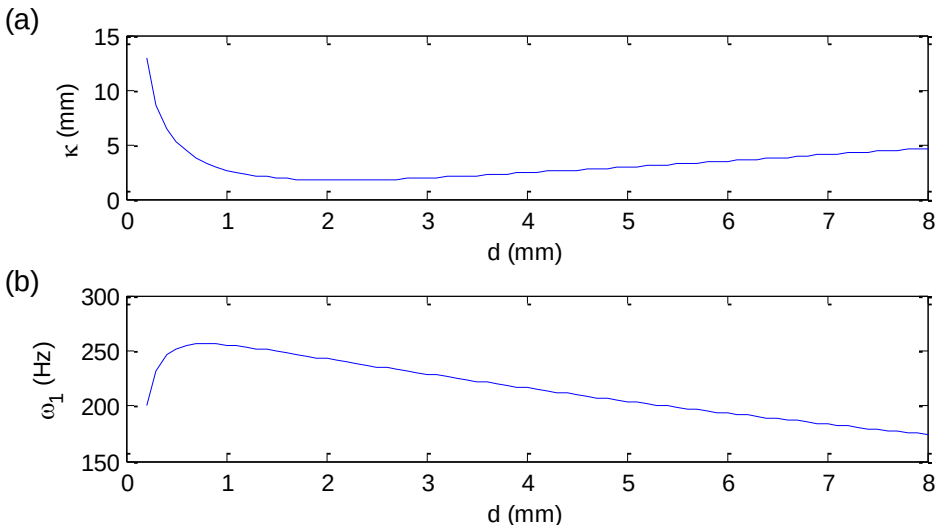

Figure 4.36 (a) The relation between *d* and *κ* (b) The fundamental natural frequency varies with *d*

4.5 Chapter conclusions

The theoretical model for a cantilever piezoelectric energy harvester developed in Chapter 3 has been validated experimentally by considering three different configurations with various load resistances. The measurements and theoretical results match very well. Overall, there is good agreement for the resonance frequency and the amplitudes of the frequency response functions, both for

displacement and voltage.

The performance of the energy harvester with changes to load resistance has been studied. The optimum resistances have been obtained for the maximum power output. The maximum power output can be obtained using two resistance loads when the mechanical damping is low. Unexpectedly, the maximum power can only be obtained for one resistance when the damping is high. From a practical point of view, energy harvesters are rarely excited at resonance and therefore the contours of the power with excitation frequency and resistance are useful to help analyse the performance and trends.

Different parameter studies have been conducted in a design viewpoint. An investigation demonstrated the importance of materials selection as well as the thickness ratio of the substrate to piezoelectric layer, as these factors can significantly affect the power output from the energy harvester. The maximum power output and natural frequencies could be reduced easily if an inappropriate substrate material or thickness ratio is chosen. Also, the natural frequencies of the energy harvester have been shown to be tuned easily by using a suitable tip mass. The geometry of a tip mass is found to be key to the natural frequencies as the offset distance and inertia are both determined by the geometry.

Chapter 5. Cantilever piezoelectric energy harvester impacting a stop

5.1 Introduction

Energy harvesters may be subjected to high amplitude vibrations and shocks. These excitations can cause high response levels that increase the generated power but reduce the fatigue life. In this chapter, a bump stop is incorporated into the design of a piezoelectric cantilever beam energy harvester as shown in Figure 5.1. The purpose of the stop is to limit the amplitude of the displacement and reduce the maximum stress in the cantilever beam. The aim of this study is to model and quantify the influence of the stop on the generated power and to investigate the influence that the initial gap size and the position of the stop have on the mechanical response and electrical output.

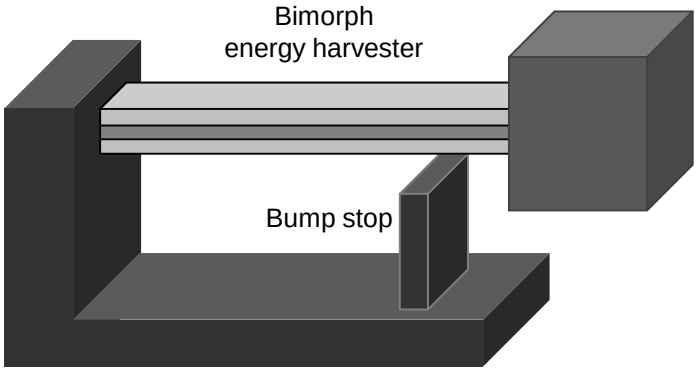

Figure 5.1 Schematic of a bimorph piezoelectric cantilever beam with and a tip mass attached

Many engineering applications feature a cantilever beam impacting against a stop and a variety of studies have been reported for different kinds of impact systems [89, 90]. Mechanical systems involving impact can result in complex dynamical behaviour which can be difficult to model. For this reason, exact solutions for the vibro-impact response are rarely derived and most theoretical predictions are only approximate [91-93].

Some studies seem to oversimplify the modelling process, leading to responses that fail to take account of important dynamical behaviour. For instance, the quasi-static approach should be used only if the nonlinearity is weak and the impact duration is relatively long compared to the period of oscillation [94]. Also, adopting an equivalent single-degree-of-freedom system based on the fundamental beam mode neglects the contribution of higher order beam modes which can be important. Moreover, sticking motion and chattering impact may not be observed in a single-degree-of-freedom model. Furthermore, if the duration of the contact force is shorter than the period of the fundamental mode, the force will excite higher frequency vibration modes.

Two basic approaches are commonly used to model the impact between two bodies. The first is based on using Newton's coefficient of restitution to relate the velocities of the colliding bodies before and after impact [95]. The main benefit of this approach is that the impact process is greatly simplified, avoiding potentially complex numerical schemes and obviating the need to determine the contact force between the two bodies. However, the major drawback in this approach is that the value of the coefficient of restitution can only be determined through experimentation and its value may vary if the contact duration changes and higher

modes are excited [96]. For this reason, the coefficient of restitution approach is not recommended for continuous systems, such as beam structures. The second basic approach involves determining the contact force acting between the bodies. This procedure is essential for modelling continuous systems [94] because it is capable of taking into account the high frequency responses that are excited by the impact. The main disadvantage of this approach is that it requires strongly coupled equations for the contact force to be solved. This approach is employed in the modelling.

In this chapter, a model is presented in Section 5.2 for a piezoelectric cantilever beam energy harvester impacting against a stop and numerical examples are used to analyse the effects of initial gap size and stop location on the performance of the harvester. Section 5.3 demonstrates the importance of obtaining converged results (number of modes and time step) in the theoretical model and it also analyses the impact system to gain better understanding. In Section 5.4, experimental results are presented and compared with the theoretical results to validate the model. Also, the effects of the stop location and the initial gap are investigated through parameter studies. Section 5.5 contains conclusions for this chapter.

5.2 Impact model for a piezoelectric energy harvester

A theoretical model for a bimorph piezoelectric cantilever beam impacting a stop is derived in this section. The configuration of the impact system is shown in Figure 5.1. The equations governing the system without impact have already been derived in Section 3.2 as follows:

$$\left(\mathbf{M}_{\mathrm{T}}+\mathbf{M}_{\mathrm{J}}\right)\ddot{\mathbf{w}}(t)+\mathbf{C}\dot{\mathbf{w}}(t)+\mathbf{K}\mathbf{w}(t)-\boldsymbol{\Theta}v(t)=\mathbf{m}_{\mathrm{T}}\ddot{b}(t), \tag{5.1}$$

$$C_{\mathrm{p}}\dot{v}(t)+\frac{v(t)}{R}=-\boldsymbol{\Theta}^{\mathrm{T}}\dot{\mathbf{w}}(t) \tag{5.2}$$

where the physical displacement of the beam is given by:

$$Y(x,t)=\sum_{\mathrm{i}=1}^{\infty}\phi_{\mathrm{bi}}(x)w_{\mathrm{i}}(t), \tag{5.3}$$

Note that the parameters and variables used in the above equations are defined in Section 3.2.

The theoretical model is used directly in the derivation for the impact system. The basic approach to modelling the impact with the bump stop is similar to that described in references [91-94]. The theoretical impact model is described in detail below.

In Figure 5.2, a rod-like-stop is located beneath the cantilever beam. In the equilibrium position, the beam is not in contact with the stop and an initial gap Δ separates them. The stop is modelled as a slender rod which is allowed to vibrate in the longitudinal direction only. It is assumed that the beam and stop are both subjected to the same base excitation.

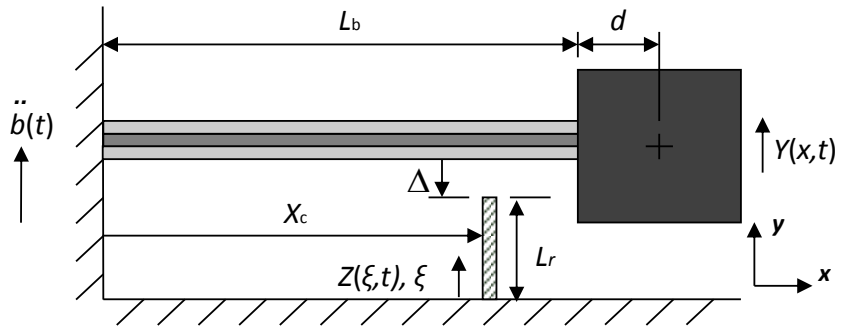

Figure 5.2 Schematics of the impact configuration of a cantilever beam and a rod

Before the beam and stop come into contact, the flexural vibration of the cantilever can be predicted using the analysis presented in Section 2.1, and the governing equations for the mechanical motion are given by equation (5.1).

When the beam is in contact with the stop, a contact force $F(t)$ acts against both the beam and the rod. In the theoretical model, the contact force between the beam and stop is estimated by considering the coupled beam and stop equations. The estimated contact force is then used to calculate the responses of the beam and stop due to the contact. The contact force is assumed to be a point force acting on both the beam and stop. Assuming that both the beam and stop are governed by linear equations, the response of the bimorph beam during contact can be expressed as:

$$Y(x,t) = Y_s(x,t) + Y_{imp}(x,t), \tag{5.4}$$

where $Y_s(x,t)$ is the beam response associated with the base excitation only and $Y_{imp}(x,t)$ is the response due to contact taking place between the beam and stop. Similarly, the generated voltage $v(t)$ can be expressed as follows:

$$v(t) = v_s(t) + v_{imp}(t), \tag{5.5}$$

where $v_s(t)$ is the voltage induced by beam response $Y_s(x,t)$, and $v_{imp}(t)$ is the voltage induced by beam response $Y_{imp}(x,t)$.

Both the beam responses $Y_s(x,t)$ and $Y_{imp}(x,t)$ are expressed in the same form as equation (5.3), but with different generalised coordinates. The generalised coordinates w_s describe the response of the beam due to base excitation. The subscript *s* is used to indicate variables associated with the base excitation only. The

generalised coordinates w_{imp} describe the response of the beam due to contact only and are governed by:

$$\left(\mathbf{M}_{\mathrm{T}}+\mathbf{M}_{\mathrm{J}}\right)\ddot{\mathbf{w}}_{\mathrm{imp}}(t)+\mathbf{C}\dot{\mathbf{w}}_{\mathrm{imp}}(t)+\mathbf{K}\mathbf{w}_{\mathrm{imp}}(t)-\boldsymbol{\Theta}v_{\mathrm{imp}}(t)=F(t)\boldsymbol{\phi}_{\mathrm{b}}(X_{\mathrm{c}}), \tag{5.6}$$

where subscript 'imp' is used to indicate variables associated with contact taking place. Equations (5.1) and (5.2) can be solved to calculate $Y_s(x,t)$ and $v_s(t)$, while equations (5.6) and (5.2) can be solved to calculate $Y_{imp}(x,t)$ and $v_{imp}(t)$. Duhamel's integral can be employed to obtain analytical expressions for $Y_s(x,t)$, $Y_{imp}(x,t)$, $v_s(t)$ and $v_{imp}(t)$ by making use of the modal impulse response functions for a beam $g_{bi}(x,t)$ [97]:

$$g_{\mathrm{bi}}(x,t)=e^{\gamma_{\mathrm{bi}}\omega_{\mathrm{bi}}t}\frac{\phi_{\mathrm{bi}}(x)}{\omega_{\mathrm{bdi}}}\sin\omega_{\mathrm{bdi}}t, \tag{5.7}$$

where γ_{bi} is the damping ratio, ω_{bi} is the undamped natural frequency and ω_{bdi} is the damped natural frequency defined as $\omega_{\mathrm{bi}}\sqrt{1-\gamma_{\mathrm{bi}}^{2}}$ for the i^{th} beam mode. Using this approach, it can be shown that $Y_s(x,t)$, $Y_{imp}(x,t)$, $v_s(t)$ and $v_{imp}(t)$ are given by:

$$Y_{\mathrm{s}}(x,t)=\sum_{\mathrm{i}=1}^{\infty}\int_{0}^{t}\left(m_{\mathrm{Ti}}(\tau)-\Theta_{\mathrm{i}}v_{\mathrm{s}}(\tau)\right)g_{\mathrm{bi}}(x,t-\tau)\mathrm{d}\tau, \tag{5.8}$$

$$Y_{\mathrm{imp}}(x,t)=\sum_{\mathrm{i}=1}^{\infty}\phi_{\mathrm{bi}}(x)\int_{0}^{t}\left(F(\tau)-\frac{\Theta_{\mathrm{i}}v_{\mathrm{imp}}(\tau)}{\phi_{\mathrm{bi}}(X_{c})}\right)g_{\mathrm{bi}}(X_{\mathrm{c}},t-\tau)\mathrm{d}\tau, \tag{5.9}$$

$$v_{\mathrm{s}}(t)=e^{-\frac{t}{RC_{\mathrm{p}}}}\int e^{\frac{t}{RC_{\mathrm{p}}}}I_{\mathrm{s}}(t)\mathrm{d}t, \tag{5.10}$$

$$v_{\mathrm{imp}}(t)=e^{-\frac{t}{RC_{\mathrm{p}}}}\int e^{\frac{t}{RC_{\mathrm{p}}}}I_{\mathrm{imp}}(t)\mathrm{d}t, \tag{5.11}$$

where the initial conditions: $v_s(0) = 0$, $v_{imp}(0) = 0$ have been used.

Of course, to solve the above equations it is necessary to have knowledge of the contact force $F(t)$, and this will depend on the displacement of the bump stop $Z(\xi,t)$ (see Figure 5.2). Based on the assumption that the stop is modelled as a slender rod

that can vibrate in the longitudinal direction only, the longitudinal displacement of the bump stop is governed by [98]:

$$E_r A_r \frac{\partial^2 Z(\xi,t)}{\partial \xi^2} - C_r \frac{\partial Z(\xi,t)}{\partial t} - \rho_r A_r \frac{\partial^2 Z(\xi,t)}{\partial t^2} = -F(t)\delta(\xi - L_r) + \rho_r A_r \frac{d^2 b(t)}{dt^2} \quad , \tag{5.12}$$

where E_r, A_r, L_r and ρ_r are the Young's modulus, the cross section area, length and density of rod, respectively, C_r is the damping coefficient of the rod, and $\delta(\xi)$ is the Dirac delta function.

Using an identical approach to that used to determine the beam response resulting from contact, the displacement of the stop can be expressed as a combination of the responses due to base excitation only $Z_s(\xi,t)$ and contact force only $Z_{imp}(\xi,t)$. i.e.

$$Z(\xi,t) = Z_s(\xi,t) + Z_{imp}(\xi,t) \tag{5.13}$$

Duhamel's integral can be used to determine analytical expressions for $Z_s(\xi,t)$ and $Z_{imp}(\xi,t)$ by making use of the modal impulse response function for a rod [97]:

$$g_{rj}(\xi,t) = e^{\gamma_{rj}\omega_{rj}t} \frac{\phi_{rj}(\xi)}{\omega_{rdj}} \sin \omega_{rdj} t \, , \tag{5.14}$$

where γ_{rj} is the damping ratio, ω_{rj} is the undamped natural frequency and ω_{rdj} is the damped natural frequency defined as $\omega_{rj}\sqrt{1-\gamma_{rj}^2}$ for the j^{th} rod mode. Using this approach, $Z_s(\xi,t)$ and $Z_{imp}(\xi,t)$ can be expressed as:

$$Z_s(\xi,t) = \sum_{j=1}^{\infty} \int_0^t m_{rj}(\tau) g_{rj}(\xi, t-\tau) d\tau \, , \tag{5.15}$$

$$Z_{imp}(\xi,t) = \sum_{j=1}^{\infty} \phi_{rj}(\xi) \int_0^t F(\tau) g_{rj}(L_r, t-\tau) d\tau \, , \tag{5.16}$$

where $m_{ri}(t)$ is the modal mechanical forcing function for the rod such that:

$$m_{rj}(t) = \rho_r A_r \ddot{b}(t) \int_0^{L_r} \phi_{rj}(\xi) \mathrm{d}\xi \,, \tag{5.17}$$

and the normalised mode shape functions for a rod are given by:

$$\phi_{rj}(\xi) = \sqrt{\frac{2}{\rho_r A_r L_r}} \sin\left(\frac{2j-1}{2L_r}\xi\right) \qquad j = 1, 2, 3, \ldots \tag{5.18}$$

Equations (5.4) and (5.13) determine the response displacement of the beam and rod and are used in what follows to estimate the contact force $F(t)$. When in contact, the displacement of the beam and the displacement of the stop at the contact point are related as follows:

$$Y(X_c, t) = Z(L_r, t) + \Delta \,, \tag{5.19}$$

where Δ is the initial gap.

An expression for the contact force at time t is obtained by substituting equations (5.4) and (5.13) into equation (5.19) and rearranging the resulting equation. This is achieved by discretising equations (5.9) and (5.16) in the time domain using a fixed time step t_s and isolating $F(t)$ from the Duhamel's integrals [94], see Appendix I. Following this procedure, it can be shown that the contact force at time t is approximated as follows:

$$F(t) \approx -\frac{S_1(t) + S_2(t) - \Delta}{S_3} \,, \tag{5.20}$$

where S_1, S_2 and S_3 are given by:

$$S_1(t) = Y_s(X_c, t) + \sum_{i=1}^{\infty} \phi_{bi}(X_c) \int_0^{t-t_s} \left(F(\tau) - \frac{\Theta_i v_{imp}(\tau)}{\phi_{bi}(X_c)} \right) g_{bi}(X_c, t-\tau) \mathrm{d}\tau \,, \tag{5.21}$$

$$S_2(t) = Z_s(L_r, t) + \sum_{j=1}^{\infty} \phi_{rj}(L_r) \int_0^{t-t_s} F(\tau) g_{rj}(L_r, t-\tau) \mathrm{d}\tau \,, \tag{5.22}$$

$$S_3 = \left[\sum_{i=1}^{\infty} \phi_{bi}(X_c) g_{bi}(X_c, t_s) + \sum_{j=1}^{\infty} \phi_{rj}(L_r) g_{rj}(L_r, t_s) \right] t_s \,. \tag{5.23}$$

Equations (5.19) to (5.23) are used to calculate the contact force when the beam and rod are in contact, and in numerical implementations the contact force is calculated when

$$Y(X_c, t) \le Z(L_r, t) + \Delta \,. \tag{5.24}$$

When there is no contact, i.e.

$$Y(X_c, t) > Z(L_r, t) + \Delta \,, \tag{5.25}$$

the contact force is zero (i.e. $F(t)$=0).

In a numerical implementation, the contact force must be monitored at every time step during contact to check the sign of the contact force. If the contact force has a positive value, then contact is maintained. However, if the contact force is negative then the beam and rod have separated. If a new contact is detected or separation takes place, then the time of the new contact or separation must be calculated. The basis of the numerical implementation used is summarised by the flowchart shown in Figure 5.3 [94].

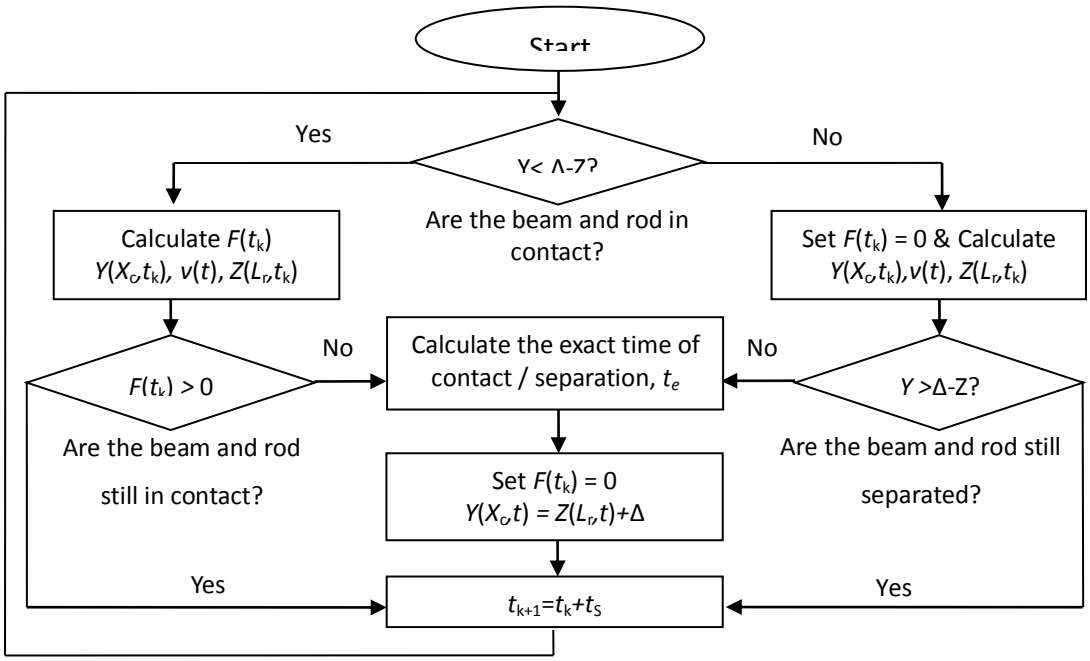

Figure 5.3 Flowchart - the basis of the numerical implementation of the impact model

5.3 Numerical simulation results

The theoretical model developed predicts the impact dynamics and electrical response of the energy harvester. In this section numerical simulation results are presented for a bimorph harvester having the dimensions and mechanical properties given in Table 5.1. A rectangular copper block is attached to the tip of the beam and the dimensions of the copper block are 6.4 mm x 6.4 mm x 3 mm. The density of copper is 8700 kg/m^3, so the mass of the tip mass is 2.14 g. The offset distance of the tip mass is 3.2 mm, whilst the radius of gyration is calculated to be 2.7x10^{-3} m and the moment of inertia of the tip mass about its geometric centre is 1.68x10^{-8} kgm^2.

In the following numerical example, both the energy harvester and the stop are subjected to a harmonic base excitation having amplitude B_{max} = 1 m/s^2 and

frequency f = 140 Hz. The excitation frequency is close to the fundamental natural frequency of the beam harvester, which is 155 Hz. The initial gap between the beam and stop is 1 μm (i.e. Δ = 1 μm) and the stop is located 2 mm from the free end of the beam (i.e. X_c = 18 mm) – this ensures that the tip mass does not make initial contact with the stop. The bimorph is connected in series to a 10 kΩ resistor. Structural damping is present in both the beam and stop, and the damping ratios for all modes of vibration in the beam and stop are chosen to have a value of 0.01.

To accurately simulate the impact dynamics and electrical power, care must be taken to ensure that a sufficiently large number of modes are used and the discretisation time step is sufficiently small. This is particularly important when impact is considered, as too large a value can significantly affect the ability to detect the resulting dynamics. In general, the duration of the impact is much shorter than the time period of the fundamental mode of the beam, and this causes higher modes of vibration to be excited. When simulating these high frequency modes it is important to use an appropriate time step to avoid aliasing the response. In this work a convergence study is performed to determine the minimum numbers of modes and the corresponding maximum time step.

	Substrate	PZT	Stop
Length, L (mm)	20	20	8
Width, W (mm)	6.4	6.4	10
Thickness, T (mm)	0.14	0.26	1
Young Modulus, E (GPa)	100	66	190
Density, ρ (kg/m^3)	8700	7800	7850
Piezoelectric constant, d_{31} (m/V)	-	$190\text{x}10^{-12}$	-
Relative Dielectric constant, k_3	-	1800	-

Table 5.1 Dimensions and mechanical properties of the beam and rod

5.3.1 **Response convergence**

Figure 5.4 shows a time-history of the beam displacement using different numbers of modes for the beam n_b and the stop n_r. From this figure it can be seen that using only the first (fundamental) modes results in simulation results that do not accurately model the impact, with contact separation occurring prematurely early compared to results obtained using a larger number of modes. The simulation results presented indicate that the first five flexural modes of the beam and the first five longitudinal modes of the stop are sufficient to obtain converged results for the particular numerical examples considered here.

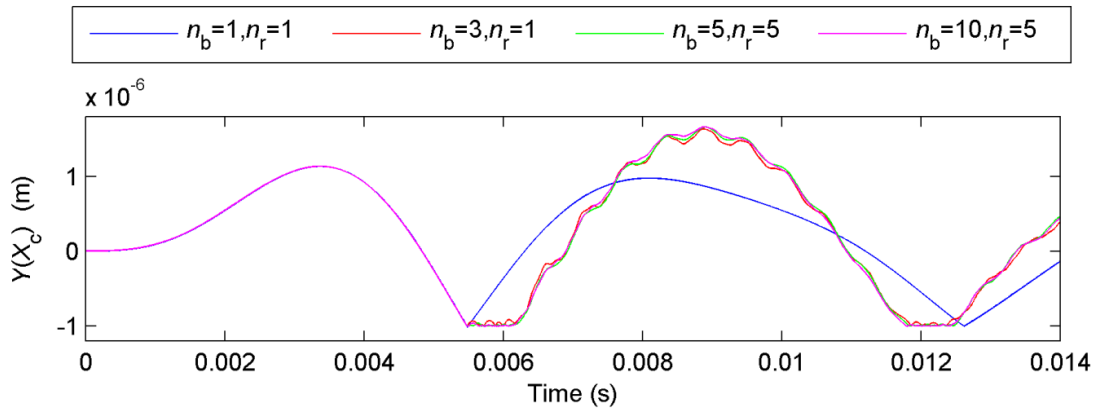

Figure 5.4 Beam displacement time histories using different combinations of numbers of modes

Based on using n_b=5 and n_r=5 (see above), the influence of different (constant) time steps on the resulting dynamics are investigated to determine the maximum time step that should be used. Figure 5.5 shows time-histories for the beam displacements using different time steps. When the time step is less than 1 μs, the

response displacements are very similar. Lo [91] suggests that the time step should be chosen to be approximately one-sixth of the period of the beam mode with the shortest time period. Fathi and Popplewell [92] suggest that the time step should be no smaller than half the period of the highest mode. This is because the estimated contact force is inversely proportional to time step (see equation (5.20)). Moreover, it is quantified by Wang [94] that it is not necessary to consider the time periods for the modes of the stop provided, or even modelling the stop as a spring, if the stop is sufficiently stiff compared to the beam. In the example considered, the shortest period of oscillation considered for the beam is 37.1 μs, meaning that a time step of 1 μs guarantees convergence.

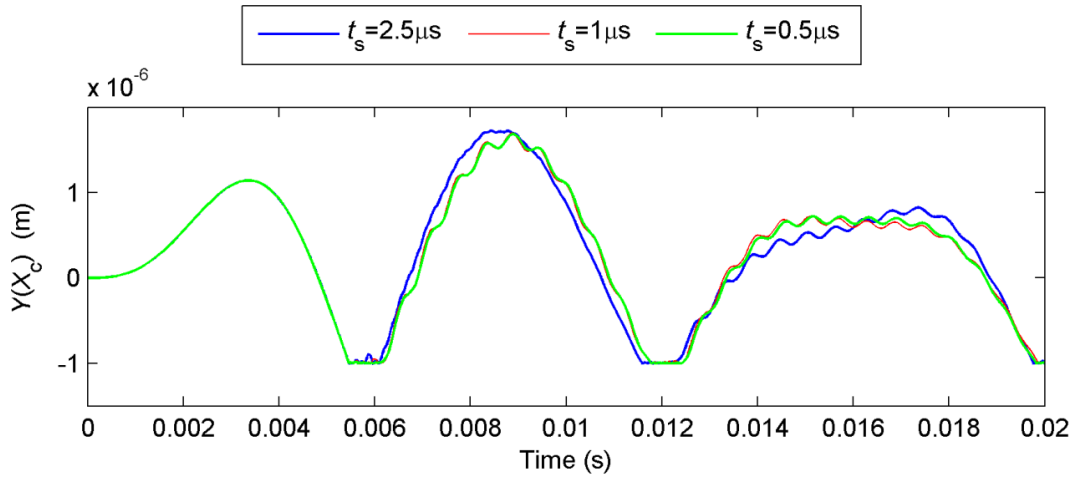

Figure 5.5 The beam displacement time-history for different time steps

5.3.2 Analysis of convergent simulation results

The key parameters for the beam-rod system analysed in what follows are summarised in Table 5.2.

Figure 5.6 shows time histories for the displacement of the beam at the contact

point, the voltage across the load resistor in the circuit, and the contact force, respectively. The base excitation causes the beam to vibrate and repeatedly impact against the stop. The beam displacement at the contact position is limited by the stop and the resulting contact force reacts against the beam. The beam does not rest against the stop continuously during contact. Instead a chattering impact occurs between the beam and the stop and a relatively large number of beam modes are excited by the contact force. The generated voltage also contains frequency components from higher modes, particularly during contact, see Figure 5.6 (b). The computational model used calculates the contact force between the beam and stop, and this is shown in Figure 5.7. During contact, the beam and stop interact, resulting in a chattering impact that induces high frequency components in the beam response. It is interesting to note (see Figure 5.6(a)) that the maximum downward and upward displacements are both similar to the original gap size Δ. This is because the response induced by the impact is out of phase with the response due to base excitation and the out of contact response not only reduces the overall response during contact, but also the out-of-contact response. This is illustrated in Figure 5.8, which shows the contributions to the response arising from pure base excitation and pure impact.

Key parameters

Number of mode		Time step	Δ	X_c	f	B_{max}	R
Beam, n_b	Stop, n_r	(μs)	(μm)	(mm)	(Hz)	(m/s^2)	(kΩ)
5	5	1	1	18	140	1	10

Table 5.2 The key parameters in the impact and electromechanical system

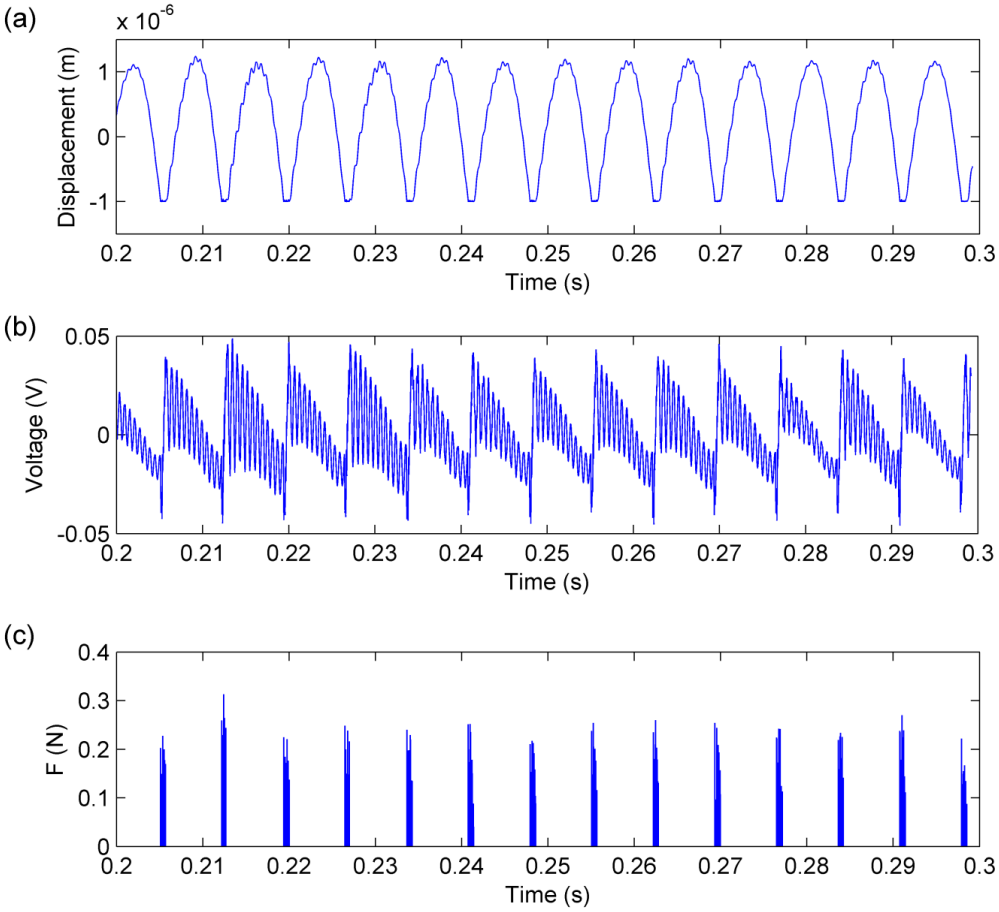

Figure 5.6 Sample simulation showing beam/stop impact: (a) displacement of the beam at the point of impact; (b) voltage across the bimorph; (c) contact force

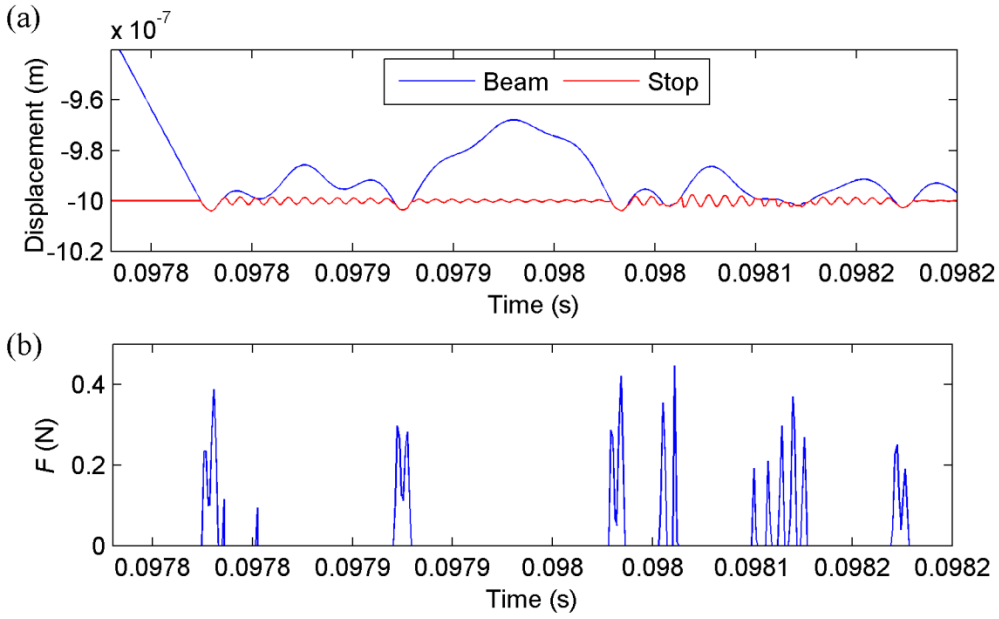

Figure 5.7 Chattering impact between the beam and stop: (a) beam and stop displacements versus time; (b) contact force versus time

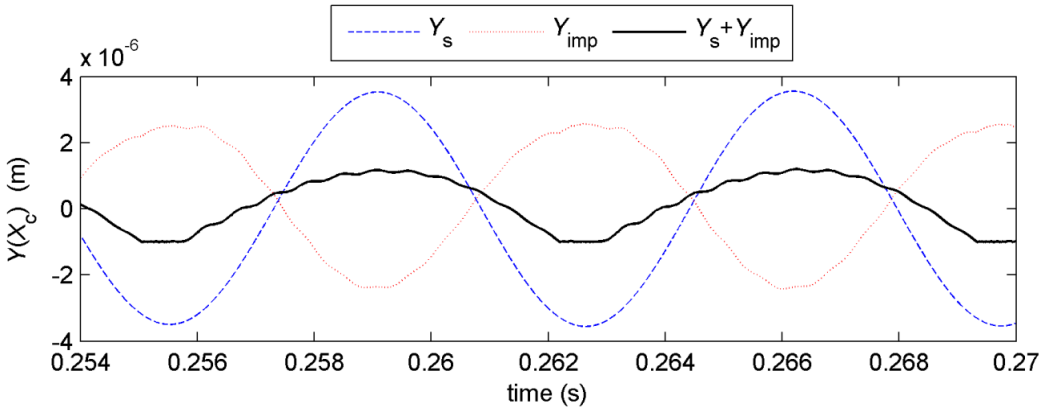

Figure 5.8 Illustration of the response due to the impact

One of the main aims of this research is to investigate how impact with a bump stop affects the electrical power output from the energy harvester. Figure 5.9 compares the voltage generated with and without impact (no stop) under the same conditions. The root-mean-square voltages (v_{rms}) with and without impact are calculated to be 0.0175 V and 0.032 V, respectively. It is interesting to note that impact almost halves the output voltage even though the maximum amplitudes are similar. The main difference between the two voltages depicted in Figure 5.9 is that impact induces high frequency components in the voltage.

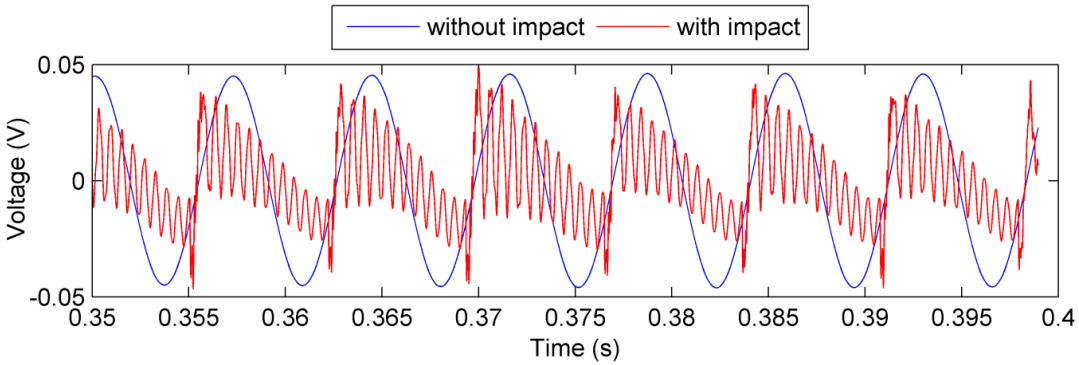

Figure 5.9 The generated voltages when impact is included and excluded in the simulation

Figure 5.10 shows the displacements of the entire beam at three instances as an

impact takes place. The curvature of the beam indicates the regions of the beam that are in tension and compression and the way in which the beam responds to the contact. Figure 5.11 shows a schematic representation of the beam just after impact and can be used to explain why the voltage is suppressed by impact. It can be seen that the top piezoelectric layer is in tension near to the clamped end of the beam, and in compression over the remainder of the beam. The opposite is seen to occur on the bottom piezoelectric layer. A consequence of this is that on the top and bottom piezoelectric layers, the positive charge is cancelled out by the negative charge due to the existence of different stress regions [83]. It is also worth noting that in the example shown, the maximum bending stress is reduced from 3.1 GPa (without a stop) to 1.1 GPa (with a stop). The maximum bending stress is discussed again in Section 5.4.3.

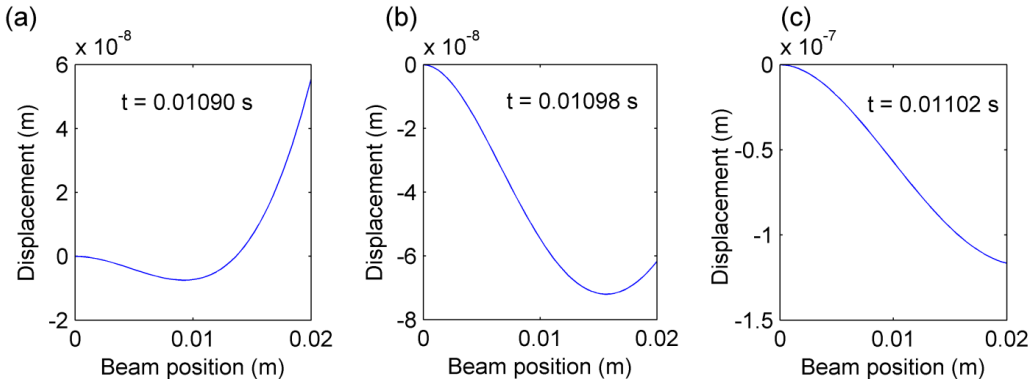

Figure 5.10 The displacement of the entire beam during the contact at (a) t = 0.01090 s; (b) t = 0.01098 s; (c) t = 0.01102 s

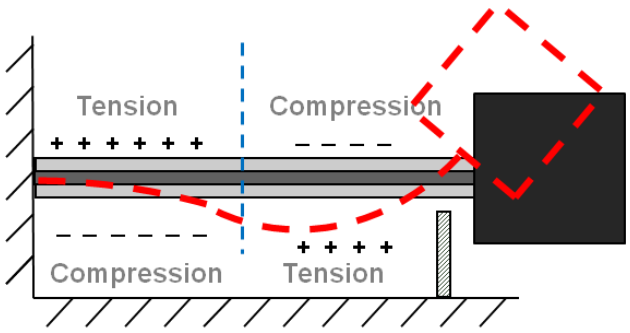

Figure 5.11 Schematic of the deflected shape of the energy harvester during impact

5.4 Experimental validations

5.4.1 Experimental setup

In this section, the model of an energy harvester impacting a stop presented in Section 5.2, is validated experimentally. The bimorph energy harvester tested in the experiment is a commercially available piezoelectric bimorph cantilever energy harvester PSI-5A4E, supplied by Piezo Systems [88]. Two identical tip masses are attached to the top and bottom surface of the bimorph. The dimensions of each block are 6.4 mm x 6.4 mm x 3 mm. This is exactly the same sample that was used in Section 4.3.3 for model validation without a stop. However, a different length of the cantilever beam is used in this experiment.

In the experiments, the energy harvester sample is mounted as a cantilever beam using a steel clamping fixture attached to a shaker that provides harmonic base excitation to the bimorph. An accelerometer (352C22A supplied by PCB Piezotronics [84]) is used to monitor the “base acceleration” of the clamping fixture. A resistor is connected in series with the energy harvester and serves to dissipate the electrical energy. A single point laser vibrometer (PolyTec OFV-055) [85] is used to measure the vibration of the centre of the tip mass, and a signal analyzer (Stanford Research Systems Model SR785 [86]) measures the voltage across the resistor. The experimental setup is modified from that described in Chapter 4, Section 4.2. A stop is mounted on a supporting platform beneath the beam harvester, as shown in Figure 5.12.

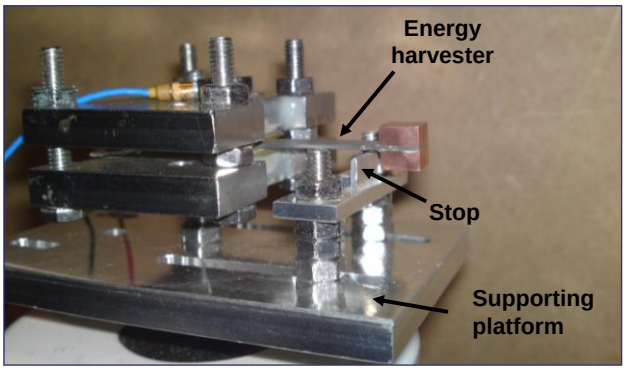

Figure 5.12 The stop is located beneath the energy harvester

5.4.2 Experimental measurements

Before carrying out the validation with impact, the bimorph is tested without a bump stop to validate the theoretical model for energy harvester once again. This validation is achieved by comparing the Frequency Response Functions (FRFs) of the steady state beam displacement at a particular location and the piezoelectric voltage output.

The measured length of the cantilever beam is 20 mm when it is mounted in the clamping fixture. The mechanical properties of the harvester are the same as those used in the numerical examples in Section 5.3. The bimorph is subjected to harmonic excitation over a range of frequencies with an amplitude of 0.5 m/s^2, and the results are used to obtain the FRFs for steady-state displacement of the tip mass and the piezoelectric voltage. To validate the theoretical model it is necessary to know the mechanical damping of the harvester. This was measured when the electrical circuit was shorted, and the damping ratio was found to be 0.0086 for the fundamental bending mode of the beam.

Figure 5.13 shows the FRF for the beam displacement at the centre of the tip mass when R=0 Ω. The difference between the measured and theoretical natural frequency is approximately 0.84%. Figure 5.14 and Figure 5.15 show comparisons of the measured and theoretical FRFs for displacement and voltage when the bimorph is connected to resistors of 3.6 kΩ and 8 kΩ. In general, the agreement between theory and measurement is very good as the percentage error in resonance frequency is less than 1 % for all cases.

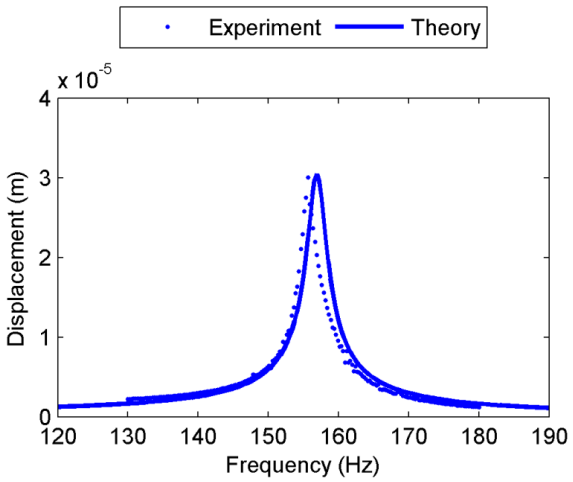

Figure 5.13 FRF for the displacement at the centre of the tip mass when R = 0 Ω

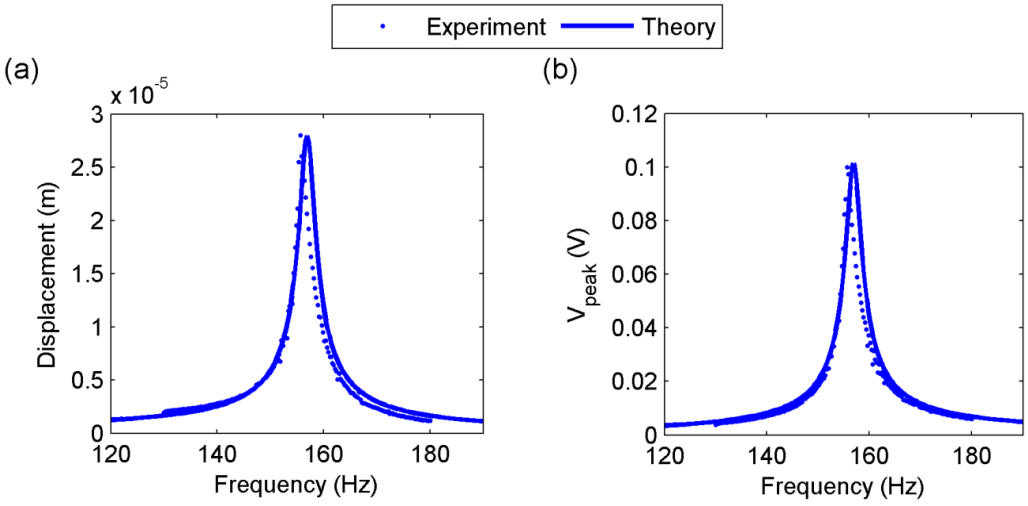

Figure 5.14 FRFs for (a) displacement and (b) voltage when R = 3.6 kΩ

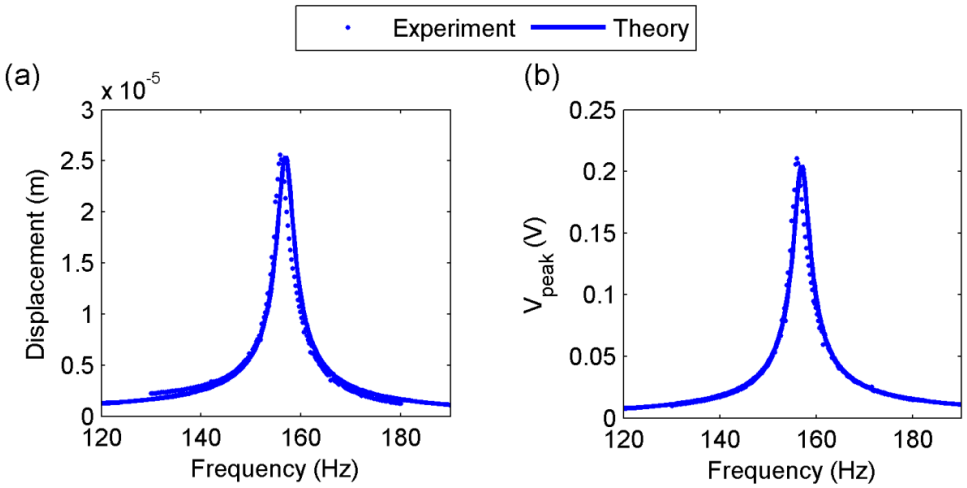

Figure 5.15 FRFs for (a) displacement and (b) voltage when R = 8 kΩ

The bimorph is now tested under impact conditions. The stop is located 2 mm away from the free end of the cantilever (X_c = 18 mm) and the initial gap size Δ between the beam and stop is measured to be 28 μm. Both the bimorph and stop are subjected to a harmonic excitation and the time-domain response of the beam at the point of impact is measured using a laser vibrometer, together with the voltage across the resistor.

In Test 1, the electrical load is disconnected from the bimorph so that the harvester simply acts as a cantilever beam impacting a stop. The base is excited at a frequency of 155 Hz, coinciding with the natural frequency of the beam, and an amplitude of 1.73 m/s^2. Figure 5.16 compares the theoretical results with measurements and shows the velocity of the beam at the point of impact. Both sets of results contain high frequency components induced by impact. When impact takes place, the beam displacement is limited by the stop and this occurs when the beam velocity is approximately 0 m/s. The results shown in Figure 5.16 indicate that the contact duration is short. The high frequency content decays away before the next impact

takes place. The amplitude of the measured velocity is slightly greater than the predicted value. This is due to the fact that the theoretical natural frequency is overestimated and the excitation frequency considered does not fully coincide with the natural frequency. The maximum displacement at the contact point is measured to be 31.12 µm, while the predicted value is 28.15 µm.

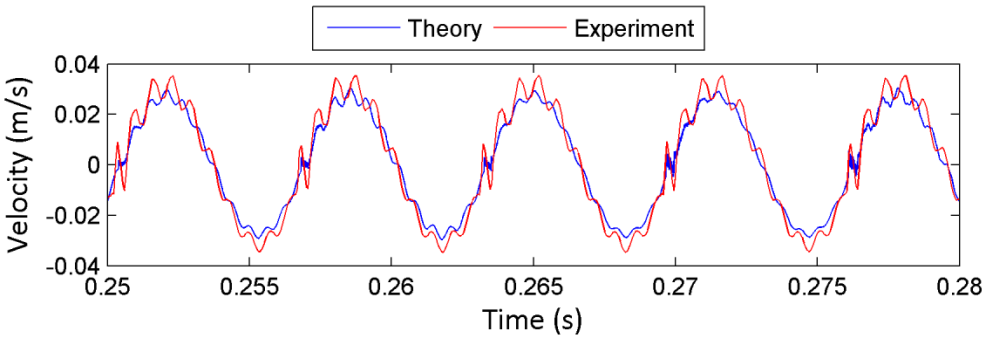

Figure 5.16 Test 1: velocity of the beam at the contact point (*R* = 0 Ω)

In Test 2 and Test 3, the energy harvester is connected in series to load resistors having resistances of 3.6 kΩ and 8 kΩ, respectively, and the predicted and measured dynamic and electrical responses for these cases are shown in Figure 5.17 and Figure 5.18, respectively. In Test 2, high frequency responses when the velocity is approximately zero indicate impact, see Figure 5.17(a). Also, the root-mean-square voltage measured is 0.129 V, while the simulation gives 0.109 V. The measured and predicted beam displacement at the contact point are 29.18 µm and 28.06 µm respectively. Figure 5.18(a) shows that the global velocities are similar in both the measured and theoretical results, although the amplitude of the high frequency components is higher in the experiment. Also, experimental and theoretical v_{rms} are 0.315 V and 0.272 V respectively, while the measured and theoretical displacements at the contact point are 30.04 µm and 28.15 µm respectively.

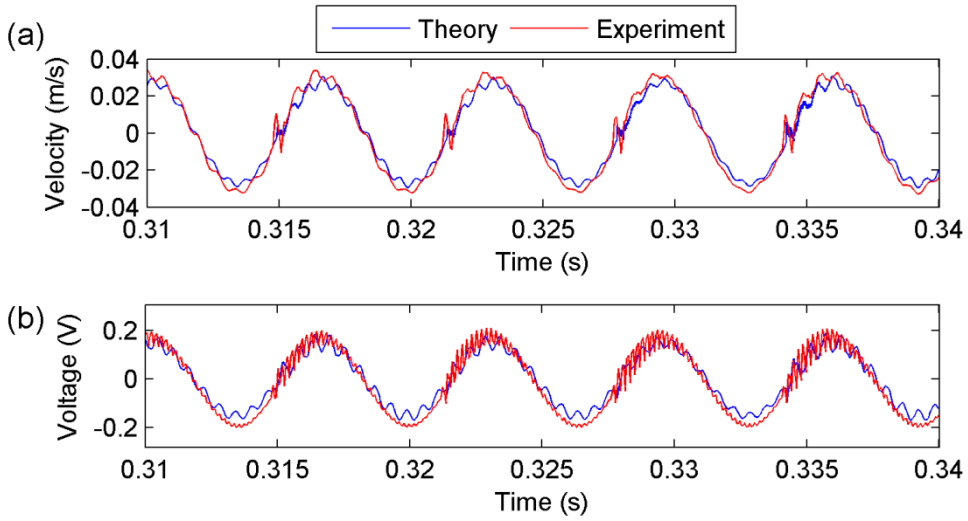

Figure 5.17 Test 2:(a) velocity of the beam at X_c; (b) voltage when R = 3.6 kΩ

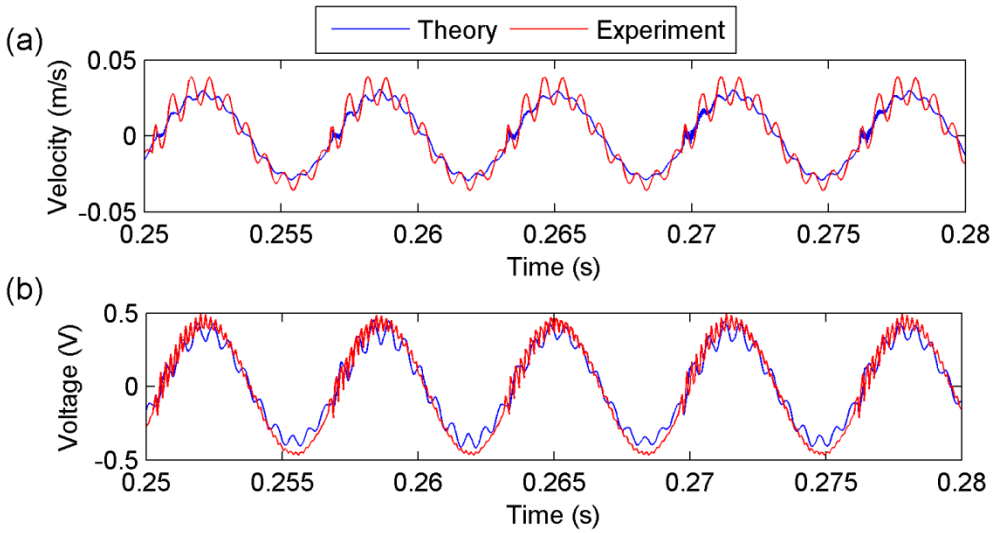

Figure 5.18 Test 3: (a) velocity of the beam at X_c; (b) voltage when R = 8000 Ω

In general, the predictions made using the theoretical impact model are in good agreement with the experimental results. As explained earlier, the resonance frequency is slightly overestimated in the theoretical model for the energy harvester, and this explains why the theoretical results are slightly lower than the measurements. It is expected that the impact model would be in even closer

agreement with experiment if the measured and theoretical FRFs in Figure 5.13 agreed more closely.

5.4.3 The effects of the gap size and stop location

The impact dynamics are modified if the stop is moved to a different location and/or the initial gap size between the beam and stop is adjusted. It is very important to know how the stop location and the gap size affect the power output from the energy harvester as well as the stress reduction for the purpose of design. Here, the performance of an energy harvester with a bump stop is investigated and the energy harvester investigated in Section 5.3.2 will be used for this purpose.

The gap size is varied in the computational model when the stop is located 2 mm from the free end of the beam (see previous example). The beam and the stop are excited at the fundamental frequency of the harvester, which is 157 Hz in this case. Figure 5.19(a) shows the displacements of the beam at the contact point for different gap sizes. From these results it is clear that the amplitude of the beam displacement at the contact point is limited to values similar to the initial gap size by the stop. The beam response is different for each gap size used, but the global dynamical behaviour is similar. The electrical response of the bimorph for different gap sizes is also shown in Figure 5.19 (b). To make comparisons, the root-mean-square voltages are calculated and compared in Figure 5.20(a). The maximum bending stress in the cantilever energy harvester has also been calculated and is plotted in the same graph. The results indicate that the voltage increases as the gap size increases, but the maximum bending stress of the beam is reduced because larger amplitudes of beam vibration are allowed. The voltage is roughly

directly proportional to the gap size, while the percentage stress reduction is approximately inversely proportional to the gap size, as seen in Figure 5.20(a).

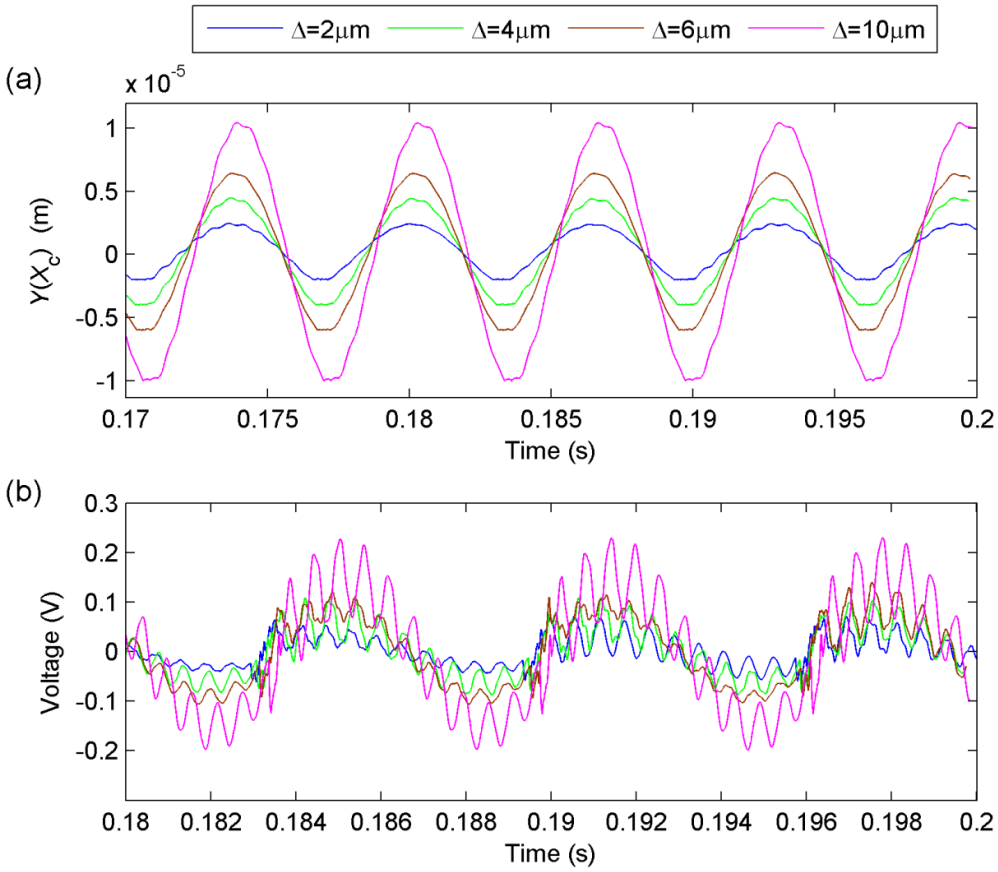

Figure 5.19 (a) The displacements of the beam at the point of impact; (b) The voltages across the resistor for different gap sizes

Moving the location of the stop effectively changes the maximum displacement of the beam. In what follows, the gap size is fixed to 1 μm while the stop is moved. Figure 5.21 compares the electrical response of the energy harvester for different stop locations. The impact dynamics of the beam is different for different stop locations and the voltage across the resistor responds differently. The root-mean-square voltage and percentage stress reduction for different stop locations are plotted in Figure 5.20 (b). As expected, the voltage increases as the stop is moved towards the clamped end because the maximum displacement is

larger. The percentage stress reduction reduces as the stop is moved towards the clamped end.

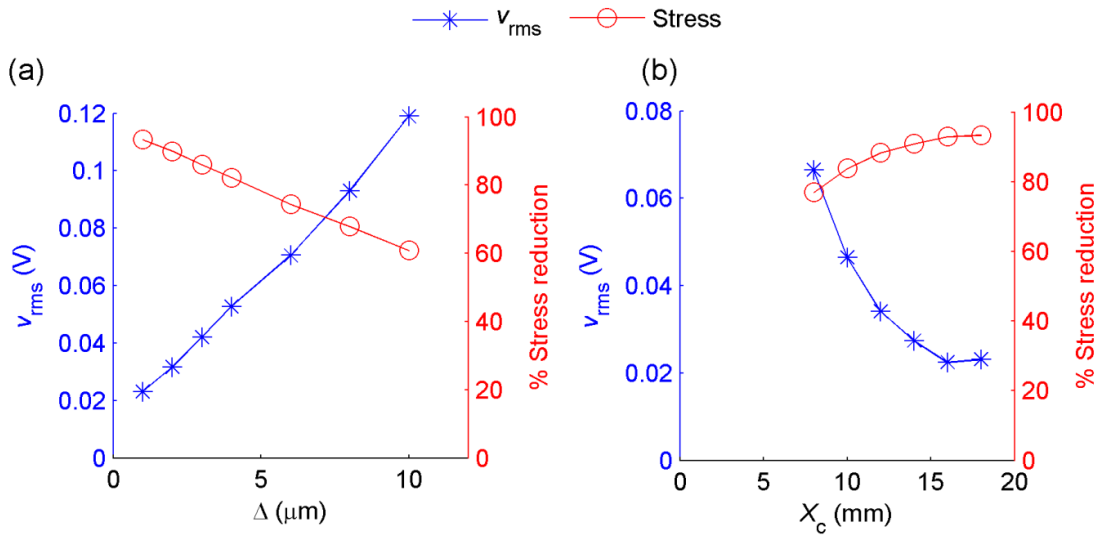

Figure 5.20 (a) The variation of voltage and the % stress reduction to the gap size; (b) The variation of voltage and the % stress reduction to the stop location

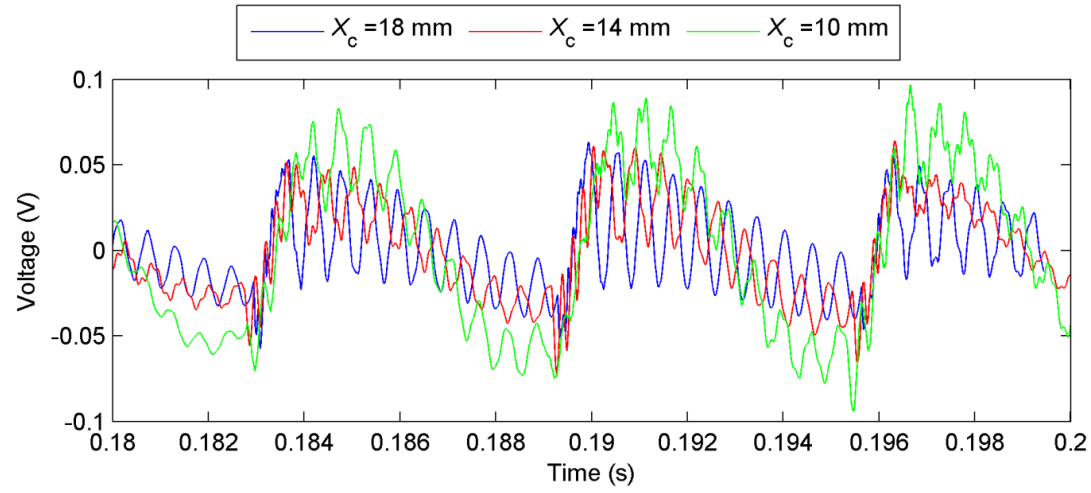

Figure 5.21 The voltage responses of the energy harvester for different stop locations

5.5 Chapter conclusions

A theoretical model has been developed to analyse the performance of a

piezoelectric cantilever energy harvester impacting a bump stop. The model estimates the contact force and predicts the dynamical and electrical responses of the harvester.

Experiments have been carried out to validate the theoretical model of a piezoelectric energy harvester with and without a bump stop. The predicted natural frequency of the fundamental mode of vibration agreed well with the measured frequency. An experimental setup was used to measure the time-domain mechanical and electrical response of a piezoelectric cantilever beam impacting a bump stop. The measured velocity and voltage were compared to theoretical predictions, and it was found that the theoretical results generally matched well with the experimental results.

Parameter studies were performed to investigate the effect of initial gap size on the generated voltage and maximum bending stress. It was found that moving the bump stop location along the beam affected the electrical output of the energy harvester because the maximum displacement allowed is altered. It was also found that the maximum beam displacement is the key factor that governs the electrical output and maximum bending stress. Reducing the maximum bending stress inevitably means reducing the maximum beam displacement and suppressing the power output at the same time.

Chapter 6. Investigation on the nonlinear behaviour in piezoelectric energy harvesters

6.1 Introduction

In the previous chapters, a linear model for piezoelectric energy harvesters was used to analyse the system behaviour and optimise performance. Given that shocks and large ambient vibrations may cause mechanical failure in the energy harvester, a bump stop was introduced in the energy harvester design to prevent large amplitude displacements. However, material and geometric nonlinearities may significantly affect the performance of the harvester when subjected to high levels of acceleration. This chapter investigates how the performance of the harvester is affected by the presence of nonlinear effects.

Theoretical models for piezoelectric energy harvesters are available in many papers [23, 27, 29], but most of them are based on linear models. Some linear models have been validated experimentally and show good agreement between theory and experiment [23, 25, 27]. However, these validations use very low levels of excitation and are not necessarily valid in all applications. In the TPMS application, an energy harvester is subjected to high levels of acceleration. In this application, it is likely that linear models of energy harvester will be unable to predict the resonance

frequency accurately, leading to inaccurate predictions for the performance of the harvester due to frequency shift. On this basis, it is advisable to take account of the nonlinear behaviour of energy harvesters in this design, particularly if the energy harvester is subjected to large levels of excitation.

Piezoelectric materials are well known for their nonlinear behaviour and this is an important research area for some applications. A number of studies have investigated the nonlinear behaviour of piezoelectric materials [13, 33-35]. However, only a very few studies focus on energy harvesting applications [36] and most interest has focused on piezoelectric sensors and actuator systems [38-40]. Some theoretical models developed in these studies have been validated against experiment [41, 42].

In this chapter, a nonlinear model for a cantilever piezoelectric energy harvester is presented. The model takes account of geometric deflection nonlinearity in the beam and material nonlinearity in the piezoelectric material. Nonlinear models are required to both analyse and quantify the mechanical response and power produced by the energy harvester, taking into account any frequency shifts present in the amplitude-frequency relationship. Experiments are carried out to determine the coefficients for higher order terms in the nonlinear piezoelectric constitutive equation. The theoretical results are then compared to the experimental results to validate the theoretical model. Studies are conducted to examine the material and geometric nonlinearities in order to quantify and compare their influences on the performance of the energy harvester.

6.2 Nonlinear piezoelectric energy harvester model

A nonlinear bimorph energy harvester is considered in this section. The energy harvester is mounted as a cantilever beam to operate in the d_{31}-mode as described in Section 3.2. Also, the harvester considered is connected to a load resistance to dissipate electric energy. The approach used to model the nonlinear energy harvester is based on modelling for a monomorph piezoelectric cantilever actuator studied by Mahmoodi *et al.* [99]. The actuator model developed in [99] considers the voltage input as an excitation force to the system, so the main difference between the actuator and energy harvester models is that an extra degree of freedom is considered for the electrical response in the energy harvester model.

Euler-Bernoulli beam theory is applied as the energy harvester considered is a slender beam. However, the cantilever beam is assumed to be inextensible throughout the analysis. Both the longitudinal, $Y_x(s,t)$, and transverse vibrations, $Y_y(s,t)$, are considered for the beam as shown in Figure 6.1. These vibrations are functions of the arclength of the beam, s, and time, t. Due to the inextensible beam assumption, there is no elongation in the axial direction along the neutral axis of the beam. Therefore, the longitudinal vibration due to the transverse vibration of the beam can be obtained using the inextensible beam condition [100]:

$$\left(1+Y_x'\right)^2+Y_y'^2=1 \tag{6.1}$$

Note that (’) represents differentiation with respect to the arclength, s.

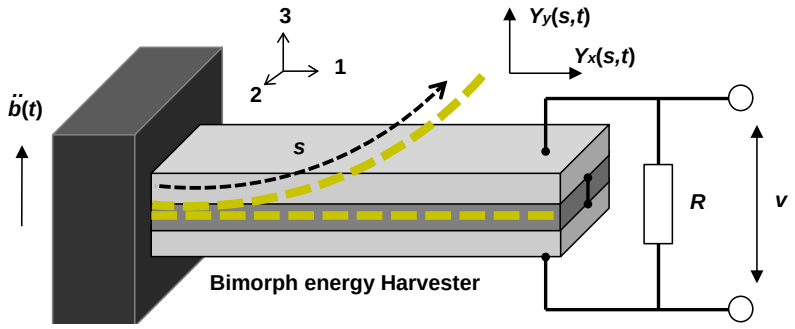

Figure 6.1 The longitudinal and transverse vibrations in an inextensible beam

Rearranging condition (6.1) and using Taylor's expansion to obtain a relation between Y_x and Y_y gives:

$$Y_x' = \left(1 - Y_y'^2\right)^{\frac{1}{2}} - 1 \approx -\frac{1}{2} Y_y'^2 \tag{6.2}$$

Hence,

$$Y_x = -\frac{1}{2}\int_0^{L_b} Y_y'^2 \, \mathrm{d}s \tag{6.3}$$

As mentioned earlier, the piezoelectric constitutive equations (3.1) used in Section 3.2 assume that the piezoelectric material properties are linear. In this analysis, the piezoelectric material is considered to be nonlinear. The nonlinear piezoelectric constitution equations used contain nonlinear terms up to second order [33], such that:

$$\sigma_p = E_p S_p + \frac{\mu_1}{2} S_p^{\,2} - E_p d_{31} E_v - \mu_2 \varepsilon_p E_v \tag{6.4}$$

$$D = E_p d_{31} \varepsilon_p + \frac{\mu_2}{2} S_p^{\,2} - \varepsilon_{31} E_v \tag{6.5}$$

Many of the parameters and variables used in equations (6.4) and (6.5) were defined in Section 3.2. The exceptions are μ_1 and μ_2 which are the nonlinear coefficients. These coefficients can be measured through experiments by performing a curve-fitting method. Also, the material nonlinearity is considered only

for the piezoelectric material, so the stress in the substrate is assumed to be linearly related to the strain as follows:

$$\sigma_s = E_s S_s \tag{6.6}$$

To use Hamilton's principle to derive the governing equations, the potential and kinetic energy terms are identified, and these are given by:

$$\begin{aligned} P_e = &\frac{1}{2}\int_0^{L_b}\int_{A_s}\sigma_s S_s \,\mathrm{d}A_s\,\mathrm{d}s + 2\cdot\frac{1}{2}\int_0^{L_b}\int_{A_p}\sigma_p S_p \,\mathrm{d}A\mathrm{d}s \\ &+\frac{1}{2}\int_0^{L_b}\left(E_s A_s + 2E_p A_p\right)\left(Y_x' + \frac{1}{2}Y_y'^2\right)^2 \mathrm{d}s - 2\cdot\frac{1}{2}\int_0^{L_b}\int_{A_p} E_v D\,\mathrm{d}A\mathrm{d}s \end{aligned} \tag{6.7}$$

$$K_e = \frac{1}{2}\int_0^{L_b} m_b\left(\dot{Y}_x^{\,2} + \dot{Y}_y^{\,2}\right)\mathrm{d}s \tag{6.8}$$

where $m_b = \rho_s A_s + 2\rho_p A_p$

The strain present in equation (6.7) is expressed in terms of the curvature of the beam which is approximated as follows [99]:

$$\rho = Y_y'' - Y_y'' Y_x' - Y_y' Y_x'' - Y_y'' Y_x'^2 \tag{6.9}$$

Using this expression, the potential energy yields:

$$\begin{aligned} P_e = &\frac{1}{2}\int_0^{L_b} E_s I_s \rho^2 \,\mathrm{d}s + \int_0^{L_b} E_p I_{p1}\rho^2 + \frac{\mu_1}{2} I_{p2}\rho^3 \\ &-\frac{1}{2}\left(\mathrm{H}(s) - \mathrm{H}(s-L_b)\right) W_p E_p d_{31} E_v T_p \left(2t_s + T_p - 2NA\right)\rho \\ &-\mu_2 E_v I_{p1}\rho^2\,\mathrm{d}s + \frac{1}{2}\int_0^{L_b}\left(E_s A_s + 2E_p A_p\right)\left(Y_x' + \frac{1}{2}Y_y'^2\right)^2 \mathrm{d}s \\ &-\int_0^{L_b}\frac{1}{2}\left(\mathrm{H}(s) - \mathrm{H}(s-L_b)\right) W_p E_p d_{31} E_v T_p \left(2t_s + T_p - 2NA\right)\rho \\ &+\frac{\mu_2}{2} I_{p1} E_v \rho^2 + W_p \varepsilon_{31} T_p E_v^{\,2}\,\mathrm{d}s \end{aligned} \tag{6.10}$$

where

$$I_s = \frac{W_s T_s^3}{12},\quad I_{p1} = \frac{W_p T_p^3}{12} + A_p\left(\frac{T_s + T_p}{2}\right)^2,\quad I_{p2} = \frac{W_p}{4}\left[\left(\frac{T_s}{2} + T_p\right)^4 - \left(\frac{T_s}{2}\right)^4\right]$$

Note that H(s) is the Heaviside function.

In addition, the energy harvester is subjected to a base acceleration $\ddot{b}$ and the external work applied to the system is given by:

$$W = \left(\int_{V_s} \rho_s Y_y \,\mathrm{d}V + \int_{V_p} \rho_p Y_y \,\mathrm{d}V\right)\ddot{b} - vq \quad , \tag{6.11}$$

where v is the voltage across the energy harvester and q is the electric charge generated by the harvester. Also, the negative sign is in the last term because the electric energy is the external work done by the system to generate electrical power.

Despite the presence of longitudinal and transverse vibrations, only the transverse vibration is of interest here. The dependence on Y_x is eliminated by using equations (6.1) – (6.3) arising from the inextensibility condition, and this eliminates the degree of freedom in the longitudinal direction. As a result of this, two governing equations are obtained for the transverse vibration and the electrical response of the system by applying the extended Hamilton's principle:

$$\delta\int_{t_1}^{t_2} \mathcal{L} + W = 0 \tag{6.12}$$

where $\mathcal{L} = K_\mathrm{e} - P_\mathrm{e}$, or

$$\begin{aligned}\mathcal{L} = \frac{1}{2}\int_0^{L_b}\Bigg\{ & m_b\left[\left(\frac{1}{2}\frac{\partial}{\partial t}\int_0^s Y_y'^2 ds\right)^2 + \dot{Y}_y^{\,2}\right] - E_s I_s\left(Y_y''^2 + Y_y''^2 Y_y'^2\right) \\ & - 2E_p I_{p1}\left(Y_y''^2 + Y_y''^2 Y_y'^2\right) - 2\frac{\mu_1}{2} I_{p2} Y_y''^3 + K_p\left(Y_y'' + \frac{1}{2}Y_y'' Y_y'^2\right)v \\ & + \frac{\mu_2}{2} I_{p1}\left(Y_y''^2 + Y_y''^2 Y_y'^2\right)\frac{v}{T_p} + K_p\left(Y_y'' + \frac{1}{2}Y_y'' Y_y'^2\right)v + \frac{W_p \varepsilon_{31}}{2T_p}v^2\Bigg\}\mathrm{d}s\end{aligned} \tag{6.13}$$

where

$$K_p(s)=\frac{1}{2}W_pE_Pd_{31}\left(2T_s+3T_p-2NA\right)\left(\mathrm{H}(s)-\mathrm{H}(s-L_b)\right)$$

The governing equations of the system with respect to Y_y and v are obtained as:

$$\begin{aligned}m_b\ddot{Y}_y+\left(E_sI_s+2E_pI_{p1}\right)&\left(Y_y''''+\left[Y_y'\left(Y_y'Y_y''\right)'\right]'\right)\\&+\frac{3\mu_1}{2}I_{p2}\left(Y_y''^2\right)''+m_b\left[Y_y'\int_L^s\int_0^s\left(\dot{Y}_y'^2+Y_y'\ddot{Y}_y'\right)\mathrm{d}s\,\mathrm{d}s\right]'-K_p''v\\&-\left[\frac{1}{2}\left(K_pY_y'^2\right)''-\left(K_pY_y'Y_y''\right)'\right]v-\frac{3\mu_2}{2T_p}I_{p1}\left(Y_y''''+\left[Y_y'\left(Y_y'Y_y''\right)'\right]'\right)v=0\end{aligned} \tag{6.14}$$

$$\int_0^{L_b}\left[K_p\left(Y_y''+\frac{1}{2}Y_y''Y_y'^2\right)+\frac{1}{2}\cdot\frac{3\mu_2}{2T_p}I_{p1}\left(Y_y''^2+Y_y''^2Y_y'^2\right)+\frac{W_p\varepsilon_{31}}{2T_p}v\right]\mathrm{d}s=q \tag{6.15}$$

with boundary conditions:

$$Y_y(0,t)=Y_y'(0,t)=Y_y''(L_b,t)=Y_y'''(L_b,t)=0 \tag{6.16}$$

The governing equations of the nonlinear energy harvester are high order partial differential equations (PDEs) and can be simplified to more familiar second order (nonlinear) ODEs by assuming that the transverse displacement of the beam, $Y_y(s,t)$, is expressed as:

$$Y_y(s,t)=\sum_{i=1}^{\infty}\phi_{bi}(s)w_i(t) \tag{6.17}$$

where ϕ_{bi}(s), and $w_i(t)$ are mode shape functions and generalised coordinates of the beam in the transverse vibration. Also the mode shapes are normalised, such that:

$$\int_0^{L_b}m_b\phi_{\mathrm{bm}}(s)\phi_{\mathrm{bn}}(s)=\delta_{mn}\qquad m,n=1,2,... \tag{6.18}$$

Substituting equation (6.17) into (6.14) and manipulating the resulting equation, the equation of motion for the transverse vibration can be obtained. In what follows, proportional damping is introduced into the equation of motion to take account of structural damping in the system. Hence, the modal equation of motion for transverse vibration can be expressed as follows:

$$\ddot{w}_i + 2\gamma\omega_{bi}\dot{w}_i + \omega_{bi}{}^2 w_i + C_{1i}w_i{}^2 + C_{2i}w_i{}^3 + C_{3i}w_i\dot{w}_i{}^2 + C_{4i}w_i{}^2\ddot{w}_i - C_{5i}w_i{}^2 v - \Theta_{1i}v - C_{6i}w_i v - C_{7i}w_i{}^3 v = m_{\mathrm{Ti}}\ddot{b} \tag{6.19}$$

where the time-independent coefficients arising in the equation of motion are defined as:

$$C_{1\mathrm{i}} = \frac{3\mu_1}{2} I_{p2}\int_0^{L_b} \phi_{bi}\left(\phi_{bi}''^2\right)'' \mathrm{d}s \qquad C_{2\mathrm{i}} = E_b I_b \int_0^{L_b} \phi_{bi}\left[\phi_{bi}'\left(\phi_{bi}'\phi_{bi}''\right)'\right]' \mathrm{d}s$$

$$C_{3\mathrm{i}} = m_b\int_0^{L_b}\phi_{\mathrm{bi}}\left[\phi_{\mathrm{bi}}'\int_{L_b}^{s}\int_0^{s}\left(\phi_{\mathrm{bi}}'^2\right)\mathrm{d}s\mathrm{d}s\right]'\mathrm{d}s \qquad C_{4\mathrm{i}} = m_b\int_0^{L_b}\phi_{\mathrm{bi}}\left[\phi_{\mathrm{bi}}'\int_{L_b}^{s}\int_0^{s}\left(\phi_{\mathrm{bi}}'\phi_{\mathrm{bi}}''\right)\mathrm{d}s\mathrm{d}s\right]'\mathrm{d}s$$

$$C_{5\mathrm{i}} = \int_0^{L_b}\frac{1}{2}\phi_{\mathrm{bi}}\left(K_{\mathrm{p}}\phi_{\mathrm{bi}}'^2\right)'' - \phi_{\mathrm{bi}}\left(K_{\mathrm{p}}\phi_{\mathrm{bi}}'\phi_{\mathrm{bi}}''\right)'\mathrm{d}s \qquad C_{6i} = \frac{3\mu_2}{2}\frac{I_{p1}}{T_p}\int_0^{L_b}\phi_{\mathrm{bi}}\phi_{\mathrm{bi}}''''\,\mathrm{d}s$$

$$C_{7\mathrm{i}} = \frac{3\mu_2}{2}\frac{I_{p1}}{T_p}\int_0^{L_b}\phi_{bi}\left[\phi_{bi}'\left(\phi_{bi}'\phi_{bi}''\right)'\right]'\mathrm{d}s \qquad \Theta_{1\mathrm{i}} = \int_0^{L_b}\phi_{bi}K_p''\,\mathrm{d}s$$

$$\omega_{bi}{}^2 = E_b I_b\int_0^{L_b}\phi_{bi}\phi_{bi}''''\,\mathrm{d}s \qquad m_{\mathrm{Ti}} = \rho_s\int_{V_s}\phi_{bi}\,\mathrm{d}V + \rho_p\int_{V_p}\phi_{bi}\,\mathrm{d}V$$

It is worth mentioning that the charge, *q*, in equation (6.15) is expressed in terms of the voltage across the resistor, *v*. The governing equation for the electrical circuit is simplified by substituting equation (6.17) into (6.15) to give:

$$C_p\dot{v} + \frac{v}{R} + \sum_{i=1}^{Nb}\Theta_{1\mathrm{i}}\dot{w}_{\mathrm{i}} + \sum_{i=1}^{Nb}\Theta_{2\mathrm{i}}w_{\mathrm{i}}{}^2\dot{w}_{\mathrm{i}} + \sum_{i=1}^{Nb}C_{8\mathrm{i}}w_{\mathrm{i}}\dot{w}_{\mathrm{i}} + \sum_{i=1}^{Nb}C_{9\mathrm{i}}w_{\mathrm{i}}{}^3\dot{w}_{\mathrm{i}} = 0 \tag{6.20}$$

where

$$C_p = \frac{W_p \varepsilon_{31} L_b}{2T_p}, \qquad \Theta_{2i} = \frac{3}{2}\int_0^{L_b} K_p \phi_{bi}'^2 \phi_{bi}'' \, \mathrm{d}s$$

$$C_{8i} = \frac{3\mu_2}{2T_p} I_{p1} \int_0^{L_b} \phi_{bi}''^2 \, \mathrm{d}s, \qquad C_{9i} = \frac{3\mu_2}{T_p} I_{p1} \int_0^{L_b} \phi_{bi}'^2 \phi_{bi}''^2 \, \mathrm{d}s$$

The equations of motion (6.19) and (6.20) contain many higher order terms caused by the geometric and material nonlinearities. The strength of the material nonlinearity is dictated by the nonlinear coefficients μ_1 and μ_2, while the geometric nonlinearity inherent in the system is based on the inextensible beam condition.

The theoretical model of the bimorph energy harvester presented above is also applicable to monomorph configurations. The only difference is that some coefficients, previously defined for the bimorph, need to be modified for the monomorph configuration, with all other coefficients remaining the same. These modified coefficients are related to mass, stiffness and coupling within the electromechanical system and are given below:

$$I_s = \frac{w_s T_s^3}{12} + A_s\left(NA - \frac{T_s}{2}\right)^2 \qquad I_{p1} = \frac{w_p T_p^3}{12} + A_p\left(T_s - \frac{T_p}{2} - NA\right)^2$$

$$I_{p2} = \frac{w_p}{4}\left[\left(T_s + T_p - NA\right)^4 - \left(T_s - NA\right)^4\right] \qquad C_1 = \frac{3\mu_1}{4} I_{p2} \int_0^{L_b} \phi_{bi}\left(\phi_{bi}''^2\right)'' \, \mathrm{d}s$$

$$C_p = \frac{W_p \varepsilon_{31} L_b}{T_p} \qquad m_{\mathrm{Ti}} = \rho_s \int_{V_s} \phi_{bi} \, \mathrm{d}V + \rho_p \int_{V_p} \phi_{bi} \, \mathrm{d}V$$

$$K_p(s) = \frac{1}{2} w_p E_p d_{31}\left(2T_s + T_p - 2NA\right)\left(H(s) - H_{L_b}(s - L_b)\right)$$

$$m_b = \rho_s A_s + \rho_p A_p$$

The main differences in the equations of motion between the bimorph and

monomorph models are the additional mass and stiffness to the mechanical structure for the bimorph, and that the equivalent capacitance is halved and the electromechanical coupling terms are doubled due to the series connection between the piezoelectric layers in the bimorph.

6.3 Experimental validation for nonlinear energy harvester model

In this section, the nonlinear energy harvester model is validated by comparing theoretical results with experimental measurements, and the bimorph energy harvester is used for this purpose. The experimental setup and procedures used are exactly the same as those described in Section 4.2, and are not repeated here.

To validate the theoretical model, the measured FRFs for the displacement and voltage are compared to the theoretical predictions. The derived equations of motion for the nonlinear energy harvester are nonlinear second order ODEs and exact solutions are not available. In contrast to the linear model, solutions cannot be expressed analytically, for example in the form of Duhamel's integral. The coupled nonlinear equations (6.19) and (6.20) for the system are complex, but can be solved using numerical time-marching methods like the Runge-Kutta method to obtain complete solutions. It is worth noting that although closed-form solutions to equations (6.19) and (6.20) can be obtained using the perturbation method [36], this approach is only applicable when the nonlinear system is subjected to a harmonic force and only steady-state solutions are available. For these reasons, the equations are solved numerically by integrating equations (6.17), (6.19) and (6.20)

for the displacement and generated voltage of the energy harvester.

6.3.1 Identification of nonlinear coefficients using a curve-fitting method

Before validating the theoretical model, the unknown nonlinear coefficients in the piezoelectric constitutive equations need to be determined. These coefficients for PZT PSI-5A4E are not provided by the supplier (Piezo Systems [88]) and are not available in the literature. Furthermore, the values of the nonlinear coefficients, μ_1 and μ_2 can vary significantly for different piezoelectric materials [33, 42]. In practice, these can only be determined through experiments using curve-fitting methods [99]. The material properties and dimensions used in the model are listed in Table 6.1.

Bimorph - mechanical properties and dimensions

	Substrate (copper)	PZT
Length, L (mm)	25.8	25.8
Width, W (mm)	6.4	6.4
Thickness, T (mm)	0.14	0.26
Young Modulus, E (GPa)	190	66
Density, ρ (kg/m^3)	8700	7800
Piezoelectric constant, d_{31} (m/V)	–	190x10^{-12}
Relative Dielectric constant, k_3	–	1800

Table 6.1 The mechanical properties and dimensions of the bimorph PSI-5A4E

6.3.1.1 Short-circuit condition

In the first experiment, the bimorph energy harvester is disconnected from the electrical load, i.e. R = 0 Ω. In this case, the voltage measurement is not available as

the circuit is shorted. Only the tip displacement of the beam is measured for different base accelerations and the measured FRFs are shown in Figure 6.2. The results indicate a nonlinear softening as the amplitude of the base acceleration B_{max} increases and the natural frequency decreases. It is also observed in the experimental results that the damping ratio increases with the amplitude of base acceleration. The damping ratio of the measured FRFs is calculated using the half-power method [101] and the calculated damping ratios are plotted against the amplitude in Figure 6.3. the results indicate typical nonlinear behaviour of the beam [102] and particularly piezoelectric material [103]. According to Yao *et al.* [103], the damping ratio increases approximately linearly with amplitude, and a similar behaviour is observed here. According to Nouira *et al.* [102], the damping ratio is expected to saturate as the base acceleration increases. However, the range of base acceleration considered in the experiment shows a linear relationship with damping ratio and accelerations beyond this range are not considered in this study.

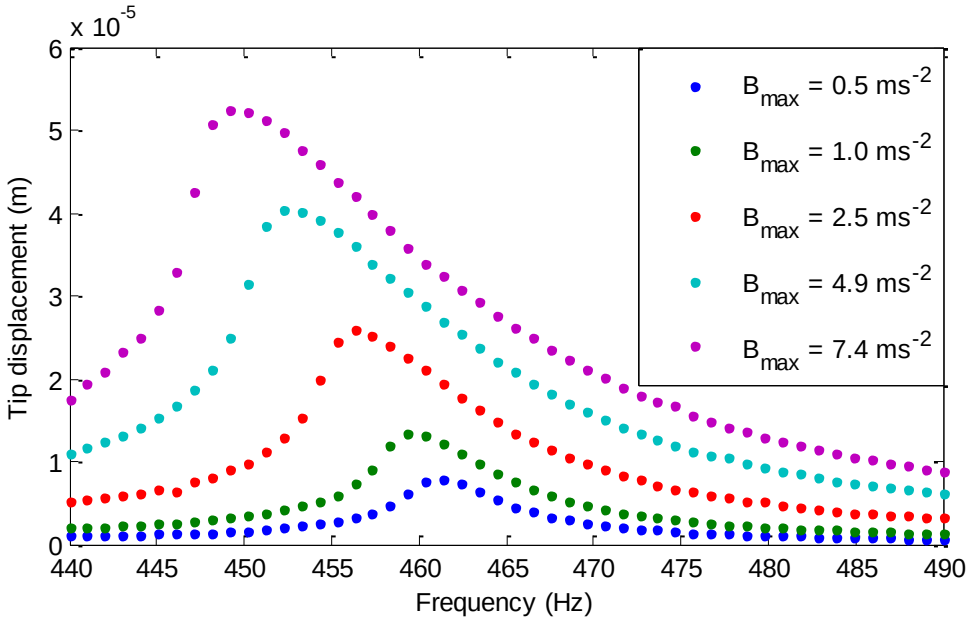

Figure 6.2 The tip displacement of the beam for different base accelerations when the circuit is shorted

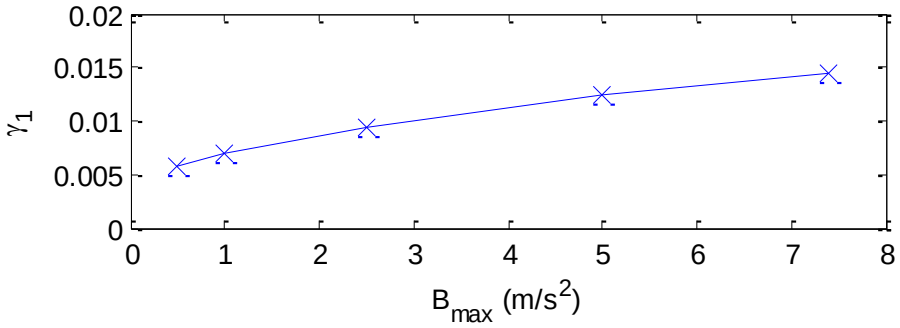

Figure 6.3 The damping ratio of the beam increases with the base acceleration

In the theoretical model, the mechanical damping is assumed to be proportional damping. However, the experimental results show that the damping is nonlinear, possibly caused by stick-slip at the clamped end of the cantilever beam, internal material damping, thermoelastic damping, acoustic radiation, viscous air damping, squeeze damping and piezoelectric heterogeneous distribution [102]. In general, damping is difficult to model and the damping characteristics are different from material to material. A detailed investigation on nonlinear damping is beyond the scope of this study and the focus here is to investigate the frequency-amplitude characteristics and examine the influence of geometric and material nonlinearities. The approach used here to model the damping is to use linear proportional damping in which the damping ratio is a function of the amplitude, $\gamma_{b1}(a)$, where a represents the amplitude of the base acceleration. The damping ratio can either be obtained experimentally from Figure 6.3 or obtained using a least square fitting method to describe the damping ratio mathematically.

The backbone curve of the nonlinear energy harvester is obtained numerically and compared to measurements. In this experiment, the energy harvesting circuit is shorted and the harvester acts as a normal cantilever beam, so that only the

nonlinear coefficient μ_1 associated with the stress-strain relationship is considered while the other nonlinear coefficient μ_2 is neglected. When μ_1 = -5.1x10^{14} Pa*, there is good agreement between the measured and theoretical backbone curves, with the natural frequencies and amplitudes matching well for different levels of base accelerations, as shown in Figure 6.4. It is also worthwhile comparing the theoretical and experimental FRFs near the fundamental resonance. Figure 6.5 compares the measured and theoretical FRFs. The comparison shows very good agreement between the experimental and theoretical results for low amplitudes of base acceleration. When the amplitude is greater than 2.5 m/s^2, there are small discrepancies at the "tails" of the FRFs despite the theoretical FRFs being similar to the measured one.

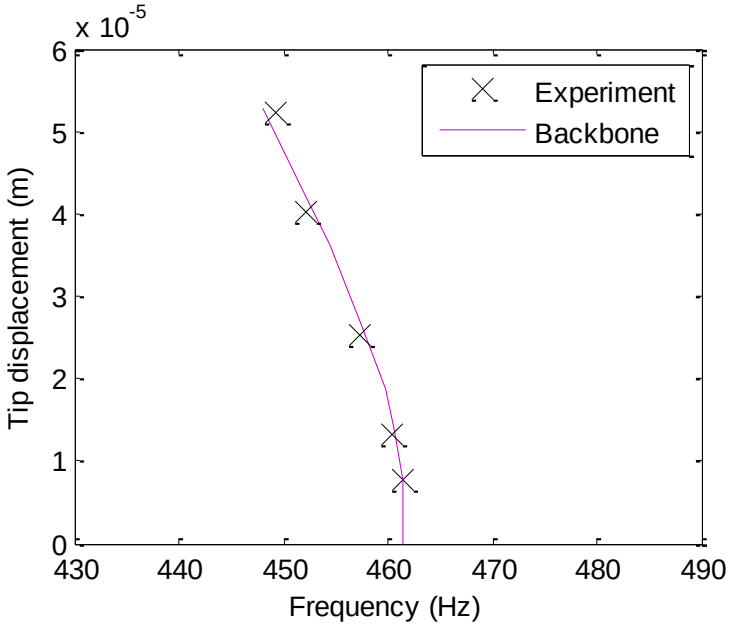

Figure 6.4 The theoretical backbone curve is fitted to the measurements

* The negative sign is due to a decrease of the Young's Modulus in compression [33].

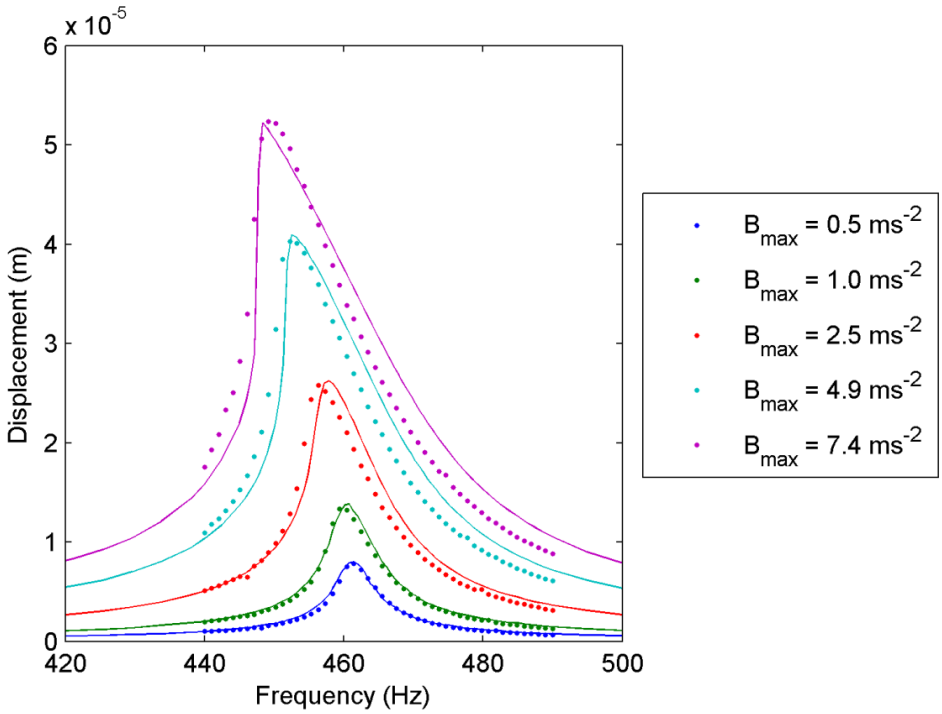

Figure 6.5 The measured (.) and predicted (-) FRFs for the tip displacement are compared

6.3.1.2 Resistive energy harvesting circuit

In the following experiments, the energy harvester is connected to different load resistors in series to measure both the tip displacement and voltage across the resistor at different amplitudes of acceleration. The experiment starts with a resistor with a low resistance of 4 kΩ. Figure 6.6(a) and (b) show the FRFs for the tip displacement of the beam and the voltage across the resistor, respectively. The nonlinear softening effect is observed in this set of measurements for both the displacement and voltage. As found in the previous experiment, the damping ratio is not constant and varies with amplitude. However, the damping ratio cannot be calculated directly using the half-power method as electrical damping is included in the system, i.e. electrical energy is dissipated through the resistor. If the damping

was calculated based on measurements using the half-power method, then it would include both electrical damping and mechanical damping.

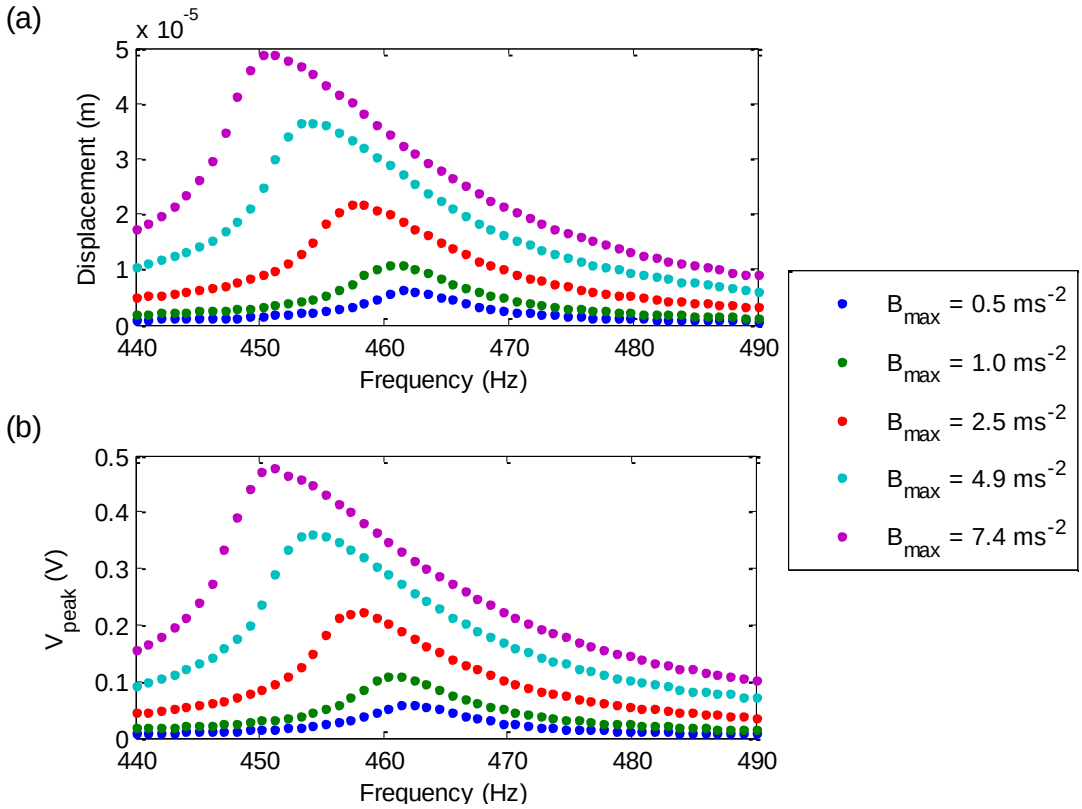

Figure 6.6 The measured FRFs for (a) the tip displacement of the beam; (b) the voltage across a resistor of 4 kΩ

The nonlinear coefficient μ_1 was determined in the previous test. Assuming the other nonlinear coefficient μ_2 is negligible, the only unknown in the experiment is the damping ratio and this can be estimated by matching the peak displacement of the beam. The estimated damping ratio is plotted against the amplitude of base acceleration in Figure 6.7 and its trend is very similar to the one in Figure 6.3. With the known nonlinear coefficients and damping ratios, the theoretical FRFs for the displacement and voltage can be obtained, and they are compared to the measurements in Figure 6.8(a) and (b) respectively. Good agreement is observed between the measurements and the predictions, despite discrepancies as the

amplitude increases.

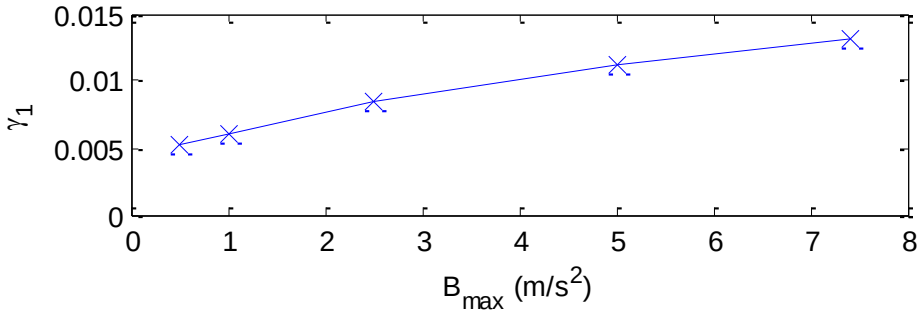

Figure 6.7 Damping ratio against the base acceleration for *R* = 4 kΩ

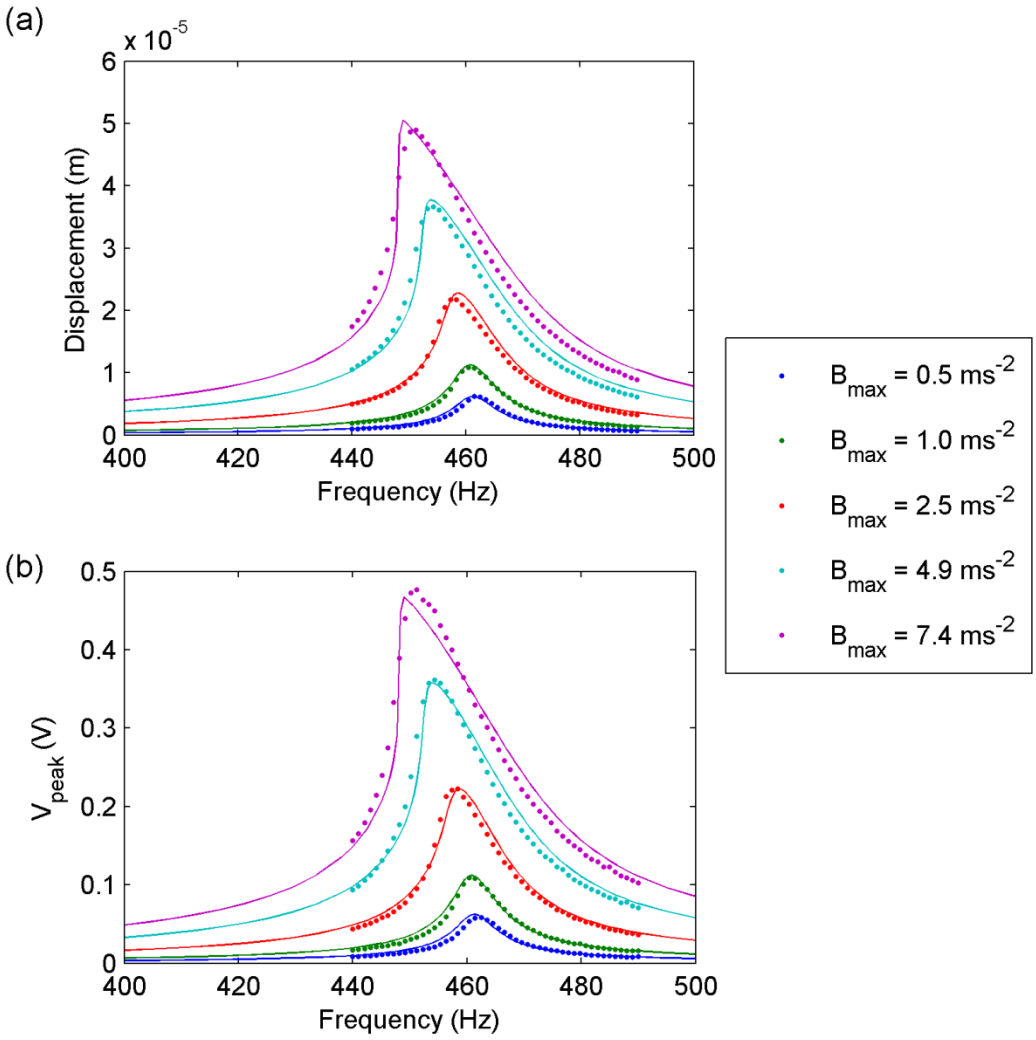

Figure 6.8 The measured and theoretical FRFs for (a) tip displacement and (b) voltage across a resistor of 4 kΩ

The energy harvester is now connected to a large load resistor with a resistance of 60 kΩ. Similarly, the FRFs for displacement and voltage are measured in the experiment and the corresponding mechanical damping ratios are estimated for different levels of amplitude (see Figure 6.9) and used in the theoretical model. Theoretical results are obtained and compared with the measurements in Figure 6.10. The predictions for high amplitudes show greater levels of discrepancy than the results for low amplitudes, as seen in previous tests. For R = 60 kΩ, the resonance frequency drops from 469.6 Hz at B_{max} = 0.5 m/s^2 to 462 Hz at B_{max} = 7.4 m/s^2. The frequency shift is 7.6 Hz while the frequency shift is 13 Hz when R = 0 Ω. Also, the nonlinear softening effect is not as strong as in the previous tests. The electrical energy is removed from the system through the resistor so the displacement and bending stress reduce. For this reason, the nonlinear softening due to the nonlinear stress-strain characteristics lessen when the energy harvester is connected to a resistive circuit.

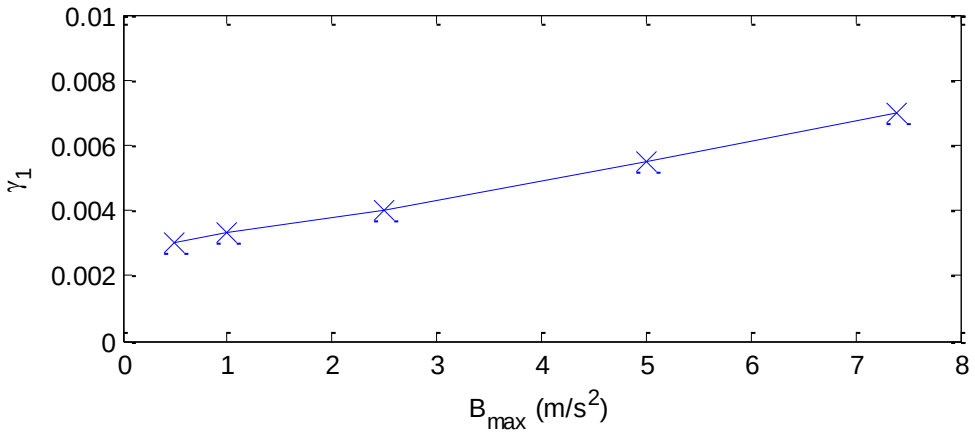

Figure 6.9 Damping ratio against the base acceleration for R = 60 kΩ

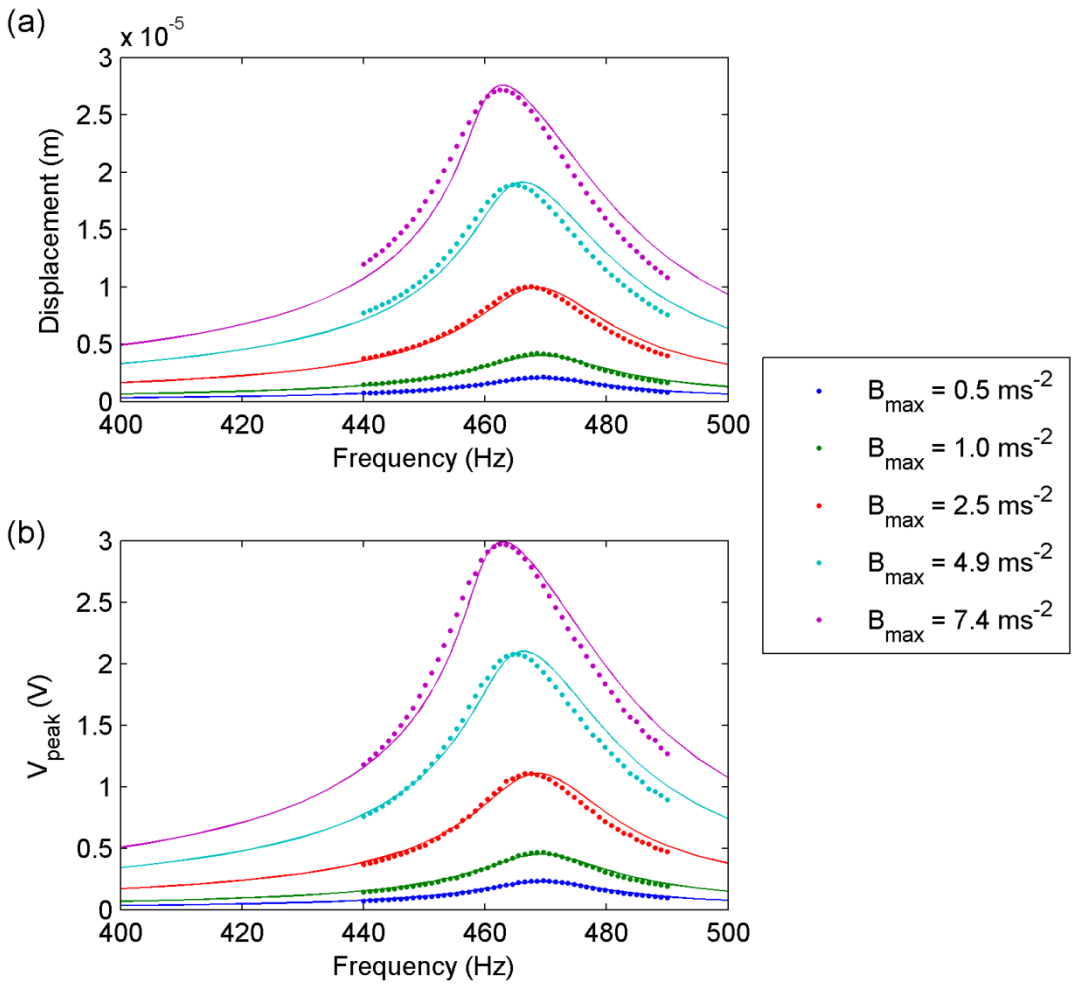

Figure 6.10 The measured and theoretical FRFs for (a) tip displacement and (b) voltage across a resistor of 60 kΩ

6.4 Investigation of nonlinear effects

A theoretical model for the nonlinear energy harvester has been developed, and the nonlinear coefficients in the piezoelectric constitutive equations have been determined using a curve-fitting approach. In addition, the theoretical model has been validated against experimental results for different resistors in the circuit. The theoretical model is now used to investigate the influence of nonlinearities on the power generated by the energy harvester.

Two types of nonlinearity are included in the theoretical model. The first is the geometric nonlinearity due to the use of the inextensible beam condition. This nonlinearity leads to the appearance of higher order terms in the coupled equations of motion (6.19) and (6.20). The other nonlinearity considered is the piezoelectric material nonlinearity. The nonlinear characteristics of the piezoelectric material are determined by the nonlinear coefficients μ_1 and μ_2. To examine the nonlinear effect of the bimorph energy harvester, the amplitude-frequency characteristics of the system are investigated under different conditions when it is subjected to harmonic excitation.

The bimorph energy harvester tested in Section 6.3 is used to investigate nonlinear effects. The material properties and dimensions of the bimorph used in the following examples are identical to those used in the previous experimental validation (see Table 6.1). Also, the nonlinear coefficients determined in Section 6.3 are used in these examples, (i.e. μ_1 = -5.1x10^{14} Pa and μ_2 = 0 Nm^{-1}V^{-1}). Although the damping ratio has been found to be dependent of the acceleration amplitude, the viscous damping ratio of the bimorph is assumed to be constant and its value is chosen to be 0.01 for the fundamental mode being investigated.

The energy harvester is connected to different resistors to understand how the resistance affects the nonlinearity. Figure 6.11(a), (b) and (c) show the FRFs for tip displacement, voltage and the power output of the energy harvester, respectively, with different resistors when the bimorph is subjected to a harmonic base acceleration of 4 m/s^2. A softening effect is observed in the results in Figure 6.11, but the strength of nonlinearity is different for different resistances, *R*. When the

resistor is equal to the optimal resistance for power generation, the presence of nonlinearity dramatically reduces the frequency shift compared to other resistances.

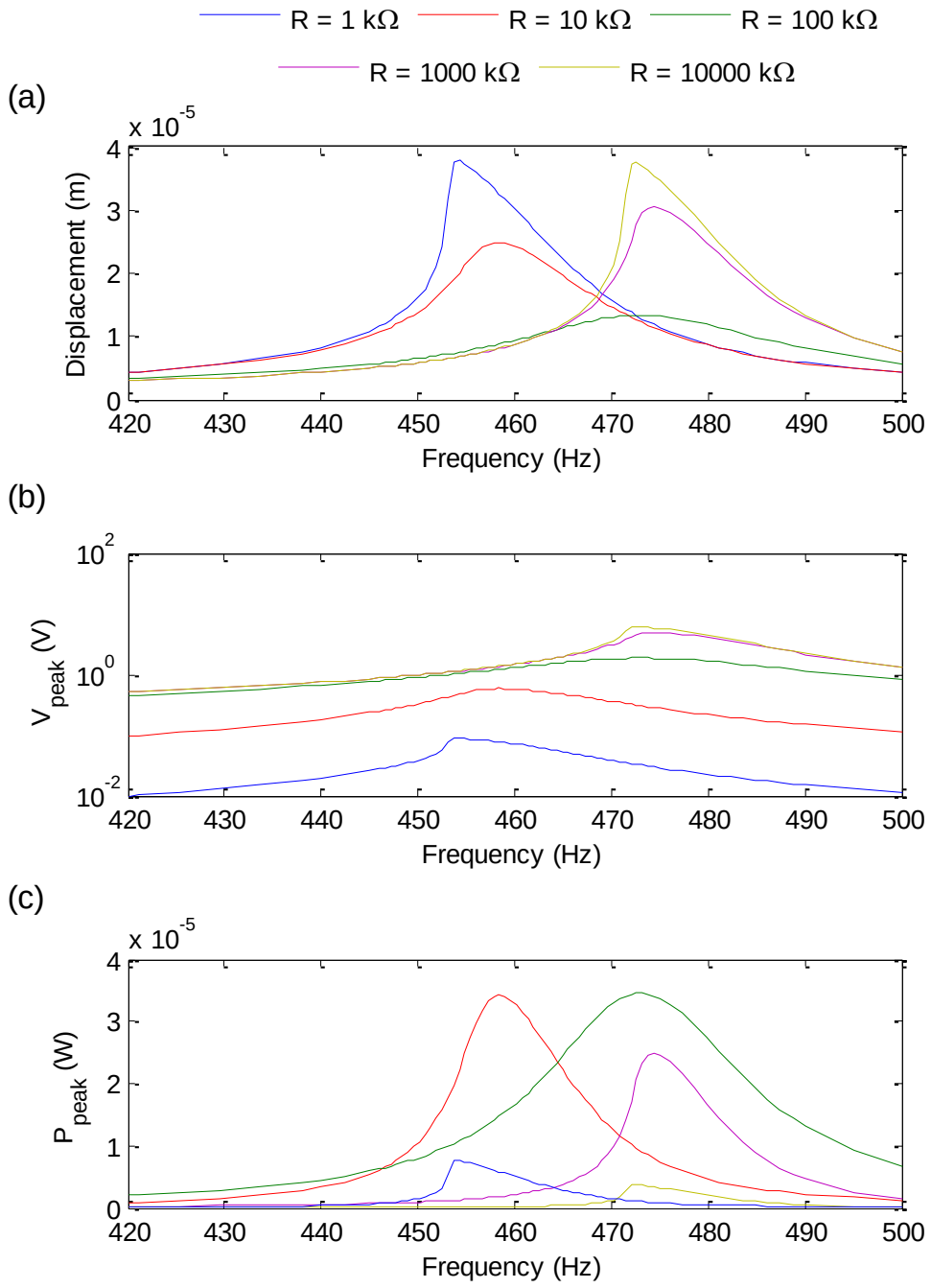

Figure 6.11 The FRFs for the (a) tip displacement, (b) voltage and (c) power of the nonlinear energy harvester with different resistors

On the other hand, it has already been seen in both experimental and theoretical results that the resonance frequency of the energy harvester increases when the load resistance increases in the circuit. However, the resonance frequency reduces due to the softening effect. Normally, the resonance frequency of the system for the open circuit condition is expected to be higher than the resonance frequency with any other resistance. However, this is not the case in this example as the resonance frequency for R = 10000 kΩ is lower than that for R = 1000 kΩ (see Figure 6.12). This is due to more electrical power being dissipated at R = 1000 kΩ than at R = 10000 kΩ and hence the displacement and stress at R = 1000 kΩ are less than those at R = 10000 kΩ. In other words, the softening effect is stronger for R = 10000 kΩ and greater frequency reduction leads to the resonance frequency being lower than the frequency obtained for R = 1000 kΩ.

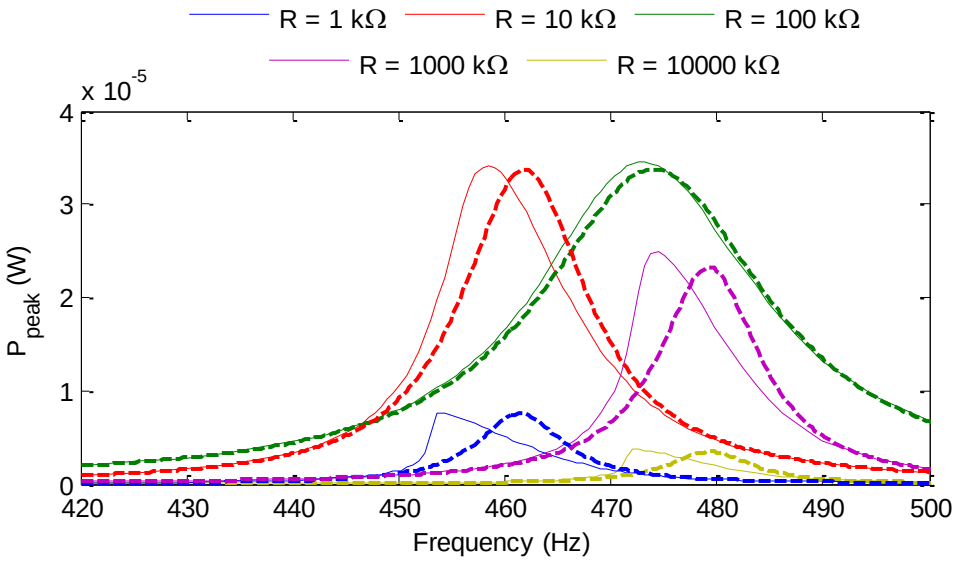

Figure 6.12 Power outputs obtained from the linear (- - -) and nonlinear (—) models are compared

The higher order terms in the equation of motion (6.19) arise due to geometric nonlinearity in the cantilever beam. To investigate the effect of geometric

nonlinearity on its own, the material nonlinearity is assumed to be negligible and the nonlinear coefficients μ_1 and μ_2 are both set to zero in the theoretical model. It is noticed that geometric nonlinearity is less sensitive to base acceleration than the material nonlinearity. As the nonlinear hardening only becomes noticeable when the base acceleration is as high as 500 m/s^2 in Figure 6.13, the geometric nonlinearity has much less influence on the frequency shift than the material nonlinearity and the strength of the nonlinear hardening relies on the dimensions and the linear material properties.

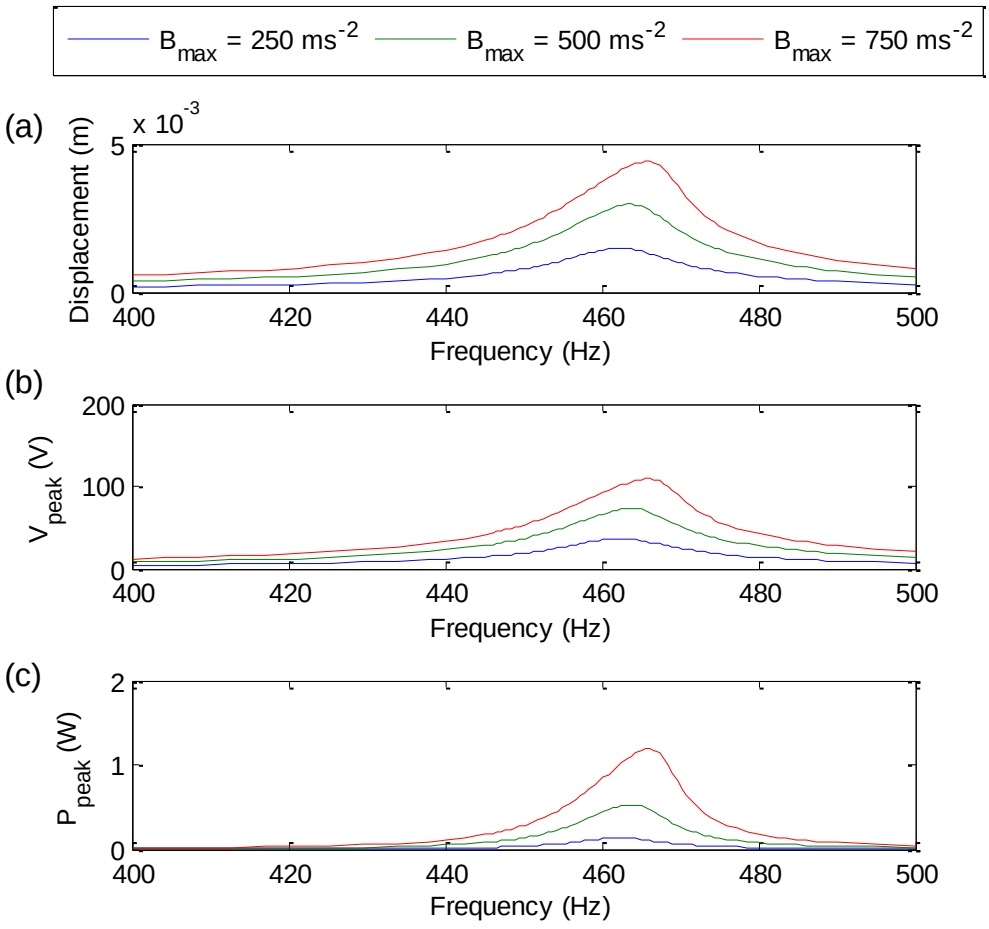

Figure 6.13 The nonlinear hardening effect is found in the energy harvester when only considering the geometric nonlinearity

It has been found from experiment that the damping ratio varies with amplitude and this will certainly affect the performance of the energy harvester. Figure 6.14 compares the FRFs for the displacement and voltage of the energy harvester for different damping ratios when the harvester is connected to a load resistor of 10 kΩ and subjected to a base acceleration of 4 m/s^2. The nonlinear softening effect can be seen in the FRFs. The frequency reduction is greater if the damping ratio is low, whereas the frequency reduction is small for high damping ratios. Thus, the damping ratio modifies the responses and also affects the resonance frequency.

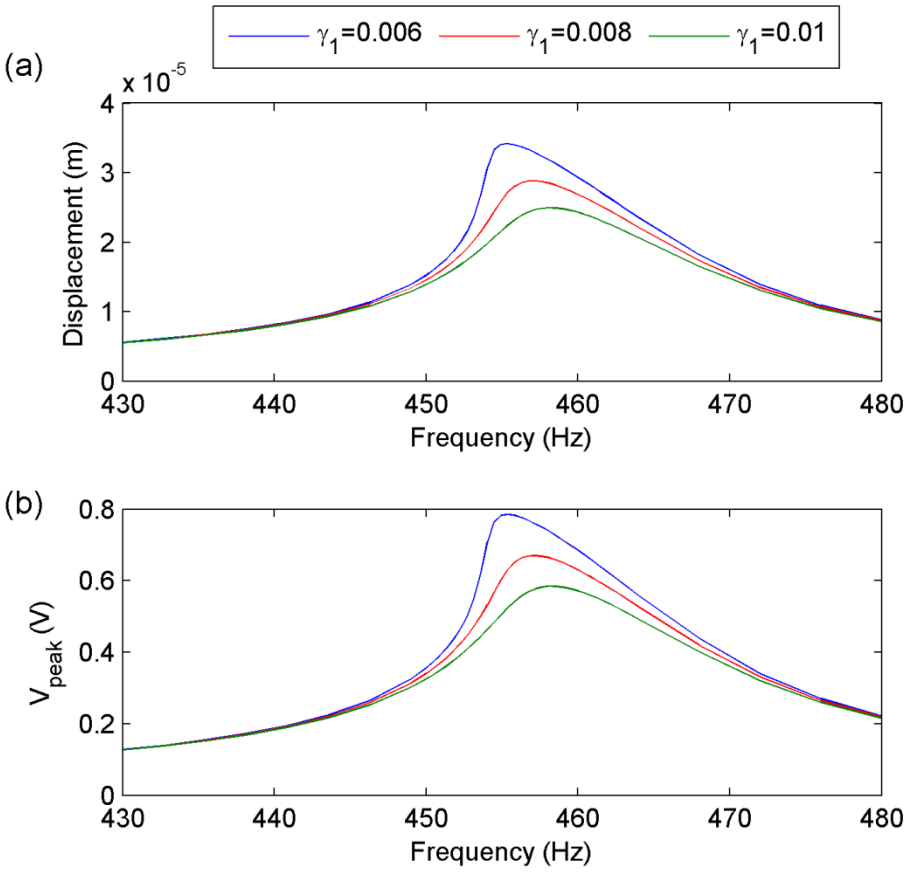

Figure 6.14 Damping ratio affects the frequency reduction

6.5 Chapter conclusions

A nonlinear piezoelectric energy harvester model has been presented in this chapter. The theoretical model takes account of the geometric nonlinearity of a cantilever beam and the material nonlinearity present in piezoelectric materials. The nonlinear model is capable of predicting both the dynamical and electrical responses of an energy harvester, as well as the frequency shift. The nonlinear coefficients used in the piezoelectric material nonlinearity have been determined experimentally using curve fitting methods. The model has also been validated with experimental results and good agreement has been observed between the theoretical results and experimental measurements. However, the discrepancies between the theoretical results and the measurements become more evident as the amplitude of the base acceleration increases. This is a limitation of the theoretical model as it is only suitable for moderate levels of amplitude.

Various studies have been carried out to investigate the effects of nonlinearity and it was found that the nonlinear softening effect is mainly caused by material nonlinearity. Also, the use of the inextensible beam condition was found to cause nonlinear stiffness hardening but this was barely noticeable compared to the softening effect. This indicates that in practice the inextensible beam assumption may be neglected to simplify the complexity of the theoretical model as the inclusion of material nonlinearity in the model should be sufficient to describe the nonlinear softening effect. Another study has shown the importance of the damping ratio as it affects both the magnitude of response and the frequency reduction.

Chapter 7. Nonlinear energy harvester with impact on a stop

7.1 Introduction

A linear model for a cantilever piezoelectric energy harvester incorporating a bump stop was developed and studied in Chapter 5. The main purpose of introducing the bump stop in the design was to limit the displacement of the cantilever beam to prevent mechanical failures caused by excessive bending of the beam. Both the theoretical model and experimental validation were presented and discussed in Chapter 5. Although the theoretical model has been validated against experiment, only low levels of excitation were used. In practice, energy harvesters can experience large amplitude vibrations and shocks, which can lead to large amplitude behaviour of the harvester, and strong nonlinear behaviour in the piezoelectric material. A nonlinear model for an energy harvester was developed in Chapter 6 that takes account of the typical piezoelectric material nonlinearity and geometric nonlinearity of a cantilever beam. It has been demonstrated that the nonlinear stiffness softening affects both the mechanical and electrical responses of the harvester significantly. On this basis, it is important to use the nonlinear energy harvester in the impact system to deal with higher levels of excitation and to investigate whether the new model will provide improved predictions over the linear model.

To use the nonlinear energy harvester in the impact model, the numerical scheme for estimating the contact force developed in Chapter 5 must be modified. The reason for this is that the coupled equations of motion for the nonlinear energy harvester cannot be solved analytically, using Duhamel's integral, as was done in Chapter 5. Time-domain solutions for the nonlinear model must be obtained numerically, to detect and estimate the contact force between the beam and stop, and this requires a new numerical modelling scheme to be developed for the impact system.

Experiments are carried out to measure the mechanical response and electrical output of a bimorph energy harvester for model validation purposes. In the experiments, the impact system is excited with different amplitudes of acceleration and different frequencies near the fundamental mode of the beam. Theoretical predictions from both the linear and nonlinear models are compared to measurements to assess the potential improvements arising from using the nonlinear model with the impact system. Also, parameter studies are carried out here to investigate how stop location and gap size affect the performance of the electrical output when the nonlinear energy harvester model is used. In particular, the maximum bending stress power output will be investigated.

7.2 Modified contact force estimation

In this work, the nonlinear model for the energy harvester replaces the linear model used in Chapter 5 with a bump stop. For the linear model, a closed-form expression

for the contact force was obtained when the beam and stop are in contact. The derived expression is only applicable for the linear energy harvester as the beam displacement was expressed in terms of Duhamel's integral. However, the coupled equations of motion for the nonlinear energy harvester cannot be solved analytically. For this reason, the modelling procedures for estimating the contact force need to be redefined for the nonlinear model.

Since the system is nonlinear, the base excitation and the contact force cannot be considered separately, and the results superimposed as done for the linear model. Instead, both the base excitation and contact force need to be gathered in the same equation. The coupled equations of motion (6.19) for the transverse vibration of the nonlinear energy harvester are modified and given by:

$$\begin{aligned}\ddot{w}_i + 2\gamma\omega_{bi}\dot{w}_i + \omega_{bi}{}^2 w_i + C_1 w_i{}^2 + C_2 w_i{}^3 + C_3 w_i \dot{w}_i{}^2 \\ + C_4 w_i{}^2 \ddot{w}_i + C_5 w_i{}^2 v - \Theta_1 v + C_6 w_i v + C_7 w_i{}^3 v = m_{Ti}\ddot{b} + F(t)\phi_{bi}(X_c)\end{aligned} \tag{7.1}$$

$$C_p \dot{v} + \frac{v}{R} + \Theta_{1i}\dot{w}_i + \Theta_{2i} w_i{}^2 \dot{w}_i + C_8 w_i \dot{w}_i + C_9 w_i{}^3 \dot{w}_i = 0 \tag{7.2}$$

and the physical response of the beam is given by:

$$Y_y(s,t) = \sum_{i=1}^{\infty} \phi_{bi}(s) w_i(t) \tag{7.3}$$

The coefficients and variables used in these equations were defined in Section 6.2.

The displacement of the beam can be obtained by solving equations (7.1), (7.2) and (7.3) numerically. When the beam and stop are out of contact, the contact force $F(t)$ is zero in equation (7.1).

One of the most important modelling procedures when analysing contact is to detect exactly when the contact takes place. This is achieved by using inequalities

(5.24) and (5.25) given in Chapter 5. When contact takes place, the following contact condition is satisfied:

$$f\left(F(t)\right)=Y_{\mathrm{y}}\left(X_{\mathrm{c}},t,F(t)\right)-Z\left(L_{\mathrm{r}},t,F(t)\right)-\Delta\equiv 0 \tag{7.4}$$

Condition (7.4) is a function of the contact force, $F(t)$. This indicates that the displacement of the beam is equal to the displacement of the stop plus the initial gap during contact. This condition was used for the linear model in Section 5.2 for the linear model. Once a contact between the beam and stop is detected, the exact time of contact, t_{e}, is determined by solving equation (7.4) for $F = 0$, i.e.:

$$f\left(F\left(t_{\mathrm{e}}\right)=0\right)=0 \tag{7.5}$$

After the initial contact, the contact force in equation (7.1) becomes non-zero until separation occurs. The contact force is unknown during contact and can be approximated by satisfying condition (7.4). This procedure needs to be carried out numerically because $Y_y(X_c,t,F(t))$ in condition (7.4) cannot be expressed analytically. In practice, the bisection method is used to calculate the root for $F(t)$. To use the bisection method [104], two initial values for the contact force, F_a and F_b are required to evaluate $f(F_a)$ and $f(F_b)$. Then, F_c, the mid-point of F_a and F_b, is used to evaluate $f(F_c)$. If condition (7.4) is not satisfied, the sign of the function indicates whether the contact force is overestimated or underestimated as illustrated in Figure 7.1. If the contact force is overestimated, the response due to the contact force will cause the beam and stop to separate from each other. If the contact force is underestimated, the beam displacement will not be limited by the stop. Only a single root of the contact force will satisfy the contact conditions. If the initial range of the contact force does not satisfy the condition (within a desired tolerance), the range $[F_{\mathrm{a}}, F_{\mathrm{b}}]$ is reduced to either $[F_a, F_c]$ or $[F_{\mathrm{c}}, F_{\mathrm{b}}]$ in the next iteration, depending on the signs of $f(F_{\mathrm{a}})$, $f(F_{\mathrm{b}})$ and $f(F_{\mathrm{c}})$. If $f(F_{\mathrm{a}})$ and $f(F_{\mathrm{c}})$ have opposite signs, the range $[F_{\mathrm{a}},$

F_c] is chosen. If $f(F_a)$ and $f(F_c)$ have the same sign, the range [F_c, F_b] is chosen. This iterative process repeats until $f(F_c)$ is zero or the desired tolerance is reached.

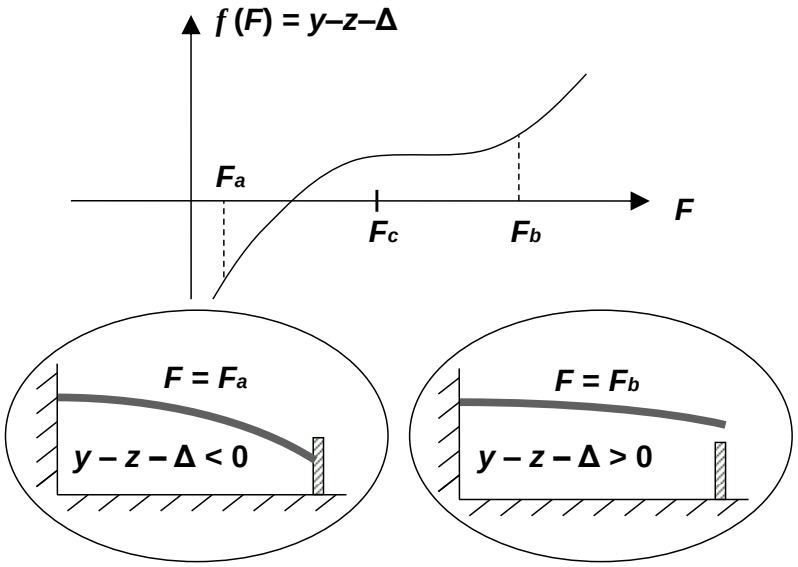

Figure 7.1 Illustration of bisection method for the contact force estimation

The modelling scheme discussed above is used to estimate the contact force with impact for the nonlinear energy harvester model, while the other modelling procedures discussed in Section 5.2 remain the same, see the flowchart for modelling procedures in Chapter 5, Section 5.2. With the new approach for calculating the contact force, the size of the time step is no longer an issue to the divergence problem. Furthermore, the contact force given in Chapter 5 is a closed-form analytical solution which was obtained by separating the contact force from the Duhamel's integrals using approximation methods, while the contact force is solved directly from the equations of motion using the numerical modelling scheme. For this reason, the numerical scheme should be more accurate than that in Chapter 5, provided that the numerical errors are insignificant.

7.3 Comparison of linear and nonlinear energy harvesters under impact condition

The nonlinear effects of the energy harvester were discussed in Section 6.4. Nonlinear softening was clearly observed in the frequency response functions and the resonance frequency of the energy harvester was observed to reduce as the base acceleration increases. In this section, the time-domain response of the energy harvester is obtained to investigate how the performance is affected by including nonlinearities in the energy harvester when a bump stop is present. In the following numerical examples, the theoretical results obtained from the approach used to model the impact in Chapter 5 are compared to the theoretical results obtained from the approach developed in Section 7.2. The bimorph sample tested experimentally in Chapter 6 is used in the examples here. The stop is located at the tip of the beam (i.e. $X_c = L_b$). The material properties of the bimorph energy harvester and stop used in the following examples are listed in Table 7.1.

	Substrate	PZT	Stop
Length, L (mm)	25.8	25.8	5
Width, W (mm)	6.4	6.4	10
Thickness, T (mm)	0.14	0.26	1
Young Modulus, E (GPa)	100	66	190
Density, ρ (kg/m^3)	8700	7800	7850
Piezoelectric constant, d_{31} (m/V)	-	$190\text{x}10^{-12}$	-
Relative Dielectric constant, k_3	-	1800	-

Table 7.1 The mechanical properties and dimensions of the bimorph PSI-5A4E and the aluminium stop

In the first example, a low amplitude (0.5 m/s^2) harmonic excitation is used in both models. The reason for using low base excitation is that the nonlinear behaviour of the harvester is insignificant and the numerical approach used to model the impact in this chapter can be validated with the approach used in Chapter 5, to make sure that the approach used for the nonlinear model is correct. The key parameters used for the system in this example are summarised in Table 7.2. The mechanical damping ratio of the bimorph was identified for different levels of amplitude experimentally and discussed in Section 6.3.1.1. The damping ratio used for the fundamental mode is 0.003. Figure 7.2 compares the time histories of the displacement and voltage of the energy harvester. The results obtained from both approaches are almost identical, and only small levels of discrepancy are found in the voltage time history. The numerical approach used to model the impact is considered to be slightly more accurate than the approach used in Chapter 5. This is due to the fact that the equation used to calculate the contact force (i.e. equation (5.20)) in Chapter 5 is approximate, while the equations are solved numerically in the numerical approach and only numerical errors affect the accuracy of these results.

Number of mode		Time step	Δ	X_c	f	B_{max}	R
Beam, n_b	Stop, n_r	(μs)	(μm)	(mm)	(Hz)	(m/s^2)	(kΩ)
5	5	1	2	L_b	460	0.5	4

Table 7.2 The key parameters used in the first example

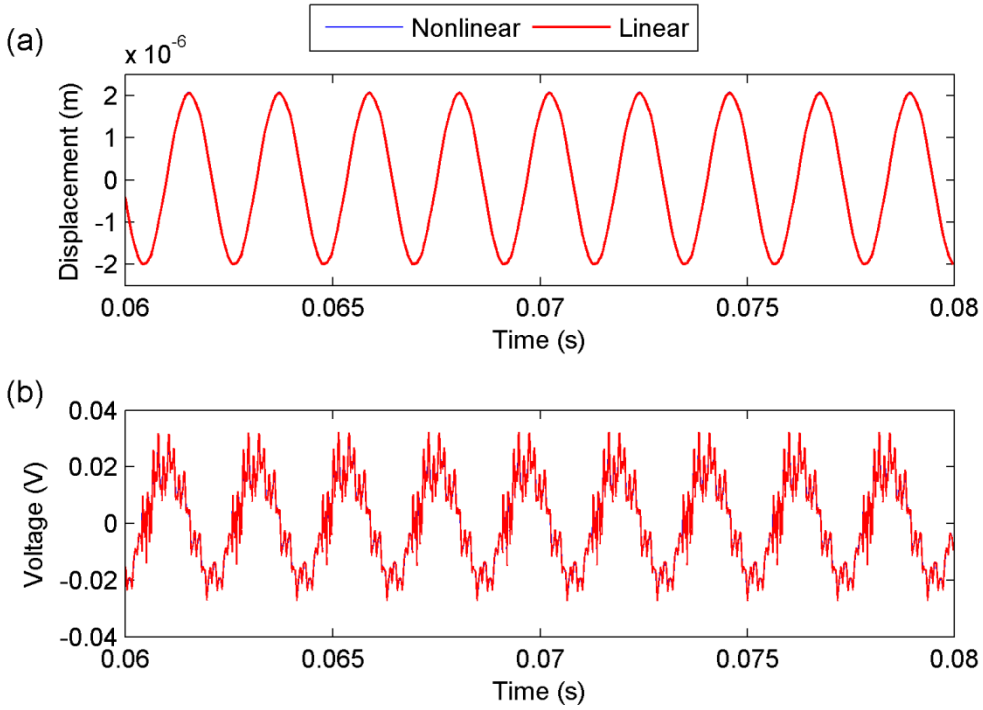

Figure 7.2 Time history responses of the linear and nonlinear energy harvester incorporating a stop: (a) displacement at X_c; (b) voltage for low acceleration

In the second example, a higher base acceleration amplitude is used to investigate if the prediction accuracy is improved when using the nonlinear energy harvester under impact condition. An acceleration amplitude of 5 m/s^2 at 455 Hz is used and the damping ratio for the fundamental mode of the harvester is 0.0118 in accordance with the experimental results discussed in Chapter 6. The parameters used are summarised in Table 7.3.

Number of mode		Time step	Δ	X_c	f	B_{max}	R
Beam, n_b	Stop, n_r	(μs)	(μm)	(mm)	(Hz)	(m/s^2)	(kΩ)
5	5	1	20	L_b	455	5	4

Table 7.3 The key parameters used in the second example

In the absence of the stop, the FRFs and time histories of the displacement and voltage of the linear and nonlinear models are compared in Figure 7.3 and Figure 7.4. The results indicate the presence of nonlinear softening and the resonance frequency reduces by 9.2 Hz. Some discrepancies are clearly seen in these responses and these can be attributed to the softening effects of the nonlinear model. The difference in voltage at 455 Hz can be seen clearly in Figure 7.3 and the linear model underestimates the voltage by 29.5 %.

When the stop is located at the tip of the beam, Figure 7.5(a) and (b) show the time histories of the displacement at X_c and the generated voltage of the harvester. The percentage difference at the peak displacement is approximately 8.7%. The root-mean-square voltage of the linear model is 0.142 V, while the nonlinear model yields 0.155 V, indicating that the linear model underestimates the voltage by 8.4% compared to the nonlinear model.

The results obtained in this numerical example show that the differences between the linear and nonlinear energy harvester models are more significant without the stop, indicating that the nonlinear effects are reduced in the presence of the stop in this particular example. This is because the stop limits the beam displacement and reduces the bending stress developed in beam, so the material nonlinearity has less influence on the energy harvester.

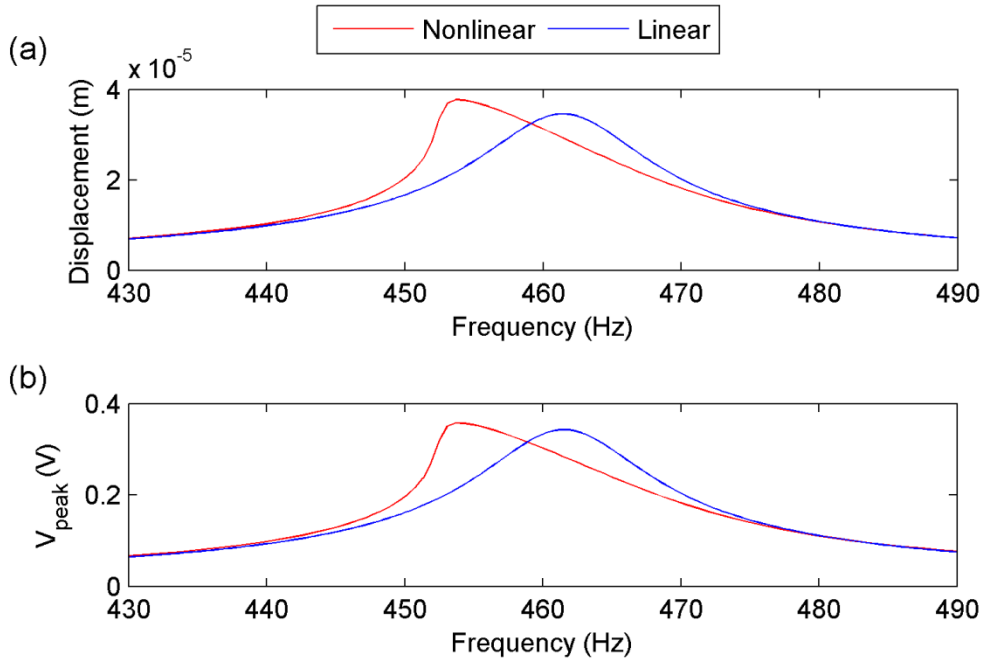

Figure 7.3 FRFs for the (a) displacement and (b) voltage of the linear and nonlinear energy harvester models

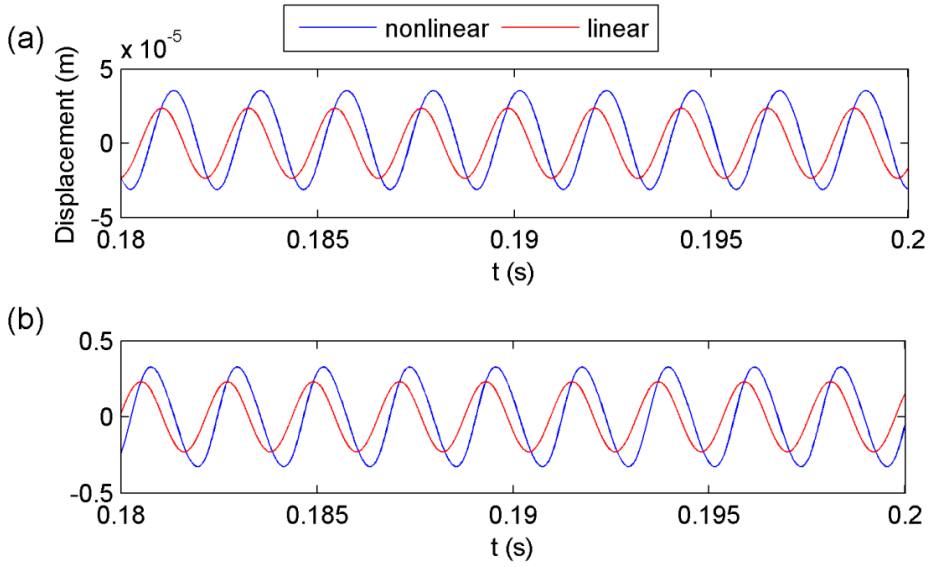

Figure 7.4 Time domain simulation of the linear and nonlinear models of energy harvester (a) tip displacement; (b) voltage

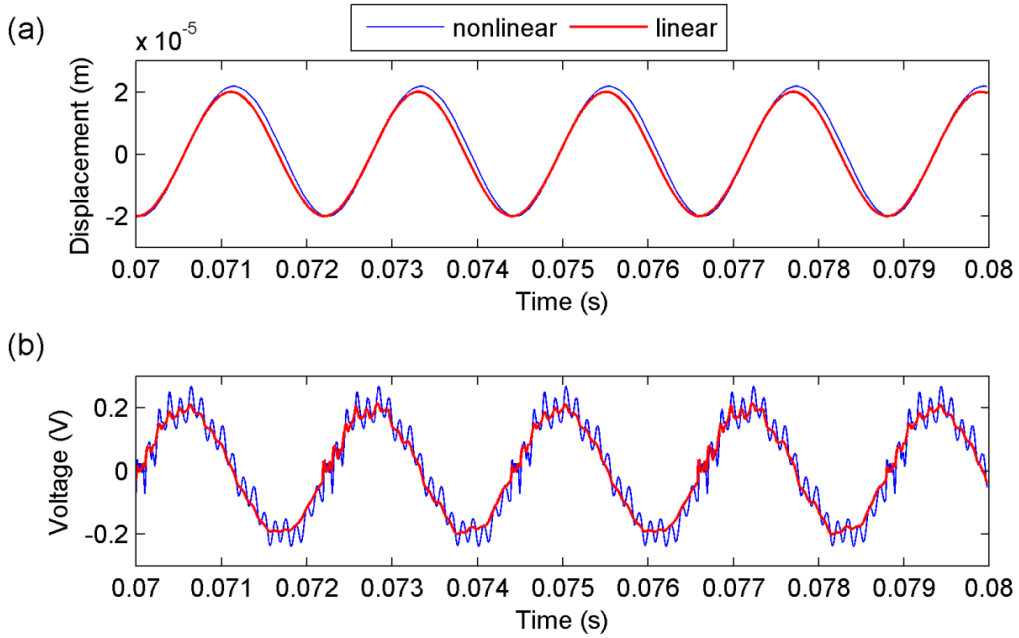

Figure 7.5 Time history responses of the linear and nonlinear models of energy harvester in the impact system: (a) displacement at X_c; (b) voltage for high acceleration

7.4 Experimental validation

The nonlinear energy harvester model has been developed to replace the linear model and improve the accuracy of predictions when the base acceleration is high. Experiments are carried out to validate the theoretical model used to model the energy harvester with a bump stop. The experimental setup and experimentation used here are exactly the same as those used for the linear energy harvester model in Chapter 5.

Four experimental tests are carried out to validate the theoretical model. The experimental results are to be compared with results obtained using the nonlinear and linear models to determine whether the accuracy of predictions is improved using the nonlinear model. The tests are summarised briefly as follows:

Test 1: Small gap and moderate level of acceleration.

Test 2: Large gap and a moderate level of acceleration.

Test 3: Same as Test 2, but a smaller load resistance.

Test 4: Large gap and stop moved to a different position, with high acceleration.

Further details on the tests will be provided later, together with the key parameters used.

In Test 1, the stop is located at the tip of the beam, i.e. $X_c = L_b$, while the initial gap size is measured to be 5 mm. A resistor of 60 kΩ is connected to the bimorph. The harmonic base acceleration is 5 m/s^2 at 455 Hz. In the simulation, the first five modes for the cantilever beam are considered. The bump stop is modelled as resilient mass-spring system to reduce the computational cost needed to model a rod-like stop. Since the stop is comparatively stiff, using a mass-spring model or a complete rod model will have no significant effects on the impact dynamics. The parameters used in the simulation are summarised in Table 7.4. The structural damping matrix of the beam is assumed to be proportional to the mass and stiffness matrices such that $\alpha\mathbf{M} + \beta\mathbf{K}$, where α *and* β are empirical constants whose values are determined through experiments and found to be 29.9 and 2.4x10^{-7} respectively. This type of damping ensures the damping ratios for the first five modes are 0.0055, 0.0030, 0.0064, 0.0121 and 0.0199 respectively.

Test 1

Number of modes		Time step	Δ	X_c	f	B_{max}	R
Beam, n_b	Stop, n_r	(μs)	(μm)	(mm)	(Hz)	(m/s^2)	(kΩ)
5	1	1	5	L_b	455	5	60

Table 7.4 The key parameters of in the impact simulation for Test 1

Time-domain simulation results are obtained using the theoretical model, and the velocity at X_c and the voltage across the resistor are compared to the measurements in Figure 7.6(a) and (b), respectively. The high frequency contents in the velocity time history is a little more noticeable in the experimental results than the theoretical results. In addition to the graphical comparison in Figure 7.6(b), the root-mean-square (rms) voltages are calculated for a more quantitative comparison. The theoretical voltage is 0.395 V, while the measured one is 0.385 V, giving a percentage error of approximately 2.6%. In general, the theoretical prediction shows good agreement to the measurement for the test. Furthermore, the V_{rms} is 0.911 V without the stop so the voltage is reduced by 56.6% by incorporating the stop. The simulation also predicts the bending stress of the entire beam and the maximum bending stress occurring at the root of the cantilever beam is 2.27 GPa, while the maximum bending stress without the stop is 4.75 GPa, indicating that the stress is reduced by about 52.2%.

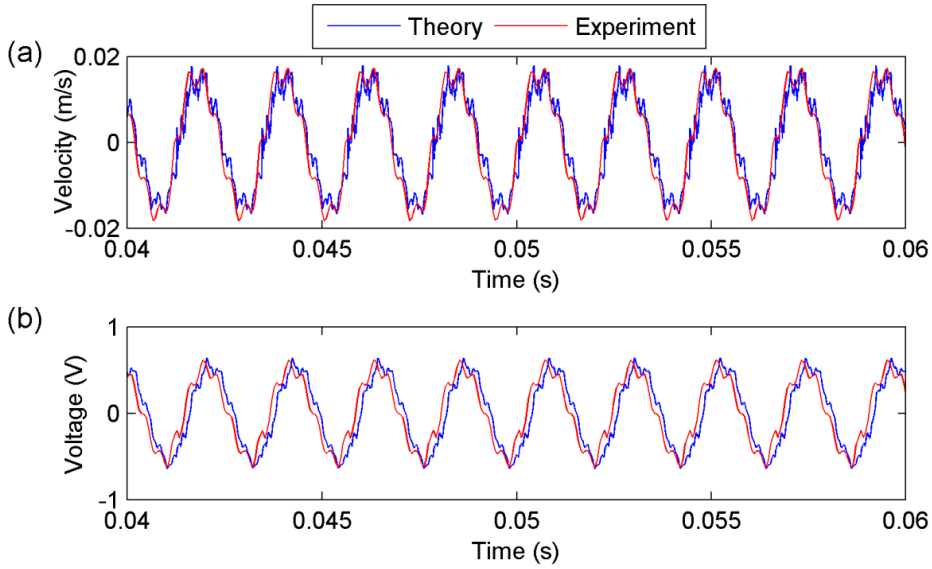

Figure 7.6 Test 1: The theoretical results obtained from the nonlinear energy harvester model are compared to the measurements

The rms voltage obtained from the linear model is 0.393 V and agree to within 2.1 % to the measurement. The velocity and voltage time histories obtained from the linear model are also compared to the measurements in Figure 7.7. The linear model offers reasonably accurate predictions to the experimental results. Since the gap size is small, the stop limits the displacement of the beam to approximately the gap size, reducing the nonlinear effects.

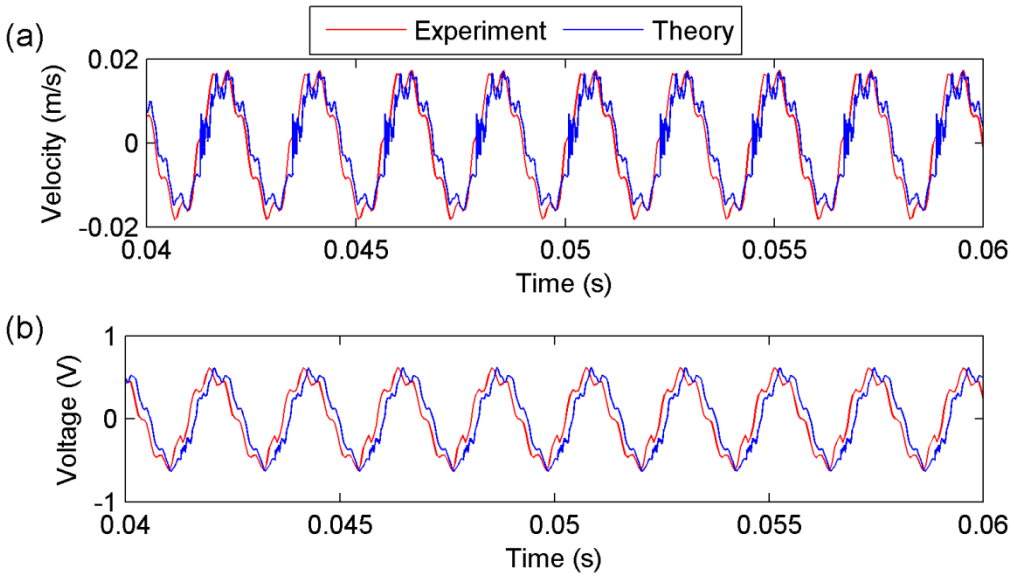

Figure 7.7 Test 1: The theoretical results obtained from the linear energy harvester model are compared to the measurements

In Test 2, the gap size is adjusted to 13 µm. The system is excited at 465 Hz with an amplitude of 4.81 m/s^2. The key parameters used in the simulation are listed in Table 7.5. Figure 7.8(a) and (b) compares the velocity and voltage obtained from the simulation with the experimental measurements. In contrast to Test 1, the contributions of the high frequency components in both the velocity and voltage are less significant.

Although the global responses of the velocity and voltage time histories match well to the theoretical results, the detailed response is not precisely the same. The measured and theoretical v_{rms} are 1.044 V and 1.054 V respectively, and the percentage error is 0.96%. The rms voltage without the stop is 1.408 V and the voltage is reduced by about 25.4% with the stop. Also, the maximum bending stress with the stop is reduced by 23.6% from 6.65 GPa to 5.08 GPa.

Test 2

Number of modes		Time step	Δ	X_c	f	B_{max}	R
Beam, n_b	Stop, n_r	(μs)	(μm)	(mm)	(Hz)	(m/s^2)	(kΩ)
5	1	1	13	L_b	465	4.81	60

Table 7.5 The key parameters in the impact simulation for Test 2

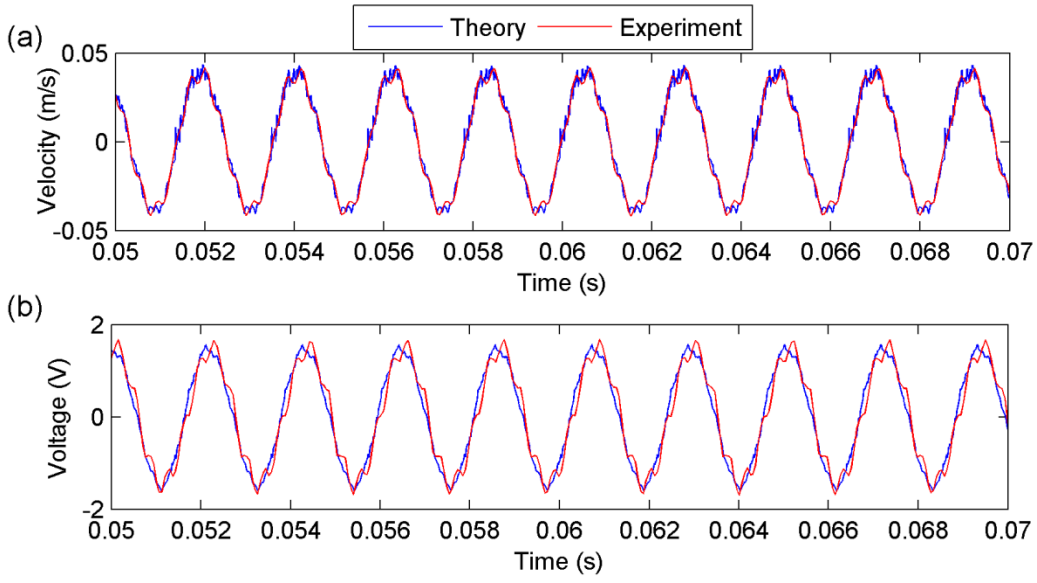

Figure 7.8 Test 2: theoretical results are compared to the measurements (a) velocity at X_c; (b) voltage

When the linear model is used to analyse the presence of a bump stop, the theoretical results are also compared to experimental results for Test 2 in Figure 7.9.

The theoretical v_{rms} calculated from the linear model is 1.015 and the percentage error is greater than that for the nonlinear model as it is underestimated by 3.2% to the measured v_{rms}.

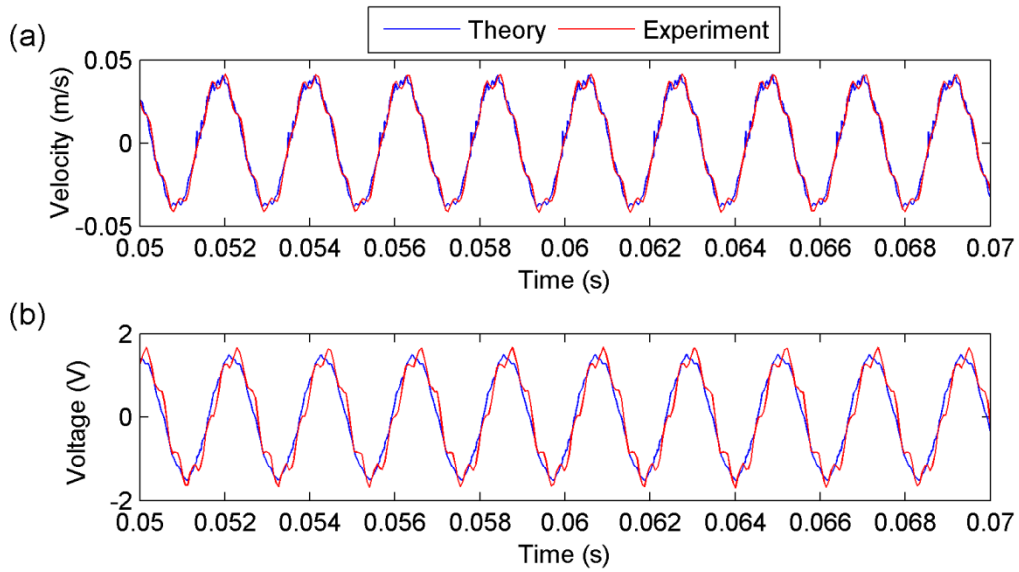

Figure 7.9 Test 2: The theoretical results obtained from the linear energy harvester model are compared to the measurements

Test 3 is the same as Test 2, except a smaller load resistance is used. This means the displacement of the energy harvester is larger since less electrical energy is dissipated through the resistor. The key parameters used in the simulation are listed in Table 7.6. Figure 7.10(a) and (b) compare the theoretical and measured velocity and voltage respectively. The presence of high frequency content in the measurements also appears in the predictions. The measured and predicted V_{rms} across the resistor are 0.108 V and 0.103 V respectively, and the percentage error is 4.6 %, indicating reasonably good agreement between the theoretical and experimental results. The maximum bending stress is reduced by 47% using the stop from 10.16 GPa to 5.38 GPa, and the voltage is also reduced by 46% from 0.192 V by the stop.

Test 3

Number of modes		Time step	Δ	X_c	f	B_{max}	R
Beam, n_b	Stop, n_r	(μs)	(μm)	(mm)	(Hz)	(m/s^2)	(kΩ)
5	1	1	13	L_b	460	4.86	4

Table 7.6 The key parameters in the impact simulation for Test 3

Figure 7.11(a) and (b) compare the theoretical velocity and voltage obtained from the linear model to the measurements, respectively. The behaviour of the responses are similar to the measurements but the amplitudes are underestimated, as the theoretical voltage is 91.2 mV and the percentage error is about 7.4%. The result shows that the nonlinear model improves the accuracy of the predictions.

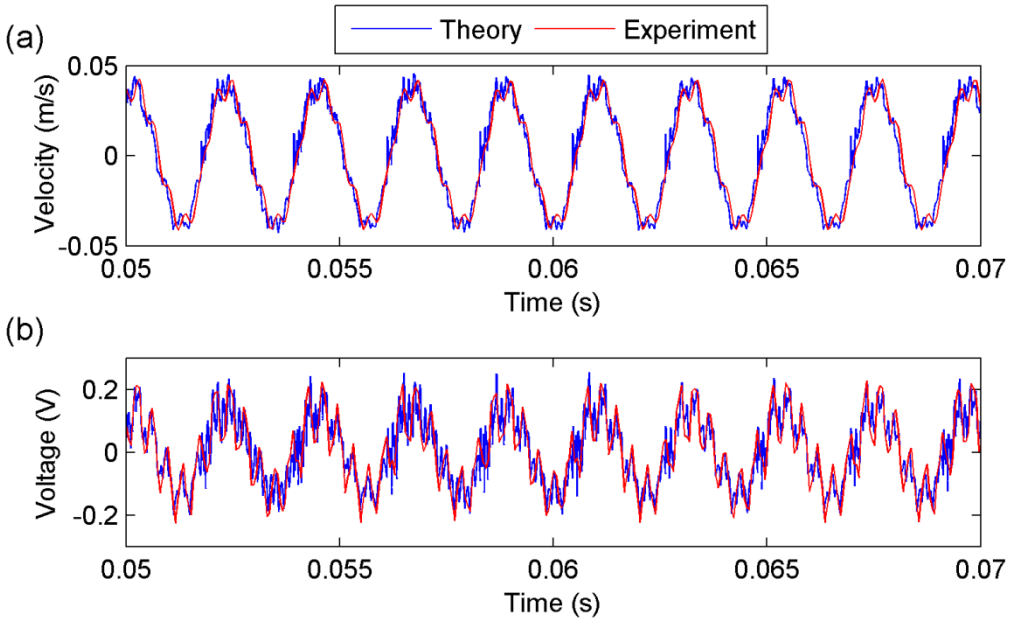

Figure 7.10 Test 3: The theoretical results are compared to the measurements (a) velocity at X_c; (b) voltage

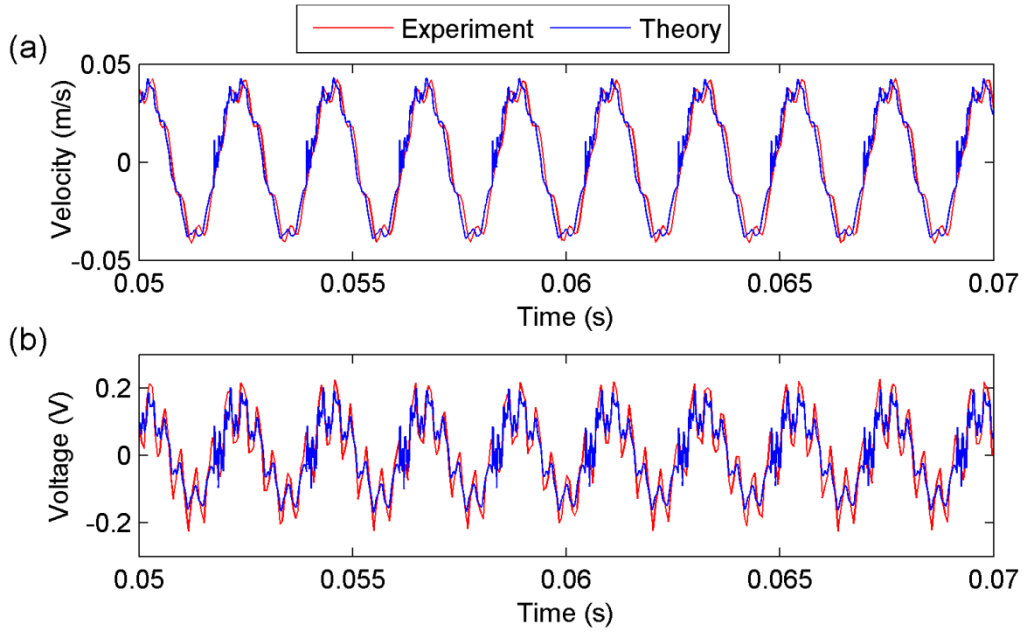

Figure 7.11 The linear model of energy harvester is used and results are compared to the measurements for Test 3

In the last test, the stop is moved 5.5 mm away from the tip of the cantilever beam, while the initial gap is measured to be 18.2 µm in the setup. The other parameters are listed in Table 7.7. The theoretical results are compared to the measurements in Figure 7.12. From both the experimental and theoretical results, it can be observed that the high frequency content is more noticeable in the voltage than the velocity. It indicates that the stop location changes the impact dynamics between the beam and stop and hence the electrical output is modified. The predictions are slightly underestimated as the theoretical and measured voltages are 47.8 mV and 52.1 mV respectively, and the percentage error is 8.3%.

Furthermore, the theoretical results show a sharp change in the voltage for each beam oscillation. This change occurs when the beam impacts the stop and the high frequency modes are excited. The voltage without the stop is 70.9 mV and the voltage with the stop is reduced by 32.6%. Also, the maximum bending stress is

calculated to be reduced by 34.2% from 15.5 GPa without the stop to 10.2 GPa with the stop.

Test 4

Number of mode		Time step	Δ	X_c	f	B_{max}	R
Beam, n_b	Stop, n_r	(μs)	(μm)	(mm)	(Hz)	(m/s^2)	(kΩ)
5	1	1	18.2	L_b-5.5	455	6.8	1

Table 7.7 The key parameters in the impact simulation for Test 4

The theoretical results obtained from the linear model are compared to the experimental results in Figure 7.13. The predicted voltage is 42.9 mV and it is 17.7% less than the measured voltage. The underestimation is even higher when using the linear model, because the nonlinear effects are strong when the acceleration is high and these effects are not considered in the linear model.

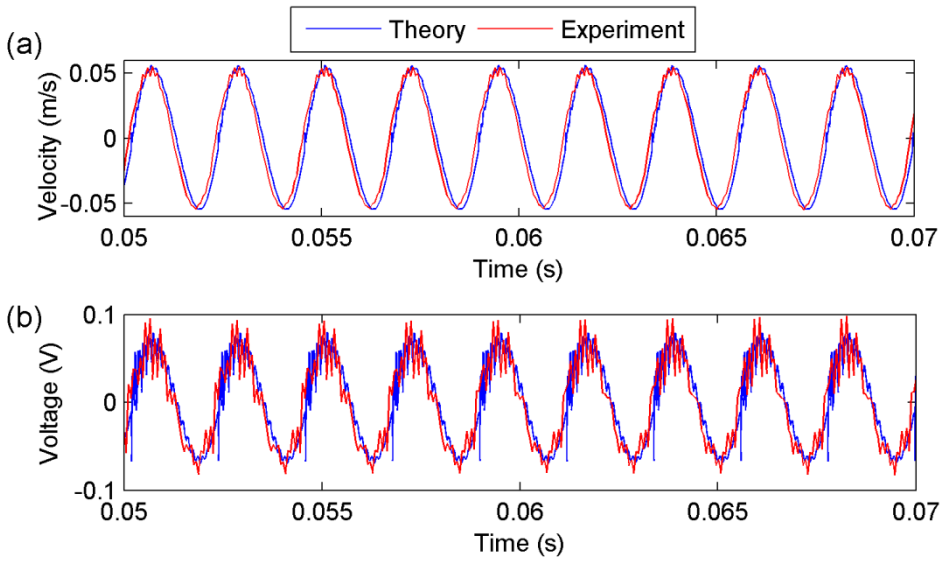

Figure 7.12 Test 4: The theoretical results are compared to the measurements (a) velocity at X_c; (b) voltage

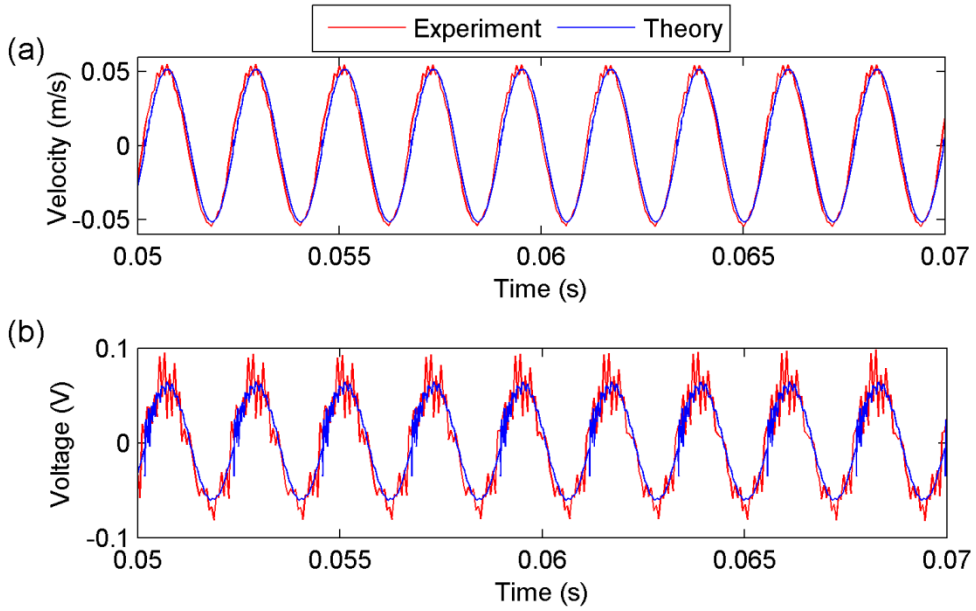

Figure 7.13 The linear model of energy harvester is used and results are compared to the measurements for Test 4

The theoretical results show good agreement with the measurements under different conditions, such as stop location, gap size, amplitude of base acceleration, etc. The theoretical model has proven itself to be capable of offering good predictions for the mechanical and the electrical output of the energy harvester.

From these tests, it can be concluded that to obtain accurate predictions it is necessary to use the nonlinear model when the base acceleration is high and the gap is large compared to the maximum beam displacement allowed at the point of impact. If the gap is sufficiently small compared the beam displacement, the linear model is sufficiently accurate, even though the base acceleration is high.

7.5 Parameter studies of the impact system

The performance of the bimorph energy harvester investigated above is studied in

this section, where the electrical output from the harvester and the maximum beam bending stress are obtained under different operating conditions, including base acceleration, stop location and initial gap size. It is clear that the bending stress is reduced in the presence of the bump stop. However it is also important to investigate how the electrical output is affected.

The effect of base acceleration amplitude is investigated first. The initial gap is fixed to 1 μm and the stop is located at the tip of the beam (i.e. $X_c = L_b$). The harvester is connected to a 60 kΩ resistor and excited by a harmonic motion at 465 Hz. Figure 7.14(a) and (b) show the time histories of the displacement at the contact point and the voltage, respectively. As the amplitude B_{max} increases from 1 m/s^2 to 6 m/s^2, both the displacement and voltage also increase. Also, the beam displacement in the downward direction is limited approximately by the initial gap size, and significantly increasing the acceleration only slightly increases the maximum displacement. Furthermore, the amplitudes of the high frequency modes are more significant as the acceleration increases. The excitation frequency is very near to the resonance frequency so the high frequency modes should be almost unresponsive to the base excitation if the stop was absent. In other words, high frequency modes can only be excited by the contact force and therefore their responses are larger when the magnitude of the contact force becomes higher. The magnitudes of the contact force with different base accelerations are compared in Figure 7.15 and this explains why the high frequency components are more significant when impacts occur for large base accelerations.

Figure 7.16(a) shows the root-mean-square voltages with and without the bump

stop as well as the maximum stress against amplitude. With the stop, the amplitude has very little influence on the voltage, while the voltage generated increases in direct proportion to the amplitude without the stop. The reductions in voltage and stress are shown in Figure 7.16(b). It is noticeable that the voltage and stress reduction trends are similar to each other.

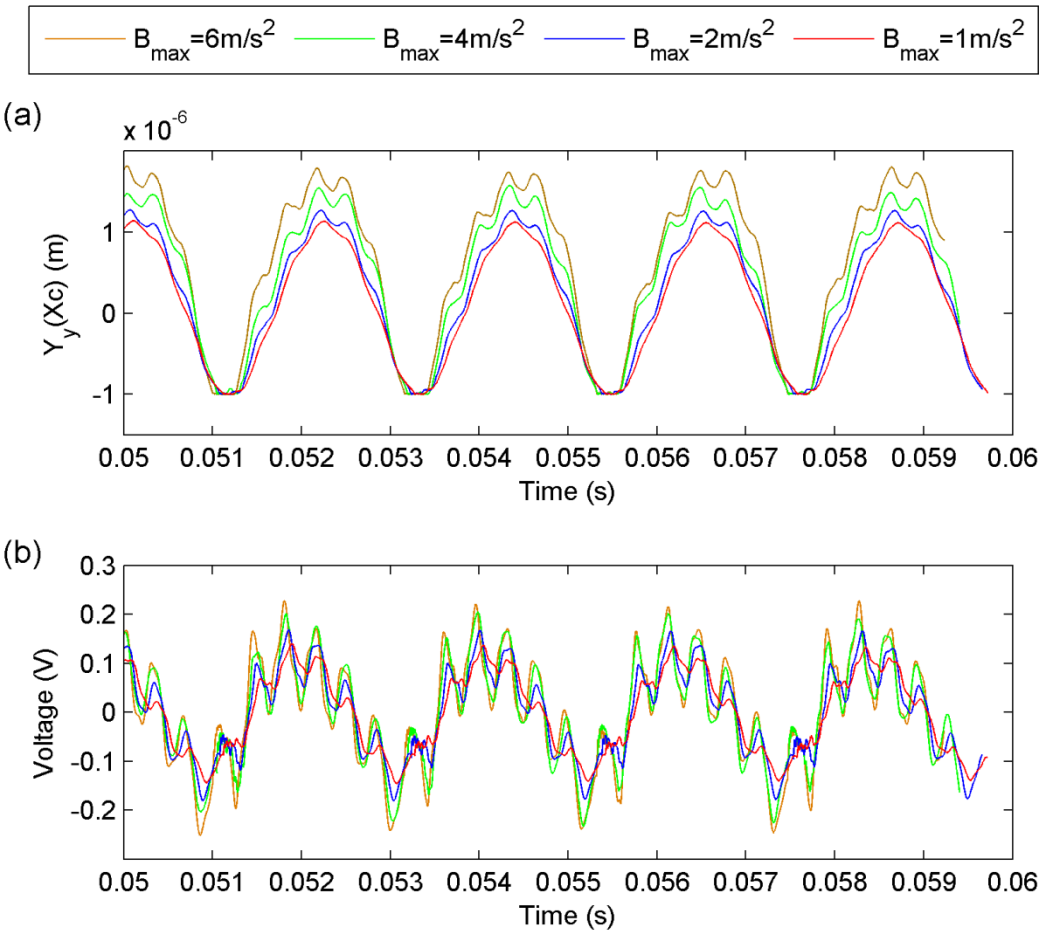

Figure 7.14 (a) The displacement at X_c and (b) voltage across 60 kΩ resistor with different amplitudes

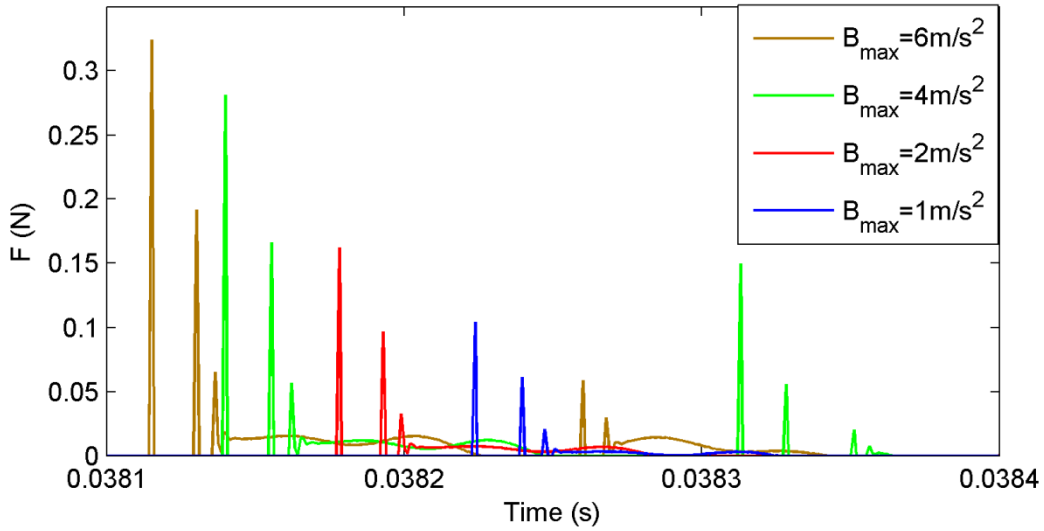

Figure 7.15 The estimated contact forces for different B_{max} used in the simulations

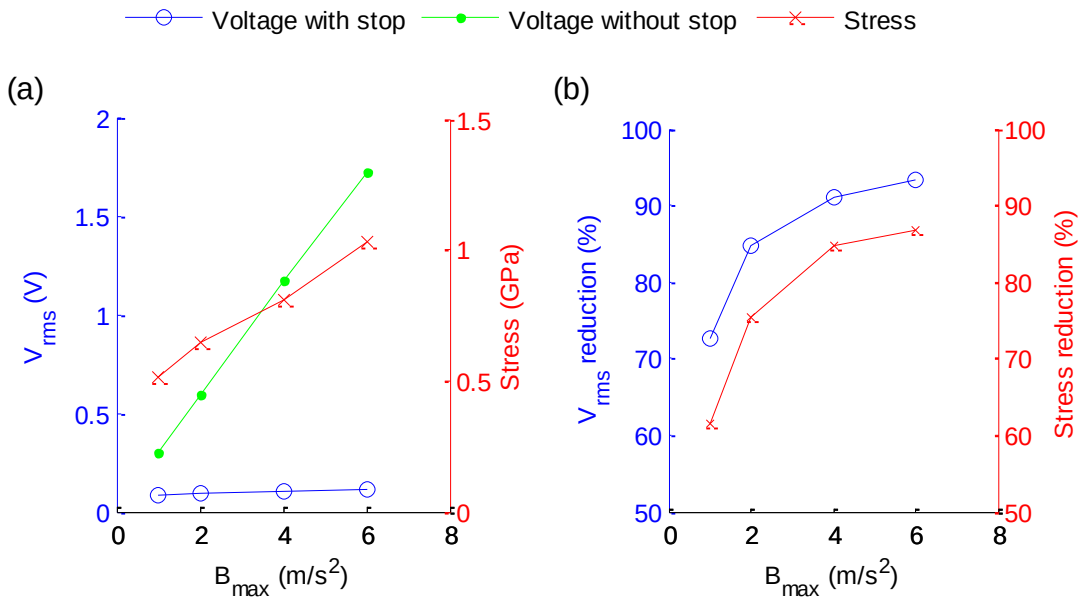

Figure 7.16 (a) Voltage and Stress; (b) voltage and stress reductions against the amplitude

The effect of gap size on the performance of the energy harvester is also related to the voltage and stress. The stop is located at the tip of the beam and the amplitude of the harmonic base acceleration is 5 m/s^2 at 465 Hz. Figure 7.17(a) and (b) show how the beam displacement at the contact point and the voltage generated vary

with the initial gap size. As expected, higher voltages are generated when the gap is larger. This is because the maximum displacement allowed increases. It is also noticeable that the magnitude of the high frequency responses decreases as the gap increases. This is because less beam-stop interaction takes place and the magnitude of the contact force reduces. Although a higher voltage is generated with a larger gap, this is at the expense of the structural integrity because the beam is allowed to vibrate at a high amplitude and high bending stresses are developed as shown in Figure 7.18(a). As expected, both the reductions in voltage and stress decrease in the same manner as the gap increases, see Figure 7.18(b), indicating an approximately linear relationship with gap size.

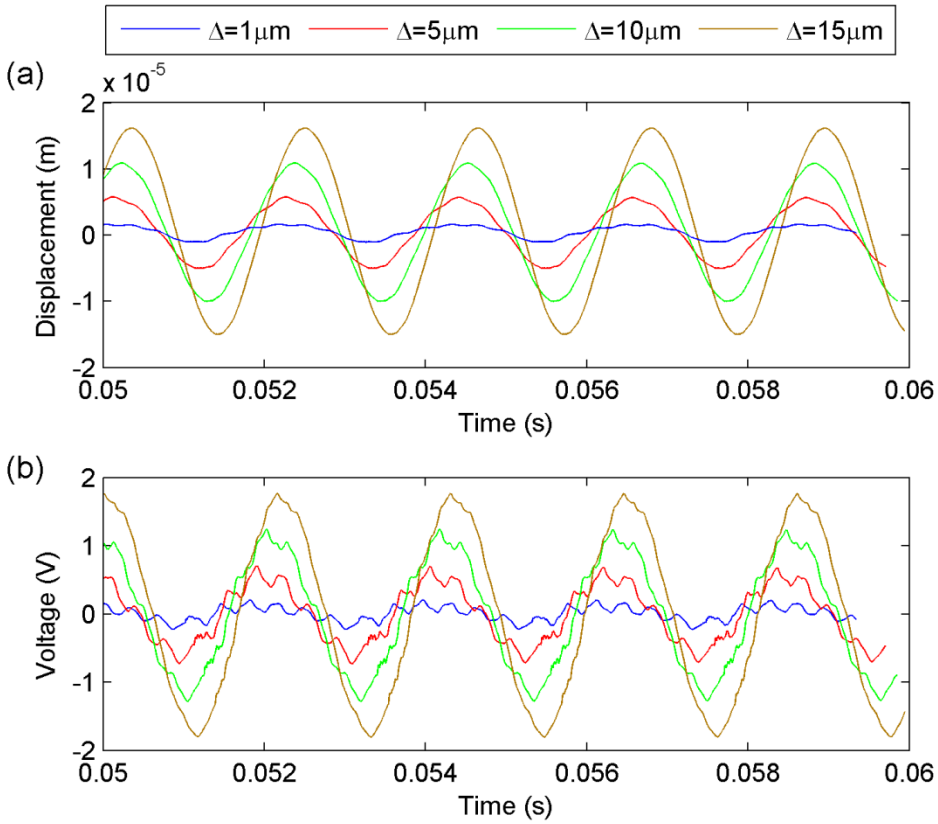

Figure 7.17 (a) The displacement at X_c and (b) voltage across 60 kΩ resistor vary with different gap size

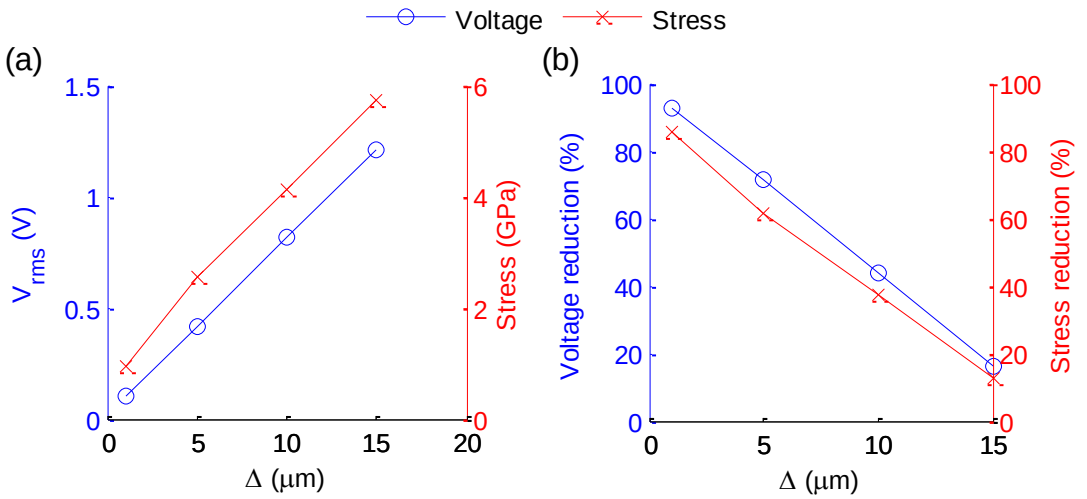

Figure 7.18 (a) Voltage and Stress; (b) voltage and stress reductions against the initial gap

Moving the stop location effectively changes the maximum displacement allowed for the beam and modifies the beam-stop interaction. In the next investigation, the stop is moved towards the clamped end of the cantilever while the other parameters remain unchanged. The system is connected to a 60 kΩ resistor and excited by a harmonic excitation with amplitude 7.5 m/s^2 and frequency 465 Hz. The initial gap is set to 5 μm. Under the criteria set for this analysis, it is meaningless to compare the displacement at the contact point because the stop location varies and the vibration amplitude depends on the location considered. Therefore, only the voltages generated by the harvester are compared, see Figure 7.19. When the stop is located closer to the clamped end, the maximum displacement allowed increases yielding higher generated voltages. Hence, both the voltage and bending stress increase when the stop is moved to the clamped end of the beam. Surprisingly, the maximum bending stress for X_c = 25.8 mm is slightly higher than the stress for X_c = 20.8 mm, while the voltage is higher for X_c = 20.8 mm than for X_c = 25.8 mm, see Figure 7.20. For the purposes of design, the stop should be located at X_c = 20.8 mm rather than X_c = 25.8 mm for higher voltage and less maximum stress.

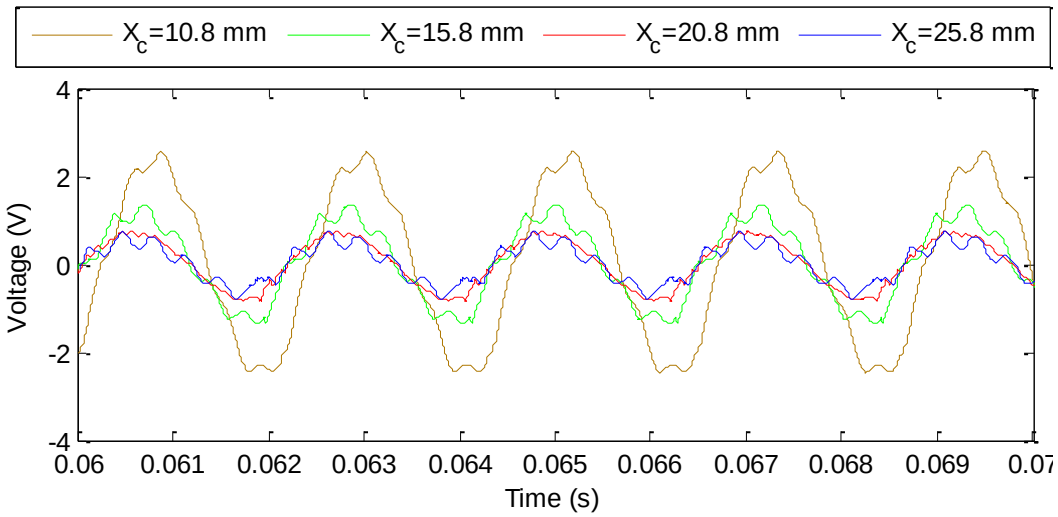

Figure 7.19 The voltages across the resistor with different stop locations

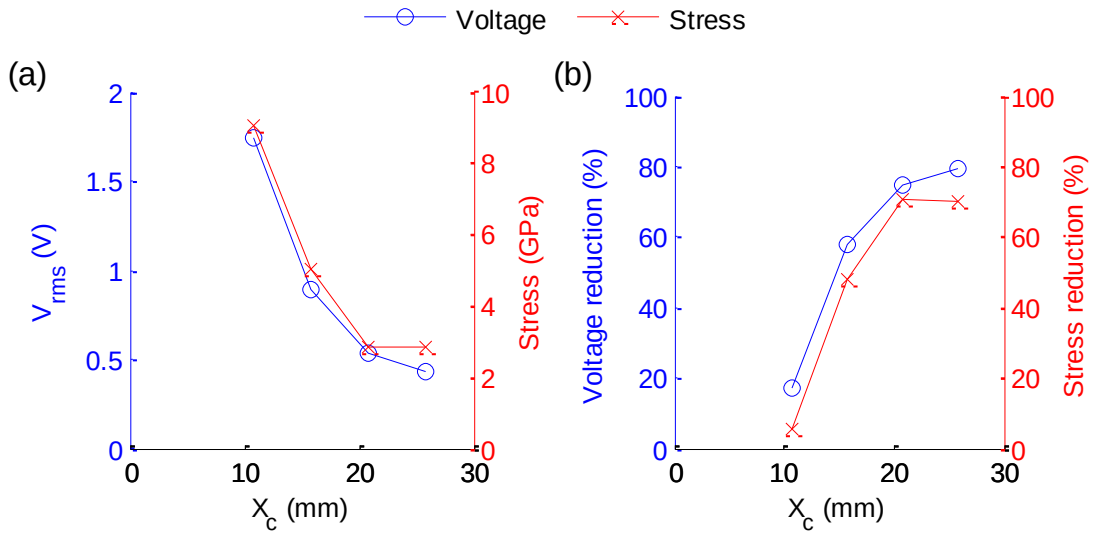

Figure 7.20 (a) Voltage and Stress; (b) voltage and stress reductions against the initial gap

7.6 Chapter conclusions

A nonlinear energy harvester model has been incorporated with a bump stop. In the modelling, a new approach is employed to estimate the contact force between the beam and stop, due to the absence of analytical solutions for the nonlinear

harvester. Also, experiments have been carried out to measure the mechanical and electrical responses of the bimorph energy harvester for the purpose of validation. The theoretical results have been compared to experimental measurements made under different test conditions, and it has been shown that the theoretical results are in good agreement with the experimental results in general.

The importance of using the nonlinear model has been demonstrated, particularly when the base excitation is high and the initial gap is large. Nevertheless, the linear model offers satisfactory predictions for mechanical and electrical responses when the gap size is significantly smaller than the maximum displacement at the impact point. It is found that the percentage error in root mean square voltage for the nonlinear model is usually less than that for linear model. Various parameter studies have been carried out to investigate how the stop location and initial gap size affect the performance of the energy harvester. When the stop is located at the tip of the beam, the maximum bending stress developed in the beam is reduced by the stop and the voltage suppressed. The reductions in stress and voltage are both approximately inversely proportional to gap size. The stop location affects the impact dynamics and modifies the deflected shape of the beam. The voltage generated is subjected to less suppression when the stop is moved towards the clamped end. It has also been found that increasing the base acceleration has little influence on the amplitude of the voltage and displacement.

Chapter 8. Case study: Car tyre sensor application

8.1 Introduction

Nowadays, vehicles are equipped with up to 100 different types of sensors and many of these are MEMS, including accelerometers, gyroscopes, inclinometers and pressure sensors. The automotive industry often stimulates the market growth of MEMS sensors as the automotive sector is the second largest MEMS market in 2008 [105]. In particular, the market growth for TPMS is driven significantly by the government legislation mentioned in Chapter 1.

The practical motivation for this project is that autonomous energy supply is a suitable solution to powering TPMS inside a car tyre. The concept of a car tyre energy harvesting using piezoelectric materials was first proposed in 2001. Some experimental work has been carried out by Brusarosco *et al.* [7] and Keck [68]. Wu [106] also carried out a simple experiment to demonstrate how a piezoelectric energy harvester charges a capacitor to power a wireless node for signal transmission. However, no devices were fitted to a car tyre for testing and instead only its theoretical potential was demonstrated for the tyre application. Hamel *et al.* [107] proposed a circuit that is capable of storing electrical energy prior to transmitting signals if the power required is not sufficient for the transmission.

In this chapter, a case study is conducted to demonstrate the electrical output generated by an energy harvester embedded in a tyre. The energy harvester considered here is attached to the inner surface of a tyre as shown in Figure 8.1. The reason for the energy harvester location is that there is abundance of vibration energy due to tyre deformation when the tyre rotates and makes contact with the road. A simple approach is used here to model the radial tyre deformation, and will be discussed later. Also, a stop model is used in the harvester design to limit large displacements caused by high accelerations due to tyre deformation. Numerical simulation results are used to investigate the performance of the energy harvester with and without a stop. Simulation results obtained from the theoretical are also compared to published experimental measurements in this chapter.

Figure 8.1 An energy harvester is embedded in the inner wall of a car tyre (pictures are downloaded from http://www.bridgestone.co.uk)

8.2 Energy harvester inside a car tyre

In this section, a piezoelectric energy harvester is modelled that is embedded in the inner surface of a tyre. A schematic representation of the energy harvester is shown in Figure 8.2. The harvester rotates with the wheel and experiences the tyre deformations that occur when the tyre makes contact with the road. The two main sources of excitation arise from the base excitation applied to the harvester and the centripetal force produced by the wheel rotation. In addition to these sources, high frequency vibrations are caused by the car body and this source is neglected in this study. The patch where the harvester is located makes contact with the road surface once per wheel revolution. The car tyre deformation consists of a combination of radial and tangential tyre deformations. The radial tyre deformation is considered to be the dominant excitation, whilst the tangential tyre deformation is relatively insignificant and neglected [7]. Further details about the radial tyre deformation are provided in Section 8.2.2.

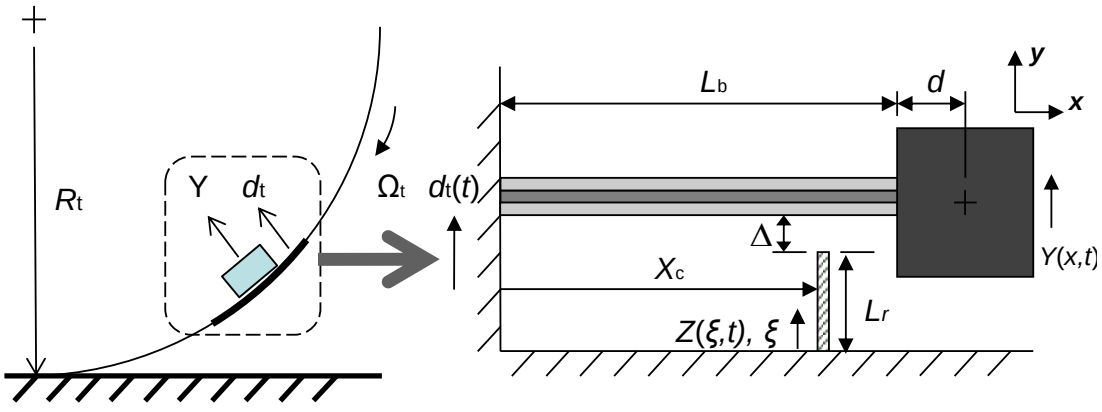

Figure 8.2 Configuration of a bimorph energy harvester inside a car tyre

8.2.1 **Equations of motion**

A bimorph energy harvester with a tip mass is considered to be embedded in a car tyre and the equations of motion are obtained taking into account the centripetal acceleration due to the wheel rotation and the shock acceleration due to the radial tyre deformation. In Chapter 7, it was shown that using a nonlinear energy harvester made little difference to the performance of the harvester if the gap size is relatively small compared to the vibration amplitude of the harvester, even if the base excitation is high. In the following examples, the gap sizes used are relatively small allowing a linear energy harvester to be used. The energy harvester considered has a bimorph configuration with a tip mass attached. The harvester also incorporates a bump stop to prevent high levels of vibration. The equations of motion are derived using Hamilton's principle, while the impact dynamics is modelled based on the numerical procedures described in Chapter 7. Figure 8.2 shows a schematic diagram of an energy harvester embedded in a tyre that is subjected to radial tyre deformation. To derive the equations of motion, both potential and kinetic energies are required and these are given by:

$$\begin{aligned} P_e = & \frac{1}{2}\int_0^{L_b}\int_{A_s}\sigma_s S_s \,\mathrm{d}A_s\,\mathrm{d}x + 2\cdot\frac{1}{2}\int_0^{L_b}\int_{A_p}\sigma_p S_p dA_p\,\mathrm{d}x \\ & -2\cdot\frac{1}{2}\int_0^{L_b}\int_A ED\,\mathrm{d}A\,\mathrm{d}x + \int_0^{L_b} m_b g\left(d_\mathrm{t}-Y\right)\cos\Omega_\mathrm{t} t\,\mathrm{d}s + Mg\left(d_\mathrm{t}-Y\right)\cos\Omega_\mathrm{t} t \end{aligned} \tag{8.1}$$

$$\begin{aligned} K_e = & \frac{1}{2}\int_0^{L_b} m_b\left(\dot{Y}+\dot{d}_t\right)^2\mathrm{d}x + \frac{1}{2}M\left(\dot{Y}_{x=L_b}+d\dot{Y}'_{x=L_b}+\dot{d}_\mathrm{t}\right)^2 + \frac{1}{2}J\dot{Y}'^{\,2}_{x=L_b} \\ & + \frac{1}{2}\int_0^{L_b} m_b\left(R_t-Y-d_\mathrm{t}\right)^2\Omega_\mathrm{t}^{\,2}\,\mathrm{d}x + \frac{1}{2}M\left(R_t-Y_{x=L_b}+dY'_{x=L_b}-d_\mathrm{t}\right)^2\Omega_\mathrm{t}^{\,2} \end{aligned} \tag{8.2}$$

In the above equations, d_t is the radial car tyre deformation and Ω_t is the angular velocity of the tyre as shown in Figure 8.2. These equations are based on the linear energy harvester model and use the same notation as used in Chapter 3. The main

difference to the equations derived in Chapter 3 is that additional terms appear for the gravitational potential energy and the rotational kinetic energy. The approach used to obtain the equations of motion is the same as that presented in Sections 3.2 and 5.2. On this basis, a detailed derivation is not presented here. Following the same procedures, it can be shown that the coupled equations of motion are given by:

$$\begin{aligned}\left(\mathbf{M}_{\mathrm{T}}+\mathbf{M}_{\mathrm{J}}\right)\ddot{\mathbf{w}}(t)+\mathbf{C}\dot{\mathbf{w}}(t)+\left(\mathbf{K}\text{-}\mathbf{M}_{\mathrm{T}}\Omega_t^{\,2}\right)\mathbf{w}(t)-\boldsymbol{\Theta}v(t)=\\ -\mathbf{m}_{\mathrm{T}}\left[\ddot{d}_t(t)-\left(R_t-d_t\right)\Omega_t^{\,2}-g\cos\Omega_t t\right]+F(t)\boldsymbol{\phi}_{\mathrm{b}}\left(X_c\right)\end{aligned} \tag{8.3}$$

$$C_{\mathrm{p}}\dot{v}(t)+\frac{v(t)}{R}=-\boldsymbol{\Theta}^{T}\dot{\mathbf{w}}(t) \tag{8.4}$$

where the physical displacement of the cantilever beam is given by:

$$Y(x,t)=\sum_{i=1}^{\infty}\phi_{bi}(x)w_i(t)=\boldsymbol{\phi}_{\mathrm{b}}(x)\mathbf{w}(t) \tag{8.5}$$

The coefficients and variables used in equations (8.3)–(8.5) were defined in Chapter 5. The base acceleration considered arises from the radial tyre deformations in this application and is defined in Section 8.2.2. Due to the wheel rotation, the centripetal force acts on the energy harvester and this is indicated by the appearance of the second term on the right hand side of equation (8.3). The third last term in equation (8.3) indicates the fluctuating weight due to wheel rotation.

8.2.2 Tyre deformation and wheel rotation

It is essential that the radial tyre deformation is defined appropriately as it is the main source of excitation in the application. The deformation of a car tyre is defined by using the tyre kinematics and a schematic representation of simple tyre deformation model is shown in Figure 8.3. It is assumed that the tyre radius is

constant and the tyre only deforms when it makes contact with the road. The contact patch angle $2\alpha_c$ is used to define the extent of the deformed sector of the tyre and specifies the size of the contact patch. Based on the geometry defined in Figure 8.3, the planar radial deformation, $d_t(t)$, can be expressed in terms of the radius of a unloaded tyre R_t, the constant angular velocity of the tyre Ω_t and half contact patch angle α_c, as follows:

$$d_t(t) = \begin{cases} p(t) = R_t\left(1 + \dfrac{\cos\alpha_c}{\cos\Omega_t t}\right) & \pi - \alpha_c \le \Omega_t t \le \pi + \alpha_c \quad (8.6) \\ \\ 0 & \Omega_t t < \pi - \alpha_c \ \cap \ \Omega_t t > \pi + \alpha_c \quad (8.7) \end{cases}$$

The radial tyre deformation is a discrete function as it only occurs when the tyre deforms. It is also worth mentioning that the maximum radial deformation is determined by the contact patch and is independent of the car speed using the approach described here, but the acceleration $\ddot{d}_t$ due to radial deformation will increase with car speed and is obtained by differentiating d_t twice with respect to time.

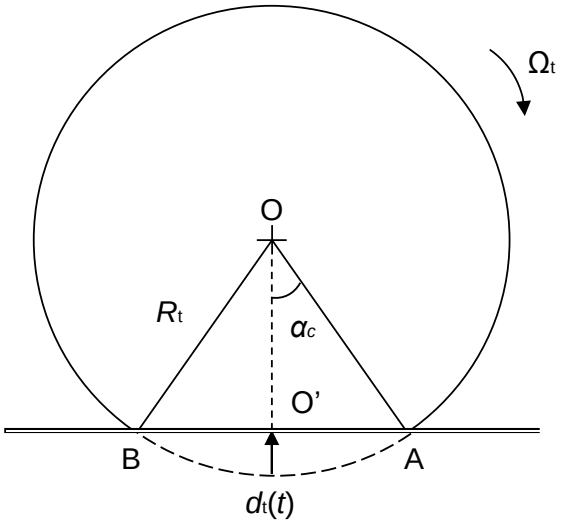

Figure 8.3 The schematic representation of a deformed car tyre

It is clear seen from equation (8.6) that the radial acceleration is infinite at the entrance and exit points of the contact patch. This leads to an overestimation in predictions when the energy harvester enters and exits the contact patch. To achieve a more realistic representation of the accelerations, two functions are introduced to smooth the transitions arising from equations (8.6) to (8.7) for the entrance and exit of the contact patch, see Figure 8.4.

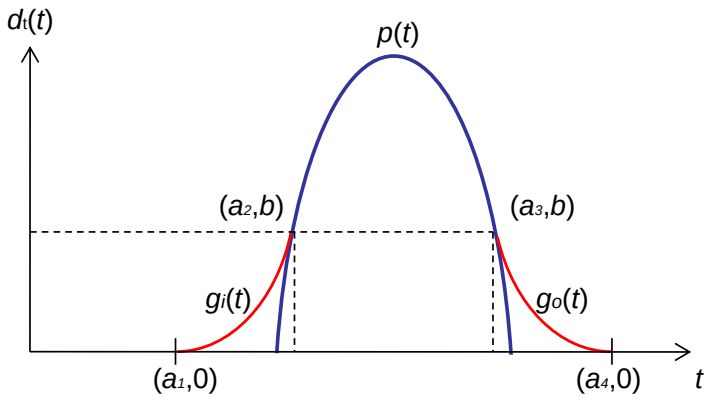

Figure 8.4 The polynomials are used to smooth the deformation at the entrance and exit of the contact patch

Polynomials, $g_i(t)$ and $g_o(t)$, are introduced to provide an improved representation of the tyre deformation that is differentiable at the entrance and exit respectively. This representation smooths the radial deformation as shown in Figure 8.4. The polynomials are used to replace the radial deformation described by equations (8.6) and (8.7) for the intervals $t=a_1$ to $t=a_2$ and $t=a_3$ to $t=a_4$, respectively.

To determine the polynomials, continuity conditions are needed at $t = a_1$, a_2, a_3 and a_4 to match the radial deformation, velocity and acceleration. For $g_i(t)$ at $t=a_1$, three boundary conditions for radial displacement, velocity and acceleration are used. For

$g_i(t)$ at $t=a_2$, it is found that the third derivative of $g_i(t)$ with respect to time needs to be included to ensure the gradient of the acceleration is the same as the gradient of the acceleration of p(t) at $t=a_2$. The boundary conditions for $g_i(t)$ at $t=a_3$ and $t=a_4$ are also deduced in the similar way. Hence, the polynomials, $g_i(t)$ and $g_o(t)$, for the entrance and exit must satisfy the following continuity conditions:

For the entrance:

$$g_i(a_1)=0,\ \dot{g}_i(a_1)=0,\ \ddot{g}_i(a_1)=0, \tag{8.8}$$

$$\begin{aligned} &g_i(a_2)=p(a_2)=b\ \ ,\dot{g}_i(a_2)=\dot{p}(a_2)=c_i \\ &\ddot{g}_i(a_2)=\ddot{p}(a_2)=d_i\ \ ,\dddot{g}_i(a_2)=\dddot{p}(a_2)=e_i\ \ . \end{aligned} \tag{8.9}$$

For the exit:

$$g_o(a_4)=0,\ \dot{g}_o(a_4)=0,\ \ddot{g}_o(a_4)=0, \tag{8.10}$$

$$\begin{aligned} &g_o(a_3)=p(a_3)=b\ \ ,\dot{g}_o(a_3)=\dot{p}(a_3)=c_o \\ &\ddot{g}_o(a_3)=\ddot{p}(a_3)=d_o\ \ ,\dddot{g}_o(a_3)=\dddot{p}(a_3)=e_o\ \ . \end{aligned} \tag{8.11}$$

where b is denoted in Figure 8.4, while c, d and e are the first, second and third derivatives of $p(t)$ at $t = a_2$, respectively.

Since there are seven continuity conditions for each polynomial, a sixth order polynomial can be used to satisfy the conditions for the entrance and exit of the contact patch, i.e.

$$g_i(t)=h_{i,6}t^6+h_{i,5}t^5+h_{i,4}t^4+h_{i,3}t^3+h_{i,2}t^2+h_{i,1}t+h_{i,0} \tag{8.12}$$

$$g_o(t)=h_{o,6}t^6+h_{o,5}t^5+h_{o,4}t^4+h_{o,3}t^3+h_{o,2}t^2+h_{o,1}t+h_{o,0} \tag{8.13}$$

Boundary conditions (8.8) and (8.9) to polynomial (8.12) are applied to determine the seven unknowns $h_{i,0} - h_{i,6}$. Similarly, the unknowns $h_{o,0} - h_{o,6}$ in polynomial (8.13)

are determined through continuity conditions (8.10) and (8.11).

8.2.3 Numerical simulation examples

In this section, numerical examples are presented to illustrate the expected energy harvester performance for a car tyre application. The energy harvester used in the following examples is based on Model PSI-5A4E (see Section 4.3.2), which has a bimorph configuration with a series connection between the piezoelectric layers. The harvester is connected to a 10 kΩ resistor to dissipate electrical energy generated. A brass block is attached to the tip of the cantilever beam to act as a tip mass. The mechanical properties and dimensions of the harvester are listed in Table 8.1. In the following examples, the energy harvester is embedded inside a tyre for which the loaded radius of the tyre is assumed to be 25 cm and the thickness of the tyre is assumed to be 2 cm. On this basis, the distance from the centre of the tyre to the energy harvester is 23 cm. When the harvester does not coincide with the contact patch, the radius of the tyre is assumed to remain unchanged regardless of the car speed. The contact patch angle normally varies with the vertical load of a car and the contact patch angle, $2\alpha_c$, used in the simulations is chosen to be 29˚. More specifically, the angular displacement between a1 and a2 is 7˚, α_2 and α_3 is 15˚, and α_3 and α_4 is 7˚.

In the first example, an energy harvester without a bump stop is considered. The car is assumed to travel at a constant speed of 30 mph. Figure 8.5 shows the radial displacement and acceleration of the tyre deformation profile at this speed. Also, the radial displacement and acceleration are highlighted to see clearly in Figure 8.5 when they are in the contact patch. The displacement profile is calculated using

equations (8.6), (8.7), (8.12) and (8.13). Using the polynomials at the entrance and exit prevents a very sudden change in acceleration as seen in Figure 8.5(b).

PSI-5A4E - Dimensions and mechanical properties

	Substrate	PZT	Brass block
Length, *L* (mm)	20	20	4
Width, *w* (mm)	6.4	6.4	6.4
Thickness, *t* (mm)	0.14	0.26	4.6
Young Modulus, *E* (GPa)	100	66	100
Density, ρ (kg/m^3)	8700	7800	8700
Piezoelectric constant, d_{31} (m/V)	-	190x10^{-12}	-
Relative Dielectric constant, *k3*	-	1800	-

Table 8.1 The mechanical properties and dimensions of the bimorph PSI-5A4E

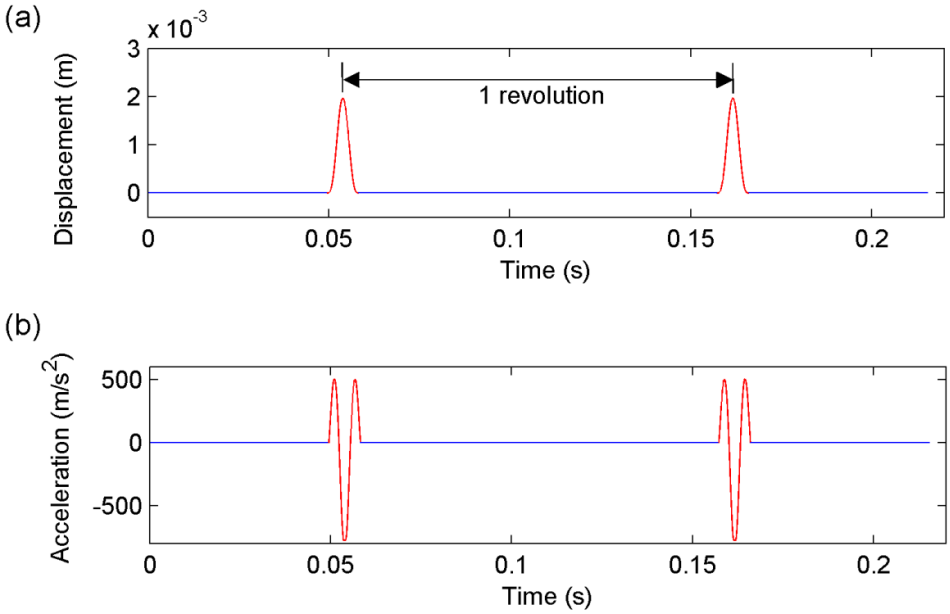

Figure 8.5 (a) Tyre deformation; (b) Acceleration due to tyre deformation

The tyre deformation profiles above are used to predict the responses of the energy harvester. Figure 8.6 shows the displacement at the centre of the tip mass, the

voltage across the resistor and the power output. It is clear to see that the vibration of the beam is offset from its neutral axis. This is because the centrifugal force produced by the wheel pushes the beam outwards from the centre of the wheel. The simulation results show four revolutions of the wheel. When the deformation takes place, the harvester responds rapidly as a consequence of generating maximum electrical power, particularly when the harvester coincides with the contact patch, as seen in Figure 8.6(c). When the harvester leaves the contact patch, the power output decreases, indicating that the tyre deformation is the dominant source of energy. In principle, the rotation of the wheel should produce power. However, the wheel frequency is well below the fundamental frequency of the bimorph, and this effect is small as a consequence.

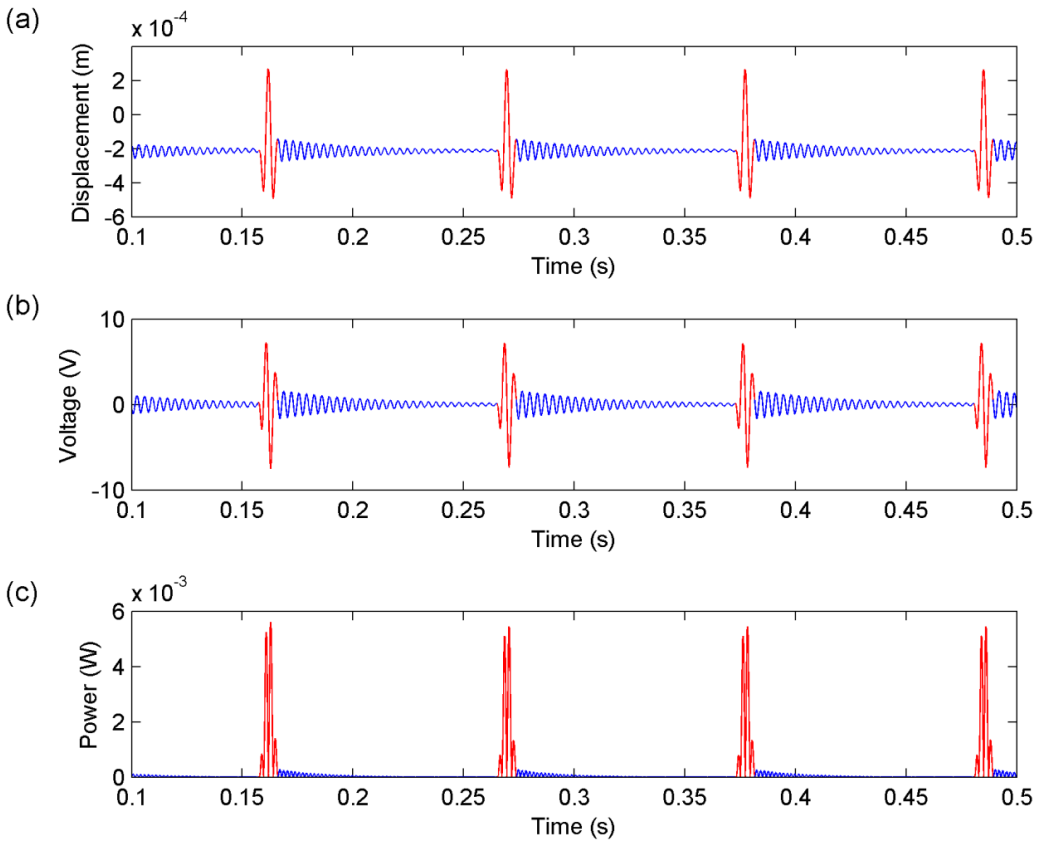

Figure 8.6 (a) The displacement at the centre of the tip mass; (b) voltage across the resistor; (c) power output

In the next example, the car speed is increased to 60 mph. This has the effect that the radial acceleration due to the tyre deformation increases as shown in Figure 8.7(a). The key parameters used are listed in Table 8.2. Figure 8.7 (b–d) show the predicted displacement, voltage and power of the energy harvester, respectively. Compared to the previously example, the offset deformation of the energy harvester increases from the neutral axis, and this can be attributed to the increased centrifugal force as the rotational speed of the wheel increases. The electrical power output also increases.

It is clear that more electrical energy is generated when the car travels at a higher speed due to the higher acceleration levels produced by the radial tyre deformation. However, the displacement of the cantilever beam also has increased amplitude and this can cause mechanical failure if the bending stress exceeds the maximum stress that the piezoelectric material can withstand. For this reason, a bump stop is introduced in the energy harvesting design to reduce the maximum beam displacement. The stop should be placed beneath the beam because the energy harvester always experiences the centrifugal force that pushes the beam outwards. In the following example, the stop is located beneath 1 mm away from the tip of beam to avoid any clash between the tip mass and the stop.

Impact parameters

Number of modes		Time step	Δ	X_c	R	Speed
Beam, n_b	Stop, n_r	(μs)	(mm)	(mm)	(kΩ)	(mph)
5	1	1	1	16	10	60

Table 8.2 Key parameters used in the presence of a stop

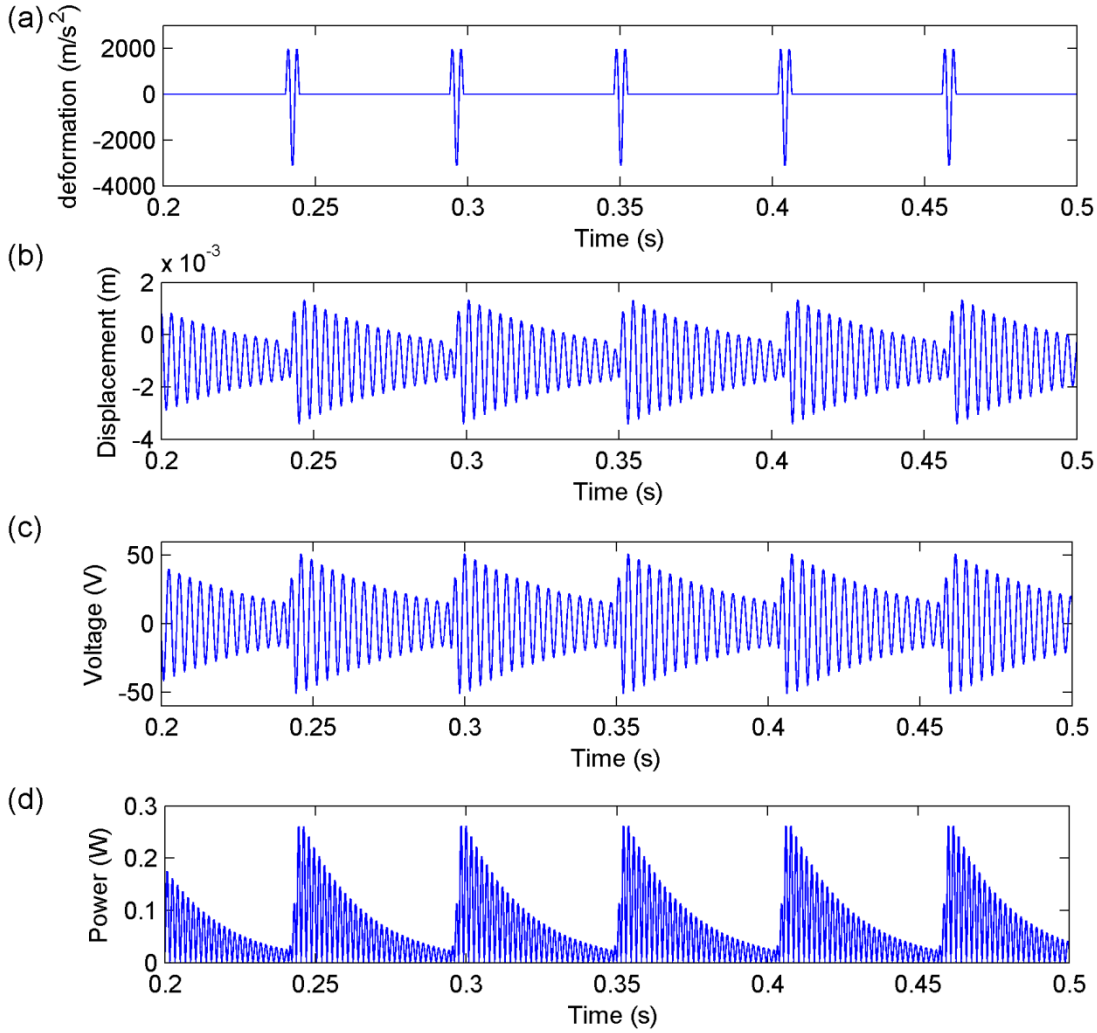

Figure 8.7 **(a) Acceleration due to car tyre deformation; (b) displacement at the centre of the tip mass; (c) voltage across the resistor; (d) power output**

Figure 8.8 shows the simulation results for the energy harvester. It is clearly seen in Figure 8.8(a) that the displacement of the beam at the impact point is limited by the stop and takes values approximately equal to the size of the initial gap. Surprisingly, the voltage time history in Figure 8.8(b) shows that the maximum voltage has a large value compared to the previous example where the stop is absent. The maximum voltage is found when the tyre deforms and impact takes place. However, the high voltage occurs once in each wheel revolution and decays once the energy

harvester exits the contact patch. These high voltages are induced by the impact between the beam and stop. In this particular example, the energy harvester generates the majority of the electrical energy during the tyre deformation. The power time histories with and without the stop are compared in Figure 8.9, and the root-mean-square powers are calculated as 28.7 mW and 53.6 mW, respectively. Hence, although the peak power with the stop is higher, the harvester without the stop indeed generates more power. Moreover, the maximum bending stress is calculated to be 1330 GPa at the root of the cantilever beam and this stress is 40% lower than the value obtained without a stop.

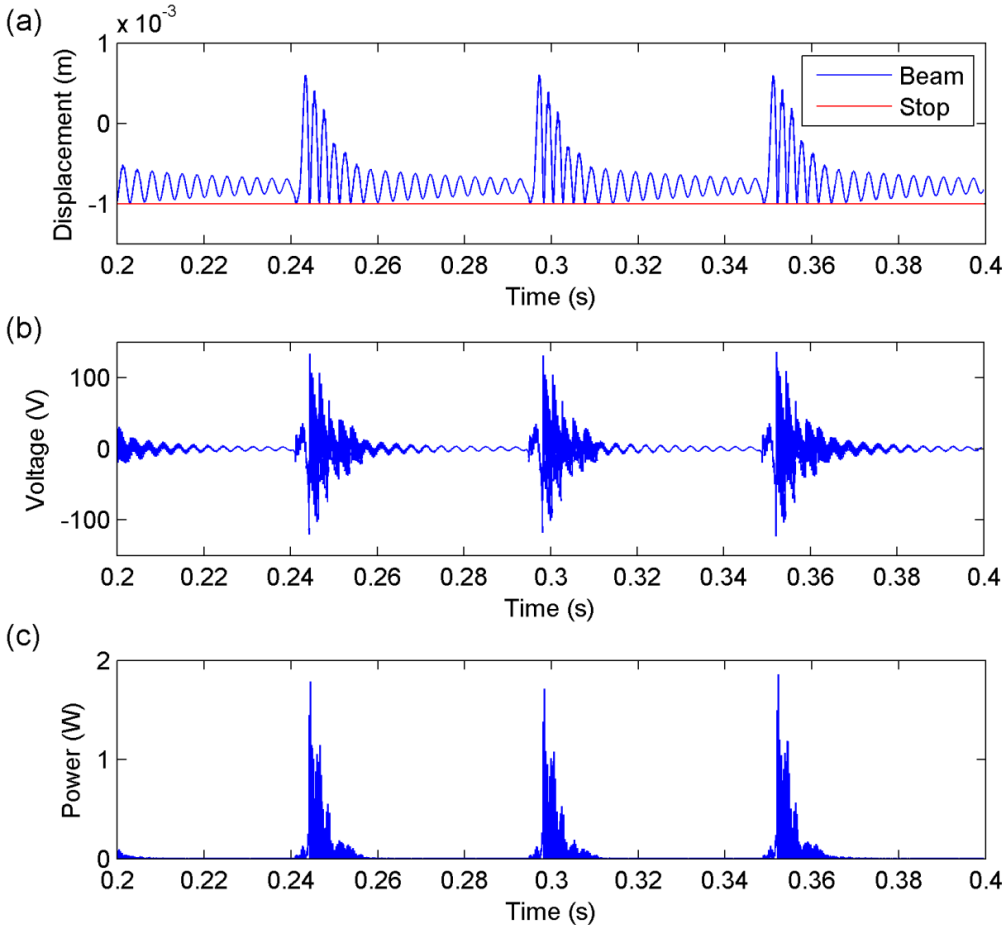

Figure 8.8 (a) Displacements of the beam and stop; (b) voltage across the resistor; (c) power output

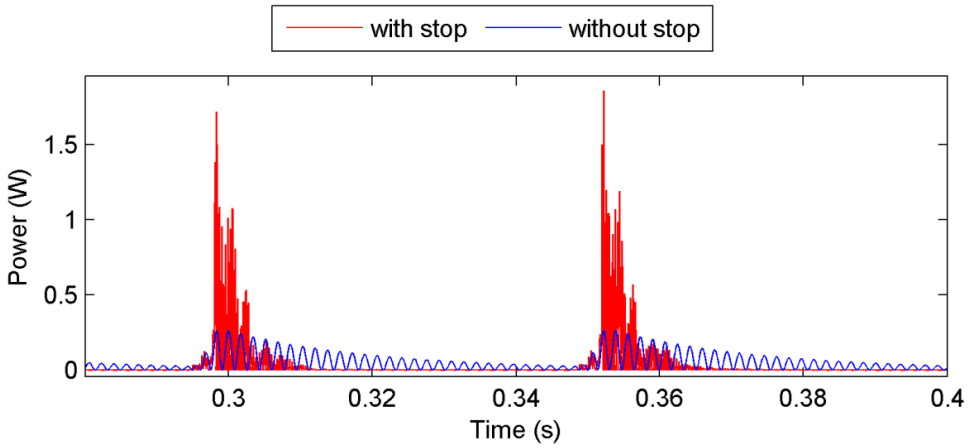

Figure 8.9 Comparison between power outputs with and without stop

8.2.4 Theoretical predictions against published results

In this section, previous published experimental work for the tyre application is compared to simulation results obtained using the developed theoretical model. Measured radial acceleration profiles for a car tyre are reported in the literature [7, 68, 80]. Figure 8.10(a) shows a measured acceleration profile, which was presented in [68], when the car speed is 62 mph. The profile shows the resulting radial acceleration over one wheel revolution. There are some high frequency ripples in the profile and these may be caused by vibrations of the car body and interactions between the tyre and road. Figure 8.10(b) shows the theoretical acceleration profile obtained using the model described in Section 8.2.2. This acceleration profile is the resulting radial acceleration caused by tyre deformation and centrifugal acceleration. It is clear that the acceleration is constant at 270g when no radial tyre deformation takes place. During the deformation, the acceleration rapidly drops to approximately zero. These characteristics are found in both the measured and theoretical

acceleration profiles. Generally, there is reasonably good agreement between the measured and theoretical acceleration profiles.

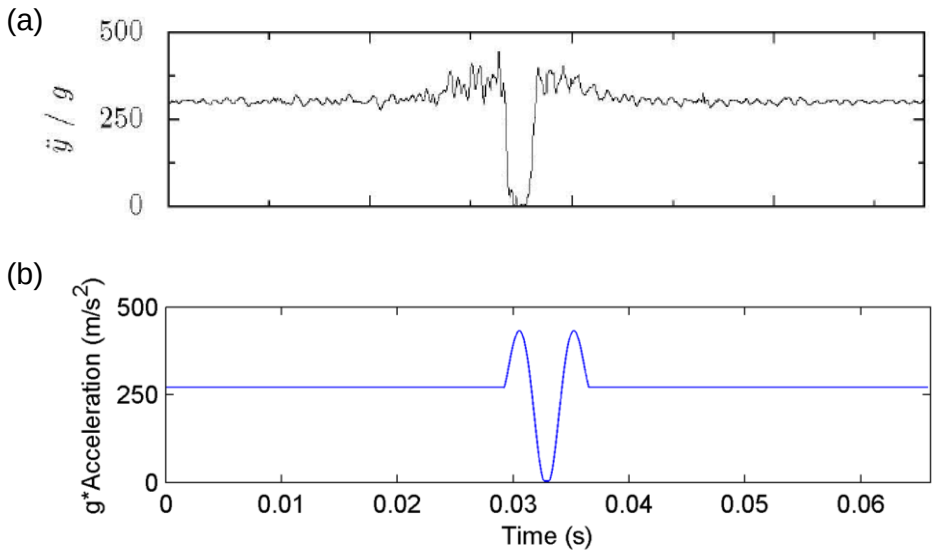

Figure 8.10 The acceleration that the energy harvester is subjected to: (a) in the patent [68]; (b) simulation

In what follows, simulation results obtained using the theoretical model are compared to the experimental results reported by Brusarosco *et al.* [7]. The bimorph energy harvester tested had a fundament natural frequency in the range 350 Hz – 400 Hz, and is slightly different to the configuration modelled in the simulation. One of the reasons for this is that only some dimensions of the energy harvester device are provided and limited information is available. Also, in the experiment contact is made between the tip mass and the casing of the device, while the tip mass impacts a bump stop in this model. Therefore, it is expected that differences will exist between the theoretical results and the experimental measurements in [7].

In the experiment, a tip mass of 0.97 g is attached to the bimorph and the shape of the tip mass is as shown in Figure 8.11. The overall thickness of the bimorph is 0.46 mm but the thickness of each layer is not provided. Table 8.3 lists the dimensions, and mechanical properties used in the theoretical model. The tip mass used ensures the theoretical fundamental natural frequency of this bimorph model is 386 Hz, which compares well to the measured natural frequency [7].

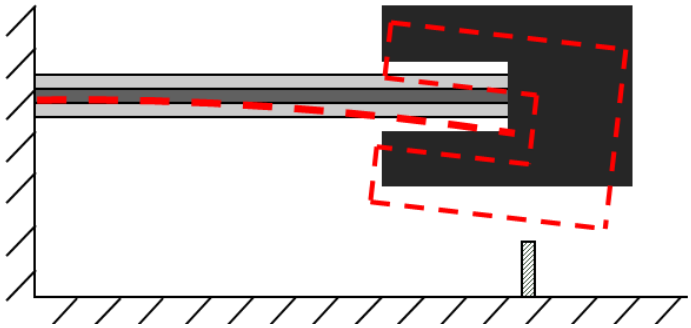

Figure 8.11 The tip mass impacts the stop during contact

	Substrate	PZT
Length, L (mm)	11	11
Width, w (mm)	5	5
Thickness, t (mm)	0.1	0.18
Young Modulus, E (GPa)	100	66
Density, ρ (kg/m^3)	8700	7800
Piezoelectric constant, d_{31} (m/V)	-	190x10^{-12}
Relative Dielectric constant, k_3	-	1800

Table 8.3 Parameters used in the simulation for the comparison to experimental measurements

Number of modes		Time step	Δ	X_c	R	Speed
Beam, n_b	Stop, n_r	(μs)	(μm)	(mm)	(kΩ)	(mph)
5	1	1	125	L_b+d	10	30

Table 8.4 Parameters used in the simulation for the comparison to the results in [7]

Figure 8.12 compares the measured voltage against the simulation. The simulated voltage still shows some similarities to the measurements. For instance, large responses in the voltage occur during the tyre deformations and these responses decay quickly once the energy harvester exits the contact patch. As mentioned earlier, the main reason for the differences is that the theoretical model is slightly different to the energy harvester used in the experiment. Furthermore, the theoretical model also predicts the interaction between the tip mass and stop in Figure 8.13(a), which is very difficult to be measured experimentally. Figure 8.13(b) shows the power dissipated through the resistor and indicates that the maximum power output is always obtained during the tyre deformation.

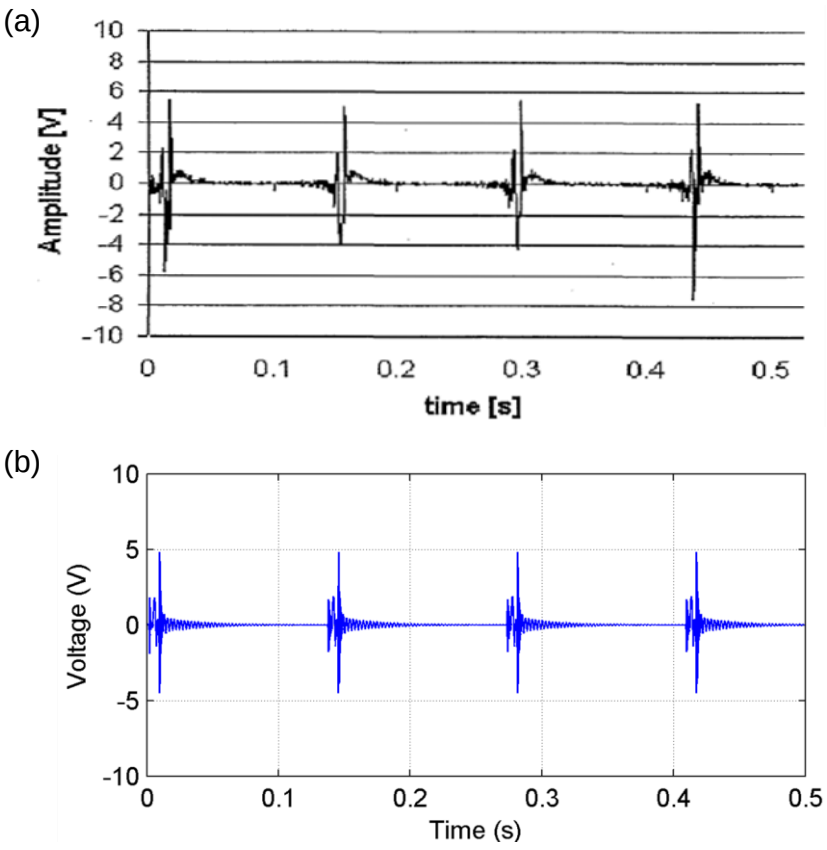

Figure 8.12 At 30 mph: (a) measured voltage in [7]; (b) predicted voltage obtained from the simulation

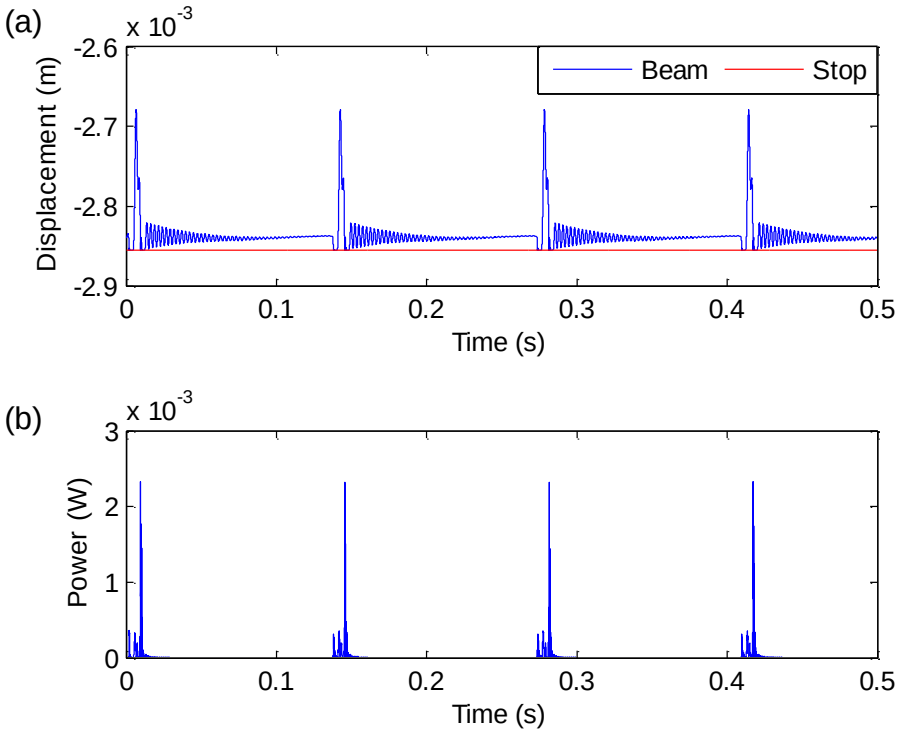

Figure 8.13 (a) The bottom surface of the tip mass impacts the stop; (b) the power output from the energy harvester

8.3 Chapter conclusions

A theoretical model has been developed to predict the dynamics and electrical output of a piezoelectric energy harvester used to power a car tyre pressure sensor. The radial tyre deformation has been modelled based on a simple mode of the kinematics of a car tyre as it is the main source of vibration in the application. Numerical examples have been used to demonstrate how the energy harvester responds to the radial deformation mechanically and electrically. The harvester generates the maximum electrical power during deformation and little power is generated when the contact patch does not coincide with the road. Also, it was observed that the harvester experiences the centripetal force produced by the wheel rotation and this results in an offset from the neutral axis. For this reason, a

bump stop should be located beneath the energy harvester to prevent large beam deflection caused by the centripetal force as well as the vibration caused by the radial tyre deformation.

Comparisons have been made using theoretical results obtained with and without a bump stop, and it was found that the generated power is reduced with the stop but that the maximum stress generated is also reduced. Furthermore, the theoretical results for the radial tyre deformation have been compared to published experimental measurements and overall these are in good agreement. Also, the predictions obtained using the energy harvester model have been compared to the published experimental work. Similarities are found in the voltage output between the predictions and experimental measurements, and the way the energy harvester responds to the radial tyre deformation electrically.

Chapter 9. Conclusions and future work

9.1 Review and contribution of current work

The work presented in the previous chapters is reviewed here to offer an overview of the achievements, as well as identifying the contributions of the work.

A general introduction, motivation and objectives of the project were given in Chapter 1. The project was motivated by the market demand for TPMS, which has become a mandatory feature for new cars in the US and this will be applied to the EU in 2012 as well. The state-of-the-art TPMS are MEMS wireless sensors, normally embedded within car tyres. Using battery-less TPMS is always a necessary step forward because the short lifetime of batteries does not meet the power supply requirements. Vibration-based piezoelectric energy harvesting has been targeted as the desired solution to achieve this goal. Supplying sufficient power to the sensor is of primary importance, whilst maintaining the structural integrity of the energy harvesting device must also be considered. The literature review in Chapter 2 indicated that recent literature lacks awareness of the structural integrity issues for energy harvesters using piezoelectric materials. For these reasons, it is desirable to incorporate a bump stop in the harvester design to prevent mechanical failures by limiting the magnitude of displacement and reducing the bending stresses.

A theoretical model for a piezoelectric energy harvester was developed in Chapter 3.

The theoretical model developed was extended based on previous work. The main contribution from the model was the derivation and use of mode shape functions that considered the geometry of a tip mass. This enables the improved model to accurately predict the mechanical and electrical responses when a tip is attached. The theoretical model has been validated experimentally and good agreement was observed between the measurements and predictions. Additionally, parameter studies conducted in Chapter 4 demonstrated that maximum power output is achieved by using the optimal load resistance. It was also found that the choice of material and thickness ratio of the substrate to piezoelectric layers can affect the power generation significantly.

A theoretical model for an energy harvester incorporating a bump stop was developed in Chapter 5. The model was validated against experimental measurements and good agreement was observed in the different tests performed. The design of the bump stop was investigated to consider the influence of the initial gap size and stop location. It was found that using a small gap reduces the maximum bending stress and the voltage generated. It was also found that moving the bump stop location along the beam affected the electrical output of the energy harvester because the maximum displacement allowed was modified. The contributions from Chapter 5 were the development of a model incorporating the influence of a bump stop on the mechanical and electrical responses of a linear energy harvester, and the experimental validation.

Although the linear model and results presented in Chapter 5 provided insight into the influence of a bump stop, nonlinear behaviour of piezoelectric energy harvesters

was observed in experiments that could affect the accuracy of the theoretical predictions significantly, both with and without the stop. Chapter 6 investigated the nonlinear effects of a piezoelectric energy harvester and considered piezoelectric material nonlinearity and geometric nonlinearity in the model. The nonlinear coefficients arising in the piezoelectric constitutive equations were determined experimentally and were shown to induce a nonlinear softening effect. In contrast, the geometric nonlinearity was found to exhibit a nonlinear hardening behaviour. The nonlinear energy harvester model was validated experimentally, and good agreement was observed for and the natural frequency and frequency response measurements. The piezoelectric material nonlinearity was found to be the dominant source of nonlinearity, causing the energy harvester to exhibit a softening behaviour.

In Chapter 7, the nonlinear energy harvester model derived in Chapter 6 was incorporated with the bump stop model introduced in Chapter 5. A modified scheme using numerical methods was developed to model the impact between the energy harvester and stop for the nonlinear model. Simulation results obtained using the linear and nonlinear models were compared to the experimental results. It was found that both the linear and nonlinear models offered reasonably accurate predictions when the initial gap between the beam and stop was relatively small compared to the maximum beam displacement allowed at the impact point. However, the results also suggested that the nonlinear model yielded more accurate predictions when the initial gap is large and the base acceleration is high. The contributions of this study were the development of an improved numerical scheme for impact, which can be applicable to both linear and nonlinear models and

demonstrating the importance of using a nonlinear model in the impact system under different circumstances

A case study for a piezoelectric energy harvester embedded in a car tyre was presented in Chapter 8. The radial tyre deformation at the contact patch was modelled based on the tyre kinematics and used as the dominant source of excitation. Numerical examples demonstrated that the energy harvester generates maximum electrical power during deformation and little power is generated when the contact patch does not coincide with the road. Also, the centripetal force produced by the wheel rotation acts on the harvester, yielding an offset from its neutral axis. For this reason, the stop is located beneath the energy harvester (when the harvester is on the contact patch) to limit excessive beam bending. Numerical simulation results were compared with published experimental results to validate the model. Overall, there was reasonably good agreement between the results.

9.2 Suggestions for future work

Based on the work accomplished in this project, the current research may be extended based as described below.

Incorporating a bump stop model was studied in Chapter 5 and Chapter 7. Studies demonstrated that the voltage inevitably reduces in the presence of a stop. It was found that this is due to limiting the beam displacement and cancellation of the positive and negative charges. To minimise the reduction in generated voltage, the electrode coating on the piezoelectric layers could be divided into two or more

segments relating to tensile and compressive stress regions of the beam. The positive and negative charges could be collected separately to avoid charge cancelling to each other, and reducing the net charge generated by the piezoelectric layers.

The nonlinear model for the piezoelectric energy harvesters derived in Chapter 6 is only valid for low to moderate levels of acceleration. For accelerations beyond this range, the theoretical model overestimates the frequency shift and hence fails to predict the resonance frequency accurately. An alternative model is needed to predict the dynamical behaviour for high levels of base acceleration. Experimental results indicated that the damping ratio of the harvester varies approximately linearly with base acceleration prior to saturation occurring. The cause of this nonlinear damping behaviour is not well understood and should be investigated in future work. On the other hand, the nonlinear coefficients used in the piezoelectric material nonlinearity need to be determined experimentally as these values are not provided by material manufacturers, and the values of the nonlinear coefficients are different for different piezoelectric materials. A future investigation should be carried out to investigate the nonlinear coefficients in detail.

Chapter 8 demonstrated the power output generated by a tyre-embedded energy harvester incorporating a bump stop in a TPMS application. The developed model can be used as a design tool to investigate or optimise the performance of the harvester. A more detailed experimental investigation needs to be carried out and a micro-scale piezoelectric energy harvester should be used. As mentioned in Chapter 5 and Chapter 7, the initial gap size has a significant influence to both the electrical

output and bending stress of the energy harvester. However, fabricating or assembling a stop with a precise gap size may be challenging for a micro-scale energy harvester.

References

[1] J.M. Pearce, J.T. Hanlon, Energy conservation from systematic tire pressure regulation, Energy Policy, 35 (2007) 2673-2677.
[2] Tyre pressure sensor markets, III-Vs Review, 16 (2003) 9-9.
[3] T.P.M.S. Market, Tire pressure monitoring system market: Market satus and future challenges, 2007.
[4] Type-approval requirements for the general safety of motor vehicles ***I, 2009
[5] Policy department economic and scientific policy, 2008.
[6] http://en.wikipedia.org/wiki/European_Union_Emission_Trading_Scheme,
[7] R. Brusarosco, F. Massimo, F. Mancosu, A. Calatroni, Method and system for generating electrical energy within a vehicle tyre, United States, 2005.
[8] M. Raju, M. Grazier, Ultra-Low-Power Meets Energy Harvesting, Texas Instruments, 2010.
[9] S. Roundy, P.K. Wright, J. Rabaey, A study of low level vibrations as a power source for wireless sensor nodes, Computer Communications, 26 (2003) 1131-1144.
[10] M. Tanaka, An industrial and applied review of new MEMS devices features, Microelectronic Engineering, 84 1341-1344.
[11] S.R. Anton, H.A. Sodano, A review of power harvesting using piezoelectric materials (2003–2006), Smart Materials and Structures, 16 (2007) R1.
[12] S. Priya, D. Inman, Energy harvesting technologies, Springer, 2009.
[13] G.H. Haertling, Ferroelectric Ceramics: History and Technology, Journal of the American Ceramic Society, 82 (1999) 797-818.
[14] H.A. Sodano, J. Lloyd, D.J. Inman, An experimental comparison between several active composite actuators for power generation, Smart Materials and Structures, 15 (2006) 1211.
[15] D. Koyama, K. Nakamura, Electric power generation using vibration of a polyurea piezoelectric thin film, Applied Acoustics, 71 (2010) 439-445.
[16] M. Umeda, K. Nakamura, S. Ueha, Analysis of the Transformation of Mechanical Impact Energy to Electric Energy Using Piezoelectric Vibrator, Japanese Journal of Applied Physics, 35 (1996).
[17] R. Patel, A.A. Popov , S. McWilliam, Vibrational Energy Harvesting Devices Recent Patents on Mechanical Engineering, (2009) 80-92.

[18] A. Erturk, P.A. Tarazaga, J.R. Farmer, D.J. Inman, Effect of Strain Nodes and Electrode Configuration on Piezoelectric Energy Harvesting From Cantilevered Beams, Journal of Vibration and Acoustics, 131 (2009) 011010.
[19] S. Saadon, O. Sidek, A review of vibration-based MEMS piezoelectric energy harvesters, Energy Conversion and Management, 52 (2011) 500-504.
[20] J. Ajitsaria, S.Y. Choe, D. Shen, D.J. Kim, Modeling and analysis of a bimorph piezoelectric cantilever beam for voltage generation, Smart Materials and Structures, 16 (2007) 447.
[21] S. Roundy, P.K. Wright, A piezoelectric vibration based generator for wireless electronics, Smart Materials and Structures, 13 (2004) 1131.
[22] Y.C. Shu, I.C. Lien, Analysis of power output for piezoelectric energy harvesting systems, Smart Materials and Structures, 15 (2006) 1499.
[23] H.A. Sodano, G. Park, D.J. Inman, Estimation of electric charge output for piezoelectric energy harvesting, Strain, 40 (2004) 49-58.
[24] S.-N. Chen, G.-J. Wang, M.-C. Chien, Analytical modeling of piezoelectric vibration-induced micro power generator, Mechatronics, 16 (2006) 379-387.
[25] A. Erturk, D.J. Inman, A Distributed parameter electromechanical model for cantilevered piezoelectric energy harvesters, Journal of Vibration and Acoustics, 130 (2008) 041002.
[26] M. Kim, M. Hoegen, J. Dugundji, B.L. Wardle, Modeling and experimental verification of proof mass effects on vibration energy harvester performance, Smart Materials and Structures, 19 (2010) 045023.
[27] S. Rafique, P. Bonello, Experimental validation of a distributed parameter piezoelectric bimorph cantilever energy harvester, Smart Materials and Structures, 19 (2010) 094008.
[28] M. Renaud, et al., Optimization of a piezoelectric unimorph for shock and impact energy harvesting, Smart Materials and Structures, 16 (2007) 1125.
[29] A. Erturk, D.J. Inman, An experimentally validated bimorph cantilever model for piezoelectric energy harvesting from base excitations, Smart Materials and Structures, 18 (2009) 025009.
[30] J.-H. Lin, X.-M. Wu, H. Chen, X. Liu, T.-L. Ren, L.-T. Liu, Analyses of vibration-based piezoelectric power generator in discontinuous operation mode, Sensors and Actuators A: Physical, 152 (2009) 48-52.
[31] G.K. Ottman, H.F. Hofmann, A.C. Bhatt, G.A. Lesieutre, Adaptive piezoelectric energy harvesting circuit for wireless remote power supply, Power Electronics, IEEE Transactions on, 17 (2002) 669-676.
[32] A. Preumont, Mechatronics: Dynamics of Electromechanical and Piezoelectric Systems, Springer, Brussels, 2006.

[33] D. Guyomar, N. Aurelle, L. Eyraud, Piezoelectric ceramics nonlinear behavior. Application to Langevin transducer, J. Phys. III France, 7 (1997) 1197-1208.
[34] H. Man, T. Furukawa, M. Hoffman, S. Imlao, An indirect implicit technique for modelling piezoelectric ceramics, Computational Materials Science, 43 (2008) 629-640.
[35] K. Ishii, S. Tashiro, K. Nagata, Nonlinear piezoelectric coefficient of Pb(Ni,Nb)O3-Pb(Zn,Nb)O3-PbZrO3-PbTiO3 system ceramics, Journal of the European Ceramic Society, 24 (2004) 1699-1702.
[36] A. Triplett, D.D. Quinn, The effect of non-linear piezoelectric coupling on vibration-based energy harvesting, Journal of Intelligent Material Systems and Structures, 20 (2009) 1959-1967.
[37] S.C. Stanton, A. Erturk, B.P. Mann, D.J. Inman, Nonlinear piezoelectricity in electroelastic energy harvesters: Modeling and experimental identification, Journal of Applied Physics, 108 (2010) 074903-074903-074909.
[38] S. Belouettar, L. Azrar, E.M. Daya, V. Laptev, M. Potier-Ferry, Active control of nonlinear vibration of sandwich piezoelectric beams: A simplified approach, Computers & Structures, 86 (2008) 386-397.
[39] L.Q. Yao, J.G. Zhang, L. Lu, M.O. Lai, Nonlinear static characteristics of piezoelectric bending actuators under strong applied electric field, Sensors and Actuators A: Physical, 115 (2004) 168-175.
[40] S.K. Parashar, A. DasGupta, U. von Wagner, P. Hagedorn, Non-linear shear vibrations of piezoceramic actuators, International Journal of Non-Linear Mechanics, 40 (2005) 429-443.
[41] U. Von Wagner, P. Hagedorn, Peizo-Beam Systems Subjected to Weak Electric Field: Experiments and Modellig of Non-Linearities, Journal of Sound and Vibration, 256 (2002) 861-872.
[42] S.N. Mahmoodi, M.F. Daqaq, N. Jalili, On the nonlinear-flexural response of piezoelectrically driven microcantilever sensors, Sensors and Actuators A: Physical, 153 (2009) 171-179.
[43] G. Frank, W. Peter, Characterization of different beam shapes for piezoelectric energy harvesting, Journal of Micromechanics and Microengineering, 18 (2008) 104013.
[44] M.I. Friswell, S. Adhikari, Sensor design for piezoelectric cantilever beam energy harvesters;RASD, Sothampton, 2010; 140-148
[45] S. Roundy, E.S. Leland, J. Baker, E. Carleton, E. Reilly, E. Lai, B. Otis, J.M. Rabaey, P.K. Wright, V. Sundararajan, Improving power output for vibration-based energy scavengers, Pervasive Computing, IEEE, 4 (2005) 28-36.
[46] Y. Liao, H.A. Sodano, Optimal parameters and power characteristics of

piezoelectric energy harvesters with an RC circuit, Smart Materials and Structures, 18 (2009) 045011.
[47] Y. Hu, T. Hu, Q. Jiang, Coupled analysis for the harvesting structure and the modulating circuit in a piezoelectric bimorph energy harvester, Acta Mechanica Solida Sinica, 20 (2007) 296-308.
[48] J. Liang, W.-H. Liao, Energy flow in piezoelectric energy harvesting systems, Smart Materials and Structures, 20 (2011) 015005.
[49] K. Makihara, et al., Low energy dissipation electric circuit for energy harvesting, Smart Materials and Structures, 15 (2006) 1493.
[50] D. Maurath, C. Peters, T. Hehn, M. Ortmanns, Y. Manoli, Highly efficient integrated rectifier and voltage boosting circuits for energy harvesting applications, Adv. Radio Sci., 6 (2008) 219-225.
[51] R. D'Hulst, T. Sterken, R. Puers, G. Deconinck, J. Driesen, Power Processing Circuits for Piezoelectric Vibration-Based Energy Harvesters, Industrial Electronics, IEEE Transactions on, 57 (2010) 4170-4177.
[52] E. Dallago, D. Miatton, G. Venchi, G. Frattini, G. Ricotti, Self-Supplied Integrable Active High-Efficiency AC-DC Converter for Piezoelectric Energy Scavenging Systems;Circuits and Systems, 2007. ISCAS 2007. IEEE International Symposium on, 2007; 1633-1636
[53] E. Lefeuvre, A. Badel, C. Richard, L. Petit, D. Guyomar, A comparison between several vibration-powered piezoelectric generators for standalone systems, Sensors and Actuators A: Physical, 126 (2006) 405-416.
[54] J.M. Renno, M.F. Daqaq, D.J. Inman, On the optimal energy harvesting from a vibration source, Journal of Sound and Vibration, 320 (2009) 386-405.
[55] L. Chao, C.Y. Tsui, W.H. Ki, Vibration energy scavenging and management for ultra low power applications, Proceedings of the 2007 international symposium on Low power electronics and design, ACM, Portland, OR, USA, 2007, pp. 316-321.
[56] C. Mathuna, T. O'Donnell, R.V. Martinez-Catala, J. Rohan, B. O'Flynn, Energy scavenging for long-term deployable wireless sensor networks, Talanta, 75 (2008) 613-623.
[57] L. Chao, V. Raghunathan, K. Roy, Micro-scale energy harvesting: A system design perspective;Design Automation Conference (ASP-DAC), 2010 15th Asia and South Pacific, 2010; 89-94
[58] H.-B. Fang, J.-Q. Liu, Z.-Y. Xu, L. Dong, L. Wang, D. Chen, B.-C. Cai, Y. Liu, Fabrication and performance of MEMS-based piezoelectric power generator for vibration energy harvesting, Microelectronics Journal, 37 (2006) 1280-1284.
[59] Y.B. Jeon, R. Sood, J.h. Jeong, S.G. Kim, MEMS power generator with transverse mode thin film PZT, Sensors and Actuators A: Physical, 122 (2005) 16-22.

[60] M. Marzencki, Y. Ammar, S. Basrour, Integrated power harvesting system including a MEMS generator and a power management circuit, Sensors and Actuators A: Physical, 145-146 (2007) 363-370.
[61] P. Muralt, M. Marzencki, B. Belgacem, F. Calame, S. Basrour, Vibration Energy Harvesting with PZT Micro Device, Procedia Chemistry, 1 (2009) 1191-1194.
[62] M. Renaud, K. Karakaya, T. Sterken, P. Fiorini, C. Van Hoof, R. Puers, Fabrication, modelling and characterization of MEMS piezoelectric vibration harvesters, Sensors and Actuators A: Physical, 145-146 (2007) 380-386.
[63] D. Shen, J.-H. Park, J.H. Noh, S.-Y. Choe, S.-H. Kim, H.C. Wikle Iii, D.-J. Kim, Micromachined PZT cantilever based on SOI structure for low frequency vibration energy harvesting, Sensors and Actuators A: Physical, 154 (2009) 103-108.
[64] S.M. Shahruz, Design of mechanical band-pass filters with large frequency bands for energy scavenging, Mechatronics, 16 (2006) 523-531.
[65] J.-Q. Liu, H.-B. Fang, Z.-Y. Xu, X.-H. Mao, X.-C. Shen, D. Chen, H. Liao, B.-C. Cai, A MEMS-based piezoelectric power generator array for vibration energy harvesting, Microelectronics Journal, 39 (2008) 802-806.
[66] M. Ferrari, V. Ferrari, M. Guizzetti, D. Marioli, A. Taroni, Piezoelectric multifrequency energy converter for power harvesting in autonomous microsystems, Sensors and Actuators A: Physical, 142 (2008) 329-335.
[67] G. Park, T. Rosing, M.D. Todd, C.R. Farrar, W. Hodgkiss, Energy Harvesting for Structural Health Monitoring Sensor Networks, Journal of Infrastructure Systems, 14 (2008) 64-79.
[68] M. Keck, A new approach of a piezoelectric vibration-based power generator to supply next generation tire sensor systems;Sensors, 2007 IEEE, 2007; 1299-1302
[69] D. Guyomar, Y. Jayet, L. Petit, E. Lefeuvre, T. Monnier, C. Richard, M. Lallart, Synchronized switch harvesting applied to selfpowered smart systems: Piezoactive microgenerators for autonomous wireless transmitters, Sensors and Actuators A: Physical, 138 (2007) 151-160.
[70] E. Cantatore, M. Ouwerkerk, Energy scavenging and power management in networks of autonomous microsensors, Microelectronics Journal, 37 (2006) 1584-1590.
[71] R. Amirtharajah, J. Wenck, J. Collier, J. Siebert, B. Zhou, Circuits for energy harvesting sensor signal processing;Design Automation Conference, 2006 43rd ACM/IEEE, 2006; 639-644
[72] R. Wahab, Y.-S. Kim, H.-S. Shin, Fabrication, characterization and growth mechanism of heterostructured zinc oxide nanostructures via solution method, Current Applied Physics, 11 (2011) 334-340.
[73] Z.L. Wang, J. Song, Piezoelectric nanogenerators based on zinc oxide nanowire

arrays, Science, 312 (2006) 242-246.
[74] H. Tong, B.-L. Wang, Z.-C. Ou-Yang, Electric potential generated in ZnO nanowire due to piezoelectric effect, Thin Solid Films, 516 (2008) 2708-2710.
[75] Y. Qin, X. Wang, Z.L. Wang, Microfibre-nanowire hybrid structure for energy scavenging, Nature, 451 (2008) 809-813.
[76] C.H. Park, Dynamics modelling of beams with shunted piezoelectric elements, Journal of Sound and Vibration, 268 (2003) 115-129.
[77] J. Wilhelm, R. Rajamani, Methods for Multimodal Vibration Suppression and Energy Harvesting Using Piezoelectric Actuators, Journal of Vibration and Acoustics, 131 (2009) 011001.
[78] A. Erturk, D.J. Inman, On mechanical modeling of cantilevered piezoelectric vibration energy harvesters, Journal of Intelligent Material Systems and Structures, 19 (2008) 1311-1325.
[79] C.W.S. To, Vibration of a cantilever beam with a base excitation and tip mass, Journal of Sound and Vibration, 83 (1982) 445-460.
[80] S.J. Roundy, Energy scavenging for wireless sensor nodes with a focus on vibration to electricity conversion, The University of California, Berkeley, 2003.
[81] G.B. Warburton, The dynamical behaviour of structures, Pergamon Press, Oxford, 1976.
[82] S.G. Kelly, Fundamentals of mechanical vibrations, 2nd ed., McGraw Hill, 2000.
[83] M.J. Ramsay, W.W. Clark, Piezoelectric energy harvesting for bio-MEMS applications;2001; 429-438
[84] http://www.pcb.com/, PCB, 2010
[85] http://www.polytec.com/, Polytec, 2010
[86] http://www.thinksrs.com/products/SR785.htm, Stanford Research Systems, 2009
[87] http://www.piceramic.com/index.php, PI Ceramic, 2010
[88] http://piezo.com/prodbg1brass.html, Piezo Systems, 2009
[89] V.I. Babitsky, Theory of vibro-impact systems and applications, Meccanica, 34 (1999) 299-300.
[90] K.J.L. Fegelman, K. Grosh, Dynamics of a flexible beam contacting a linear spring at low frequency excitation: experiment and analysis, Journal of Vibration and Acoustics, 124 (2002) 237-249.
[91] C.C. Lo, A cantilever beam chattering against a stop, Journal of Sound and Vibration, 69 (1980) 245-255.
[92] A. Fathi, N. Popplewell, Improved approximations for a beam Impacting a stop, Journal of Sound and Vibration, 170 (1994) 365-375.
[93] H.C. Tsai, M.K. Wu, Methods to compute dynamic response of a cantilever with

a stop to limit motion, Computers & Structures, 58 (1996) 859-867.
[94] C. Wang, J. Kim, New analysis method for a thin beam impacting against a stop based on the full continuous model, Journal of Sound and Vibration, 191 (1996) 809-823.
[95] D.J. Wagg, S.R. Bishop, Application of non-smooth modelling techniques to the dynamics of a flexible impacting beam, Journal of Sound and Vibration, 256 (2002) 803-820.
[96] D.J. Wagg, A note on coefficient of restitution models including the effects of impact induced vibration, Journal of Sound and Vibration, 300 (2007) 1071-1078.
[97] S.J. Ahn, W.B. Jeong, W.S. Yoo, Improvement of impulse response spectrum and its application, Journal of Sound and Vibration, 288 (2005) 1223-1239.
[98] K.H. Mak, S. McWilliam, A.A. Popov, C.H.J. Fox, Vibro-Impact Dynamics of a Piezoelectric Energy Harvester, IMAC-XXVIII, Jacksonville, Florida USA, 2010.
[99] S.N. Mahmoodi, N. Jalili, M.F. Daqaq, Modeling, nonlinear dynamics, and identification of a piezoelectrically actuated microcantilever sensor, IEEE/ASME Transactions on Mechatronics, 13 (2008) 58-65.
[100] M.R.M.C.d. Silva, C.C. Glynn, Nonlinear flexural-flexural-torsional dynamics of inextensional beams. I. Equations of motion, Journal of Structural Mechanics, 6 (1978) 437 - 448.
[101] W.T. Thomson, Theory of Vibration with Applications, Prentice Hall, 1988.
[102] H. Nouira, E. Foltete, L. Hirsinger, S. Ballandras, Investigation of the effects of air on the dynamic behavior of a small cantilever beam, Journal of Sound and Vibration, 305 (2007) 243-260.
[103] L.Q. Yao, J.G. Zhang, L. Lu, M.O. Lai, Nonlinear dynamic characteristics of piezoelectric bending actuators under strong applied electric field, Microelectromechanical Systems, Journal of, 13 (2004) 645-652.
[104] R.L. Burden, J.D. Faires, Numerical Analysis, 7th ed., Brooks/Cole, Boston, 2001.
[105] Prospects for MEMS in the automotive industry, http://www.memsinvestorjournal.com/2007/08/prospects-for-m.html, 2008
[106] L. Wu, Y. Wang, J. Chen, Z. Chun, Battery-less piezoceramics mode energy harvesting for automobile TPMS;ASIC, 2009. ASICON '09. IEEE 8th International Conference on, 2009; 1205-1208
[107] M.J. Hamel, S.W. Arms, C.P. Townsend, D.L. Churchill, Energy harvesting for wireless sensor operation and data transmission, Micro Strain, Inc., United States, 2008.